

Dissertation zur Erlangung des Doktorgrades
der Fakultät für Chemie und Pharmazie
der Ludwig-Maximilians-Universität München

Lead Sulfide Quantum Dot-Based Nanostructured Solar Cells

Askhat N. Jumabekov

aus

Almaty, Kasachstan

2014

Erklärung

Diese Dissertation wurde im Sinne von § 7 der Promotionsordnung vom 28. November 2011 von Herrn Prof. Dr. Thomas Bein betreut.

Eidesstattliche Versicherung

Diese Dissertation wurde eigenständig und ohne unerlaubte Hilfe bearbeitet.

München, 26.09.2014

.....
(Unterschrift des Autors)

Dissertation eingereicht am 26.09.2014

1. Gutachter: Prof. Dr. Thomas Bein
2. Gutachter: Prof. Laurence M. Peter

Mündliche Prüfung am 28.10.2014

Acknowledgements

First and foremost, I would like to express my deepest gratitude to my supervisor, Prof. Thomas Bein, for assigning me an interesting research topic and his constant support and encouragement throughout my PhD studies. I have gained invaluable experience and knowledge from him over the past four years. I sincerely appreciate his kindness, patience and generosity both in scientific and social aspects of my studies in Germany.

I would also express my greatest gratitude to my second supervisor, Prof. Laurence M. Peter from the University of Bath in the UK, for mentoring and providing me with a constant support throughout my PhD studies. It was a great honour to work with him and learn from him.

I am very much grateful to the German Academic Exchange Service for the postgraduate DAAD scholarship that financially supported the first three years of my PhD studies. This scholarship has made my dream to pursue my PhD studies come true.

I would like to thank Dr. Mihaela Nedelcu, Prof. Ulrich Wiesner and Dr. Hiroaki Sai from Cornell University in the USA, and Prof. Jochen Feldmann and Dr. Felix Deschler from the LMU physics department for fruitful collaborations.

Many thanks to my research trainees Daniel Böhm, Pelle Garbus, Simone Meroni, Ashish Kulkarni, Timothy D. Siegler and Niklas Cordes for their work with me. I learned a lot by teaching and mentoring these wonderful and talented young students.

I would like to thank my fellow colleagues in the Bein group who in one way or another helped me to progress and accomplish my research endeavours and successfully complete my

studies. I am particularly grateful to Alesja Ivanova, Ksenia Fominykh and Dr. Dana Medina for their kind and joyful companionship, I deeply value our friendship established during these years. I would like to thank Dr. Steffen Schmidt for his help with the electron microscopy analysis of my samples. I am also grateful to Regina Huber and Tina Reuther for all the organisational help they have provided during my time in the group of Prof. Bein.

I also would like to thank my brother and sister as well as my friends for their encouragement, support and care.

Finally, I thank my parents, Sakhypzhamal and Nurkanat. Words are inadequate to express my gratitude for their love, encouragement and support throughout my life.

Abstract

The use of PbS quantum dots (QDs) acting as light absorbers in a range of nanostructured solar cell devices has been investigated. The impact of different QD deposition methods, of the nature and structure of different metal oxides serving as electrodes, as well as interface and surface effects on device performance has been explored. Chapter 3 describes the application of *in situ* grown PbS QDs as absorber layer for extremely thin absorber solar cells with the inorganic solid hole transporter CuSCN. A polystyrene-block-poly(ethylene oxide) block copolymer was employed as a structure-directing agent for the synthesis of mesoporous TiO₂ metal oxide thin films with high surface area and ordered porous structure. Chapter 4 outlines further work in which water-solubilized *ex situ* grown QDs capped with L-glutathione ligands were employed in order to improve the loading of the PbS QDs onto the internal surface of the porous oxide. Successful sensitization was achieved by inducing opposite surface charges on the surfaces of the QDs and the oxide in order to attract and attach QDs onto the surface of the porous supporting oxide film. The sensitized TiO₂ electrodes were used to make efficient liquid electrolyte quantum-dot-sensitized solar cells (QDSCs). Chapter 5 describes the use of SnO₂, which has a lower lying conduction band than TiO₂, to fabricate scaffolding electrodes that were sensitized with water-solubilized PbS QDs. Passivation of the SnO₂ electrodes with a thin layer of MgO, TiO₂ and a combination of both was utilized to investigate the effect of surface treatments on the performance of solid-state QDSCs, using Spiro-OMeTAD as organic hole transporter. Chapters 6 and 7 deal with different approaches towards interface tuning in solid-state QDSCs. This part of the work involved the study of solar cell devices utilizing *in situ* grown PbS QDs with and without organic and inorganic surface passivation, and *ex situ* grown PbS QDs anchored on mesoporous TiO₂ via organic linker molecules. The performance of the fabricated solar cells

was evaluated with standard current-voltage and incident-photon-to-collected-electron efficiency measurements, and physical parameters of the devices were characterised with frequency- and time-resolved techniques such as electrochemical impedance spectroscopy, intensity-modulated photovoltage/photocurrent spectroscopy, and open circuit voltage decay measurements, respectively. Overall, the work highlights the importance of surface passivation of QDs, loading of the QDs onto porous semiconducting oxide electrodes, as well as the significance of interfacial effects between QDs, oxides and hole transporter to achieve high-efficiency devices.

Table of Contents

1 Introduction	1
1.1 The Need for Sustainable Energy Sources	1
1.2 Photovoltaic Solar Cells	2
1.3 Quantum Dots.....	8
1.4 Quantum Dots as Sensitizers in Solar Cell Applications	11
1.5 Aims of the Present Thesis	14
References	15
2 Characterization.....	19
2.1 X-Ray Diffraction.....	19
2.2 Sorption	21
2.3 Electron Microscopy	24
2.3.1 Transmission Electron Microscope	27
2.3.2 Scanning Electron Microscope.....	29
2.4 Ultraviolet-Visible-Near Infrared Spectroscopy	31
2.5 Current-Voltage Characterisation.....	32
2.6 Incident-Photon-to-Collected-Electron Efficiency.....	34
2.7 Open Circuit Photovoltage Decay	35
2.8 Intensity-Modulated Photovoltage and Photocurrent Spectroscopy.....	37
2.9 Electrochemical Impedance Spectroscopy	39
References	42
3 Extremely Thin Absorber Solar Cells with PbS Quantum Dots and CuSCN Hole Conductor.....	46
3.1 Introduction	46
3.2 Results and Discussion.....	51
3.3 Conclusions	67
3.4 Experimental Section	68
3.4.1 Materials.....	68
3.4.2 Preparation of Mesoporous TiO ₂ Electrodes.....	69
3.4.3 Fabrication of Solar Cells.....	69
3.4.4 Characterization Methods.....	71
References	72
4 Quantum-Dot-Sensitized Solar Cells with Water-Soluble and Air-Stable PbS Quantum Dots	81

4.1 Introduction	82
4.2 Results and Discussion	85
4.3 Conclusions	104
4.4 Experimental Section	105
4.4.1 Materials	105
4.4.2 Preparation of Water-Soluble PbS QDs	105
4.4.3 Zeta Potential Measurements	106
4.4.4 Photoluminescence Experiments	106
4.4.5 TiO ₂ Photoanode Preparation	106
4.4.6 Fabrication of Solar Cells	107
4.4.7 Determination of the Amount of Adsorbed PbS QDs	108
4.4.8 Characterization Methods	108
References	110
5 Hybrid Solid-State PbS Quantum-Dot-Sensitized Solar Cells with SnO ₂ Electrodes	115
5.1 Introduction	115
5.2 Results and Discussion	118
5.3 Conclusion	130
5.4 Experimental Section	131
5.4.1 Materials	131
5.4.2 Preparation of Colloidal QDs	131
5.4.3 Preparation of SnO ₂ Electrodes	131
5.4.4 Fabrication of Solar Cells	132
5.4.5 Characterisation Methods	133
References	134
6 Comparison of Solid-State Quantum-Dot-Sensitized Solar Cells with <i>Ex Situ</i> and <i>In Situ</i> Grown PbS Quantum Dots	137
6.1 Introduction	138
6.2 Results and Discussion	139
6.3 Conclusions	157
6.4 Experimental Section	158
6.4.1 Materials	158
6.4.2 Preparation of Colloidal QDs	159
6.4.3 Preparation of TiO ₂ Electrodes	159
6.4.4 Estimation of Roughness Factor	160

6.4.5 Fabrication of Solar Cells	160
6.4.6 Characterization Methods.....	161
References	163
7 Effect of L-Glutathione and Iodide Passivation on the Performance of PbS Quantum-Dot-Sensitized Solar Cells	168
7.1 Introduction	169
7.2 Results and Discussion.....	171
7.2.1 GSH-Passivation	171
7.2.2 Iodide-Passivation	177
7.3 Conclusions	185
7.4 Experimental Section	186
7.4.1 Materials	186
7.4.2 TiO ₂ Photoanode Preparation	186
7.4.3 Synthesis of Methylammonium Iodide.....	187
7.4.4 Fabrication of Solar Cells.....	187
7.4.5 Characterization Methods.....	188
References	189
8 Conclusions and Outlook	194
9 Appendices	198
Appendix A: Supplementary Information	198
Appendix B: Glossary of Symbols	219
10 Curriculum Vitae	222
11 Publications and Presentations	223
11.1 Publications	223
11.2 Poster Presentations.....	223
11.3 Oral Presentations.....	224

1 Introduction

1.1 The Need for Sustainable Energy Sources

It is predicted that the rate of global energy consumption will increase by 93% by the year 2040 and triple by the end of the century compared to the world's primary energy consumption in 2010, which was about 20.2 Terawatts.¹ It is clear that carbon-rich sources such as oil, coal and natural gas are not the solution for the increasing energy demand due to their negative environmental impact such as CO₂ emission, and their finite natural abundance.¹⁻³ Nuclear power could be a feasible way to meet the energy demand, but it has major safety issues.

Solar energy, on the other hand, is the most sustainable and clean energy source that provides the earth with about 120,000 Terawatts of radiation, thus making it a very attractive source for green, sustainable and efficient energy conversion devices such as solar cells that can ultimately be combined with hydrogen fuel cells and storage devices such as batteries. These devices, particularly solar cells, could be very promising candidates for the partial solution of the energy issues. Solar cells are photovoltaic devices that convert solar energy into electrical energy. However, the cost of electricity produced by conventional silicon-based or thin film solar cells such as copper-indium-gallium-selenide (CIGS) is still relatively high, and further developments are needed to reduce the cost and CO₂ impact of manufacture.⁴

1.2 Photovoltaic Solar Cells

The field of photovoltaics deals with the conversion of light into electricity. The term *photovoltaic* derives from the combination of two words, *phos* (Greek word for light) and *volt* (unit for electrical voltage named after the Italian physicist Alessandro Volta). The first experimental observation of the photovoltaic effect was made by the French physicist Edmond Becquerel, who established the foundations of the field. In his experiments Becquerel detected current passing between two platinum electrodes immersed into an electrolyte with metal halide salts when illuminated by sunlight.^{5, 6} Since then, many different types of photovoltaic and photoelectrochemical solar cell devices have been developed,⁶ and remarkable progress has been achieved in understanding the basics and operation principles of solar cells. Nowadays, a range of materials is used to fabricate solar cells, and photoelectric conversion efficiencies as high as ~45% have been achieved with modern devices (Figure 1.1).

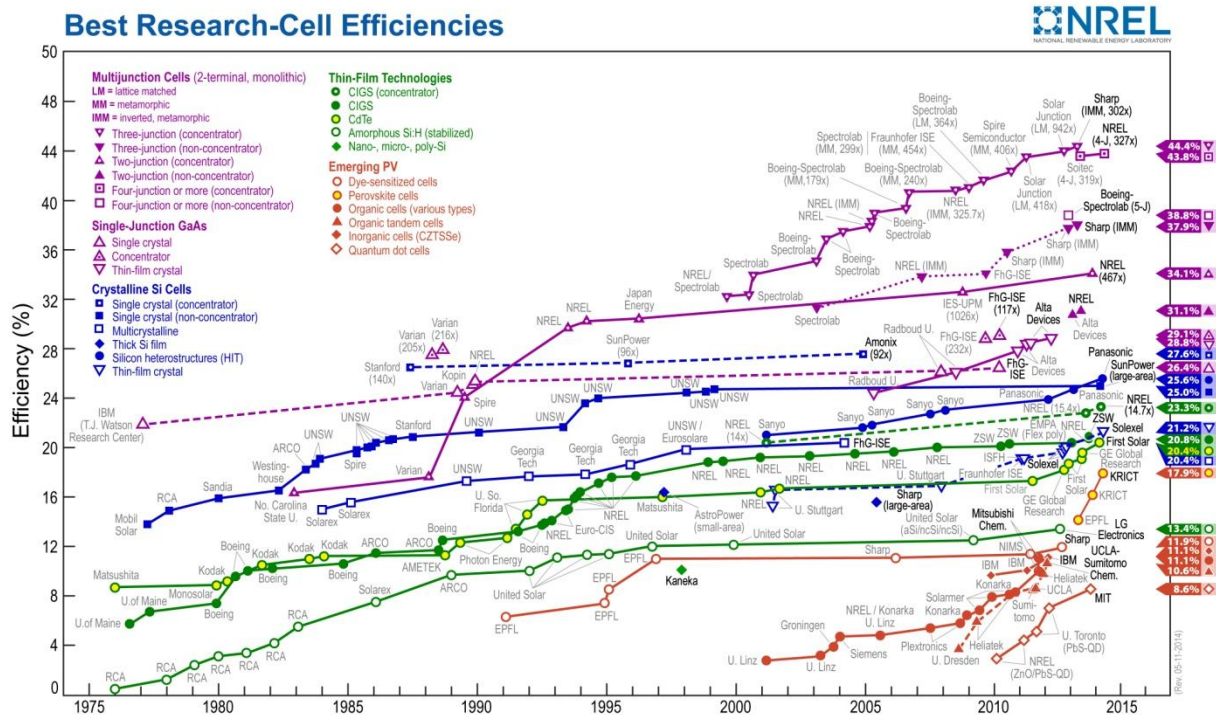


Figure 1.1. Current efficiencies for the best research solar cells. National Renewable Energy Laboratory (NREL), Golden, CO.⁷

In general, photovoltaic solar cell devices can be loosely grouped into three categories - first, second and third generation solar cells - based on the nature of the materials, maximum achievable performance, production and installation costs.⁶ First generation solar cells employ high purity and high quality materials such as single crystals. Examples are single junction crystalline GaAs and Si solar cells. The working principle of these solar cells is based on the separation of photogenerated electron-hole pairs at the interface between n-doped (electron-rich) and p-doped (electron-deficient) semiconductors. When n-type (Fermi level closer to conduction band) and p-type (Fermi level closer to valence band) semiconductors are brought together, electrons move from the n-type section into the p-type section so as to equilibrate the Fermi level (in the dark). The negative and positive space charge built up at the vicinity of p-type and n-type materials results in formation of a depletion layer in the p-n junction, with the electric field directed from n-type material towards the p-type material (Figure 1.2).⁶ Under illumination, the Fermi level at the p-n junction splits into two quasi-Fermi levels in

the p-type and n-type sections, respectively. The difference between the p-type and n-type quasi-Fermi levels gives the open circuit voltage. In the neutral regions both quasi-Fermi levels become the same as the majority-Fermi level.

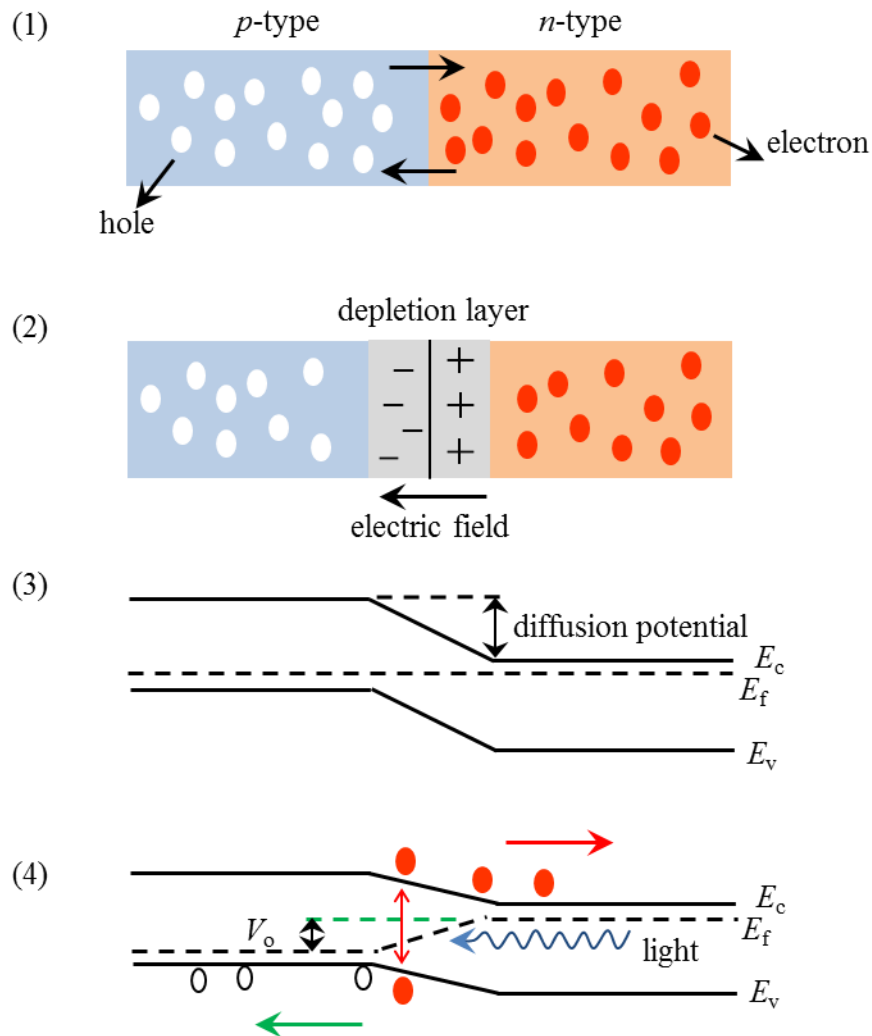


Figure 1.2. Schematic representation of a p-n junction. (1) Diffusion of charge carriers; (2) formation of depletion region at the p-n junction; (3) band structure in the dark; (4) band structure under illumination. (Figure reproduced after Ref. 6)

To date, first generation solar cells produce the highest efficiencies both in single and multijunction devices (see Figure 1.1). However, due to high production and installation costs these solar cells exceed the cost of US \$1/watt photoelectric power conversion.⁶

Second generation solar cells, also referred to as thin film solar cells, employ less material and low-cost manufacturing techniques, which helps to bring down the price for photoelectric power conversion to less than US \$1/watt.⁶ Cadmium telluride (CdTe) and CIGS are typical examples of second generation solar cells (Figure 1.3).⁸ Despite the low-cost fabrication methods, these solar cells produce high efficiencies (e.g. 23.3% for CIGS) relative to single crystal Si solar cells (27.6%). Despite these very good efficiencies, issues such as the use of rare (In) and/or toxic elements (Cd) remain.

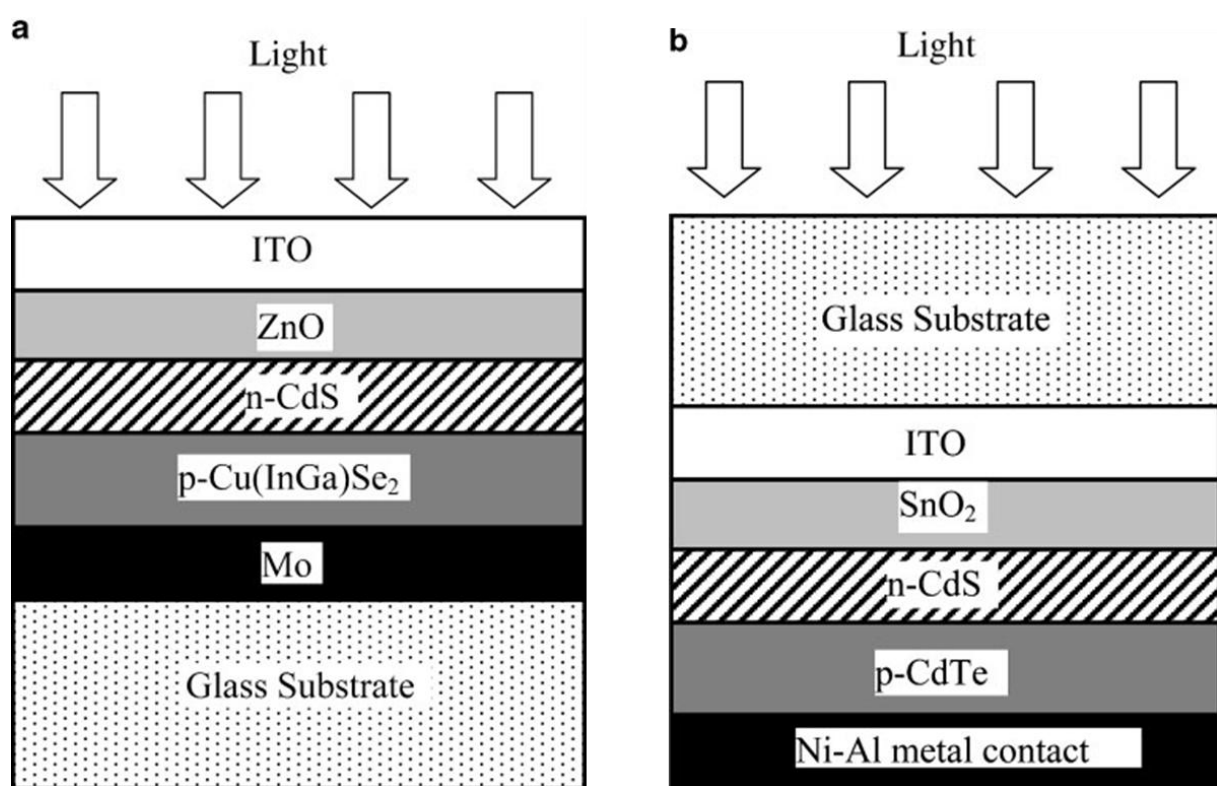


Figure 1.3. Schematic cross-section view of thin film (a) CIGS and (b) CdTe solar cells. (Figure adapted from Ref. 8)

In 1961 Shockley and Queisser reported a so called “detailed balance limit” of the efficiency of single junction solar cells.⁹ They calculated the maximum theoretical efficiency for single p-n junction solar cells and found it to be about 30% for an energy gap of 1.1 eV under 1 sun illumination.⁹ The analysis shows that this limit is due to loss mechanisms such as non-usage

of the photon energies smaller than the bandgap and thermalisation of photon energies higher than the bandgap.⁶

There have been several approaches proposed to overcome the Shockley-Queisser limit. One of these is up- and down-conversion, in which use of a material that can absorb more than one low-energy photons and emit one photon with energy above the band gap (also referred to as anti-Stokes optical process) is proposed in the case of up-conversion. On the other hand, use of another material is proposed that can absorb a high-energy photon and emit two low-energy photons with energies just above the band gap (also referred to as quantum cutting) in the case of down-conversion.^{6, 10} So-called multiple exciton generation (MEG), which uses photons with energies at least twice greater than the bandgap energy to generate and split two excitons out of one absorbed energetic photon is another promising approach under investigation.^{6, 10, 11} Extraction of “hot” charge carriers before they thermalize is also an additional way to make use of energetic photons and thus increase the voltage of the cells.⁶ In view of these developments, it has been predicted that successful application of all these approaches to decrease the nonradiative losses will help to break the Shockley-Queisser limit for single junction solar cells. Solar cell devices that employ these approaches are often referred to as third generation solar cells.^{6, 10} The physical basis for these strategies could include, for instance, dye-sensitized, quantum-dot-sensitized and organic bulk-heterojunction solar cells.⁶ It should be noted that strictly speaking so far only quantum-dot-sensitized solar cells fulfill some of the criteria for the third generation solar cells. If successful, these devices promise to bring down the cost for photoelectric power conversion to less than US \$0.5/watt.⁶

The pioneering endeavors of Grätzel and O'Regan from the Swiss Federal Institute of Technology in Lausanne (EPFL, Switzerland) resulted in the development of dye-sensitised solar cells (DSCs) around 1991.¹² Although not as good as the crystalline Si or CIGS solid-state solar cells in terms of efficiency, DSCs promise to be relatively inexpensive (one of the

main cost factors is the transparent conducting oxide substrate) and easy to make.¹³ The record efficiency values of the state-of-the-art DSCs with liquid and solid hole transporting materials (HTMs) are about 13% and 7.2% respectively.^{14, 15} DSCs are comprised of a mesoporous TiO₂ anode sensitized with a light absorbing dye layer and permeated by a liquid redox couple or solid HTM (Figure 1.4).¹⁶ Under illumination the dye molecule absorbs a photon and becomes excited by the transfer of an electron from the highest occupied molecular orbital (HOMO) to lowest unoccupied molecular orbital (LUMO). The excited dye molecule then injects the excited electron into the conduction band of TiO₂, and the dye is regenerated from its oxidized state by accepting an electron from the redox couple. The redox couple then transports the 'holes' to the cathode, where they accept electrons to complete the regenerative cycle.

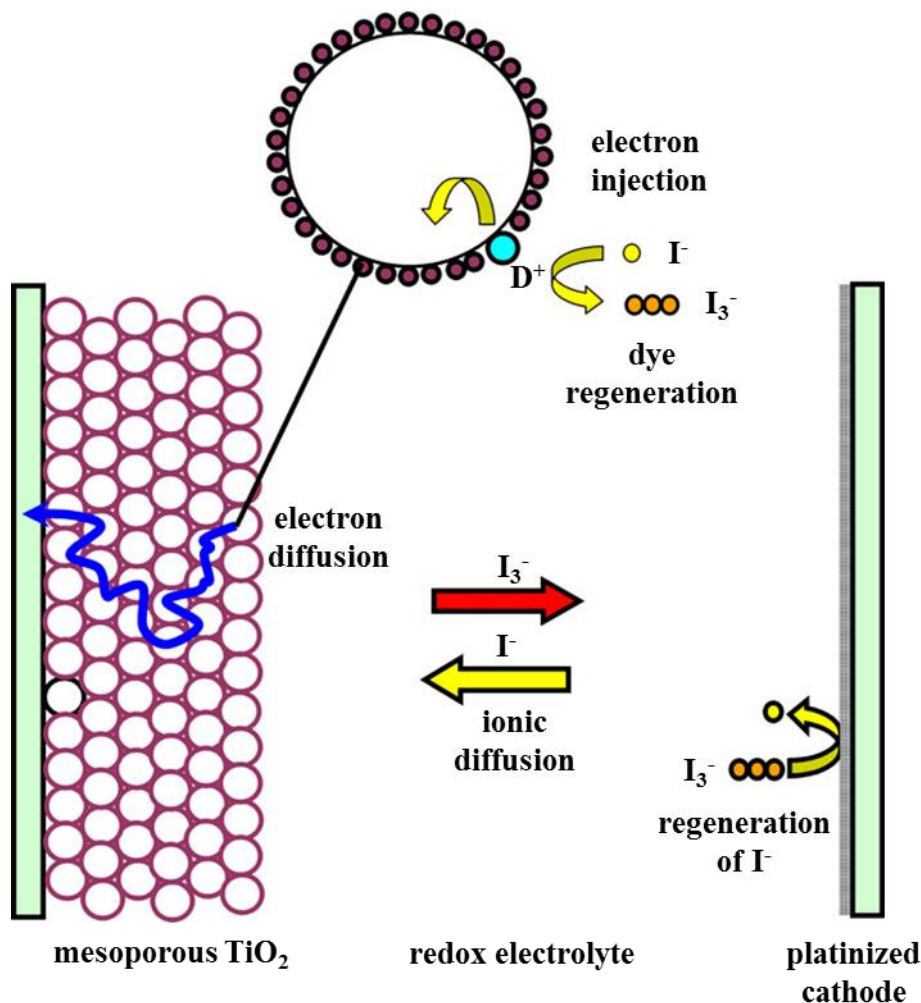


Figure 1.4. Schematic diagram of working principle of a DSC. (Figure adapted from Ref. 16)

1.3 Quantum Dots

Quantum dots (QDs) are small nanoparticles of semiconducting materials that have hybrid molecular/solid-state electronic properties. QDs are also referred to as artificial atoms due to their discrete electronic energy levels, which are analogous to those in atoms or individual molecules; however, the spacing between these electronic energy levels can be controlled by changing the size of the nanoparticle.¹⁷ In 1984 Brus could show that the electronic properties of ultrafine particles (~5 nm diameter) of ZnO, CdS, GaAs and InSb differ from those of

bulk.¹⁸ He demonstrated that the energy of the lowest excited electronic state is a function of particle size, i.e., the band gap of these materials becomes larger as the size of nanoparticles decreases (Figure 1.5).

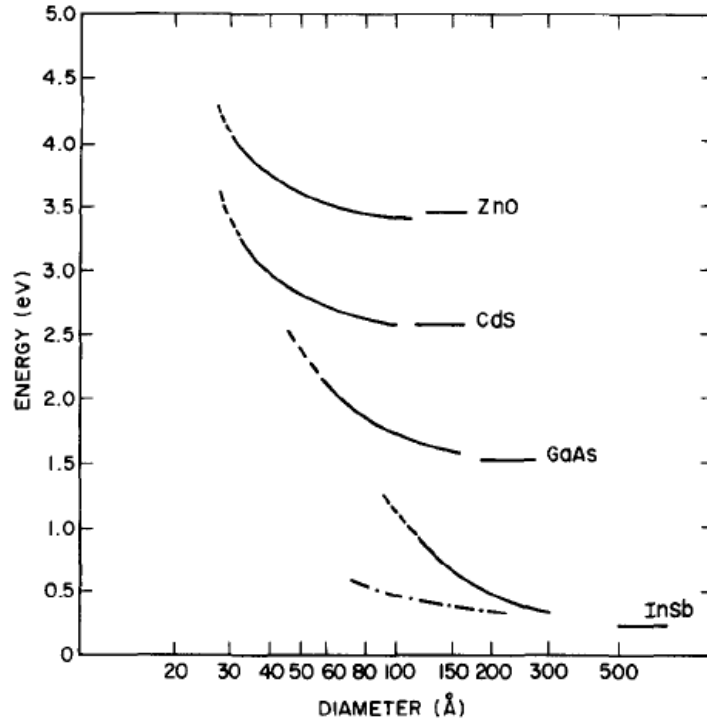


Figure 1.5. Calculated dependencies of the LUMO energy levels of ZnO, CdS, GaAs and InSb on particle size. (Figure adapted from Ref. 18)

Brus also derived an analytical approximation for the energy of the first excited electronic state (lowest eigenvalue) as expressed in the following:^{19, 20}

$$E^* \simeq E_g + \frac{\hbar^2 \pi^2}{2R_p^2} \left[\frac{1}{m_e} + \frac{1}{m_h} \right] - \frac{1.8e^2}{\epsilon \cdot R_p} + \text{smaller terms}, \quad (1.1)$$

where E_g is the bulk bandgap, \hbar is the reduced Planck constant, m_e and m_h are the masses of electrons and holes, respectively, R_p is radius of the particle and ϵ is the semiconductor dielectric constant. The second term on the right hand side of equation (1.1), which is known

as the Brus equation, is the quantum confinement energy, also referred to as the particle-in-a-box quantum energy, whereas the third term is the Coulomb interaction energy. The Brus equation was obtained by using a Hamiltonian in which the interaction between electron and hole is assumed to be a shielded Coulomb interaction (1.2):¹⁸⁻²⁰

$$E^* = \frac{-\hbar^2}{2m_e} \nabla_e^2 - \frac{-\hbar^2}{2m_h} \nabla_h^2 - \frac{e^2}{\epsilon|r_e-r_h|} + \textit{polarization terms} \quad (1.2)$$

The confinement term in equation (1.1) shifts the energy of the first excited electronic state upwards, whereas the Coulomb term shifts it downwards. It should be noted that in equation (1.1), E^* is proportional to the size of QD as R_p^{-2} in the second, confinement term, whereas in the Coulomb term $E^* \sim R_p^{-1}$. Therefore, as the size of particle becomes smaller, the confinement effect gets stronger than the Coulomb interaction, which leads to the widening of the bandgap. In general, the confinement in QDs can be divided into three types – strong, intermediate and weak. The criterion according to which these confinement types are recognized is based on a comparison of the size of the QD with its Bohr exciton radius, a_B . The Bohr exciton radius is the average distance between the excited electron in the conduction band and the hole in the valence band and is calculated from the following relationship:¹⁹

$$a_B = \left[\frac{m_e \cdot \epsilon}{m_e \cdot m_h} \right] a_0^H \quad (1.3)$$

Here a_0^H is the Bohr radius of the hydrogen atom. If the size of the QD, d_{QD} , is much smaller than twice the exciton Bohr radius ($d_{QD} \ll 2a_B$), the QD possesses a strong confinement, whereas in the case where $d_{QD} \sim 2a_B$ or $d_{QD} \gg 2a_B$ there is an intermediate or weak confinement, respectively.

1.4 Quantum Dots as Sensitizers in Solar Cell Applications

An exciton (weakly bound electron-hole pair) is generated when semiconductor materials absorb a photon with energy higher than the bandgap. It is possible to split the exciton if the electron can be physically separated from the hole. One way to achieve this is to use a material, for instance, another semiconductor with a conduction band edge lying lower than that of the donor semiconductor, to accept the electron from donor material before it recombines with the hole. In this sense, the donor material can be referred to as a 'sensitizer'. Here, the energy difference between the conduction band edges of the donor and acceptor makes it energetically favorable for the excited electron to inject into the conduction band of the acceptor material, thus leaving the hole in the donor material. This process is of fundamental scientific importance since it is a basis for all photovoltaic devices.

QDs are very attractive for the purpose of sensitizing acceptor semiconducting materials due to possibility to tune the bandgap by changing the size of the QD nanocrystals (Figure 1.6).²¹ Another important aspect of QDs is based on their molecule-like electronic energy levels. QDs could make it possible to slow down the thermalisation of excitons via phonon emission when energetic photons are absorbed by the QDs. This would allow implementation of processes such as hot carrier extraction and multiple exciton generation and splitting.⁶

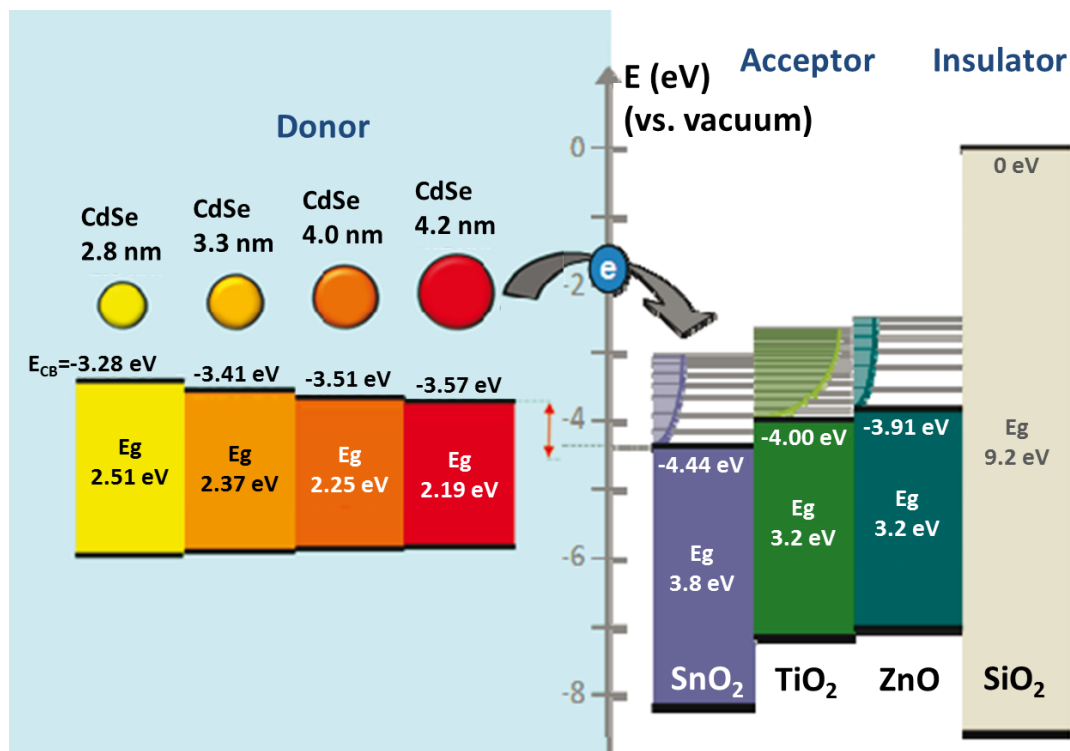


Figure 1.6. Band energy diagrams of donor CdSe QDs (with different sizes) and metal oxides (SnO₂, TiO₂, ZnO and SiO₂) acting as acceptors. (Figure adapted from Ref. 21)

In 1986 Gerischer and L ubke demonstrated that the incident-photon-to-collected-electron efficiency (IPCE) of CdS-sensitized TiO₂ shifts towards lower energy relative to a blank, non-sensitized TiO₂ electrode. They proposed that under illumination the CdS sensitizer layer injects electrons into the conduction band of TiO₂.²² A few years later in 1990 Vogel and co-workers reported the first working solar cell with porous, polycrystalline TiO₂ electrode sensitized with CdS QDs. They obtained a solar cell with an open circuit voltage of $V_{OC} = 395$ mV, a short circuit current density of $J_{SC} = 0.017$ mA cm⁻², a fill factor of $FF = 75\%$ and power conversion efficiency of $\eta = 6\%$ when illuminated with $\lambda = 460$ nm monochromatic light with an incident light power of $P_{in} = 0.086$ mW cm⁻².²³

The working principle of quantum-dot-sensitized solar cells (QDSCs) is similar to DSCs. QDs are deposited onto wide-bandgap scaffolding metal oxide semiconductor electrodes such as TiO₂, SnO₂ or ZnO and permeated by a liquid redox couple or solid HTM (Figure 1.7).²⁴

Under illumination, the exciton generated in the QD injects an electron into the conduction band of the metal oxide. The hole left in the QD then accepts an electron from the redox couple, and transport of the oxidized redox species to the counter electrode to accept an electron completes the regenerative cycle.

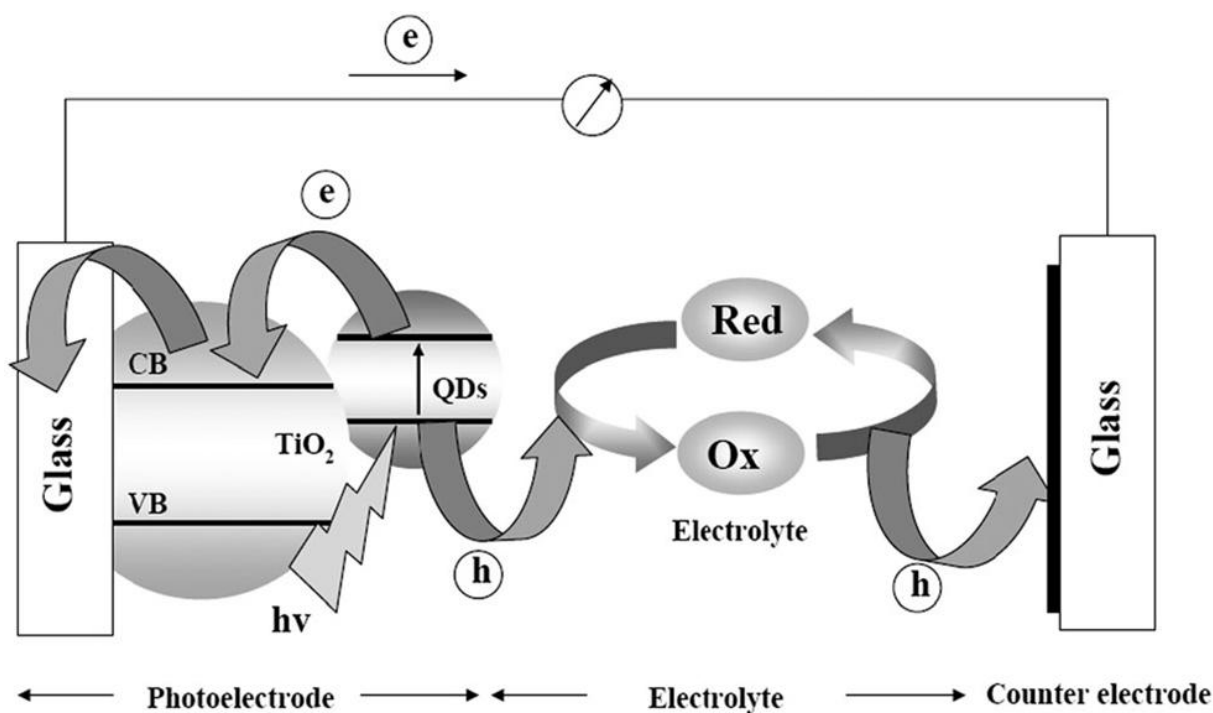


Figure 1.7. Schematic diagram of the working principle of a QDSC. (Figure adapted from Ref. 24)

It has been proposed that QDSCs could offer favorable features compared to their DSC counterparts based on the facile synthesis and processing of QDs and the abundance and variety of different materials that can be used.⁴ In principle, the size-dependent bandgap tunability of QDs allows for harvesting photons over the optimum spectral range and the design multi-junction tandem solar cells.^{25, 26} The diversity of different possible device architectures such as liquid or solid-state QDSCs,²⁷⁻²⁹ extremely thin absorber (ETA) cells,³⁰⁻³² Schottky-junction cells,^{33, 34} fully inorganic or organic/inorganic depleted³⁵⁻³⁷ or bulk-heterojunction³⁸⁻⁴⁰ cells makes them very attractive for many different applications.

1.5 Aims of the Present Thesis

Based on their physical properties (and despite the toxicity of lead), lead-based QDs such as PbSe and PbS have shown to be some of the most attractive materials for solar cell design. Recent achievements in the implementation of hot carrier extraction and multiple exciton generation and splitting schemes with PbSe-TiO₂ and PbS-TiO₂ constructs, respectively, have demonstrated the importance of surface treatment of the QDs and the interface between electron donor QDs and electron acceptor metal oxides for the development of efficient solar cell devices.⁴¹⁻⁴³

With this in mind, we have fabricated and studied different PbS QD-based solar cell devices to characterize and understand different scenarios for QD/metal oxide, QD/hole mediator and metal oxide/hole mediator interfaces and their effect on the performance of the devices. Our main concern throughout the course of the studies was to characterize important parameters of the cells such as efficient sensitization of TiO₂ with QDs (i.e., surface coverage of TiO₂ with small enough QDs) as well as charge injection and separation. Perhaps the most exciting part of this work has been an attempt to achieve high and efficient coverage of porous metal oxide surfaces with water-soluble and air-stable PbS QDs and the use of these photoanodes in liquid electrolyte-based QDSCs. Another aspect of this work was aimed at examining different strategies to passivate and protect QDs as well as metal oxides in order to improve charge injection and separation processes. We tried to obtain a quantitative as well as qualitative estimation of physical parameters of fabricated solar cells by using frequency-resolved techniques such as electrochemical impedance spectroscopy and intensity-modulated photovoltage/photocurrent spectroscopy to shed light on the role of interfacial effects on solar cell performance.

References

1. U.S. Energy Information Administration, *International Energy Outlook 2013*, Washington, 2013.
2. World Energy Council, *World Energy Resources 2013 Survey: Summary*, London, 2013.
3. World Energy Council, *World Energy Perspective: Energy Efficiency Technologies: Overview Report*, London, 2013.
4. C. Wadia, A. P. Alivisatos and D. M. Kammen, *Environmental Science & Technology*, 2009, **43**, 2072-2077.
5. E. Becquerel, *Comptes rendus de l'Académie des sciences*, 1839, **9**, 145-149.
6. K. Kalyanasundaram, *Dye-Sensitized Solar Cells*, CRC Press, Boca Raton, 2010.
7. NREL, National Renewable Energy Laboratory, Golden, 2014.
8. K. L. Chopra, P. D. Paulson and V. Dutta, *Progress in Photovoltaics: Research and Applications*, 2004, **12**, 69-92.
9. W. Shockley and H. J. Queisser, *Journal of Applied Physics*, 1961, **32**, 510-519.
10. G. Chen, J. Seo, C. Yang and P. N. Prasad, *Chemical Society Reviews*, 2013, **42**, 8304-8338.
11. A. J. Nozik, *Nature Nanotechnol.*, 2009, **4**, 548-549.
12. B. O'Regan and M. Gratzel, *Nature*, 1991, **353**, 737-740.

13. B. E. Hardin, H. J. Snaith and M. D. McGehee, *Nature Photonics*, 2012, **6**, 162-169.
14. S. Mathew, A. Yella, P. Gao, R. Humphry-Baker, F. E. CurchodBasile, N. Ashari-Astani, I. Tavernelli, U. Rothlisberger, K. NazeeruddinMd and M. Grätzel, *Nature Chemistry*, 2014, **6**, 242-247.
15. J. Burschka, A. Dualeh, F. Kessler, E. Baranoff, N.-L. Cevey-Ha, C. Yi, M. K. Nazeeruddin and M. Grätzel, *Journal of the American Chemical Society*, 2011, **133**, 18042-18045.
16. L. M. Peter, *Philosophical Transactions of the Royal Society A: Mathematical, Physical and Engineering Sciences*, 2011, **369**, 1840-1856.
17. S. M. Reimann and M. Manninen, *Reviews of Modern Physics*, 2002, **74**, 1283-1342.
18. L. E. Brus, *The Journal of Chemical Physics*, 1984, **80**, 4403-4409.
19. L. Brus, *The Journal of Physical Chemistry*, 1986, **90**, 2555-2560.
20. M. G. Bawendi, M. L. Steigerwald and L. E. Brus, *Annual Review of Physical Chemistry*, 1990, **41**, 477-496.
21. P. V. Kamat, *Accounts of Chemical Research*, 2012, **45**, 1906-1915.
22. H. Gerischer and M. Lübke, *Journal of Electroanalytical Chemistry and Interfacial Electrochemistry*, 1986, **204**, 225-227.
23. R. Vogel, K. Pohl and H. Weller, *Chemical Physics Letters*, 1990, **174**, 241-246.
24. Z. Yang, C.-Y. Chen, P. Roy and H.-T. Chang, *Chemical Communications*, 2011, **47**, 9561-9571.

25. X. Wang, G. I. Koleilat, J. Tang, H. Liu, I. J. Kramer, R. Debnath, L. Brzozowski, D. A. R. Barkhouse, L. Levina, S. Hoogland and E. H. Sargent, *Nature Photonics*, 2011, **5**, 480-484.
26. Z. Ning, D. Zhitomirsky, V. Adinolfi, B. Sutherland, J. Xu, O. Voznyy, P. Maraghechi, X. Lan, S. Hoogland, Y. Ren and E. H. Sargent, *Advanced Materials*, 2013, **25**, 1719-1723.
27. S. D. Sung, I. Lim, P. Kang, C. Lee and W. I. Lee, *Chemical Communications*, 2013, **49**, 6054-6056.
28. H. Lee, H. C. Leventis, S.-J. Moon, P. Chen, S. Ito, S. A. Haque, T. Torres, F. Nüesch, T. Geiger, S. M. Zakeeruddin, M. Grätzel and M. K. Nazeeruddin, *Advanced Functional Materials*, 2009, **19**, 2735-2742.
29. S. Kim, S. H. Im, M. Kang, J. H. Heo, S. I. Seok, S.-W. Kim, I. Mora-Seró and J. Bisquert, *Physical Chemistry Chemical Physics*, 2012, **14**, 14999-15002.
30. C. Lévy-Clément and J. Elias, *ChemPhysChem*, 2013, **14**, 2321-2330.
31. G. Hodes and D. Cahen, *Accounts of Chemical Research*, 2012, **45**, 705-713.
32. S. H. Im, C.-S. Lim, J. A. Chang, Y. H. Lee, N. Maiti, H.-J. Kim, M. K. Nazeeruddin, M. Grätzel and S. I. Seok, *Nano Letters*, 2011, **11**, 4789-4793.
33. H. Choi, J. K. Kim, J. H. Song, Y. Kim and S. Jeong, *Applied Physics Letters*, 2013, **102**, 193902-193904.
34. C. Piliego, L. Protesescu, S. Z. Bisri, M. V. Kovalenko and M. A. Loi, *Energy & Environmental Science*, 2013, **6**, 3054-3059.

35. A. H. Ip, S. M. Thon, S. Hoogland, O. Voznyy, D. Zhitomirsky, R. Debnath, L. Levina, L. R. Rollny, G. H. Carey, A. Fischer, K. W. Kemp, I. J. Kramer, Z. Ning, A. J. Labelle, K. W. Chou, A. Amassian and E. H. Sargent, *Nature Nanotechnol.*, 2012, **7**, 577-582.
36. B. Ehrler, M. W. B. Wilson, A. Rao, R. H. Friend and N. C. Greenham, *Nano Letters*, 2012, **12**, 1053-1057.
37. N. Zhao, T. P. Osedach, L.-Y. Chang, S. M. Geyer, D. Wanger, M. T. Binda, A. C. Arango, M. G. Bawendi and V. Bulovic, *ACS Nano*, 2010, **4**, 3743-3752.
38. J. Jean, S. Chang, P. R. Brown, J. J. Cheng, P. H. Rekemeyer, M. G. Bawendi, S. Gradečak and V. Bulović, *Advanced Materials*, 2013, **25**, 2790-2796.
39. H. Park, S. Chang, J. Jean, J. J. Cheng, P. T. Araujo, M. Wang, M. G. Bawendi, M. S. Dresselhaus, V. Bulović, J. Kong and S. Gradečak, *Nano Letters*, 2013, **13**, 233-239.
40. J. Seo, M. J. Cho, D. Lee, A. N. Cartwright and P. N. Prasad, *Advanced Materials*, 2011, **23**, 3984-3988.
41. W. A. Tisdale, K. J. Williams, B. A. Timp, D. J. Norris, E. S. Aydil and X.-Y. Zhu, *Science*, 2010, **328**, 1543-1547.
42. J. B. Sambur, T. Novet and B. A. Parkinson, *Science*, 2010, **330**, 63-66.
43. I. J. Kramer and E. H. Sargent, *Chemical Reviews*, 2014, **114**, 863-882.

2 Characterization

2.1 X-Ray Diffraction

X-ray diffraction (XRD) is a standard analytical technique for structural characterization of inorganic and organic specimens such as powders, films and bulk materials. The working principle of the XRD measurement is based on the detection of elastically scattered X-rays upon interaction of incident X-ray radiation with regular arrays of atoms in the crystal lattice of a material (Figure 2.1).

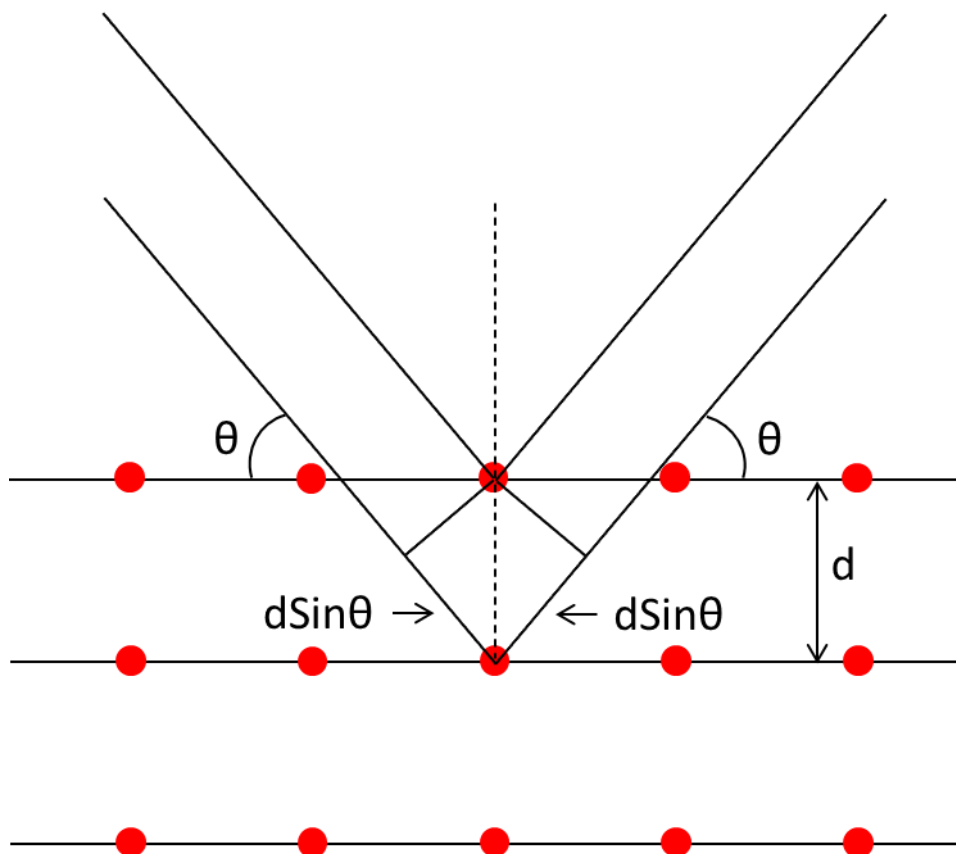


Figure 2.1. Scattering of incident X-ray radiation from atomic planes of a crystal.

The beam that is scattered from the atomic planes of crystalline material (through interactions with the electrons) yields a discrete diffraction pattern since the wavelength of X-ray radiation (usually Cu-K_α radiation with a wavelength of ~0.15 nm) is comparable to the interatomic spacings in the lattice. The diffraction pattern can be produced by plotting the intensity of the scattered X-ray radiation as a function of scattering angle. The constructive interference of scattered radiation is detected as a peak in the diffraction spectrum. The relationship between the angle of constructive interference and dimensions of the lattice planes is expressed by Bragg's law:¹

$$n\lambda = 2d \cdot \sin \theta, \quad (2.1)$$

where n is an integer, λ is wavelength of the X-ray radiation, d is spacing between the atomic planes of the crystal, and θ is the diffraction angle (also referred as Bragg angle), which is the angle between the incident beam and the scattering atomic planes. The diffraction angles at which the constructive interference occurs depend on the Bravais lattice and the parameters of the unit cell. The diffraction peak intensities of the diffraction pattern depend on atomic numbers and the arrangement of the constituent atoms in the crystal. Therefore, each material has its own unique diffraction pattern. The structure and chemical composition of the sample material can be identified by comparative analysis of its diffraction pattern with a diffraction standard (for instance, the JCPDS file in the database).¹

The broadening of the peaks in a diffraction pattern is a sensitive function of the size of the crystallites, particularly at the submicron scale. Therefore, XRD can also be used to determine the mean size of fine single-crystal nanoparticles with sizes of up to 100-200 nm. The relationship between the nanocrystallite size and peak broadening is described by the Scherrer equation (2.2):

$$D = \frac{K \cdot \lambda}{\beta \cdot \cos \theta}, \quad (2.2)$$

where D is the crystallite size, K denotes a numerical factor referred to as a shape factor (it depends on the shape of nanocrystallites and usually has approximate values of 0.9), λ is the wavelength of the employed X-ray radiation, β is the width (characterized by full-width at half maximum (FWHM)) of the peak broadening and θ is the Bragg angle.²

In this work the XRD measurements were performed with Bruker-D8 Discover diffractometer with Cu-K $_{\alpha}$ radiation ($\lambda = 1.5418 \text{ \AA}$) and equipped with a LynxEye position sensitive detector.

2.2 Sorption

Sorption measurements are a commonly used analytical technique for characterization of porous materials in terms of their surface area, porosity, pore size and pore size distribution.³

The principle of the sorption measurements is based on adsorption and desorption of an adsorptive species such as gas molecules (typically N $_2$) on a surface of a sample material referred to as adsorbent. The actual measurements are performed by recording the amount of adsorbate (e.g. N $_2$ gas molecules in the adsorbed state) on an adsorbent as a function of varying relative pressure, p/p_0 (p and p_0 being equilibrium and saturation vapor pressure, respectively), at a constant temperature (usually at 77 K, the boiling point of nitrogen). The obtained curve is referred to as sorption isotherm. Adsorption can be categorized into two types depending on the nature of the interaction between adsorbate and adsorbent – physisorption and chemisorption. Chemisorption involves formation of chemical bonds between adsorptive species and adsorbent, whereas physisorption involves relatively weak interactions such as van-der-Waals forces between adsorptive and adsorbent. In sorption

measurements the adsorption of adsorptive species on the surface of adsorbent mainly happens due to a physisorption process. The majority of measured isotherms resulting from physical adsorption of adsorptive gases can be grouped into six classes in the IUPAC classification (Figure 2.2).^{3,4}

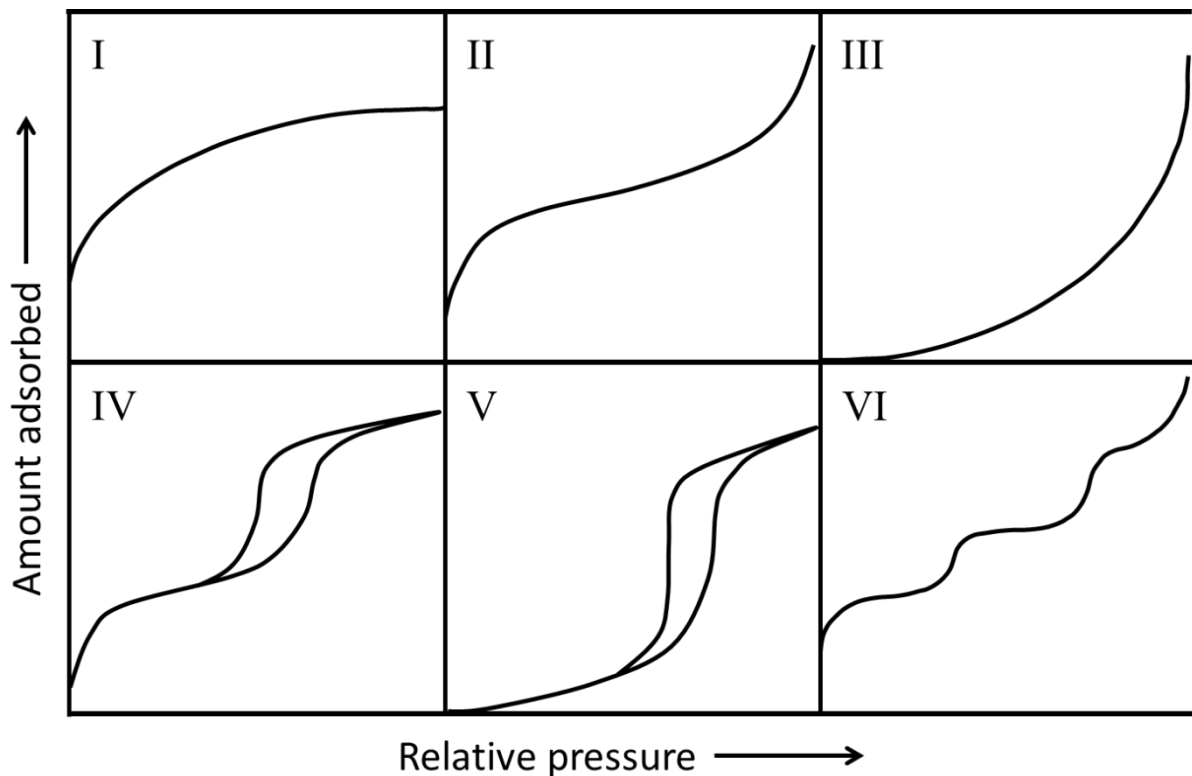


Figure 2.2. Six types of physisorption isotherms defined by the IUPAC classification. (Figure reproduced after Ref. 3)

The type I isotherm is characteristic for microporous (pores with diameters ≤ 2 nm) adsorbents. Type II and type III isotherms can be obtained with non-porous or macroporous (pores with diameters ≥ 50 nm) materials with high or low energy of adsorption, respectively. The isotherms with type IV and type V shapes are characteristic for mesoporous (pores with diameters between 2 and 50 nm) adsorbents with high and low energy of adsorption respectively. The hysteresis loop in type IV and type V isotherms is associated with pore

filling and emptying by capillary condensation in the absorbent material. Finally the type VI isotherm is characteristic for layer-by-layer adsorption on a uniform non-porous surface.³⁻⁵

Several theories have been developed to interpret the results (isotherms) of sorption measurements on microporous and non-microporous materials. One of the widely used theories employed for the analysis of isotherms obtained from non-microporous solids such as mesoporous and macroporous materials was developed by Brunauer, Emmett and Teller (BET theory). The BET theory is an extension of the Langmuir theory for unimolecular layers to multilayer adsorption. The BET theory is based on three main assumptions, which state that a) there is no interaction between adsorptive species within each layer; b) the energy of adsorption in all layers is the same except in the first layer due to the adsorbent-adsorptive interactions; c) the number of adsorbed layers becomes infinite at $p/p_0 = 1$. The BET theory can be expressed in simple and linear form by the BET equation (2.3):⁶

$$\frac{p}{n^a \cdot (p_0 - p)} = \frac{1}{n_m^a \cdot C} + \frac{(C-1)}{n_m^a \cdot C} \frac{p}{p_0}, \quad (2.3)$$

where n^a is the amount of adsorptive molecules adsorbed at the relative pressure p/p_0 , n_m^a is the monolayer capacity (which is the amount of adsorptive molecules needed for complete monolayer coverage), C is the BET constant.

It is possible to calculate the BET surface area, $A_s(BET)$, of the adsorbent material from the monolayer coverage of the surface using the equation (2.4), where the relationship between $A_s(BET)$ and monolayer capacity, n_m^a , is expressed according to following equation:³

$$A_s(BET) = n_m^a \cdot L \cdot a_m, \quad (2.4)$$

here L is the Avogadro constant and a_m is a footprint area of a single adsorptive molecule.

The pore size distribution (PSD) is another important characteristic of porous materials, and it can be obtained using a method developed by Barrett, Joyner and Halenda (BJT method) which is based on the Kelvin equation. The Kelvin equation describes the relationship between the curvature radius of the liquid meniscus formed in the pores and the relative pressure, p/p_0 , at which condensation occurs (2.5):^{3,7}

$$\frac{1}{r_1} + \frac{1}{r_2} = -\frac{R \cdot T}{\sigma^{lg} \cdot v^l} \ln\left(\frac{p}{p_0}\right) \quad (2.5)$$

Here, r_1 and r_2 are principal radii of curvature of the liquid meniscus, R is the universal gas constant, T is absolute temperature, whereas σ^{lg} and v^l are the surface tension and the molar volume of the liquid condensate respectively. More recently, advanced computational methods such as non-local density functional theory (NLDFT) or Monte Carlo molecular simulation have been used to evaluate the pore size distribution (PSD).⁴

In this thesis, all sorption measurements on meso- and macroporous powdered specimens were conducted using a NOVA 4000e surface area and pore size analyzer (Quantachrome). N_2 was used as adsorptive molecule at its boiling point (77 K). Autosorb-1 software (Quantachrome) was used to evaluate the data. Prior to measurements, all specimens were subjected to outgassing in vacuum at 150 °C for 12 hrs.

2.3 Electron Microscopy

Electron microscopy is a powerful characterisation technique that uses high-energy electrons to illuminate a specimen and obtain structural, compositional and morphological information. Using energetic electrons accelerated at high voltages it is possible to obtain electron wavelengths well below those of visible light and therefore achieve resolutions beyond the

limit of optical microscopes (about 200 to 300 nm). The relationship between the wavelength of accelerated electrons, λ , and applied voltage, V , is expressed by the de Broglie equation (corrected for the difference between the rest mass m_0 , and relativistic mass m for accelerated electrons) (2.6):¹

$$\lambda = \frac{h}{\sqrt{2m_0 \cdot e \cdot V \left(1 + \frac{e \cdot V}{2m_0 \cdot c^2}\right)}}, \quad (2.6)$$

where e is the charge of the electron, c is the velocity of light and h is Planck's constant. When the accelerated electrons are directed towards the specimen and upon interaction of the electron beam with the sample, many secondary signals can be generated (Figure 2.3).⁸

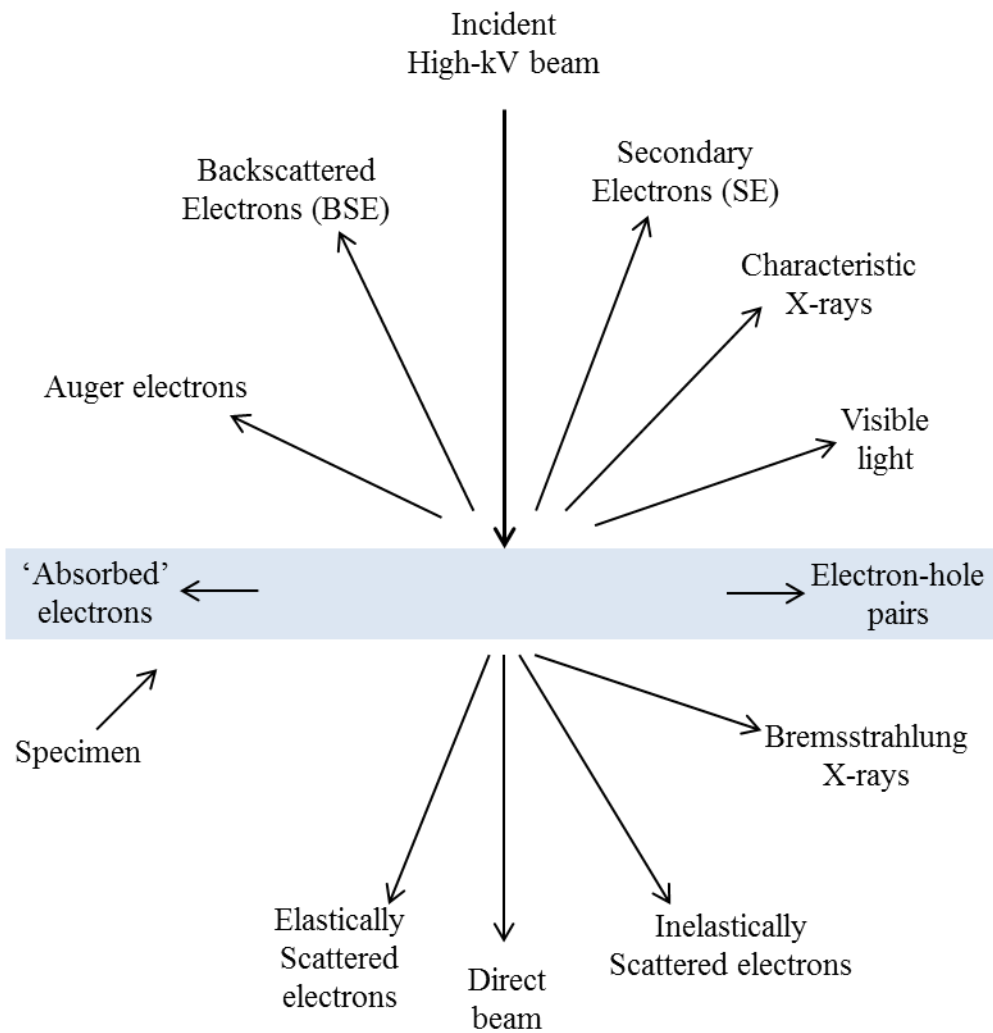


Figure 2.3. Signals generated upon interaction of an incident energetic electron beam with a thin specimen. (Figure reproduced after Ref. 8)

Depending on which of these secondary signals are used, the electron microscopes can be divided into two different types, which are transmission electron microscopy (TEM) and scanning electron microscopy (SEM). These two types of electron microscopes will be described more in detail in following two subsections.

2.3.1 Transmission Electron Microscope

In the TEM experiments the energetic electrons that penetrate through a thin specimen (typically below 100 nm) are used for the characterization of the sample (see Figure 2.3). The acceleration voltage for the electrons used in TEM is typically in the range of 80 to 400 kV. Thus, energetic electrons with very small wavelength can be generated. For instance, at 100 kV the wavelength of electrons is $\lambda \sim 4$ pm which is well below the dimensions of interatomic spacing in the solids (up to 0.1 nm) and, therefore it is possible to image lattice planes in the crystal structure.⁸ The electron beam can be generated by two approaches. In the first approach electrons are extracted by heating a tungsten filament or LaB₆ crystal to eject electrons due to thermionic emission. In the second – ‘cold’ approach – the electron beam is formed by using a field emission gun in which a high electric field is applied to a sharp tungsten tip to extract electrons.

The generated beam of energetic electrons is focused using an electromagnetic condenser lens system that can be controlled by varying the current running through it. The focused beam bombards the specimen, and electrons that are transmitted through the sample are first focused by the objective lens to create the first magnified image of the specimen that is subsequently magnified further by intermediate and projector lenses. Finally, the image is observed on a fluorescent screen or a charge-coupled device (CCD) camera (Figure 2.4).¹

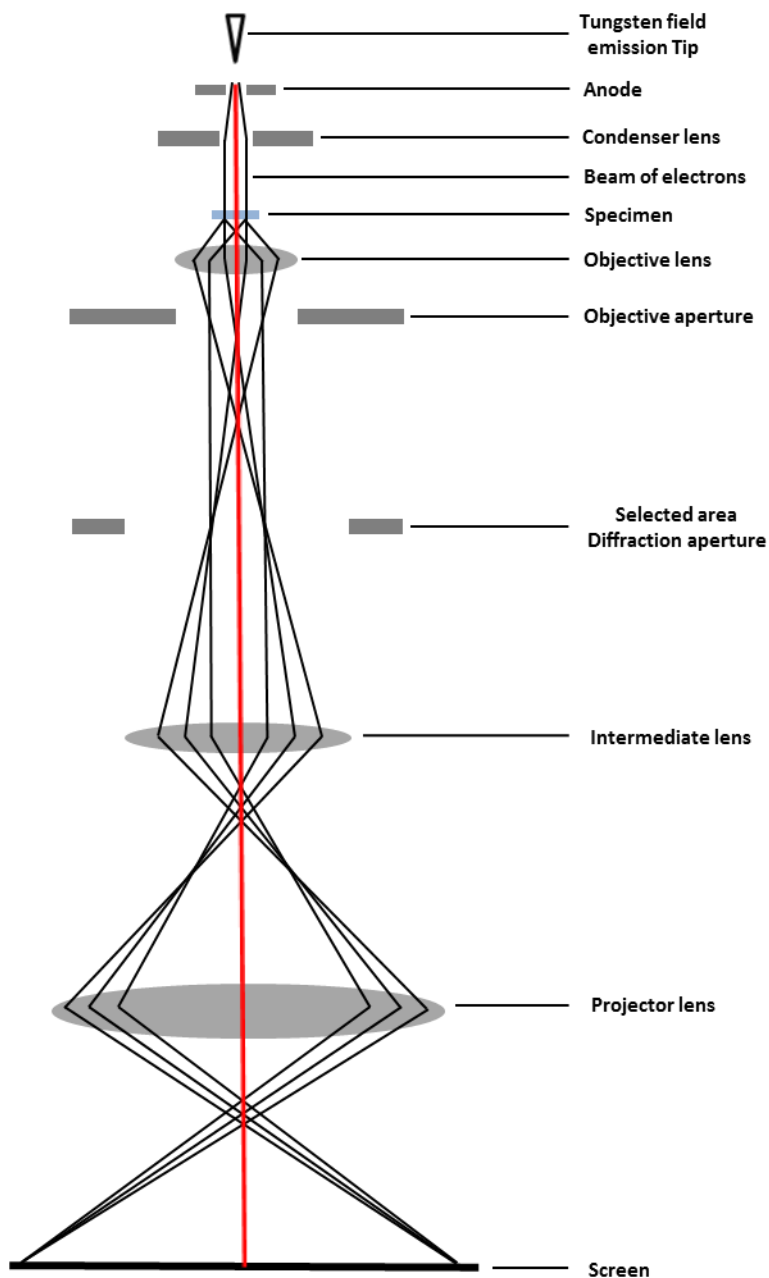


Figure 2.4. Schematic representation of the optical path in TEM. (Figure reproduced after Ref. 1)

There are different operation modes in the TEM experiments. For instance, by selectively blocking the direct transmitted or scattered electrons with the objective aperture it is possible to obtain dark- or bright-field (DF or BF) images of the specimen. Another important mode of the TEM is the scanning transmission electron microscopy (STEM) mode. Here the electron beam is focused into a focal spot on the specimen at larger convergence angle and rastered across the specimen. The transmitted electrons are collected as a function of beam location to

yield a STEM image of the specimen. It is also possible to obtain an electron diffraction pattern of the specimen by focusing the imaging system on the back focal plane of the objective and obtain information on the structure of the specimen. Finally, compositional analysis of the specimen can also be obtained by employing, for example, electron energy loss spectroscopy (EELS), an additional technique in the TEM measurements, where inelastically forward-scattered electrons are used for the analysis.¹

In this thesis, the TEM measurements were performed using a FEI TITAN 80-300 transmission electron microscope equipped with a field emission gun operating at an acceleration voltage of 300 kV.

2.3.2 Scanning Electron Microscope

In the SEM measurements energetic electrons are also used for imaging purposes. However, compared to the TEM, in the SEM measurements an electron beam with rather lower energy (usually between 0.1 to 30 kV) is employed to illuminate the specimen, and only secondary signals collected from the surface of a sample are used for the analysis and imaging (see Figure 2.3). In the actual SEM measurements, the energetic electron beam (also referred to as probe beam) is focused onto a specimen and scanned across the sample surface in television raster fashion. The electrons are inelastically scattered upon interaction of the electron beam with the specimen and generate secondary signals such as backscattered electrons (BSE), secondary electrons (SE), characteristic X-rays, Auger electrons and cathodoluminescence. These signals are detected, amplified and used for imaging and characterization of the sample (Figure 2.5). As the signals are collected from the surface of the specimen there is not much restriction for the thickness of the sample. However, the effective secondary signal collection

depth is around 2 μm , therefore this needs to be taken into account during the specimen preparation.¹

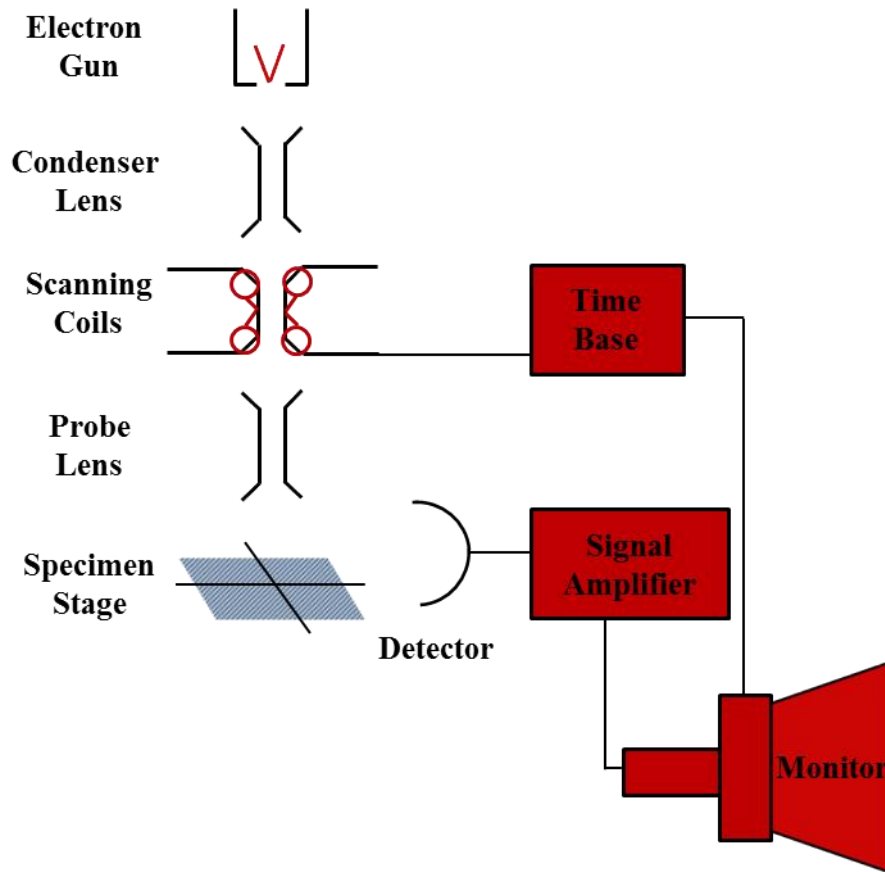


Figure 2.5. Schematic representation of an SEM. (Figure reproduced after Ref. 1)

The BSE secondary signal is sensitive to average atomic number, Z , and can provide images containing information about different phases of a specimen (e.g., composite or alloy samples), whereas the SE signal can provide images sensitive to surface topography. Characteristic X-rays emitted from the specimen can also be detected and analysed with an energy-dispersive X-ray spectrometer (EDX) to characterize the chemical constituents of a particular spot on the specimen. Moreover, it is also possible obtain a chemical concentration map of the sample by recording X-rays as a function of the incident electron beam coordinates as it rasters across the selected area of the specimen.¹

In this thesis, the SEM images were obtained by using a JEOL-JSM-6500F scanning electron microscope with a field emission gun operating at 0.5-30 kV and equipped with BSE, SE and EDS detectors.

2.4 Ultraviolet-Visible-Near Infrared Spectroscopy

Ultraviolet-visible-near Infrared (UV-Vis-NIR) spectroscopy is a widely employed analytical technique used to investigate the absorption behavior of a substance upon illumination with incident light with wavelength ranging from ultraviolet (UV), usually from 200 nm, to near-infrared (NIR), up to about 2500 nm. The absorption by the sample is associated with electronic transitions from the ground state to higher excited states due to absorption of the photon energy of the incident light. The absorbing specimen can be in liquid, powder or in thin film form. The absorption spectrum of the specimen is obtained by recording the amount of the light absorbed by the specimen as a function of wavelength of the incident light. The absorbance, A , of the substance is determined according to following relationship (2.7):⁹

$$A = -\log_{10} \frac{I}{I_0}, \quad (2.7)$$

where I_0 is the intensity of incident light and I is the intensity of light that passed through the substance. The absorbance, A , can also be used to determine the amount of the absorbing substance. The relationship between the absorbance, A , and the amount of the absorbing species is given by the Beer-Lambert law (2.8):^{9, 10}

$$A = \varepsilon \cdot c_s \cdot d_s, \quad (2.8)$$

where ε is the molar absorptivity or extinction coefficient, c_s is the concentration of absorbing species and d_s is the path length of the sample.

In this thesis, UV-Vis-NIR measurements were performed using U-3501 (Hitachi) and Lambda 1050 (PerkinElmer) spectrophotometers.

2.5 Current-Voltage Characterisation

Current-voltage (I-V) characterization is a common techniques used to determine the performance of solar cells. I-V measurements of solar cells are usually performed both in the dark and under simulated sunlight at a 100 mW cm^{-2} total light intensity, and with the spectrum similar to the air mass 1.5 global (AM 1.5 G) spectrum. AM 1.5 G is the solar spectrum arriving on Earth's surface (at a zenith angle of about 48 degrees) after passing through the atmosphere.^{11, 12} In laboratory conditions, a xenon lamp with suitable filters is used to simulate the AM 1.5 G spectrum in the I-V measurements. In order to measure I-V curves of solar cells, the current flowing through the device is recorded as a function of applied varying voltage in the dark or under illumination. The I-V curves of the devices in the dark exhibit asymmetric diode-like behavior, which shifts vertically under illumination due to light induced current generation (Figure 2.6).¹³

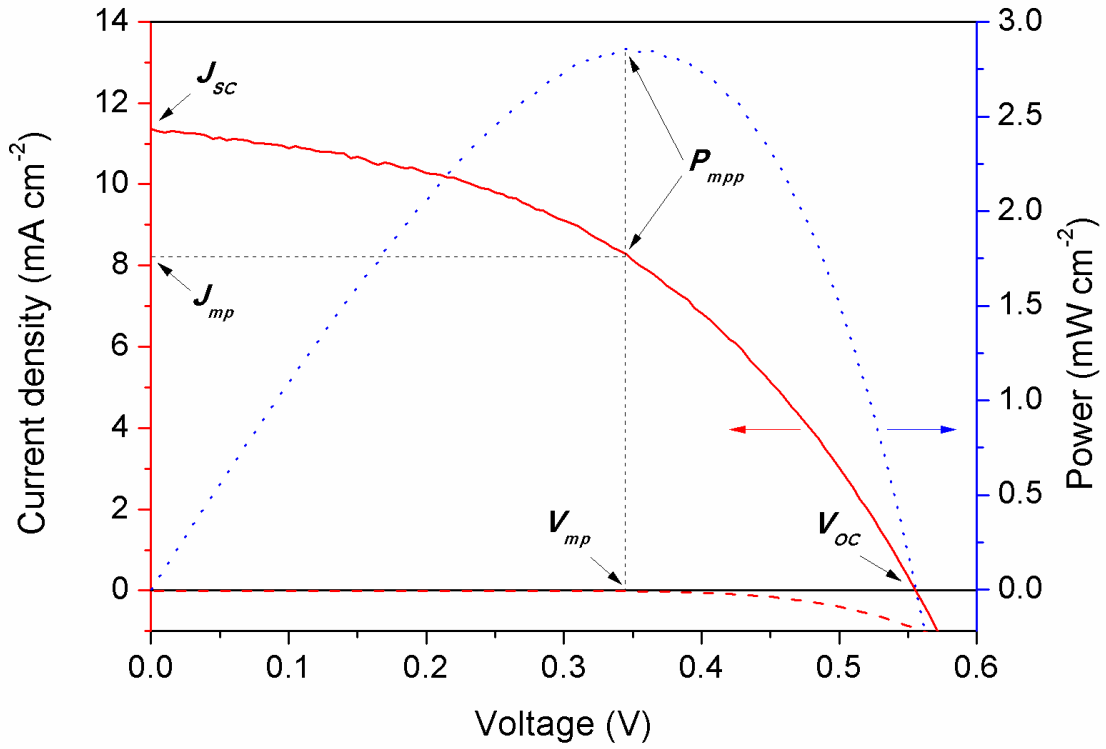


Figure 2.6. Typical I-V characteristics of a QDSC under illumination (solid red curve) and in the dark (dashed red curve) as well as power-voltage characteristic under illumination (dotted blue curve).

Several important parameters of the device such as short circuit current, J_{SC} , open circuit voltage, V_{OC} , fill factor, FF , and power conversion efficiency, η , can be obtained from the I-V curves. The short circuit current density, J_{SC} , is the value of current density at the intercept of the I-V curve with the ordinate (vertical axis), whereas the open circuit voltage, V_{OC} , is the voltage at the intercept of the I-V curve with the abscissa (horizontal axis) of the I-V diagram. The fill factor, FF , is the ratio of maximum power point, P_{mpp} , to the product of $J_{SC} \times V_{OC}$ and is expressed by the following equation (2.9):^{13, 14}

$$FF = \frac{P_{mpp}}{J_{SC} \cdot V_{OC}} = \frac{J_{mp} \cdot V_{mp}}{J_{SC} \cdot V_{OC}}, \quad (2.9)$$

where J_{mp} and V_{mp} are current density and voltage at the maximum power point, respectively. The power conversion efficiency, η , of the solar cell is derived according to the following relationship (2.10):^{13, 14}

$$\eta = \frac{J_{sc} \cdot V_{oc} \cdot FF}{P_{in}}, \quad (2.10)$$

where P_{in} is incident optical power.

In this thesis, the I-V characteristics of the solar cells were measured under simulated solar light using a 300 W xenon lamp and a filter calibrated to approximate AM 1.5 G irradiation at 100 mW cm^{-2} (model: XPS 400, Solar Light Company Inc.). The I-V characteristics were recorded using a Keithley 2400 source meter.

2.6 Incident-Photon-to-Collected-Electron Efficiency

The incident-photon-to-collected-electron efficiency (IPCE) (also known as external quantum efficiency, EQE) is a measure of the ratio of the flux of electrons in the external circuit to the flux of incident photons at a particular wavelength. The IPCE can be expressed as following (2.11):¹⁵

$$IPCE(\lambda) = \eta_{LHE} \cdot \eta_{inj} \cdot \eta_c, \quad (2.11)$$

where η_{LHE} is light harvesting efficiency, η_{inj} is the electron injection efficiency and η_c is the electron collection efficiency. The IPCE of a solar cell can be determined by recording the short circuit current, $J_{sc}(\lambda)$ as a function of incident photon wavelength and using the following relationship (2.12):¹⁵

$$IPCE(\lambda) = 1240 \frac{J_{sc}(\lambda)}{\lambda \cdot P_{in}}, \quad (2.12)$$

where λ is wavelength and P_{in} is the power of incident light. The short circuit current, J_{sc} , of a solar cell under polychromatic illumination can be estimated as the integral of the product of $IPCE(\lambda)$ and incident flux density, $F(\lambda)$, according to expression (2.13):¹⁵

$$J_{sc} = \int e \cdot F(\lambda) \cdot IPCE(\lambda) d\lambda, \quad (2.13)$$

where e is the electron charge. In the ideal case the short circuit current obtained from the ICPE should coincide with the short circuit current obtained from the I-V measurements.

In this thesis, IPCE spectra of the solar cells were recorded using the Keithley 2400 source meter and chopped monochromatic light provided by a 150 W xenon lamp (Lot-Oriel) and a monochromator (Micro HR) with order sorting filters (Thorlabs). The measurements were conducted under AM 1.5 G bias light with an irradiance of 11.5 mW cm^{-2} , and the signal was detected by a DSP lock-in amplifier (7230, Signal Recovery).

2.7 Open Circuit Photovoltage Decay

The open circuit photovoltage decay (OCVD) measurement is a widely used and straightforward technique to study electron lifetimes in DSCs and QDSCs.^{16, 17} The working principle of OCVD measurements is based on illumination of the solar cell at open circuit with light of constant intensity, I_0 , to let it establish a nonequilibrium steady state photovoltage, V_{oc} , and then interrupting the illumination and recording the decay of the photovoltage of the cell in the dark (Figure 2.7). The photovoltage decays rapidly after

interruption of the illumination and then it slows down. If measured long enough, the voltage decays to zero.

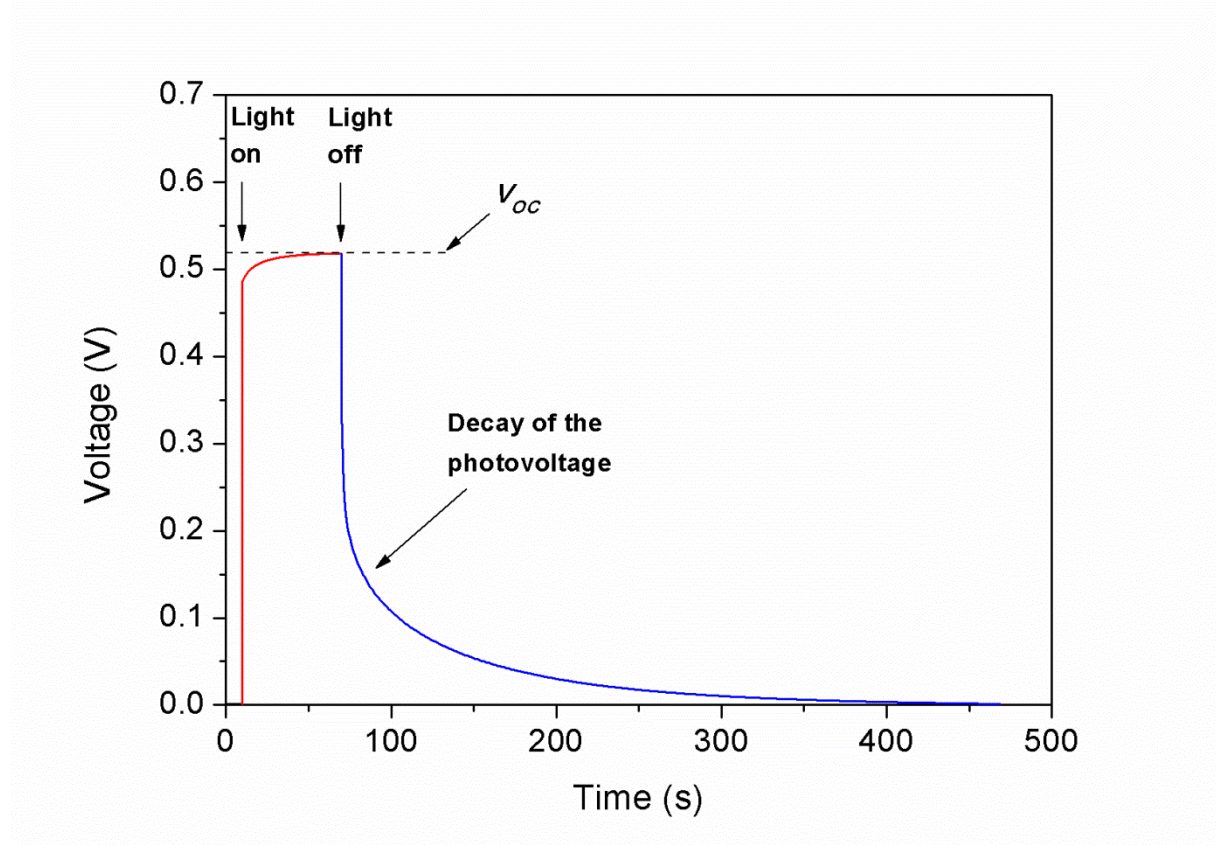


Figure 2.7. Graph of a photovoltage decay measurement of a QDSC.

The decay of the photovoltage (blue curve) can be used to calculate the electron lifetime, τ_n , according to relationship (2.14):¹⁶

$$\tau_n^{OCVD} = -\frac{k_B \cdot T}{e} \left(\frac{dV_{OC}}{dt} \right)^{-1}, \quad (2.14)$$

where k_B is Boltzmann constant, T is temperature and e is the positive elementary charge.

In this thesis, OCVD measurements were carried out using a potentiostat (PGSTAT302N, Autolab, Metrohm) and LED driver. Cool white LED (LDCCW, Metrohm) irradiation was used to illuminate the solar cells.

2.8 Intensity-Modulated Photovoltage and Photocurrent Spectroscopy

Intensity-modulated photovoltage spectroscopy (IMVS) and intensity-modulated photocurrent spectroscopy (IMPS) techniques are used to measure the dynamic photovoltage and photocurrent responses of a solar cell at open circuit and short circuit conditions, respectively, to a modulation of the intensity of incident light.^{18, 19} The response of the cell to light intensity modulation is described by so-called transfer functions (2.15 and 2.16):¹⁹

$$F_{IMVS,CELL}^*(\omega) = \frac{-V_{CELL,AC}(\omega,t)}{e \cdot \Phi_{AC}(\omega,t)} \quad (2.15)$$

$$F_{IMPS,CELL}^*(\omega) = \frac{i_{CELL,AC}(\omega,t)}{e \cdot \Phi_{AC}(\omega,t)} \quad (2.16)$$

Here, $V_{CELL,AC}(\omega, t)$ and $i_{CELL,AC}(\omega, t)$ are AC voltage and current signals caused by light intensity modulation, e is the electron charge and $\Phi_{AC}(\omega, t)$ is the modulated photon flux. The transfer function is a complex function and characterizes the dynamics of photovoltage generation in response to the light intensity modulation. During the measurements the modulation amplitude of the incident light intensity is kept rather small in order to maintain the linearity of the photovoltage response. The IMVS measurements are used to estimate the electron lifetime in solar cells.^{20, 21} Unlike in OCVD measurements, the IMVS provides the electron lifetimes, τ_n , under illumination. The electron lifetime is obtained using the following relationship (2.17):²⁰

$$\tau_n^{IMVS} = \frac{1}{\omega_{min}}, \quad (2.17)$$

where ω_{min} is the angular frequency corresponding to the minimum of the IMVS spectrum (Figure 2.8).

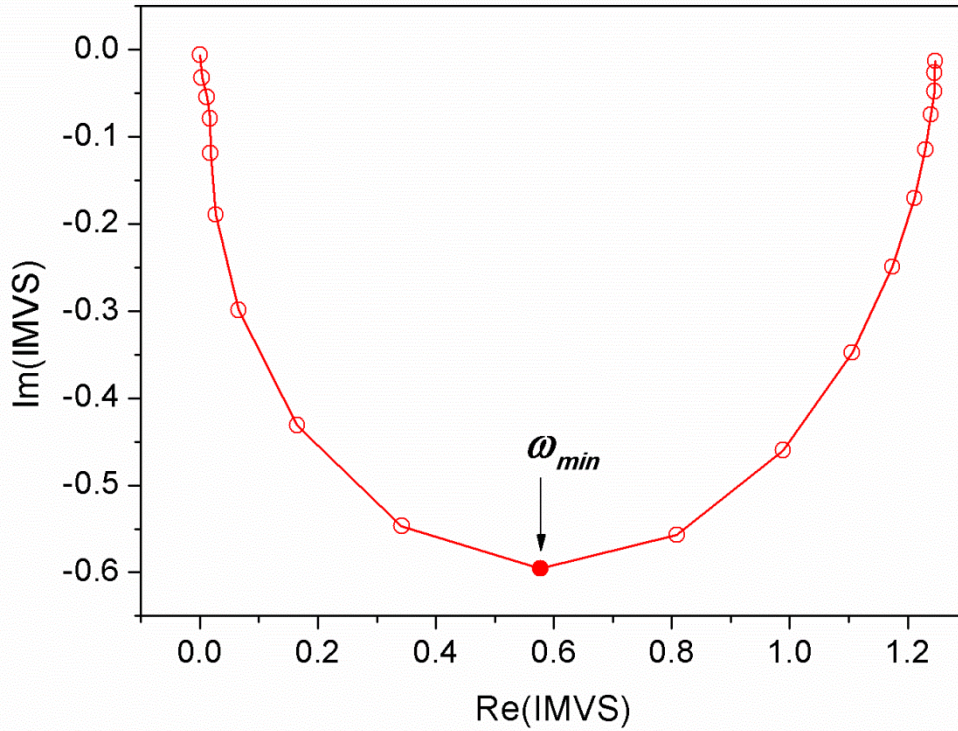


Figure 2.8. Complex plane plot of the IMVS spectrum of a QDSC.

IMPS measurements, on the other hand, are done at short circuit and can provide information on electron transport properties of solar cells. The time constant obtained from the minimum, ω_{min} , of the IMPS spectrum (Figure 2.9) is related to the diffusion coefficient, D_n , according to the following equation (2.18):²²

$$\tau_{trans}^{IMPS} = \frac{1}{\omega_{min}} = \frac{d_f^2}{\gamma \cdot D_n}, \quad (2.18)$$

where, d_f is the thickness of the photoanode film and γ is a dimensionless factor that is a function of illumination direction, absorption coefficient, $\alpha(\lambda)$, and photoanode thickness, d_f .²²

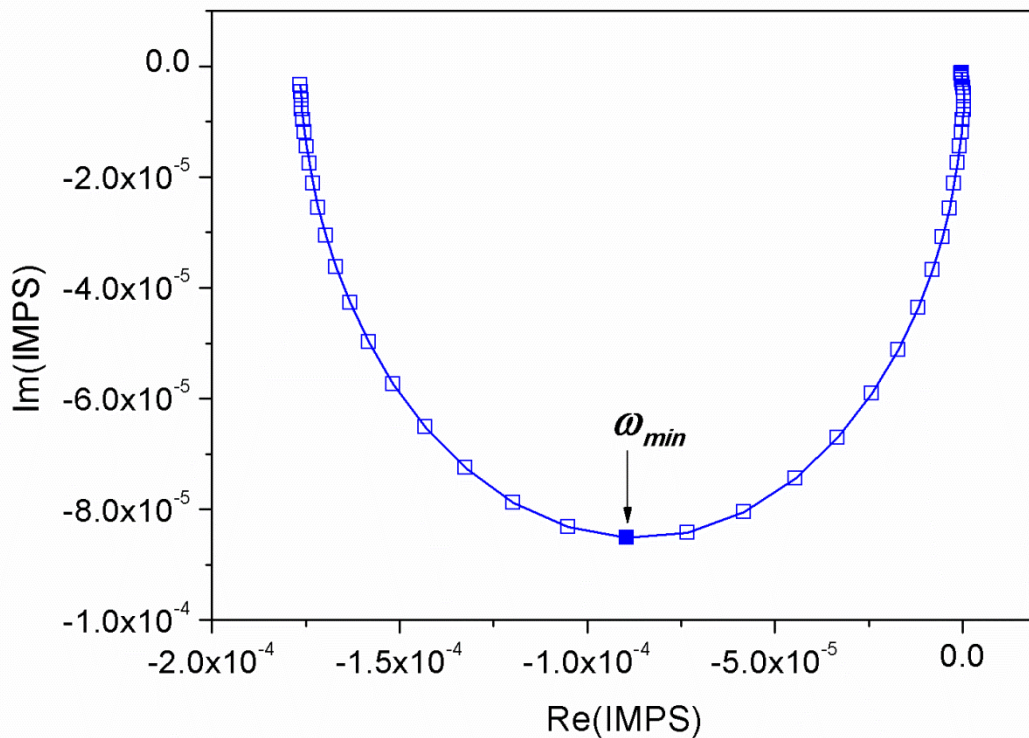


Figure 2.9. Complex plane plot of the IMPS spectrum of a QDSC.

In this thesis, the IMVS and IMPS measurements were carried out using a potentiostat equipped with a frequency response analyzer (PGSTAT302N, Autolab, Metrohm) and LED driver. The IMVS measurements were carried out under cool white LED (LDCCW, Metrohm) irradiation at open-circuit conditions over the frequency range from 10 kHz to 1 mHz. The amplitude of the AC modulation current was 10% of the DC current applied to the LED.

2.9 Electrochemical Impedance Spectroscopy

Electrochemical impedance spectroscopy (EIS) is a widely known characterization technique used to study electrochemical systems, and has been successfully employed to study DSCs

and QDSCs in recent years.^{14, 23-26} EIS is extensively used to study transport processes and electronic properties of porous metal oxide anodes as well as the electrolyte in DSCs and QDSCs.^{24, 26-28} The measurements are performed by perturbing the system (e.g. QDSC) with a sinusoidally modulated small amplitude AC voltage, $V_{AC}(\omega, t)$, that is superimposed on the DC voltage applied to the cell. The resulting AC current, $i_{AC}(\omega, t)$, is recorded as the response of the cell to the perturbation and used to obtain the impedance, $Z_{CELL}(\omega)$, of the cell according to the following equation (2.19):²⁹

$$Z_{CELL}(\omega) = \frac{V_{AC}(\omega, t)}{i_{AC}(\omega, t)} \quad (2.19)$$

By measuring the impedance for a wide range of modulation frequencies (typically from mHz to MHz) of the AC voltage it is possible to obtain the impedance spectrum of the cell. The features of the impedance spectrum at different modulation frequencies carry information on the dynamics and the nature of electrochemical processes occurring in specific components of the system. Therefore, the EIS measurements can be employed to characterize the whole system, for example, a complete QDSC, or its components – counter electrode (cathode), porous metal oxide layer (anode) and blocking layer on conducting transparent oxide – separately.^{14, 30-33} The interpretation of EIS data involves fitting the measured spectrum using an appropriate equivalent electrical circuit that is proposed to model the experimental system. It is made up of appropriately connected sub-circuits consisting of basic electrical elements such as resistance, capacitance and inductance, representing different components of the electrochemical system.^{14, 24} For instance, fitting the EIS spectra of a QDSC or DSC involves a so-called transmission line that represents the porous metal oxide layer of the cells (Figure 2.10):^{34, 35}

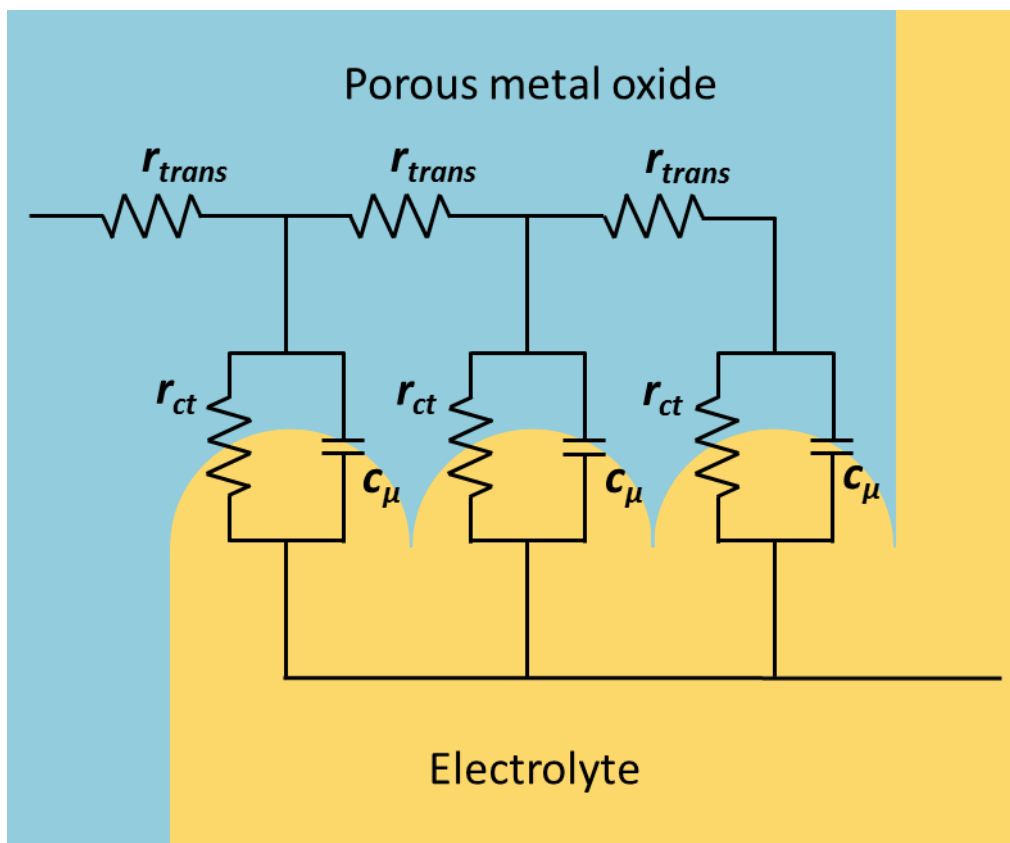


Figure 2.10. Scheme of porous metal oxide and electrolyte interface and finite transmission line equivalent circuit of the porous metal oxide. Here r_{trans} denotes the resistivity of electron transport in the porous metal oxide, r_{ct} is charge transfer (recombination) resistance at the metal oxide/electrolyte interface and c_{μ} is the metal oxide chemical capacitance.

An appropriately chosen model and correct fitting of the spectrum allows the parameters of the equivalent electrical circuit to be linked to physical parameters (e.g. electronic and transport) of the electrochemical system.²⁹

In this thesis, the EIS measurements were carried out using a potentiostat equipped with a frequency response analyzer (PGSTAT302N, Autolab, Metrohm). The measurements were conducted both in the dark and under illumination (AM 1.5 G irradiation) conditions. The modulation of the small amplitude AC voltage was varied over a frequency range from 1 MHz down to 1 mHz.

References

1. D. Brandon and W. D. Kaplan, *Microstructural Characterization of Materials*, John Wiley & Sons Ltd, Chichester, 2008.
2. U. Holzwarth and N. Gibson, *Nature Nanotechnol.*, 2011, **6**, 534-534.
3. K. S. W. Sing, D. H. Everett, R. A. W. Haul, L. Moscou, R. A. Pierotti, J. Rouquerol and T. Siemieniewska, *Pure & Applied Chemistry*, 1985, **57**, 603-619.
4. F. Rouquerol, J. Rouquerol and K. Sing, *Adsorption by Powders & Porous Solids*, Academic Press, London, 1999.
5. J. B. Condon, *Surface Area and Porosity Determinations by Physisorption: Measurements and Theory*, Elsevier, Amsterdam, 2006.
6. S. Brunauer, P. H. Emmett and E. Teller, *Journal of the American Chemical Society*, 1938, **60**, 309-319.
7. J. Rouquerol, D. Avnir, C. W. Fairbridge, D. H. Everett, J. H. Haynes, N. Pernicone, J. D. F. Ramsay, K. S. W. Sing and K. K. Uunger, *Pure and Applied Chemistry*, 1994, **66**, 1739-1758.
8. D. B. Williams and C. B. Carter, *Transmission Electron Microscopy: A Textbook for Material Science: I: basics*, Springer, New Yourk, 1996.
9. P. Atkins and J. d. Paula, *Atkins' Physical Chemistry*, W. H. Freeman and Company, New York, 2006.

10. D. P. Shoemaker and C. W. Garland, *Experiments in Physical Chemistry*, McGraw-Hill Book Company, New York, 1962.
11. H. J. Snaith, *Energy & Environmental Science*, 2012, **5**, 6513-6520.
12. G. Chen, J. Seo, C. Yang and P. N. Prasad, *Chemical Society Reviews*, 2013, **42**, 8304-8338.
13. S. Emin, S. P. Singh, L. Han, N. Satoh and A. Islam, *Solar Energy*, 2011, **85**, 1264-1282.
14. K. Kalyanasundaram, *Dye-Sensitized Solar Cells*, CRC Press, Boca Raton, 2010.
15. Z. Yang, C.-Y. Chen, P. Roy and H.-T. Chang, *Chemical Communications*, 2011, **47**, 9561-9571.
16. A. Zaban, M. Greenshtein and J. Bisquert, *ChemPhysChem*, 2003, **4**, 859-864.
17. H. Yang, W. Fan, A. Vaneski, A. S. Sussha, W. Y. Teoh and A. L. Rogach, *Advanced Functional Materials*, 2012, **22**, 2821-2829.
18. G. Schlichthörl, S. Y. Huang, J. Sprague and A. J. Frank, *The Journal of Physical Chemistry B*, 1997, **101**, 8141-8155.
19. J. Halme, *Physical Chemistry Chemical Physics*, 2011, **13**, 12435-12446.
20. L. M. Peter and K. G. U. Wijayantha, *Electrochimica Acta*, 2000, **45**, 4543-4551.
21. J. Krüger, R. Plass, M. Grätzel, P. J. Cameron and L. M. Peter, *The Journal of Physical Chemistry B*, 2003, **107**, 7536-7539.

22. E. Guillén, L. M. Peter and J. A. Anta, *The Journal of Physical Chemistry C*, 2011, **115**, 22622-22632.
23. F. Fabregat-Santiago, J. Bisquert, G. Garcia-Belmonte, G. Boschloo and A. Hagfeldt, *Solar Energy Materials and Solar Cells*, 2005, **87**, 117-131.
24. V. González-Pedro, X. Xu, I. Mora-Seró and J. Bisquert, *ACS Nano*, 2010, **4**, 5783-5790.
25. I. Mora-Seró, S. Gimenez, F. Fabregat-Santiago, E. Azaceta, R. Tena-Zaera and J. Bisquert, *Physical Chemistry Chemical Physics*, 2011, **13**.
26. F. Fabregat-Santiago, G. Garcia-Belmonte, I. Mora-Seró and J. Bisquert, *Physical Chemistry Chemical Physics*, 2011, **13**, 9083-9118.
27. A. B. F. Martinson, M. S. Góes, F. Fabregat-Santiago, J. Bisquert, M. J. Pellin and J. T. Hupp, *The Journal of Physical Chemistry A*, 2009, **113**, 4015-4021.
28. J. Bisquert, F. Fabregat-Santiago, I. Mora-Seró, G. Garcia-Belmonte and S. Giménez, *The Journal of Physical Chemistry C*, 2009, **113**, 17278-17290.
29. J. Halme, P. Vahermaa, K. Miettunen and P. Lund, *Advanced Materials*, 2010, **22**, E210-E234.
30. M. Deng, Q. Zhang, S. Huang, D. Li, Y. Luo, Q. Shen, T. Toyoda and Q. Meng, *Nanoscale Research Letters*, 2010, **5**, 986 - 990.
31. C. Justin Raj, K. Prabakar, A. Dennyson Savariraj and H.-J. Kim, *Electrochimica Acta*, 2013, **103**, 231-236.

32. F. Fabregat-Santiago, G. Garcia-Belmonte, J. Bisquert, A. Zaban and P. Salvador, *The Journal of Physical Chemistry B*, 2002, **106**, 334-339.
33. P. J. Cameron and L. M. Peter, *The Journal of Physical Chemistry B*, 2003, **107**, 14394-14400.
34. J. Bisquert, G. Garcia-Belmonte, F. Fabregat-Santiago, N. S. Ferriols, P. Bogdanoff and E. C. Pereira, *The Journal of Physical Chemistry B*, 2000, **104**, 2287-2298.
35. J. Bisquert, *The Journal of Physical Chemistry B*, 2002, **106**, 325-333.

3 Extremely Thin Absorber Solar Cells with PbS Quantum Dots and CuSCN Hole Conductor

The chapter is based on a collaboration with Dr. Mihaela Nedelcu as well as Dr. Hiroaki Sai and Prof. Ulrich Wiesner from the Department of Materials Science and Engineering at Cornell University, USA.

Abstract

Polystyrene-block-poly(ethylene oxide) block copolymer was employed as a structure-directing agent for the synthesis of mesoporous TiO₂ films with a regular pore structure. The resulting templated TiO₂ films were characterized by thermogravimetry, differential scanning calorimetry, X-ray diffraction and nitrogen sorption measurements. The calcined TiO₂ films, which are in the anatase phase, exhibit a high specific surface area and porosity. Extremely thin absorber solar cells were fabricated by coating the mesoporous TiO₂ films with PbS quantum dots and infiltrating a CuSCN hole transporter layer. The AM 1.5 G solar cell performance of the cells was tested with current-voltage and incident-photon-to-collected-electron efficiency measurements and physical parameters of the cells were analysed with impedance spectroscopy.

3.1 Introduction

Since the original development of dye-sensitized solar cells (DSCs) by O'Regan and Grätzel,¹ considerable experimental effort has been directed at improving performance and stability. In

their original form, DSCs are fabricated using a mesoporous TiO₂ anode sensitized with a dye that acts as light absorber. The TiO₂ film is permeated by a redox electrolyte (usually I₃⁻/I) that regenerates the dye from its oxidized state following electron injection into the TiO₂ from the excited state. The electrolyte also transports 'holes' (in the form of I₃⁻ ions) to the cathode, where they accept electrons to complete the regenerative cycle. Due to potential issues arising from leakage of liquid electrolytes, efforts have been made to replace the redox couple by solid hole-transporting materials (HTMs) such as CuSCN, spiro-OMeTAD (2,2',7,7'-tetrakis(N,N-di-methoxy-phenylamine)-9,9'-spirobifluorene), P3HT (poly-3-hexylthiophene), and P3OT (poly(3-octylthiophene)).²⁻⁵ Current champion solid-state DSCs using spiro-OMeTAD HTM and an organic C220 sensitizer dye have achieved AM 1.5 G power conversion efficiencies greater than 7.2 %.⁶

It has been shown that inorganic absorber layers (CdS,⁷ CdSe,⁸ CdTe,⁹ CuInS₂¹⁰ etc.¹¹), quantum dots (QDs) (Bi₂S₃,¹² CdS,¹³ CdSe,¹⁴ InP,¹⁵ etc.¹⁶) and more recently perovskites¹⁷ can replace dyes as light harvesting sensitizers.¹⁸⁻²⁰ The relative ease of synthesis and processing of these materials make them an appealing research topic.²¹⁻²³ Inorganic absorber materials can be grown *in situ* on the walls of mesoporous metal oxide films by chemical bath deposition (CBD),²⁴ successive ionic layer adsorption/reaction (SILAR),²⁵ and ion layer gas adsorption/reaction (ILGAR) methods.¹⁰ Alternatively the mesoporous film can be soaked in a colloidal solution of absorber QDs.¹⁵ Due to the size-dependent quantization effect, it is possible to tune the highest occupied molecular orbital and lowest unoccupied molecular orbital (HOMO-LUMO) gap of the QDs by controlling their size in order to harvest photons over the optimum spectral range.^{12, 18, 26, 27} Under optimum conditions, inorganic sensitizer layers can have significantly higher optical absorbance than dye monolayers, particularly in the low energy onset region.

An attractive type of device that uses a layer of inorganic material for light harvesting is the extremely thin absorber (ETA) solar cell.¹⁰ The ETA cell architecture is similar to a solid-state DSC with the only difference being a use of a thin inorganic absorbing layer instead of dye molecules. Typically, the cell architecture comprises a thin layer of absorber material with intrinsic (i-type) conductivity coated onto the high internal surface area of a porous n-type supporting material with a large band gap (e.g. TiO₂, ZnO or SnO₂). The pores are filled with an optically transparent semiconductor with p-type conductivity to create a p-i-n junction distributed over the high interfacial area of the porous structure. Light absorption in the thin i-type layer creates electron-hole pairs that are separated and transported to the contacts via the n-type and p-type layers, respectively.^{28, 29}

Interest in ETA cells has increased steadily¹⁹ over the last decade due to higher stability and low production cost of the cells compared to solid-state DSCs as well as the abundance of a variety of materials that can be used as absorber layer. Performance values of ETA solar cells have improved progressively, reaching 5.7% for a cell with Sb₂S₃ absorber and TiO₂/CuSCN interpenetrating electron/hole conductors.³⁰ This is already a higher conversion efficiency value than the one reported for a solid-state DSC with the same CuSCN HTM and N719 dye sensitizer (3.39%).^{31, 32} Nevertheless, the performance of ETA cells is still rather modest and the full potential of the cells has not been fully realized. Key issues for further development of ETA cells are: 1) control of the metal oxide structure in terms of pore size, surface area and crystallinity,⁷ 2) improvement of light harvesting,^{17, 23} 3) improvement of HTM infiltration into the pores,^{33, 34} 4) reduction of electron-hole recombination,^{11, 35} and 5) enhancement of hole transport.^{32, 36}

Porous TiO₂ layers are widely used for the fabrication of the metal oxide electrodes for the mesoporous solar cells.^{20, 37} So far, the best cells have been made by sintering ~20 nm and ~50 nm sized TiO₂ nanoparticles (NPs) to obtain mesoporous electrodes for solid-state DSCs

and ETA cells, respectively.^{6, 38} Further improvements in the performance of both types of cell may be possible by optimizing the mesoporous TiO₂ layers to enhance their porosity, crystallinity and structural regularity. An excellent way to control the small scale morphology (≥ 10 nm) of TiO₂ layers is based on the self-assembly of organic-inorganic hybrid materials using block-copolymers (BCPs) as structure-directing templates.³⁹⁻⁴¹ It has also been reported by Docampo et al.⁴² that solid-state DSCs made using the BCP-templated TiO₂ electrodes resulted in a similar or better solar cell performance compared to ones made with sintered NPs.⁴³ In their work the authors showed that BCP-templated TiO₂ electrodes exhibited a large density of relatively low energy sub-bandgap states with a narrow distribution that resulted in superior performance of cells due to improved charge transfer from the dye to TiO₂ compared to the cells with conventional sintered TiO₂ NP electrodes.⁴² Therefore, use of the BCP-templated TiO₂ electrodes for ETA solar cells might be beneficial due to desirable electronic properties of the metal oxide. Moreover, a higher available internal surface area could offer some room for improvement in the light harvesting ability of the cells via enhanced deposition of the absorber layer, and at the same time keep the thickness of the electrode rather thin (between 2 to 3 nm). Also, thin electrodes with regular pore structure are expected to result in better infiltration of the solid hole transporter.³³

With this aim in mind, we investigated the fabrication of ETA solar cells with BCP-templated TiO₂ electrodes and the CuSCN solid hole transporter. Structure-directing polystyrene-*b*-poly(ethylene oxide) (PS-*b*-PEO) BCPs were employed for the preparation of mesoporous TiO₂ films with well-defined pore structure. The porous TiO₂ was obtained by mixing PS-*b*-PEO BCPs with a non-hydrolytic titania sol-gel, followed by calcining in air to remove the polymer and to transform the amorphous precursor structure into the pure crystalline anatase phase of TiO₂. A PbS QD layer was used as light harvesting thin absorber layer for the mesoporous TiO₂ electrodes.²⁵ Due to the size-dependent quantization effect,^{26, 44} it is possible

to inject photogenerated electrons from small enough PbS QDs (up to 4 nm) into the conduction band of TiO₂. Also, it has been shown that it is possible to generate and dissociate multiple excitons in PbS QDs, which according to theoretical estimations promises to exceed the thermodynamic Shockley-Queisser limit for solar cell efficiency.^{45, 46}

We note that ETA solar cells with PbS absorber layer in which PEDOT:PSS was used as hole conductor have already been reported by Bayon et al.⁴⁷ Efficiencies of up to 1% were obtained by Oja et al.⁴⁸ for similar cells with Nb-doped TiO₂ scaffolding coated with a In(OH)_xS_y buffer layer. Although remarkable short circuit currents were obtained ($J_{SC} = 10.2 \text{ mA cm}^{-2}$), the cells showed rather low open circuit voltages ($V_{OC} = 170 \text{ mV}$). CuSCN, on the other hand, has been shown to produce open circuit voltages between 400 – 700 mV in ETA cells with CdS absorber and ZnO anode, and it is inexpensive and abundant compared to other HTMs.⁴⁹ Therefore, in this work we report on the use of CuSCN as hole transporter for our ETA cells. The performance of the fabricated ETA solar cells was characterised with current-voltage (I-V) and incident-photon-to-collected-electron efficiency (IPCE) measurements. The cells were also studied by electrochemical impedance spectroscopy (EIS), and the experimental EIS results were fitted to an equivalent circuit to derive the parameters of interest. The values obtained were used to calculate effective electron diffusion lengths and electron lifetimes.

PS-*b*-PEO BCPs were synthesised and provided by Dr. Hiroaki Sai and Prof. Ulrich Wiesner. The synthetic protocol for PS-*b*-PEO BCP-templated mesoporous TiO₂ was developed by Dr. Mihaela Nedelcu and preliminary experimental studies of ETA solar cells were also conducted by Dr. Mihaela Nedelcu.

3.2 Results and Discussion

Numerous BCPs have been used in the synthesis of nanostructured porous films.⁵⁰ Here we employed PS-*b*-PEO BCP (approximate number of monomers in the PS and PEO blocks is 210 and 84, correspondingly) as structure directing agent in the sol-gel synthesis of the mesoporous TiO₂ electrodes.⁵¹ PS-*b*-PEO is a diblock copolymer composed from two different monomers, polystyrene (PS) and poly(ethylene oxide) (PEO), which are covalently joined to each other from one end. The PS side of the BCP is hydrophobic, whereas the PEO side is hydrophilic. It is this property of PS-*b*-PEO that is employed to synthesise the porous films. When adding the precursor of inorganic material, e.g. titania, to a solution with BCPs, it selectively swells the PEO side resulting in the formation of PS-*b*-PEO micelles (Figure 3.1).⁵²

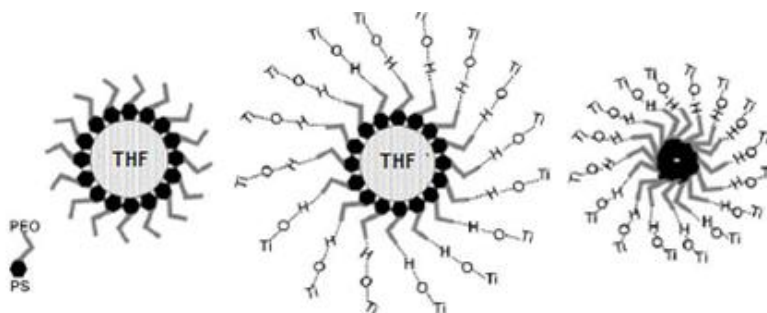


Figure 3.1. Formation of micelles (schematic). The process is shown for titania precursor in which tetrahydrofuran (THF) is used as a solvent. (Figure adapted from Ref. 52)

These micelles then self-organise as the solvent evaporates resulting in an organic-inorganic composite film in which the body of the inorganic film is filled with the ordered BCP micelles. The process is referred to as evaporation-induced self-assembly (EISA).⁵³ In order to obtain the desired porous TiO₂ network, the composite sample needs to be calcined at elevated temperatures to burn away all the templating organic material. The thermogravimetric analysis (TGA) and differential scanning calorimetry (DSC) experiments

(Figure 3.2) indicate that the organic material completely burns away during the heat treatment at 450 °C, which is consistent with the studies reported by other authors.^{52, 54} A high calcination temperature is required due to the high decomposition temperature (400 – 450 °C) of the PS block of PS-*b*-PEO BCP.

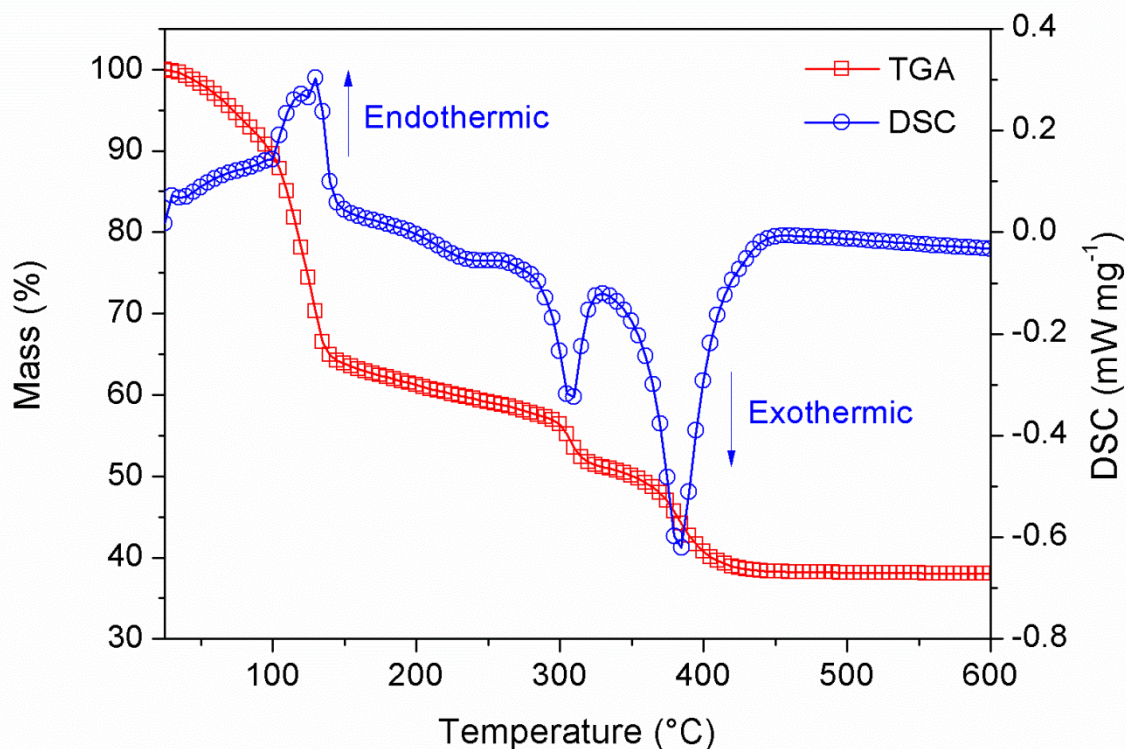


Figure 3.2. TGA and DSC curves for the PS-*b*-PEO BCP/TiO₂ composite.

It is important to note that the combustion temperature of PS-*b*-PEO BCP (400 – 450 °C) is higher than the crystallization temperature of TiO₂ (around 300 °C), so that it is possible to obtain crystalline TiO₂ films scaffolded with BCP whilst avoiding the collapse of the pores that often occurs when heating amorphous TiO₂.⁵⁵ This templating method therefore offers the possibility to make thicker multi-layered porous metal oxide films without the need for more involved synthetic protocols such as the combined assembly of soft and hard (CASH) chemistry method.⁵⁶⁻⁵⁹

Observation of the samples with an optical microscope shows smooth films with few occasional minor cracks at the edges of mesoporous TiO₂ on fluorine-doped tin oxide glass substrates (FTO). The scanning electron microscope (SEM) images of the film also show a porous smooth film (Figure 3.3a) with well-connected pores with diameters between 20 and 30 nm and a locally ordered structure (Figure 3.3b).

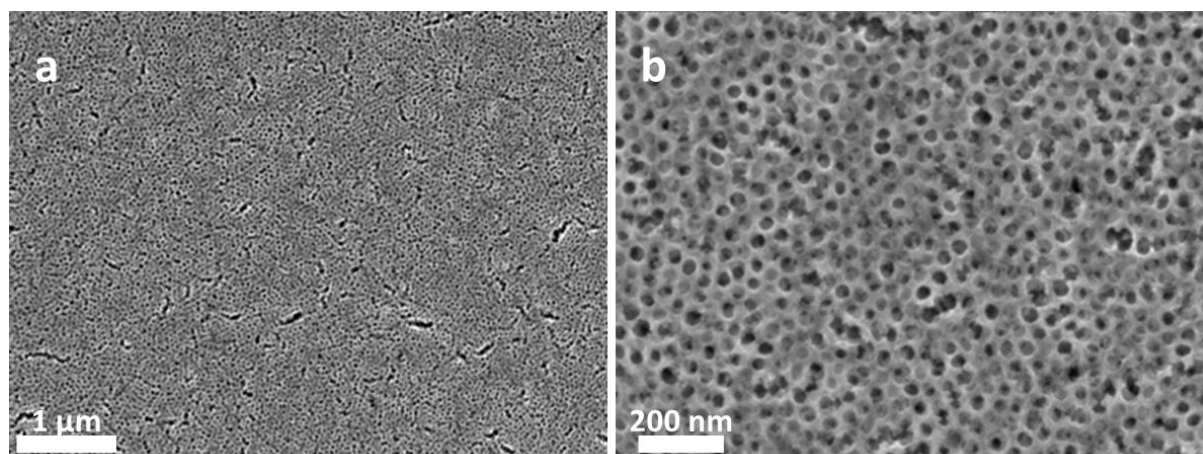


Figure 3.3. SEM images of a BCP-templated mesoporous TiO₂ films.

The porosity of the BCP-templated TiO₂ films was confirmed by transmission electron microscope (TEM) analysis as well. The image presented in Figure 3.4a shows the same locally ordered morphology seen in the SEM images. The electron diffraction pattern (inset in Figure 3.4a) indicates the presence of the anatase phase. The high-resolution transmission electron micrograph (HRTEM) in Figure 3.4b shows crystal fringes, indicating that the templated films are highly crystalline.

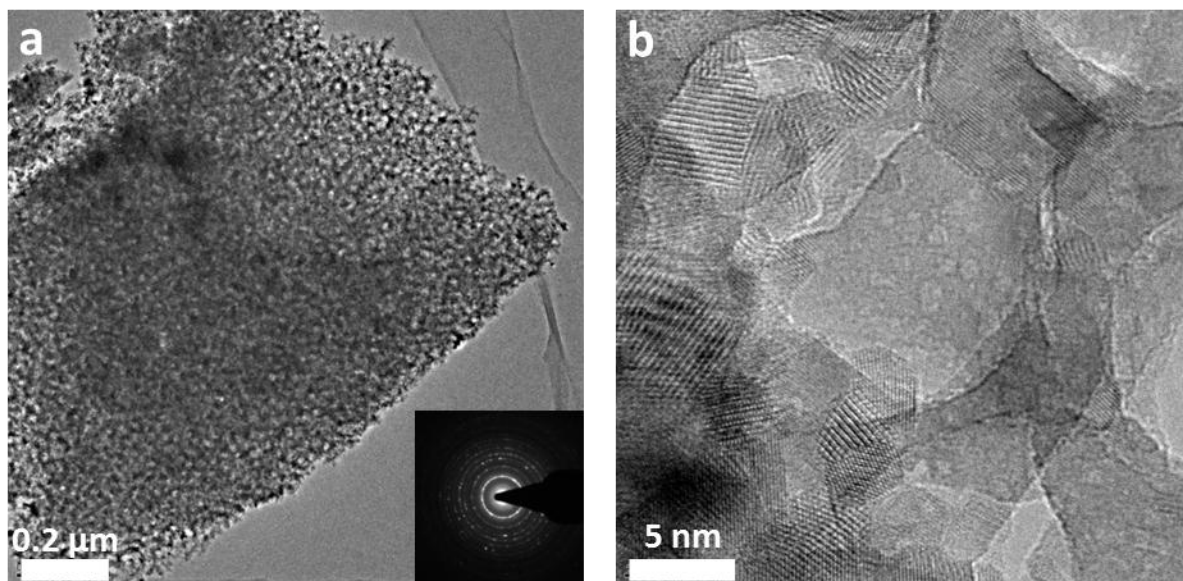


Figure 3.4. (a) TEM image showing the morphology of the BCP-templated mesoporous TiO₂ film. The inset shows the corresponding electron diffraction pattern. (b) HRTEM of the same material showing the crystal fringes.

Wide angle X-ray diffraction (XRD) measurements also confirmed the anatase phase of TiO₂ (cf. Figure A-1.1 in Appendix) and nitrogen sorption studies yielded a type IV isotherm, which provides evidence of the mesoporous structure (cf. Figure A-2.1 in Appendix).⁶⁰ The BET surface area of $84 \pm 1 \text{ m}^2 \text{ g}^{-1}$, the total pore volume of $0.5 \pm 0.01 \text{ cm}^3 \text{ g}^{-1}$ at the highest relative pressure $p/p_0 = 0.995$ and the DFT pore size distribution (inset of Figure A-2.1 in Appendix) was calculated from the nitrogen sorption isotherm. The average pore size of the BCP-templated mesoporous TiO₂ films is about 25 nm. The roughness factor (i.e. the ratio of internal area to projected geometric area), calculated by taking the density of anatase as 3.8 g cm^{-3} and using the measured BET surface area and total pore volume was found to be 190 ± 2 for a $1.4 \pm 0.1 \text{ μm}$ thick TiO₂ film.

The mesoporous TiO₂ electrodes were sensitized with PbS QDs using the SILAR method (6.5 cycles) described in the experimental section, producing a brown coloration of the initially transparent photoanodes.⁶¹ The scanning tunnelling electron microscopy (STEM) image of the

PbS QD-sensitized mesoporous electrode shows that most of the PbS QDs (white spots in the image) formed on the surface of TiO₂ have sizes of only a few nanometers (Figure 3.5a). There is also evidence of larger agglomerates of PbS QDs seen in the STEM image. Energy-dispersive X-ray (EDX) spectroscopy measurements were performed on a few selected areas on the PbS QD-sensitized mesoporous TiO₂ electrode to identify the presence of the expected elements (Figure 3.5b). As seen on the EDX images, the concentration of Pb is much higher in the area rich with white spots (area 1, Figure 3.5c). A lower Pb signal is recorded for the areas with a moderate concentration of white spots (areas 2 and 3, Figures 3.5d-3.5e) and almost no PbS signal in the area showing very few spots (area 4, Figure 3.5f).

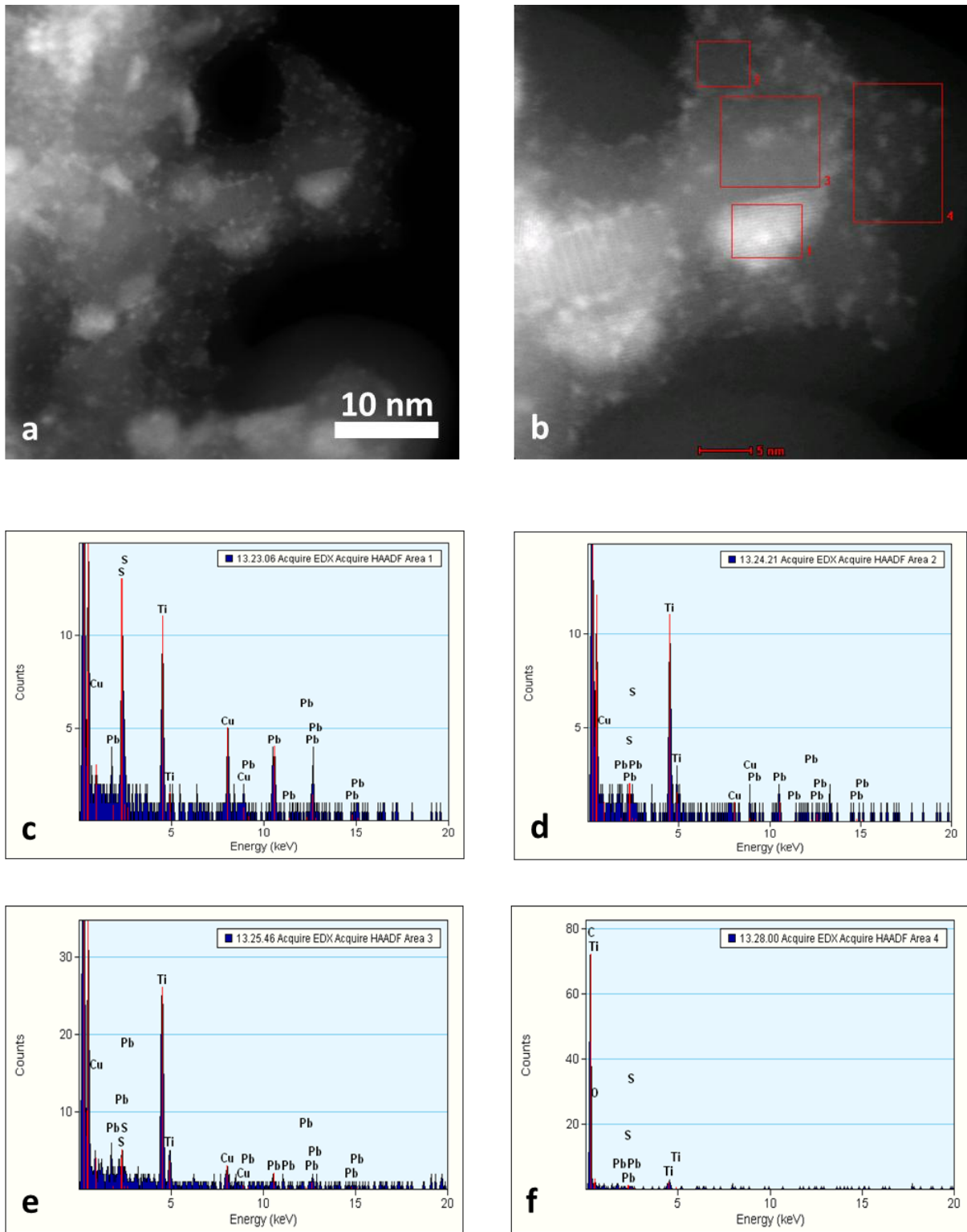


Figure 3.5. (a) and (b) STEM image of a mesoporous TiO_2 film sensitized with PbS QDs, (c) – (f) EDX of selected areas in image (b).

The PbS QD-sensitized mesoporous TiO_2 photoanodes were used to fabricate ETA solar cells as described in the experimental section. The cells had a standard sandwich structure

incorporating a 2 mm glass substrate, 200 nm FTO, ~60 nm of dense blocking layer of TiO₂, 1.4±0.1 μm of active layer (mesoporous TiO₂/PbS QDs/CuSCN), around 200 nm of a CuSCN capping layer and 100 nm thick sputtered gold contacts. The SEM cross-section image of a typical ETA cell is presented in Figure 3.6.

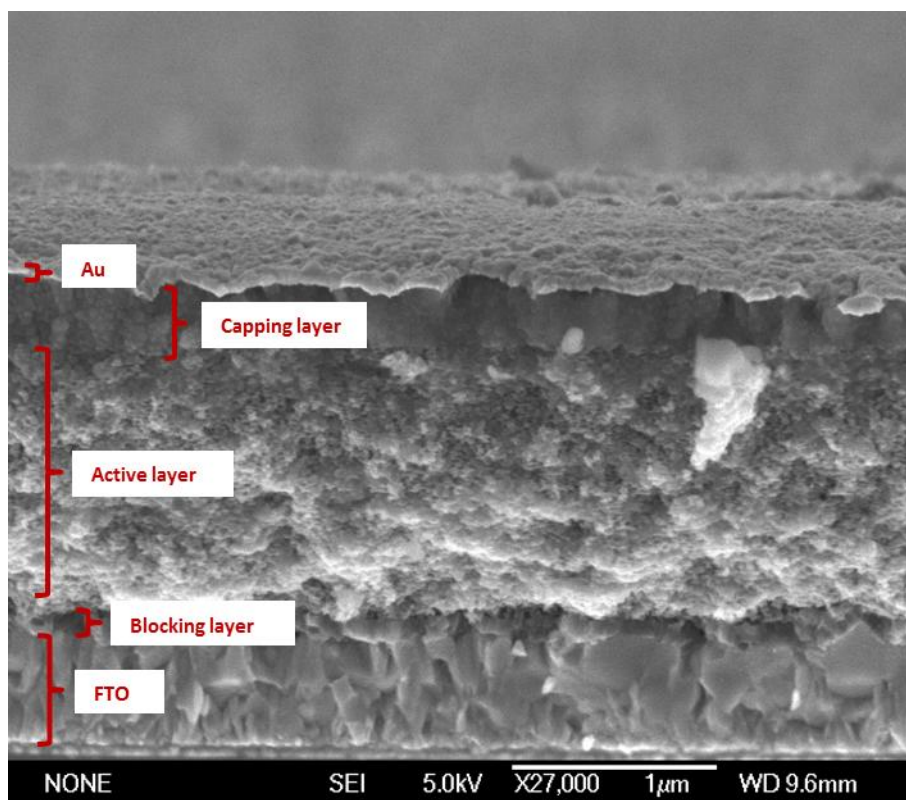


Figure 3.6. SEM cross-section image of ETA solar cell.

To evaluate the solar cell characteristics of the ETA cells, the performance of the solar cells was tested under standard global AM 1.5 G irradiation with 0.1 cm² masked area. The I-V measurements of the fabricated solar cells showed that the overall conversion efficiency of the best complete ETA cell under full sun is 0.26%, with an average conversion efficiency of 0.18±0.04% for 21 tested samples. Values of the short circuit current density $J_{SC} = 1.1 \text{ mA cm}^{-2}$, open circuit voltage $V_{OC} = 456 \text{ mV}$ and fill factor (FF) = 51% were derived from the I-V characteristic of the best complete ETA cell (Figure 3.7). The intercept of the I-V curve with the current density axis at a small angle and the rather steep intercept with the

voltage axis suggest that there is not much shunting and no high series resistance in the cell. This is also reflected in relatively high value of the fill factor (51%). For comparison, blank ETA cells without PbS sensitizer were also prepared. The comparison of the I-V characteristics of the blank and complete ETA cells shows that the short circuit current and also the open circuit voltage improved dramatically for the complete cell with respect to the blank cell.

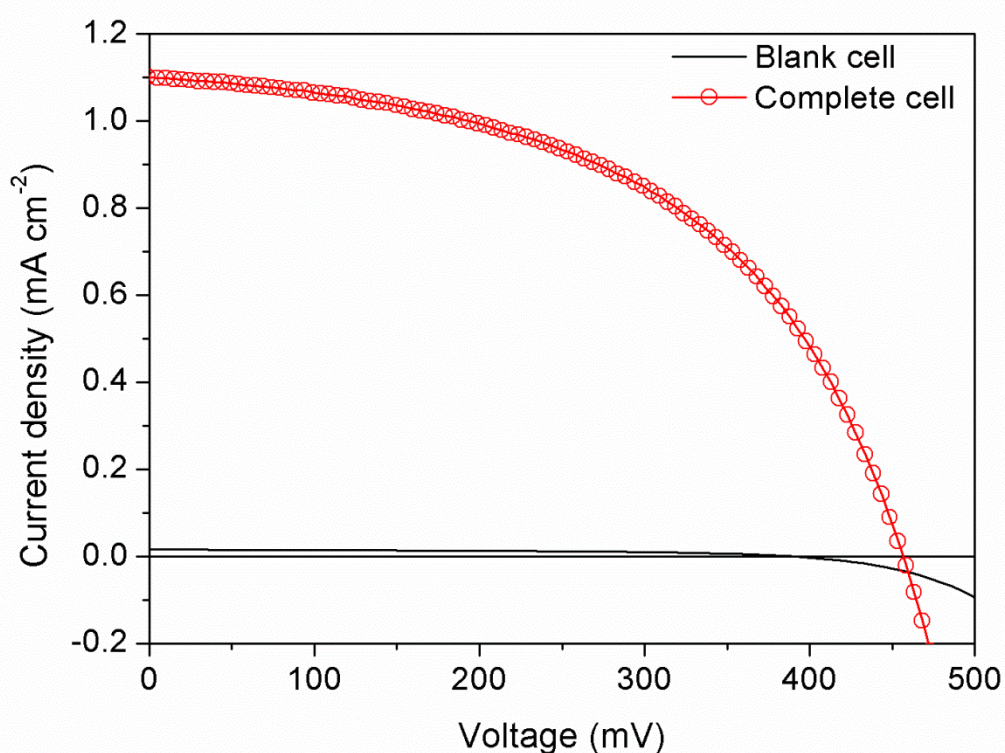


Figure 3.7. I-V characteristics for the blank and complete ETA cells.

The IPCE measurements were performed on blank and complete ETA cells in order to obtain the spectral response of the devices. As expected, the IPCE spectrum for the complete cell follows the ultraviolet-visible (UV-Vis) absorbance spectrum of the PbS QDs deposited onto a $1.4 \pm 0.1 \mu\text{m}$ thick mesoporous TiO_2 electrode and shows a value of around 15% at 400 nm (Figure 3.8). Calculation of the short circuit current from the IPCE spectrum yielded a value

of 1.18 mA cm^{-2} for the complete cell. The magnitude of short circuit current obtained from IPCE is in a good agreement with the results of the I-V measurements (1.1 mA cm^{-2}). The IPCE spectrum of the blank cell did not show any significant features throughout the entire measurement range except a small rise in the lower wavelength region (below 400 nm). This feature most possibly originates from the absorption of the ultraviolet (UV) component of the illumination light by TiO_2 and subsequent exciton generation and splitting at the interface of $\text{TiO}_2/\text{CuSCN}$.⁶² This can also be observed in the I-V measurements, as the blank cell also delivers a small photocurrent and photovoltage.

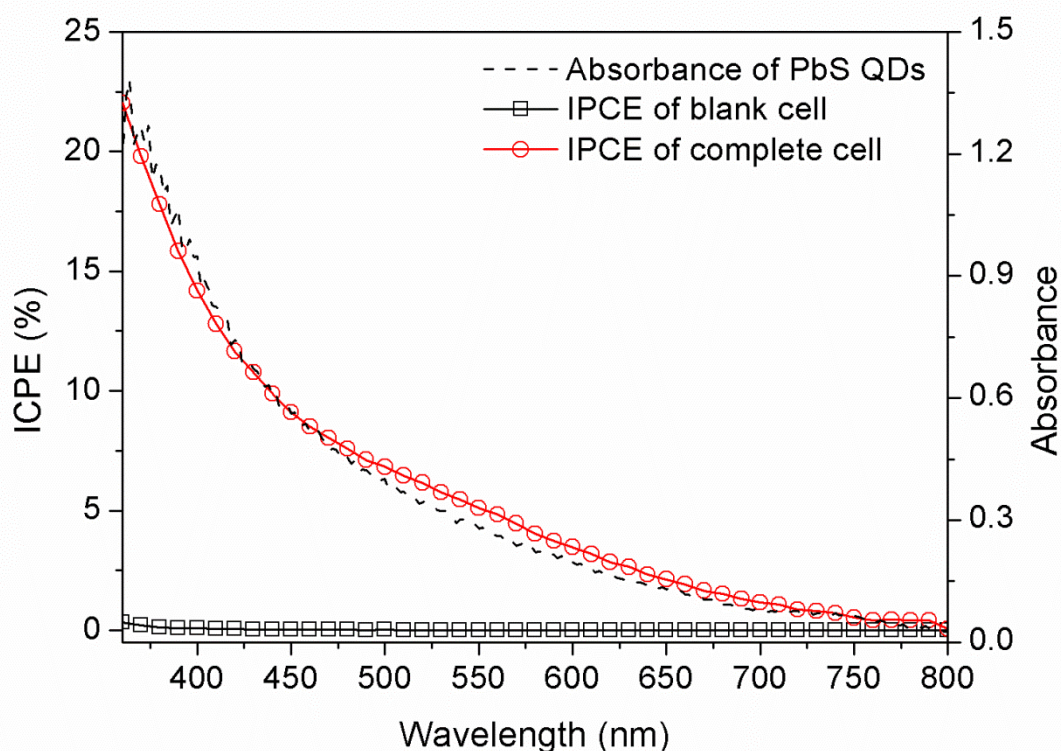


Figure 3.8. IPCE spectra of the blank and complete ETA cells and absorbance spectrum of PbS QDs grown on the walls of $1.4 \pm 0.1 \mu\text{m}$ thick mesoporous TiO_2 .

The absorbance spectrum of PbS QDs (Figure 3.8) was used to calculate the theoretical short circuit current for the device using the relationship (3.1):²⁰

$$J_{SC} = \int e \cdot F(\lambda) \cdot \eta_{LHE} \cdot \eta_{inj} \cdot \eta_c d\lambda, \quad (3.1)$$

where e is the electron charge, $F(\lambda)$ is incident photon flux density,⁶³ η_{LHE} is the light harvesting efficiency, η_{inj} is the electron injection efficiency and η_c is the electron collection efficiency. Integration was performed over the wavelength range from 360 up to 800 nm. η_{LHE} is calculated using the following relationship (3.2):

$$\eta_{LHE} = 1 - 10^{-A(\lambda)}, \quad (3.2)$$

where $A(\lambda)$ is absorbance of PbS QDs. The theoretical short circuit current calculated from the equation (3.1) assuming that η_{inj} and η_c are unity yielded a value of 10.4 mA cm⁻². Comparison of the experimental short circuit current (1.1 mA cm⁻²) with the calculated theoretical value (10.4 mA cm⁻²) shows that only one tenth of the possible short circuit current was realised in the experiments. This indicates that not all the excitons generated in PbS QDs are split at the TiO₂/PbS interface or/and not all the injected photoelectrons are collected to contribute to the photocurrent obtained with the device. Therefore, very likely neither the injection efficiency nor the collection efficiency are unity in the real experimental cells.

To gain a better understanding of these processes, the complete ETA cell was further characterized with EIS in order to obtain a quantitative estimation of the collection efficiency. Impedance spectra of the ETA cell were recorded under AM 1.5 G irradiation at open-circuit. Different open-circuit values were obtained by changing the intensity of the AM 1.5 G irradiation using neutral density (ND) filters. The experimental EIS data obtained were analysed using the ZView software with a model proposed by Bisquert et al.⁶⁴ (Figure 3.9).

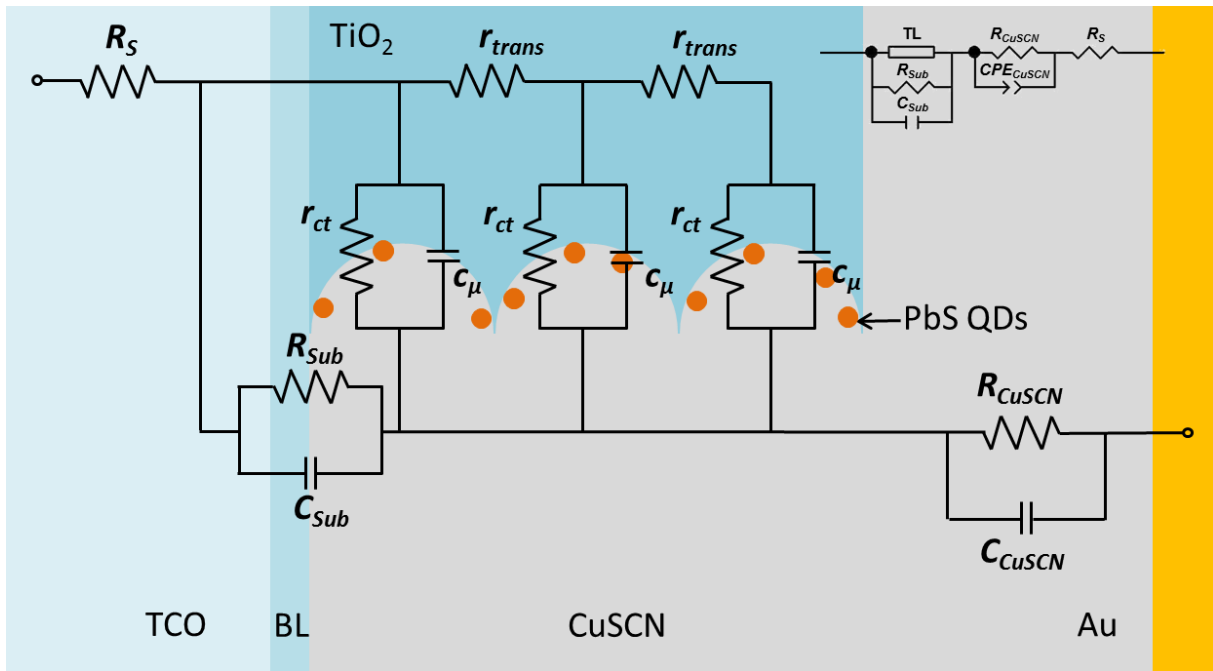


Figure 3.9. Equivalent circuit of the ETA solar cell.

In the model, a transmission line (TL) together with R_{Sub} and C_{Sub} represent the photoanode, whereas R_{CuSCN} and C_{CuSCN} and R_s represent the hole conductor and the series resistance, respectively. The R_{Sub} and C_{Sub} subcircuit connected parallel to the TL is introduced to represent shunting through the blocking layer.⁶⁵ A constant phase shift element (CPE_{CuSCN}) instead of capacitor is employed in order to take into account non-ideal behavior of the CuSCN HTM (inset of Figure 3.9).^{64, 66, 67}

The Nyquist, Bode and phase angle plots of experimental and fit spectra are presented in Figure 3.10.

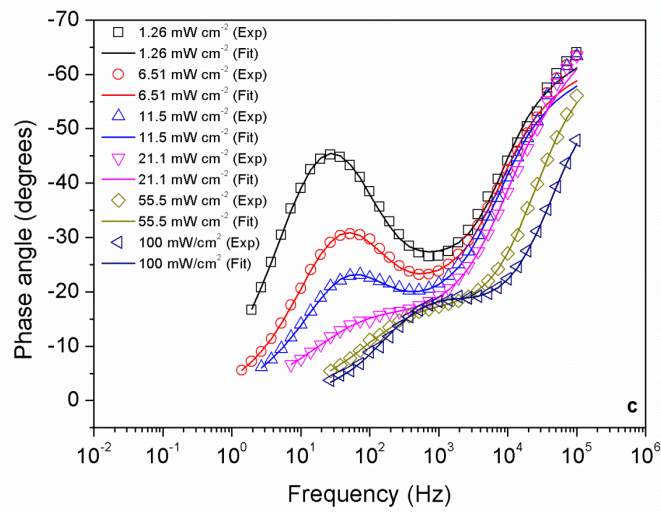
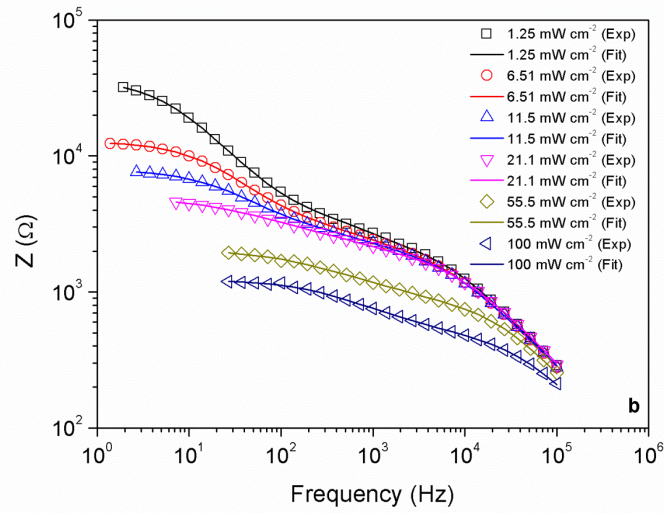
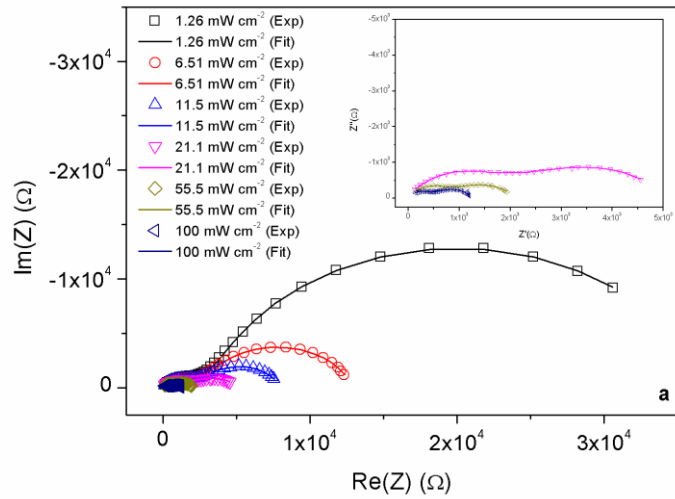


Figure 3.10. (a) Nyquist, (b) Bode, and (c) phase angle plots of experimental (symbols) and fit (solid lines) impedance spectra of the complete ETA cell under different illumination intensities.

Fitting of the experimental data showed that the resistance of the hole conductor, R_{CuSCN} , decreases dramatically as illumination intensity goes up, whereas CPE_{CuSCN} is rather insensitive to the changes in light intensity. This effect could also be due to photo-doping of the CuSCN which results in increased conductivity of the hole transporter.⁶⁸ The parameter of nonideality, n_{CPE} , for CPE_{CuSCN} varied around a value of 0.8 throughout (Table A-3.1 in Appendix).

The light intensity dependence of the values for the total recombination resistance, R_{ct} , transport resistance, R_{trans} , and chemical capacitance, C_{μ} , are presented in Figure 3.11. The values for R_{ct} , R_{trans} and C_{μ} obtained correspond well with findings of Boix et al.⁶⁴ for a similar system.

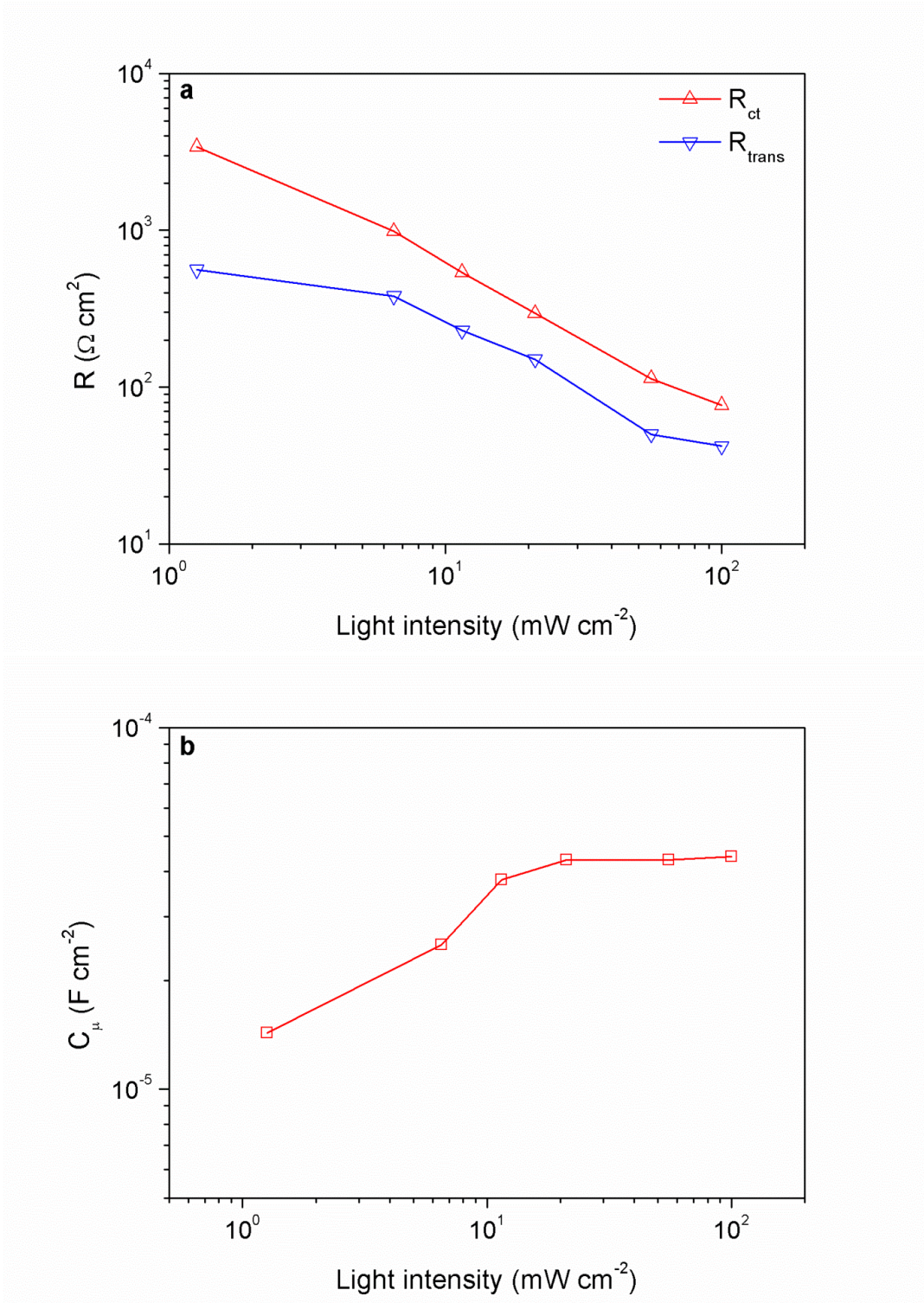


Figure 3.11. Light intensity dependence of (a) recombination resistance, transport resistance and (b) chemical capacitance of the complete PbS QD ETA cell.

Using values for R_{ct} and R_{trans} , we calculated the effective electron diffusion length, L_n , according to a model proposed by Bisquert et al.⁶⁹ using the relationship $L_n = d_f * (R_{ct} * R_{trans}^{-1})^{1/2}$. Here, d_f denotes the thickness of the film (active layer) of the solar cell. Our calculations showed that the effective electron diffusion length is 3.5 μm at the lowest light intensity and that it drops to 1.9 μm as the intensity of illumination light increases to 100 mW cm^{-2} (Figure 3.12a). The value for L_n at 100 mW cm^{-2} (1 Sun) is only a little higher than the thickness of the active layer, d_f , which is $1.4 \pm 0.1 \mu\text{m}$. This means that the electrons generated at the top contact region barely reach the bottom contact. For efficient working cells, however, the value of L_n , needs to be at least three times larger than the thickness of the active layer in order to ensure efficient electron collection.⁷⁰ Therefore, the values of L_n obtained from our experimental measurements suggest that the cell is not working efficiently and the collection efficiency, η_c , of the cell is much less than unity. The light intensity dependence of the electron lifetime obtained from EIS using the relationship $\tau_n = R_{ct} * C_\mu$ also shows rather low values (Figure 3.12b).⁷¹ At least one order of magnitude higher values for the electron lifetime would be required in order to obtain efficient electron collection.⁷²

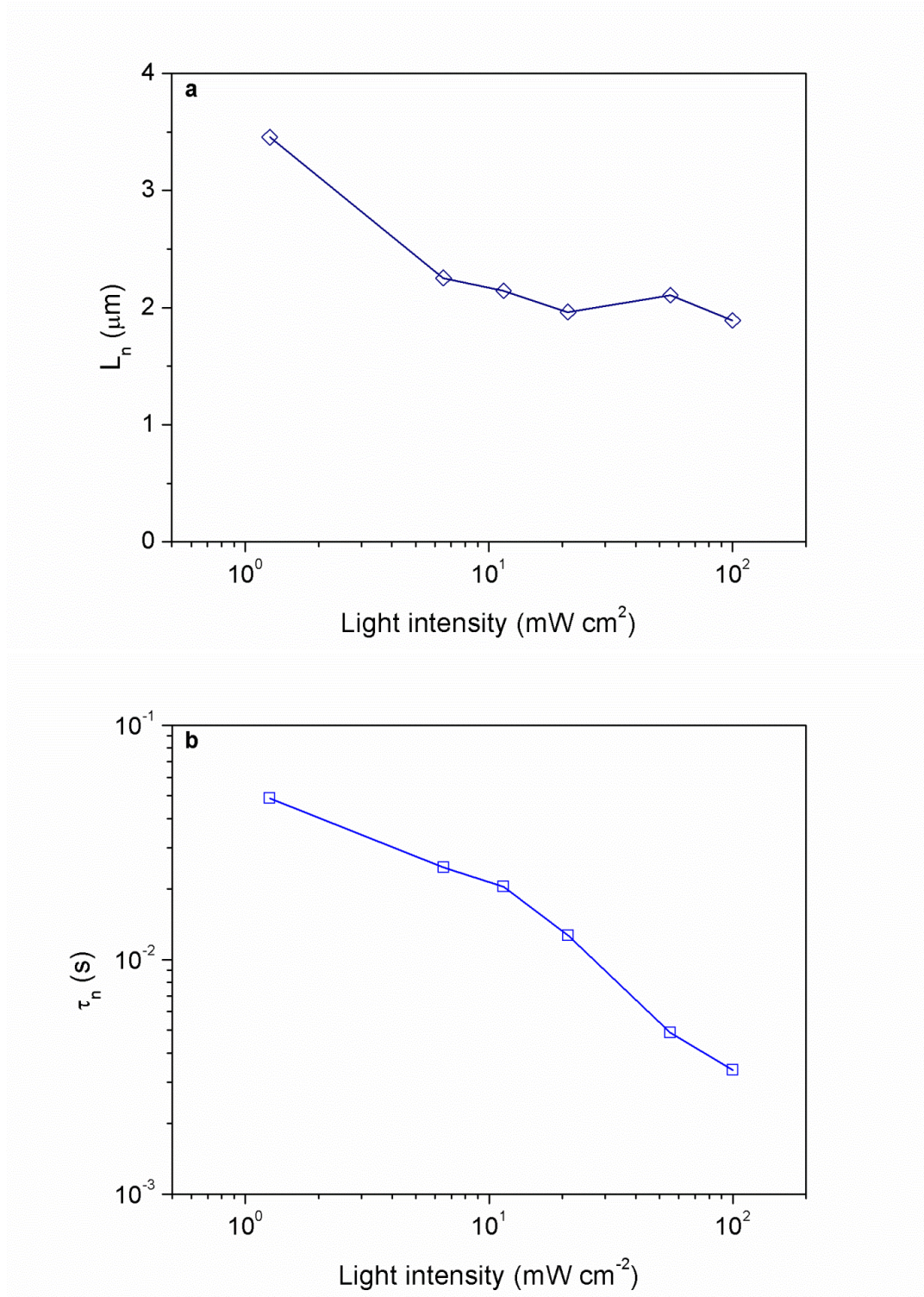


Figure 3.12. Light intensity dependence of (a) the effective electron diffusion length in the TiO_2 scaffold of the PbS QD ETA cell, and (b) the corresponding electron lifetime.

Overall, the analysis of I-V, IPCE and EIS results indicates that the complete ETA cells suffer from recombination losses, which are reflected in rather moderate values of the short circuit

current and the small effective electron diffusion length. The TEM image of the PbS QD-sensitized TiO₂ electrode (Figure 3.5a) suggests that the problems most possibly originate from the low PbS QD surface coverage. The latter leaves large contact areas between TiO₂ and CuSCN open, which could lead to increased recombination losses.^{49, 73} The possibly incomplete contact between CuSCN and the PbS layer as a consequence of poor infiltration of the HTM may also imply that holes generated close to the bottom of the mesoporous TiO₂ cannot be transferred from the PbS to the cathode contact. Also, the low conductivity of pure CuSCN HTM used in the ETA cells may also be a reason for the low values of the photocurrent.^{32, 74} We view these to be the main factors that can contribute to non-unity electron collection efficiency ($\eta_c < 1$).

At the same time, light harvesting by larger PbS QDs may not be followed by separation of electron hole pairs because the LUMO of the PbS QDs larger than 4 nm is lower than the conduction band energy of the TiO₂.²⁶ Low photocurrents obtained for the complete ETA cells could also be a result of some PbS oxidation inherent to the SILAR process.⁷⁵ Trap states with a depth of 0.3 to 0.5 eV introduced upon surface oxidation of PbS QDs by forming PbSO₄ and PbSO₃ during production and measurements can dramatically reduce the performance of the cells since these states can act as recombination centers.⁷⁶ All these factors lead to non-unity electron injection efficiency ($\eta_{inj} < 1$).

3.3 Conclusions

In conclusion, ETA cells have been fabricated using BCP-templated porous TiO₂ films serving as anodes. The PbS absorber layer was deposited onto the walls of the mesoporous TiO₂ by the SILAR method, and the CuSCN HTM was deposited from the solution phase by

doctor blading. The ETA solar cells were characterised with I-V, IPCE and EIS techniques. The performance of the complete ETA cells is still quite moderate as shown, for instance, by the fact that only 10% of the theoretical short circuit current was realized in the experiments. It was concluded from the analysis of I-V and EIS measurements that the device-limiting factors for the cells originate from significant recombination losses. A possible solution for this would be to use a continuous conformal buffer underlayer such as $\text{In(OH)}_x\text{S}_y$ or Al_2O_3 between porous TiO_2 and the absorber layer, and also well-protected PbS QDs of well-defined size.^{48, 77, 78} If a high coverage of such quantum dots on the surface of the porous TiO_2 could be achieved without agglomeration, the fabrication of high performance cells should be possible, provided that good contact to CuSCN HTM with sufficient conductivity is established.³²

3.4 Experimental Section

3.4.1 Materials

Copper(I) thiocyanate (Sigma-Aldrich), titanium(IV) ethoxide (Alfa Aesar), titanium(IV) chloride (Sigma-Aldrich), lead(II) nitrate (Sigma-Aldrich), sodium sulfide (Alfa Aesar), potassium thiocyanate (Acros Organics), hydrochloric acid 37% (Sigma-Aldrich), di-n-propyl sulphide (ABCR GmbH&Co, Germany), tetrahydrofuran (Sigma-Aldrich), methanol (Sigma-Aldrich).

3.4.2 Preparation of Mesoporous TiO₂ Electrodes

Mesoporous TiO₂ electrodes deposited onto FTO (Pilkington, TEC7) glass substrates (1.5×2 cm²) pre-coated with a ~60 nm dense blocking layer^{79, 80} (BL) (cf. subsection A-4 in Appendix) were prepared by a sol-gel method using PS-*b*-PEO BCP as structure directing template. PS-*b*-PEO BCP with 25.8 kg mol⁻¹ molecular weight was (synthesized via sequential anionic polymerization as described by Hillmyer et al.⁸¹) provided by group of Prof. Ulrich Wiesner from Cornell University in the USA. The weight fraction of the PEO units and polydispersity of the BCP were 15% and 1.04 respectively. The approximate number of monomers in the PS and PEO blocks is 210 and 84, correspondingly. The sol-gel solution was prepared by mixing 0.235 mL of hydrochloric acid (37%) with a solution of 0.36 mL (0.86 M) of titanium(IV) ethoxide and 0.07 g (1.3 mM) of PS-*b*-PEO BCP dissolved in 2 mL of anhydrous tetrahydrofuran in a 5 mL volume glass vial. After stirring for one day at room temperature (RT) the resulting sol-gel solution (~2.8 mL) was spin-coated onto FTO/BL substrates (900 rpm for 1 min) and calcined at 450 °C for 90 min in air with a heating ramp of 0.9 °C min⁻¹ to remove the templating polymer and to obtain crystalline porous TiO₂ films. The thickness of the resulting mesoporous TiO₂ electrodes was 1.4±0.1 μm.

3.4.3 Fabrication of Solar Cells

PbS QDs were deposited *in situ* by the SILAR process.²⁵ As-prepared TiO₂ electrodes (1.5×1 cm²) were immersed alternately into 0.02 M solutions of Pb(NO₃)₂ and Na₂S each in methanol (usually 10 mL) for 1 min. The films were washed with pure methanol between each immersion step in order to remove excess precursor solution and then dried with a

stream of compressed air. The sequence of immersion, washing and drying completes one cycle of the SILAR process. To grow PbS QDs onto the walls of the mesoporous TiO₂ films, six complete SILAR cycles were performed followed by one incomplete cycle in which the reaction was terminated after immersion of the film into Pb(NO₃)₂ and washing with pure methanol. The last incomplete cycle is expected to produce PbS QDs with Pb²⁺-terminated surfaces, which according to Lee et al.⁸² have shown to give a better cell performance than S²⁻ terminated surfaces. This is most probably related to a decrease in the formation of oxidized sulfur species on the surface of QDs upon terminating with Pb²⁺ cations.⁷⁶ The CuSCN HTM was prepared as described by Page et al.;¹¹ 0.1 g of CuSCN was dissolved in 5 mL of di-n-propyl sulphide in a 10 mL volume glass vial and stirred for 1 day at RT under ambient atmosphere. The mixture was then left to rest for at least one day before use in order to obtain a clear and saturated solution of CuSCN/di-n-propyl sulphide mixture, whereas excess CuSCN settles down at the bottom of the reaction vial. The final HTM solution was prepared by taking 0.2 mL aliquots of the CuSCN/di-n-propyl sulphide mixture and diluting them with 0.2 mL of di-n-propyl sulphide. The PbS QD-sensitized TiO₂ films were immersed into 10 mL of a 0.5 M aqueous solution of KSCN for 5 min and dried with a stream of compressed air. This treatment is reported to improve the contact between the PbS layer and CuSCN.⁷ The substrates were then placed on a hot plate at 80 °C, and the HTM solution was impregnated into the heated substrates by repeated doctor blading (typically 20 times) to fill up the pores and also to create a ~200 nm CuSCN capping layer. The deposition of HTM solution was performed under ambient atmosphere. The resulting composite films were placed into a Schlenk tube and evacuated down to 10⁻³ mbar for 2 hrs before storing them under nitrogen atmosphere overnight. Finally, 100 nm gold contacts were deposited onto the substrates through a mask using a Univex 350 sputter system (Oerlikon Leybold).

3.4.4 Characterization Methods

The structure and phase of the porous TiO₂ films were characterized by wide angle XRD using a Bruker D8 Discover diffractometer with Cu-K_α radiation ($\lambda = 1.5418 \text{ \AA}$) and equipped with a Vantec-1 position sensitive detector. Average film thickness values were measured with a profilometer (model Dektak 150). UV-Vis absorbance spectra of sensitized electrodes were recorded using a U-3501 spectrophotometer (Hitachi) and were corrected for the absorbance of the TiO₂ electrodes. Nitrogen sorption measurements on powder samples prepared by removing the templated TiO₂ films from the substrate were performed by using a NOVA 4000e surface area and pore size analyser (Quantachrome), and Autosorb-1 software (Quantachrome) was used to evaluate the data. The cross-section image of the ETA cell was observed using a JEOL-JSM-6500F SEM equipped with a 4 kV field emission gun. HRTEM and STEM analyses of the samples were performed using an FEI TITAN 80-300 TEM equipped with a field emission gun operating at 300 kV. The I-V characteristics of the ETA cells were measured under simulated solar light using a 300 W xenon lamp and a filter calibrated to approximate AM 1.5 G irradiation at 100 mW cm^{-2} (model: XPS 400, Solar Light Company Inc.). Calibration was performed using a pyranometer (model: PMA2144, Solar Light Company Inc.). The I-V characteristics were recorded with a potentiostat (Zahner Elektrik XPot) and LabVIEW software. The active area of the cells for I-V characterization was 0.1 cm^2 . The IPCE spectra of the cells were measured using chopped monochromatic light provided by a 150 W xenon lamp (Lot-Oriel) and a monochromator (Micro HR) with order sorting filters (Thorlabs). Measurements were done with bias light intensity (11.5 mW cm^{-2}). The signal was detected by a DSP lock-in amplifier (Model 7265, Signal Recovery). The IPCE data were recorded with a potentiostat (Zahner Elektrik XPot) using LabVIEW software. The incident light intensity of the chopped illumination was measured with a calibrated silicon photodetector. EIS measurements were obtained using a potentiostat

equipped with a frequency response analyser (model: FRA2 μ AUTOLAB III, Metrohm). The measurements were carried out under AM 1.5 G irradiation at open-circuit conditions over the frequency range from 1 kHz to 1 Hz with 10 mV amplitude AC perturbation voltage.

References

1. B. O'Regan and M. Gratzel, *Nature*, 1991, **353**, 737-740.
2. U. Bach, D. Lupo, P. Comte, J. E. Moser, F. Weissortel, J. Salbeck, H. Spreitzer and M. Gratzel, *Nature*, 1998, **395**, 583-585.
3. B. C. O'Regan and F. Lenzmann, *The Journal of Physical Chemistry B*, 2004, **108**, 4342-4350.
4. E. Lancelle-Beltran, P. Prené, C. Boscher, P. Belleville, P. Buvat and C. Sanchez, *Advanced Materials*, 2006, **18**, 2579-2582.
5. R. Zhu, C.-Y. Jiang, B. Liu and S. Ramakrishna, *Advanced Materials*, 2009, **21**, 994-1000.
6. J. Burschka, A. Dualeh, F. Kessler, E. Baranoff, N.-L. Cevey-Ha, C. Yi, M. K. Nazeeruddin and M. Grätzel, *Journal of the American Chemical Society*, 2011, **133**, 18042-18045.
7. G. Larramona, C. Choné, A. Jacob, D. Sakakura, B. Delatouche, D. Péré, X. Cieren, M. Nagino and R. Bayón, *Chemistry of Materials*, 2006, **18**, 1688-1696.

8. C. Lévy-Clément, R. Tena-Zaera, M. A. Ryan, A. Katty and G. Hodes, *Advanced Materials*, 2005, **17**, 1512-1515.
9. K. Ernst, I. Sieber, M. Neumann-Spallart, M. C. Lux-Steiner and R. Könenkamp, *Thin Solid Films*, 2000, **361–362**, 213-217.
10. I. Kaiser, K. Ernst, C. H. Fischer, R. Könenkamp, C. Rost, I. Sieber and M. C. Lux-Steiner, *Solar Energy Materials and Solar Cells*, 2001, **67**, 89-96.
11. M. Page, O. Niitsoo, Y. Itzhaik, D. Cahen and G. Hodes, *Energy & Environmental Science*, 2009, **2**, 220-223.
12. R. Suarez, P. K. Nair and P. V. Kamat, *Langmuir*, 1998, **14**, 3236-3241.
13. L. M. Peter, D. J. Riley, E. J. Tull and K. G. U. Wijayantha, *Chemical Communications*, 2002, 1030-1031.
14. I. Robel, V. Subramanian, M. Kuno and P. V. Kamat, *Journal of the American Chemical Society*, 2006, **128**, 2385-2393.
15. A. Zaban, O. I. Mičić, B. A. Gregg and A. J. Nozik, *Langmuir*, 1998, **14**, 3153-3156.
16. P. Yu, K. Zhu, A. G. Norman, S. Ferrere, A. J. Frank and A. J. Nozik, *The Journal of Physical Chemistry B*, 2006, **110**, 25451-25454.
17. S. Ito, S. Tanaka, H. Vahlman, H. Nishino, K. Manabe and P. Lund, *ChemPhysChem*, 2014, **15**, 1194-1200.
18. H. J. Lee, J.-H. Yum, H. C. Leventis, S. M. Zakeeruddin, S. A. Haque, P. Chen, S. I. Seok, M. Grätzel and M. K. Nazeeruddin, *The Journal of Physical Chemistry C*, 2008, **112**, 11600-11608.

19. T. Dittrich, A. Belaidi and A. Ennaoui, *Solar Energy Materials and Solar Cells*, 2011, **95**, 1527-1536.
20. Z. Yang, C.-Y. Chen, P. Roy and H.-T. Chang, *Chemical Communications*, 2011, **47**, 9561-9571.
21. C. Wadia, A. P. Alivisatos and D. M. Kammen, *Environmental Science & Technology*, 2009, **43**, 2072-2077.
22. L. M. Peter, *Philosophical Transactions of the Royal Society A: Mathematical, Physical and Engineering Sciences*, 2011, **369**, 1840-1856.
23. L. M. Peter, *The Journal of Physical Chemistry Letters*, 2011, **2**, 1861-1867.
24. H. Rahnamai, H. J. Gray and J. N. Zemel, *Thin Solid Films*, 1980, **69**, 347-350.
25. R. Vogel, P. Hoyer and H. Weller, *The Journal of Physical Chemistry*, 1994, **98**, 3183-3188.
26. B.-R. Hyun, Y.-W. Zhong, A. C. Bartnik, L. Sun, H. D. Abruña, F. W. Wise, J. D. Goodreau, J. R. Matthews, T. M. Leslie and N. F. Borrelli, *ACS Nano*, 2008, **2**, 2206-2212.
27. J. Tang, K. W. Kemp, S. Hoogland, K. S. Jeong, H. Liu, L. Levina, M. Furukawa, X. Wang, R. Debnath, D. Cha, K. W. Chou, A. Fischer, A. Amassian, J. B. Asbury and E. H. Sargent, *Nature Materials*, 2011, **10**, 765-771.
28. K. L. Chopra, P. D. Paulson and V. Dutta, *Progress in Photovoltaics: Research and Applications*, 2004, **12**, 69-92.

29. S. Emin, S. P. Singh, L. Han, N. Satoh and A. Islam, *Solar Energy*, 2011, **85**, 1264-1282.
30. S. Ito, K. Tsujimoto, D.-C. Nguyen, K. Manabe and H. Nishino, *International Journal of Hydrogen Energy*, 2013, **38**, 16749-16754.
31. E. V. A. Premalal, G. R. R. A. Kumara, R. M. G. Rajapakse, M. Shimomura, K. Murakami and A. Konno, *Chemical Communications*, 2010, **46**, 3360-3362.
32. E. V. A. Premalal, N. Dematage, G. R. R. A. Kumara, R. M. G. Rajapakse, M. Shimomura, K. Murakami and A. Konno, *Journal of Power Sources*, 2012, **203**, 288-296.
33. B. O'Regan, F. Lenzmann, R. Muis and J. Wienke, *Chemistry of Materials*, 2002, **14**, 5023-5029.
34. L. Sun, Y. Huang, M. A. Hossain, K. Li, S. Adams and Q. Wang, *Journal of The Electrochemical Society*, 2012, **159**, D323-D327.
35. K. Tsujimoto, D.-C. Nguyen, S. Ito, H. Nishino, H. Matsuyoshi, A. Konno, G. R. A. Kumara and K. Tennakone, *The Journal of Physical Chemistry C*, 2012, **116**, 13465-13471.
36. J. A. Christians and P. V. Kamat, *ACS Nano*, 2013, **7**, 7967-7974.
37. P. Tiwana, P. Docampo, M. B. Johnston, H. J. Snaith and L. M. Herz, *ACS Nano*, 2011, **5**, 5158-5166.
38. S. H. Im, C.-S. Lim, J. A. Chang, Y. H. Lee, N. Maiti, H.-J. Kim, M. K. Nazeeruddin, M. Grätzel and S. I. Seok, *Nano Letters*, 2011, **11**, 4789-4793.

39. P. Yang, D. Zhao, D. I. Margolese, B. F. Chmelka and G. D. Stucky, *Nature*, 1998, **396**, 152-155.
40. E. J. W. Crossland, S. Ludwigs, M. A. Hillmyer and U. Steiner, *Soft Matter*, 2007, **3**, 94-98.
41. E. J. W. Crossland, M. Kamperman, M. Nedelcu, C. Ducati, U. Wiesner, D. M. Smilgies, G. E. S. Toombes, M. A. Hillmyer, S. Ludwigs, U. Steiner and H. J. Snaith, *Nano Letters*, 2008, **9**, 2807-2812.
42. P. Docampo, M. Stefik, S. Guldin, R. Gunning, N. A. Yufa, N. Cai, P. Wang, U. Steiner, U. Wiesner and H. J. Snaith, *Advanced Energy Materials*, 2012, **2**, 676-682.
43. S. Guldin, P. Docampo, M. Stefik, G. Kamita, U. Wiesner, H. J. Snaith and U. Steiner, *Small*, 2012, **8**, 432-440.
44. I. Moreels, K. Lambert, D. Smeets, D. De Muynck, T. Nollet, J. C. Martins, F. Vanhaecke, A. Vantomme, C. Delerue, G. Allan and Z. Hens, *ACS Nano*, 2009, **3**, 3023-3030.
45. R. J. Ellingson, M. C. Beard, J. C. Johnson, P. Yu, O. I. Micic, A. J. Nozik, A. Shabaev and A. L. Efros, *Nano Letters*, 2005, **5**, 865-871.
46. M. T. Trinh, L. Polak, J. M. Schins, A. J. Houtepen, R. Vaxenburg, G. I. Maikov, G. Grinbom, A. G. Midgett, J. M. Luther, M. C. Beard, A. J. Nozik, M. Bonn, E. Lifshitz and L. D. A. Siebbeles, *Nano Letters*, 2011, **11**, 1623-1629.
47. R. Bayon, R. Musembi, A. Belaidi, M. Bär, T. Guminskaya, M. C. Lux-Steiner and T. Dittrich, *Solar Energy Materials and Solar Cells*, 2005, **89**, 13-25.

48. I. Oja, A. Belaidi, L. Dloczik, M. C. Lux-Steiner and D. Th, *Semiconductor Science and Technology*, 2006, **21**, 520.
49. E. Edri, H. Cohen and G. Hodes, *ACS Applied Materials & Interfaces*, 2013, **5**, 5156-5164.
50. M. C. Orilall and U. Wiesner, *Chemical Society Reviews*, 2011, **40**, 520-535.
51. Z. Liu, Y. Li, Z. Zhao, Y. Cui, K. Hara and M. Miyauchi, *Journal of Materials Chemistry*, 2010, **20**, 492-497.
52. B. Ma, J. Ma and G. K. L. Goh, *Journal of Materials Science*, 2008, **43**, 4297-4302.
53. C. J. Brinker, Y. Lu, A. Sellinger and H. Fan, *Advanced Materials*, 1999, **11**, 579-585.
54. J. Gutierrez, A. Tercjak, I. Garcia, L. Peponi and I. Mondragon, *Nanotechnology*, 2008, **19**, 155607.
55. J. M. Szeifert, J. M. Feckl, D. Fattakhova-Rohlfing, Y. Liu, V. Kalousek, J. Rathousky and T. Bein, *Journal of the American Chemical Society*, 2010, **132**, 12605-12611.
56. J. Lee, M. Christopher Orilall, S. C. Warren, M. Kamperman, F. J. DiSalvo and U. Wiesner, *Nature Materials*, 2008, **7**, 222-228.
57. M. Nedelcu, J. Lee, E. J. W. Crossland, S. C. Warren, M. C. Orilall, S. Guldin, S. Huttner, C. Ducati, D. Eder, U. Wiesner, U. Steiner and H. J. Snaith, *Soft Matter*, 2009, **5**, 134-139.
58. J. Procházka, L. Kavan, M. t. Zúkalová, O. Frank, M. Kalbáč, A. t. Zúkal, M. Klementová, D. Carbone and M. Graetzel, *Chemistry of Materials*, 2009, **21**, 1457-1464.

59. Y. Zhang, Z. B. Xie and J. Wang, *Nanotechnology*, 2009, **20**, 505602.
60. K. S. W. Sing, D. H. Everett, R. A. W. Haul, L. Moscou, R. A. Pierotti, J. Rouquerol and T. Siemieniewska, *Pure & Applied Chemistry*, 1985, **57**, 603-619.
61. H. Lee, H. C. Leventis, S.-J. Moon, P. Chen, S. Ito, S. A. Haque, T. Torres, F. Nüesch, T. Geiger, S. M. Zakeeruddin, M. Grätzel and M. K. Nazeeruddin, *Advanced Functional Materials*, 2009, **19**, 2735-2742.
62. S. M. Hatch, J. Briscoe, A. Sapelkin, W. P. Gillin, J. B. Gilchrist, M. P. Ryan, S. Heutz and S. Dunn, *Journal of Applied Physics*, 2013, **113**, 204501-204509.
63. Reference Solar Spectral Irradiance: ASTM G-173, <http://rredc.nrel.gov/solar/spectra/am1.5/ASTMG173/ASTMG173.html>, 2013.
64. P. P. Boix, G. Larramona, A. Jacob, B. Delatouche, I. Mora-Seró and J. Bisquert, *The Journal of Physical Chemistry C*, 2012, **116**, 1579-1587.
65. F. Fabregat-Santiago, G. Garcia-Belmonte, I. Mora-Seró and J. Bisquert, *Physical Chemistry Chemical Physics*, 2011, **13**, 9083-9118.
66. I. Mora-Seró, S. Gimenez, F. Fabregat-Santiago, E. Azaceta, R. Tena-Zaera and J. Bisquert, *Physical Chemistry Chemical Physics*, 2011, **13**.
67. A. Dualeh, T. Moehl, M. K. Nazeeruddin and M. Grätzel, *ACS Nano*, 2013, **7**, 2292-2301.
68. S. Nezu, G. Larramona, C. Choné, A. Jacob, B. Delatouche, D. Péré and C. Moisan, *The Journal of Physical Chemistry C*, 2010, **114**, 6854-6859.
69. J. Bisquert, *The Journal of Physical Chemistry B*, 2002, **106**, 325-333.

70. J. R. Jennings and L. M. Peter, *The Journal of Physical Chemistry C*, 2007, **111**, 16100-16104.
71. J. Bisquert, F. Fabregat-Santiago, I. Mora-Seró, G. Garcia-Belmonte and S. Giménez, *The Journal of Physical Chemistry C*, 2009, **113**, 17278-17290.
72. A. Braga, S. Giménez, I. Concina, A. Vomiero and I. Mora-Seró, *The Journal of Physical Chemistry Letters*, 2011, **2**, 454-460.
73. E. Edri, E. Rabinovich, O. Niitsoo, H. Cohen, T. Bendikov and G. Hodes, *The Journal of Physical Chemistry C*, 2010, **114**, 13092-13097.
74. V. P. S. Perera, M. K. I. Senevirathna, P. K. D. D. P. Pitigala and K. Tennakone, *Solar Energy Materials and Solar Cells*, 2005, **86**, 443-450.
75. M. A. Hossain, Z. Y. Koh and Q. Wang, *Physical Chemistry Chemical Physics*, 2012, **14**, 7367-7374.
76. J. Tang, L. Brzozowski, D. A. R. Barkhouse, X. Wang, R. Debnath, R. Wolowiec, E. Palmiano, L. Levina, A. G. Pattantyus-Abraham, D. Jamakosmanovic and E. H. Sargent, *ACS Nano*, 2010, **4**, 869-878.
77. S. Kim, S. H. Im, M. Kang, J. H. Heo, S. I. Seok, S.-W. Kim, I. Mora-Seró and J. Bisquert, *Physical Chemistry Chemical Physics*, 2012, **14**, 14999-15002.
78. T. P. Brennan, O. Trejo, K. E. Roelofs, J. Xu, F. B. Prinz and S. F. Bent, *Journal of Materials Chemistry A*, 2013, **1**, 7566-7571.
79. L. Kavan and M. Grätzel, *Electrochimica Acta*, 1995, **40**, 643-652.

80. P. J. Cameron and L. M. Peter, *The Journal of Physical Chemistry B*, 2003, **107**, 14394-14400.
81. M. A. Hillmyer and F. S. Bates, *Macromolecules*, 1996, **29**, 6994-7002.
82. H. J. Lee, P. Chen, S.-J. Moon, F. d. r. Sauvage, K. Sivula, T. Bessho, D. R. Gamelin, P. Comte, S. M. Zakeeruddin, S. I. Seok, M. Grätzel and M. K. Nazeeruddin, *Langmuir*, 2009, **25**, 7602-7608.

4 Quantum-Dot-Sensitized Solar Cells with Water-Soluble and Air-Stable PbS Quantum Dots

The chapter is based on the following publication:

Askhat N. Jumabekov, Felix Deschler, Daniel Böhm, Laurence M. Peter, Jochen Feldmann and Thomas Bein, *Journal of Physical Chemistry C*, 2014, **118**, 5142-5149.

Abstract

The sensitization of dispersed P25 TiO₂ nanoparticles and macroporous TiO₂ films with water-soluble and air-stable PbS quantum dots (QDs) capped with L-glutathione (GSH) ligands was investigated. Optimum sensitization was achieved by careful adjustment of the surface charges of TiO₂ and PbS QDs by controlling the pH of the QD solution. Efficient electron transfer from photoexcited PbS QDs via the GSH ligands into the conduction band of TiO₂ was demonstrated by photoluminescence spectroscopy of PbS QD-sensitized P25 nanoparticles. The PbS QD-sensitized porous TiO₂ electrodes were used to prepare quantum-dot-sensitized solar cells utilizing a Cu_xS_y counter electrode and aqueous polysulfide electrolyte. Cells with up to 64% injection efficiency, 1.1% AM 1.5 G conversion efficiency and short circuit current density of 7.4 mA cm⁻² were obtained. The physical parameters of the cells were investigated using electrochemical impedance spectroscopy.

4.1 Introduction

The relative ease of producing PbS quantum dot-sensitized metal oxide (MO) semiconductors such as TiO₂, SnO₂ or ZnO makes quantum dot sensitized solar cells (QDSCs) an appealing research topic.^{1, 2} One of the significant advantages of using PbS quantum dots (QDs) as sensitizers is the possibility to tune the highest occupied molecular orbital and lowest unoccupied molecular orbital (HOMO-LUMO) gap of the QDs by controlling their size, which allows for photon harvesting over the optimum spectral range.³⁻⁶ It has also been shown that it is possible to generate and dissociate multiple excitons in PbS QDs, holding out the promise of exceeding the thermodynamic Shockley-Queisser limit for solar cell efficiency.^{7, 8}

PbS QDs and thin films can be deposited on the walls of semiconducting metal oxides *in situ* by chemical bath deposition (CBD) or by successive ionic layer adsorption/reaction (SILAR).^{4, 9} Alternatively, the PbS QDs can be pre-synthesised and attached by soaking the metal oxide surface in a solution of PbS QDs.^{3, 5, 10, 11} The latter method has become more common in recent years since it gives better control over the size, size distribution and surface functionalization of the adsorbed QDs.¹²

Generally, pre-synthesized PbS QDs are capped with hydrophobic oleic acid (OA) and dispersed in organic solvents.³ The OA moieties bind to the PbS surface with their carboxyl-group and extend the hydrophobic tails outwards, thus preventing aggregation of the quantum dots. However, due to the hydrophobic and hydrophilic nature, respectively, of OA-capped PbS (PbS-OA) QDs and oxides such as TiO₂ it is difficult to achieve high coverage of quantum dots. OA also acts as an effective insulating shell that inhibits electron transfer from the PbS QDs to the TiO₂.¹³

Three main approaches have been developed over the past few years for the attachment of

pre-synthesized QDs to a metal oxide semiconductor. The first approach, reported originally by Zaban et al.,¹⁰ involves assembly by direct attachment where sensitization is achieved by immersion of porous TiO₂ electrodes into a solution of InP QDs in hexane or toluene. Similar examples with InAs and CdSe QDs were reported by Yu et al.¹⁴ and by Giménez et al.¹⁵ In the second approach – assembly by electrophoretic deposition (EPD) – an external electrostatic force is used to assist the sensitization. An example of the EPD approach was first reported by Smith et al.,¹⁶ where deposition of CdSe nanocrystals (NCs) onto a flat TiO₂ substrate was demonstrated. The EPD method was used by Salant et al.¹⁷ to deposit CdSe QDs on porous TiO₂ and by Benekohal et al.¹⁸ to deposit PbS QDs.

The final approach involves linker-assisted assembly, which can be divided into three methods.¹² In the first method, a metal oxide substrate (e.g. porous TiO₂ film) is functionalized with bifunctional linker molecules and then immersed into a QD solution.¹¹ Hyun et al.⁵ showed that this method can be applied for the attachment of PbS QDs to TiO₂ using 3-mercaptopropionic acid (MPA) to functionalize a porous TiO₂ electrode. The second method is a combination of linker-assisted assembly and *in situ* fabrication of the QDs.¹² This method was demonstrated by Peter et al.¹⁹ for the case of CdS QD sensitization of porous TiO₂ electrodes, and Ratanatawanate et al.²⁰ reported a similar method with PbS QDs. In the third method, which was chosen for the experiments reported here, after synthesis QDs are coated with bifunctional linker molecules and then adsorbed onto the untreated substrate surface via the interaction of the terminal functional groups of the linker molecules.¹² The hydrophobic long-chained capping groups such as OA of organic-soluble QDs are displaced by bifunctional linkers such as MPA via ligand exchange, and the surface-modified QDs are used to sensitize the metal oxide semiconductor.¹² An example for this method was reported by Leschkies et al.²¹ for the case of CdSe QD sensitization of ZnO and was extended later by Sambur et al.²² for the deposition of PbS QDs.

The development of the methods described above has led to substantial progress in the attachment of QDs to porous metal oxide semiconducting scaffolds.¹² Improvements in device performance are also based on a deeper understanding of the role of substrate morphology, the chemisorption of the QDs and the dynamics of generated charge carrier pairs.²³ Nevertheless, some fundamental questions still remain unsolved concerning the structure and surface-attachment functionality and the solvation of the QDs.¹² One of the main problems remaining is how to achieve water solubility of the QDs while protecting the QDs from oxidation. The formation of surface oxides causes a drastic reduction of device performance due to deep trap states.^{24, 25} Another problem causing low device performance is an imbalance between the number of ligands and the excess lead atoms on the QD surface, which, according to density functional theory (DFT) calculations, leads to the introduction of sub-band trap states.²⁶ It is therefore essential to provide the best possible surface passivation by the linker molecules and possibly by other treatments as well.²⁶

Here we report on the successful sensitization of TiO₂ NPs and macroporous TiO₂ electrodes with water-soluble and air-stable PbS QDs capped with L-glutathione (GSH) ligands by using a modified version of the method of linker-assisted assembly. We investigated the optical properties of water-soluble PbS QDs and dispersed QD-TiO₂ complexes with ultraviolet-visible-near infrared (UV-Vis-NIR) and photoluminescence (PL) spectroscopy. Based on our findings, we show that the GSH ligand provides excellent protection and stabilization of PbS QDs as well as a good charge carrier conductance. We assembled sensitized macroporous TiO₂ electrodes into solar cells and characterized photovoltaic properties with current-voltage (I-V) and electrochemical impedance spectroscopy (EIS) measurements. Our results show that the QD-sensitized cells prepared in this way have reasonably good performance with high electron lifetime and diffusion length as well as electron injection efficiencies in excess of 60%.

4.2 Results and Discussion

There have been major developments in the synthesis of colloidal PbS QDs. Most synthetic routes for making a high quality QDs are based on the ‘hot injection’ method originally developed by Murray et al.²⁷ for CdX (X = S, Se, Te) and extended by Hines. et al.³ for the synthesis of PbS QDs. In our experiments, we used the synthetic route described by Tang et al.¹³ for making colloidal PbS QDs (cf. section A-5 in Appendix). The structure of the PbS-OA QDs was confirmed by wide-angle X-ray diffraction (XRD) analysis (JCPDS File No. 00-005-0592). Estimation of the size from the (220) peak of the XRD pattern using the Scherrer equation resulted in a value of ~3 nm for the PbS-OA QDs (Figure 4.1).²⁸

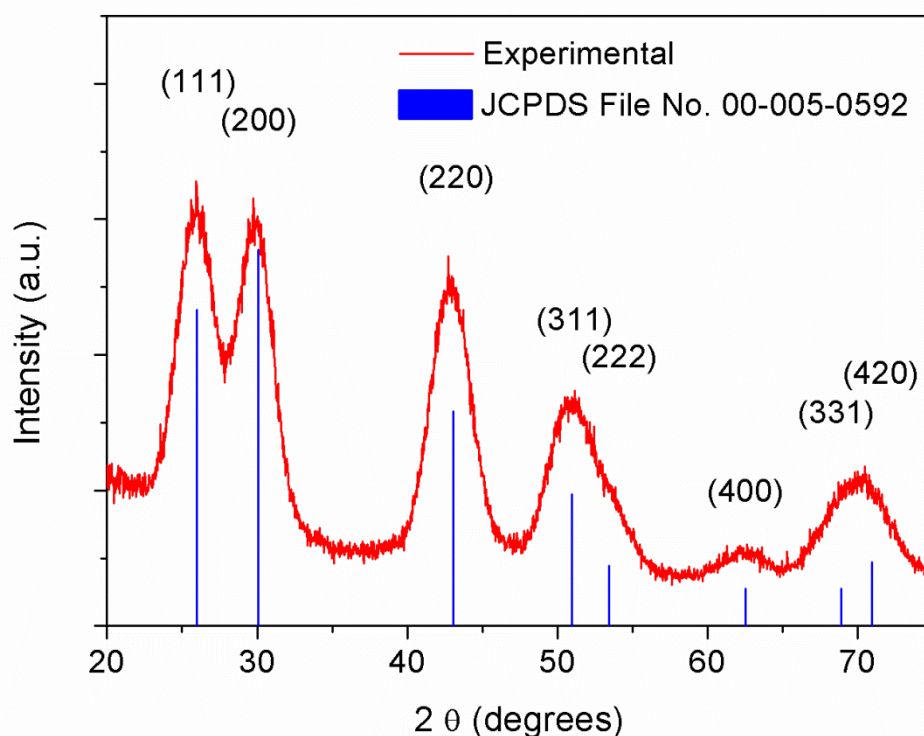


Figure 4.1. Wide angle XRD spectra of PbS-OA QDs.

The UV-Vis-NIR absorbance measurements of the PbS-OA QDs in chloroform showed a characteristic first excitonic peak at 900 nm which indicates presence of well-dispersed PbS-

OA QDs with narrow size distribution (Figure 4.2).³ It is possible to estimate the size of QDs based on the position of the first excitonic peak of the UV-Vis-NIR spectra by using the Brus equation.^{6, 29} The calculation gave 2.9 nm for the average size of the PbS-OA QDs, which is consistent with the value (~3 nm) obtained from the XRD measurements.

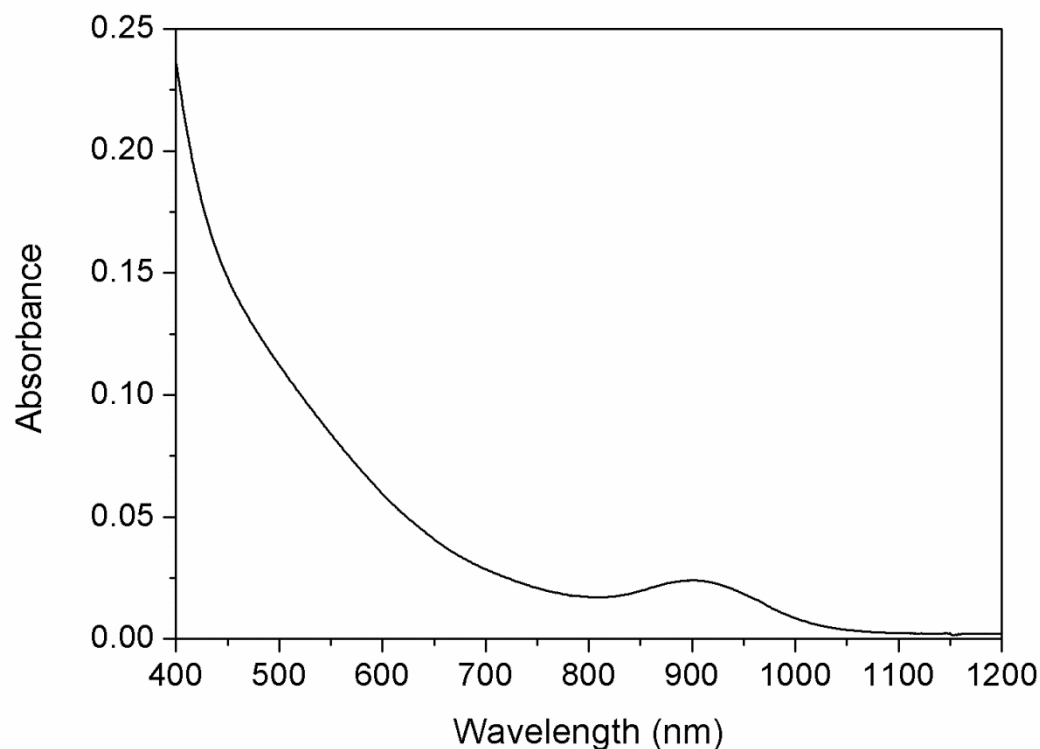


Figure 4.2. Absorbance of PbS-OA QDs dispersed in chloroform.

The PbS-OA QDs, which are soluble in nonpolar solvents such as octane or chloroform, were water solubilised by replacing OA by L-Glutathione (GSH) ligand (cf. Scheme A-6.1 in Appendix) using the ligand exchange procedure described by Deng et al.³⁰ The comparison of UV-Vis-NIR absorbance spectra shows that the size of PbS QDs slightly increases after ligand exchange, as indicated by the red shift of the first excitonic peak for the PbS-GSH QD water solution relative to PbS-OA QDs in chloroform (inset in Figure 4.3). This may indicate Ostwald ripening during the ligand exchange procedure. Nonetheless, the change in size is

relatively minor; according to a calculation based on the first excitonic peak of the UV-Vis-NIR spectra, the diameter of the PbS QDs only changes from 2.9 to 3.1 nm.

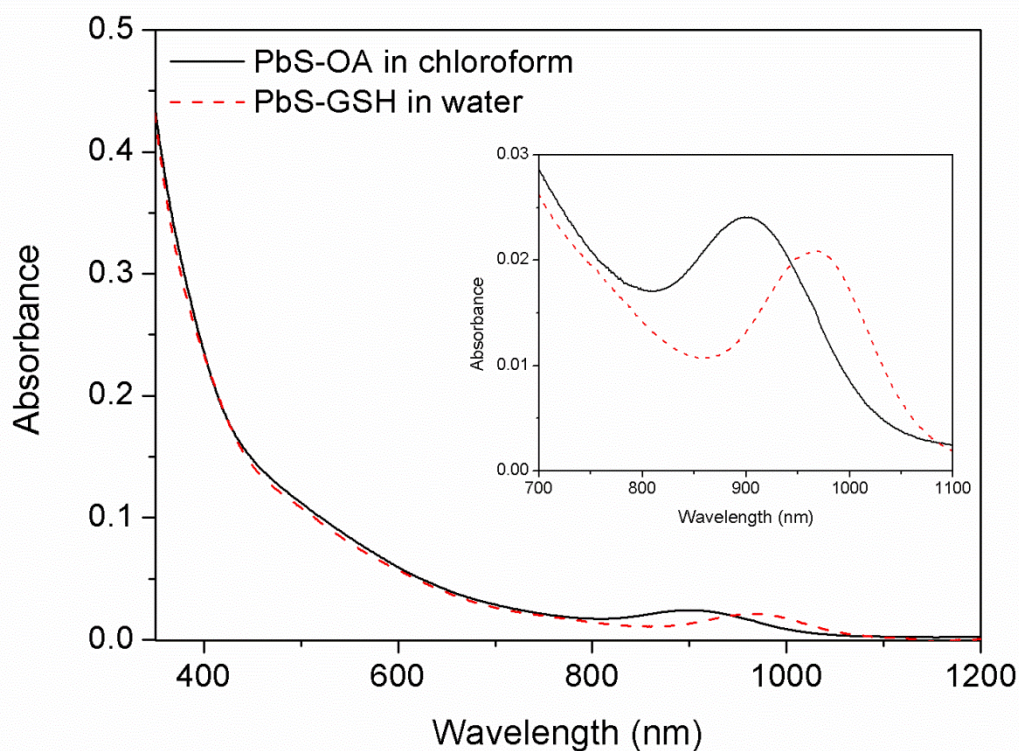


Figure 4.3. UV-Vis-NIR absorbance of the PbS-OA QDs in chloroform and the PbS-GSH QDs in water.

The wavelength-dependent absorption coefficient, $\alpha(\lambda)$, for PbS-GSH QDs was also calculated from the UV-Vis-NIR spectrum using the Lambert-Beer law: $A(\lambda) = 2.303 \times \alpha(\lambda) \times d$, where d is the optical path length (~ 35 nm) in the the PbS calculated from the concentration (0.11 mM) of PbS-GSH QD solution (cf. Figure A-7.1 in Appendix).³¹

Water-solubilised PbS-GSH QDs were further investigated with transmission electron microscopy (TEM). Figure 4.4a shows a high resolution TEM (HRTEM) image of a PbS-GSH QD with the (111) crystallite plane facing perpendicular to the incident electron beam. The analysis of TEM images confirmed about 3 nm for the size of PbS-GSH QDs, similar to the values obtained from UV-Vis-NIR absorbance measurements. The size distribution

diagram for PbS-GSH QDs estimated by measuring diameters of over 200 PbS-GSH QDs using TEM imaging revealed a narrow size distribution of PbS-GSH QDs with average size of ~3.2 nm (Figure 4.4b).

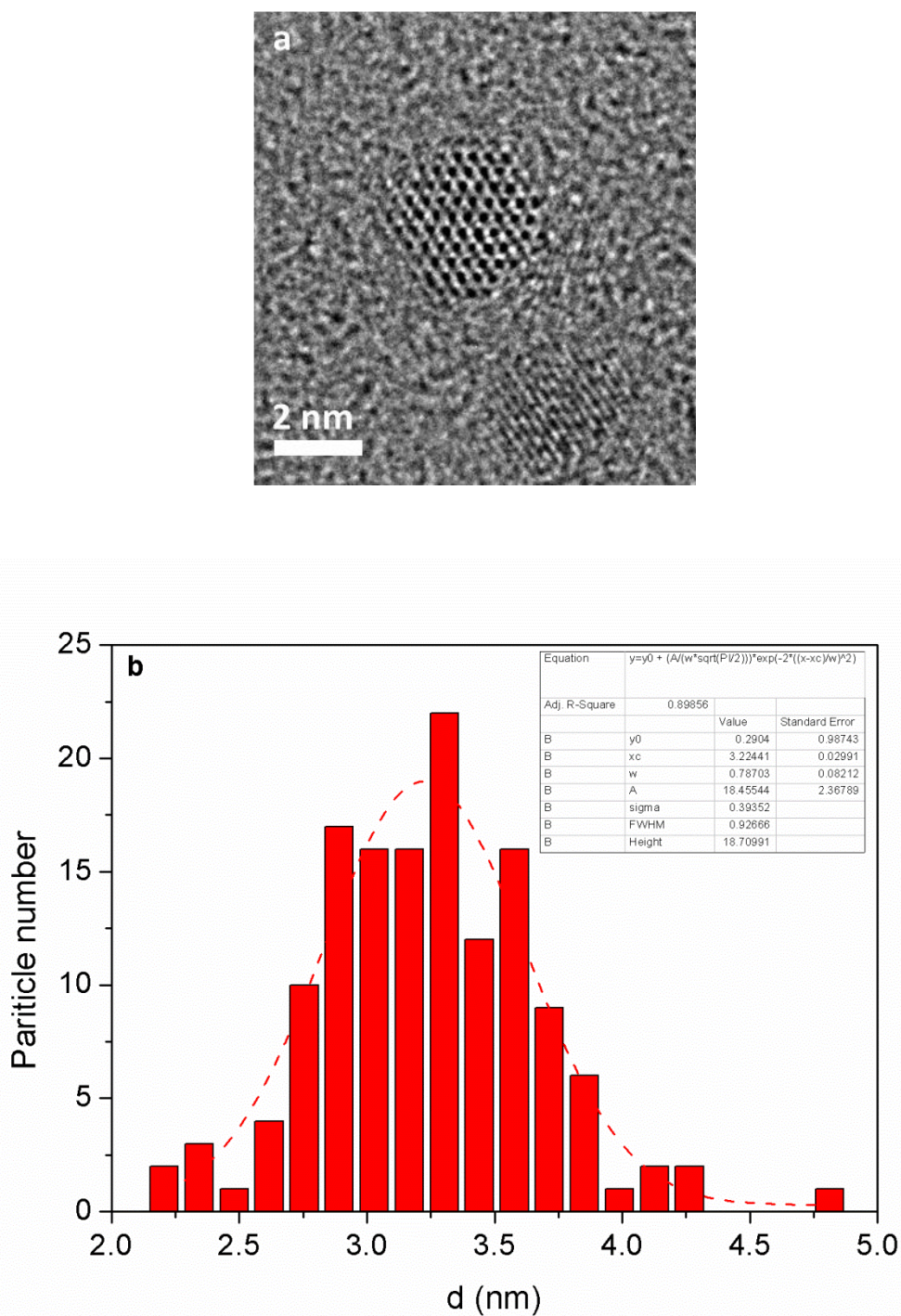


Figure 4.4. (a) HRTEM image of (111) plane of PbS-GSH QD and (b) size distribution of PbS-GSH QDs estimated by TEM imaging. The dashed thin line in graph (b) is Gauss fit.

The comparison of PL spectra for PbS-OA QDs in chloroform and PbS-GSH QDs in water (at pH 5) shows (Figure 4.5) that the PL of the QDs decreased only by about 38% after ligand exchange, which is consistent with findings of Deng et al.³⁰ The reduction in PL intensity may be due to the introduction of trap states on the surface of PbS QDs during ligand exchange which results in quenching of the photogenerated excitons.²⁶ A small feature in the PL spectra of the PbS-OA QDs in chloroform at 1155 nm possibly originates from the solvent. It is noteworthy to mention that the width of the PL spectrum for PbS-GSH QDs is smaller compared to PbS-OA QDs which indicates narrower size distribution in former.

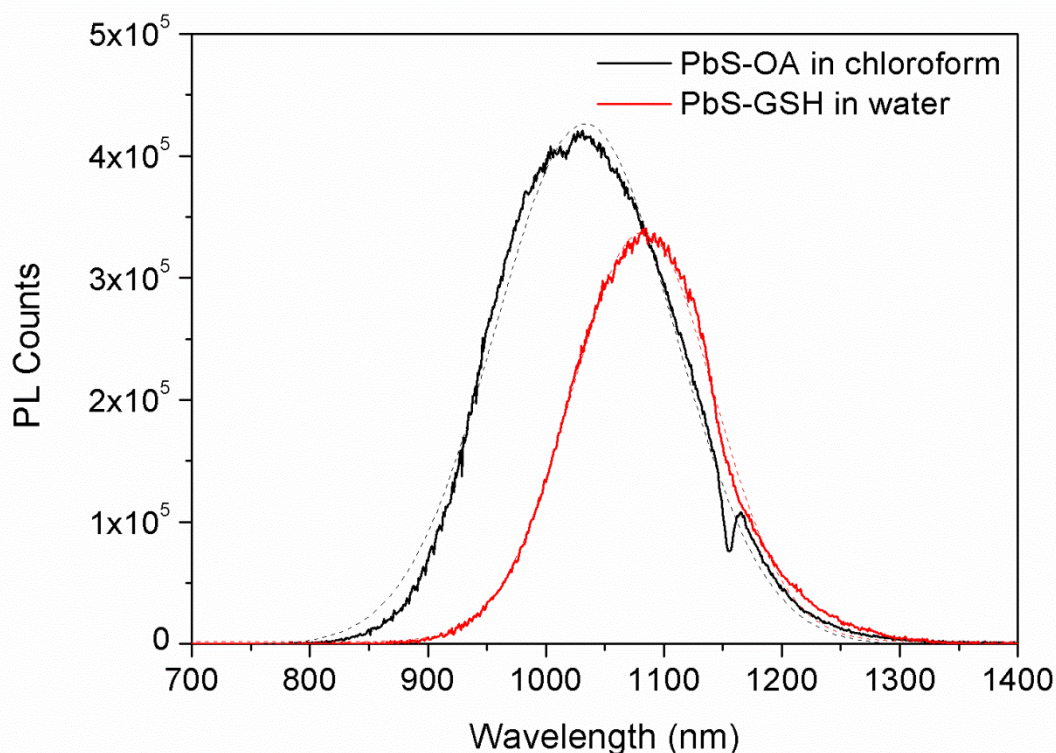


Figure 4.5. PL spectra of the PbS-OA QDs in chloroform and the PbS-GSH QDs in water. The dashed thin lines are Gaussian fits.

The stability of the PbS-GSH QDs in solutions with different pH values was also monitored. PbS-GSH QDs in water with pH values between 5 and 7 showed excellent stability in ambient

conditions for storage times of up to one year. The GSH molecules are bound to the QD via strong sulphur-metal bonds, and the two branches of negatively charged -COO^- groups stretch out from the surface of PbS QD, thus ensuring good protection and dispersion of the QDs as shown schematically in Figure 4.6.^{30, 32} The excess of free GSH molecules (about 1000 free GSH molecules per single QD) in the PbS-GSH QD solution may also contribute to the stabilization of the QDs. However, QD solutions with pH values below 5 and above 7 showed lower stability and start forming agglomerates after storing them for several weeks to several months. The agglomeration in these pH regions most probably originates from changes in surface charge of the PbS-GSH QDs. At low pH values (below 5) surface charge loss may result from protonation of carboxyl and amine groups of the GSH ligand, possibly leading to a collapse of the ligand onto the PbS QD surface. At high pH values (above 7), on the other hand, surface charge loss may result from bond formation between deprotonated carboxyl groups with the surface atoms of PbS QD.

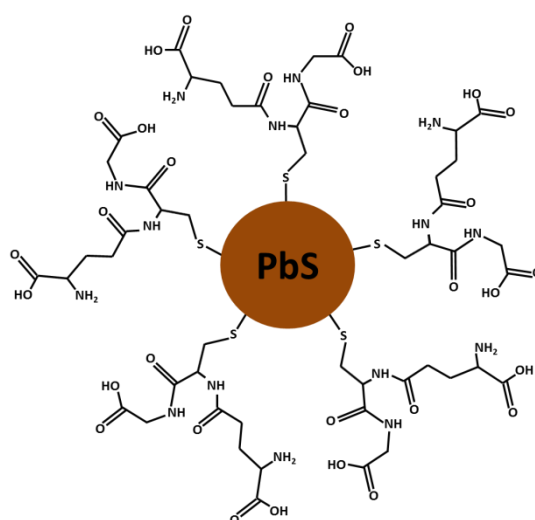


Figure 4.6. Schematic representation of a PbS QD capped with L-glutathione ligands.

PL quenching experiments with P25 suspensions were performed in order to examine the exciton quenching process when PbS-GSH QDs were brought into contact with TiO_2 nanoparticles (NPs). For this purpose, we chose a PbS-GSH QD solution (0.11 mM) with pH

value of 5. The surface of the TiO₂ P25 NPs at pH 5 is positively charged which was confirmed with zeta potential measurements (cf. Figure A-8.1 in Appendix).^{33, 34} Therefore, using the PbS-GSH QD solution with pH 5 creates an additional electrostatic attractive force between surfaces of positively charged TiO₂ P25 NPs and negatively charged PbS-GSH QDs.³⁰ This helps to drive the reaction in the desired direction, shortening the time required for sensitization. Recently, Sakai et al.³⁵ showed that the adsorption of gold clusters protected with GSH on the surface of porous TiO₂ is dependent on the pH value of the solution. It was suggested that the deprotonated and thus negatively charged carboxyl groups of the GSH facilitate the adsorption on the positively charged TiO₂ surface since the pK_a values of the carboxyl groups of GSH are 2.05 and 3.40 respectively and the isoelectric point of the TiO₂ (anatase) surface is 6.89.^{34, 35}

The comparison of PL spectra of PbS-GSH and PbS-GSH-TiO₂ colloidal solutions (containing the same concentration of PbS-GSH QDs) shows that for the latter the PL signal is decreased by 77% (Figure 4.7a). The quenching indicates that another non-radiative decay channel for the initial excitations in PbS-GSH QDs opens up in the presence of TiO₂ NPs. It is proposed that specific binding occurs between PbS-GSH QDs and TiO₂ NPs (Figure 4.7b). This allows for charge transfer at the interface between PbS-GSH QDs and TiO₂ NPs upon excitation of electrons into the LUMO of PbS QDs. It also suggests that the GSH ligands act not only as good stabilizers but that they also allow injection of excited electrons into the TiO₂ conduction band. The incomplete quenching of the generated excitons can be explained by the presence of excess free PbS-GSH QDs. Considering that the diameter of the PbS-GSH QDs is 3.1 nm and the average diameter of the P25 TiO₂ NPs is around 20 nm, for the given concentrations there are around 50 PbS-GSH QDs per 1 TiO₂ NP in the PbS-GSH-TiO₂ solution. It is worth mentioning that the PL quenching experiments were done in the linear regime of absorbance; adding more TiO₂ particles into the PbS-GSH water solution

introduces scattering and therefore complicates the evaluation.

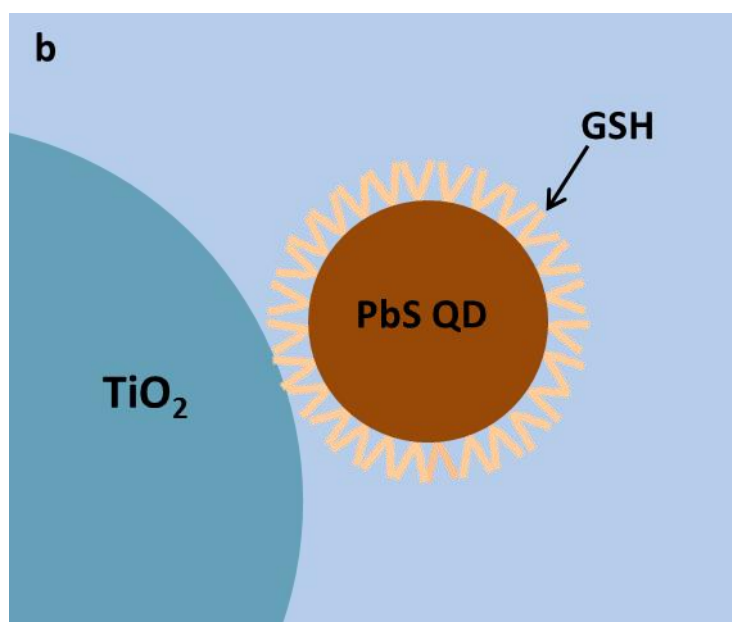
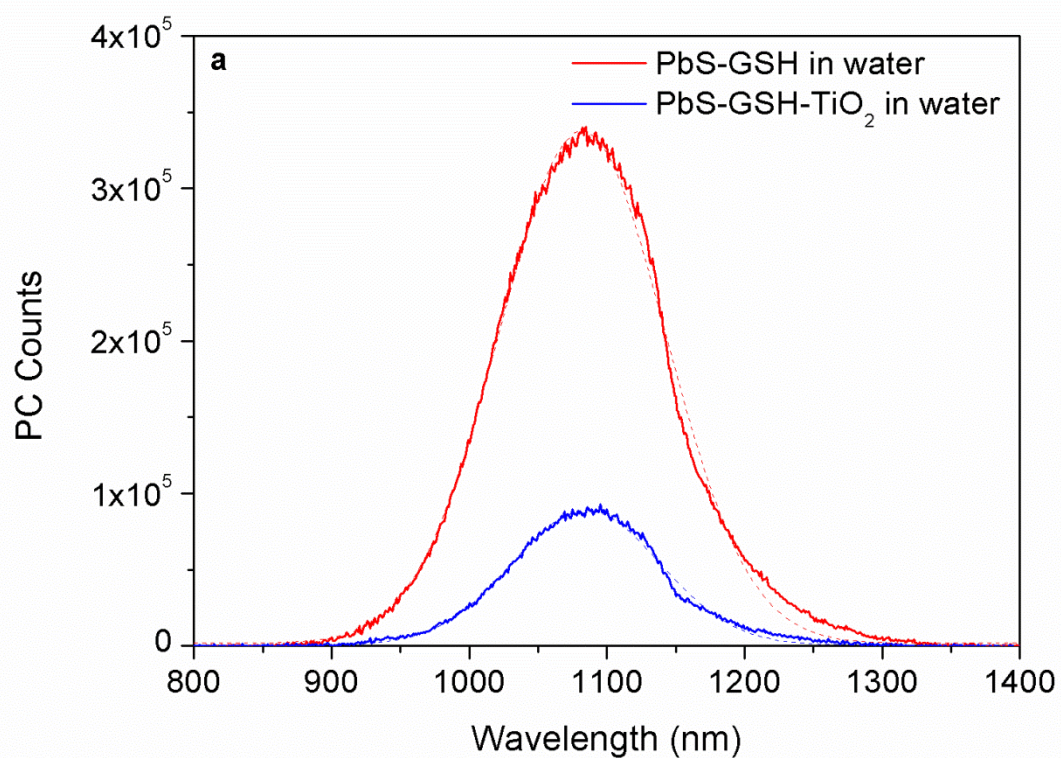


Figure 4.7. (a) PL spectra of the PbS-GSH QDs in water and the PbS-GSH-TiO₂ complex in water and (b) schematic representation of the PbS-GSH-TiO₂ complex. The dashed thin lines in graph (a) are Gaussian fits.

The solutions of PbS-GSH QDs in water were used for sensitization of QDSCs. For this purpose, scaffolding macroporous TiO₂ electrodes on fluorine-doped tin oxide (FTO) glass substrates were prepared using hard template approach in which ~100 nm sized Poly(methyl methacrylate) (PMMA) spheres were used as templating agent.³⁶ The wide-angle XRD analysis of the macroporous TiO₂ electrodes deposited onto FTO substrates (cf. Figure A-1.2 in Appendix) shows that the films correspond to the anatase phase of TiO₂, and nitrogen sorption studies yielded 58 m² g⁻¹ for the Brunauer-Emmett-Teller (BET) surface area of the macroporous TiO₂ electrodes (cf. Figure A-2.2 in Appendix). The scanning electron microscopy (SEM) top view image of the TiO₂ electrodes shows well-connected pores sized about 80-90 nm Figure 4.8.

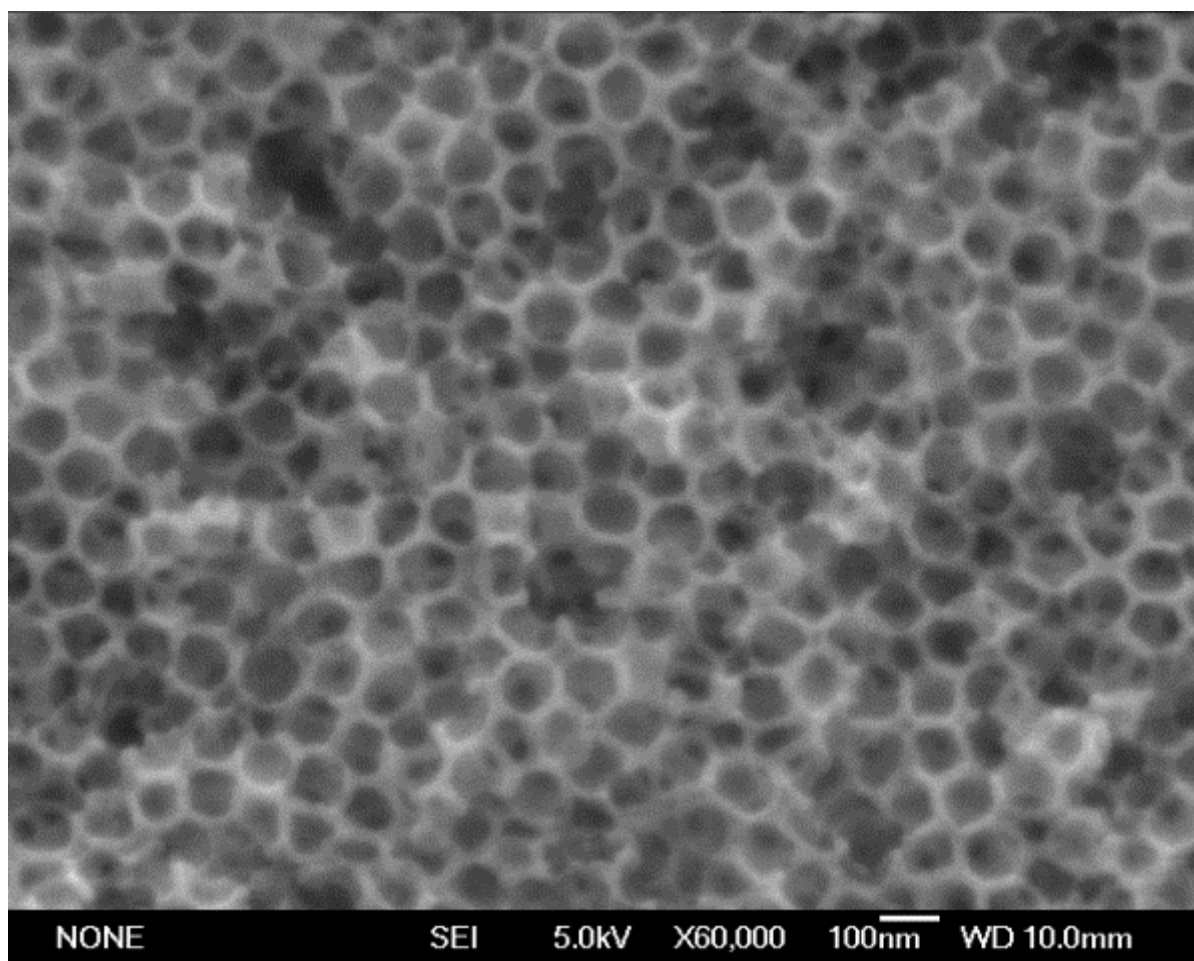


Figure 4.8. SEM top view image of macroporous TiO₂ film on FTO.

For PbS QD sensitization, the as-prepared macroporous TiO₂ electrodes with different thicknesses were soaked in the PbS-GSH QD solution overnight. After sensitization, brown-coloured TiO₂ electrodes were obtained (Figure 4.9). Electrodes with thicker macroporous TiO₂ layers resulted in deeper colouration due to higher loading of PbS-GSH QDs.

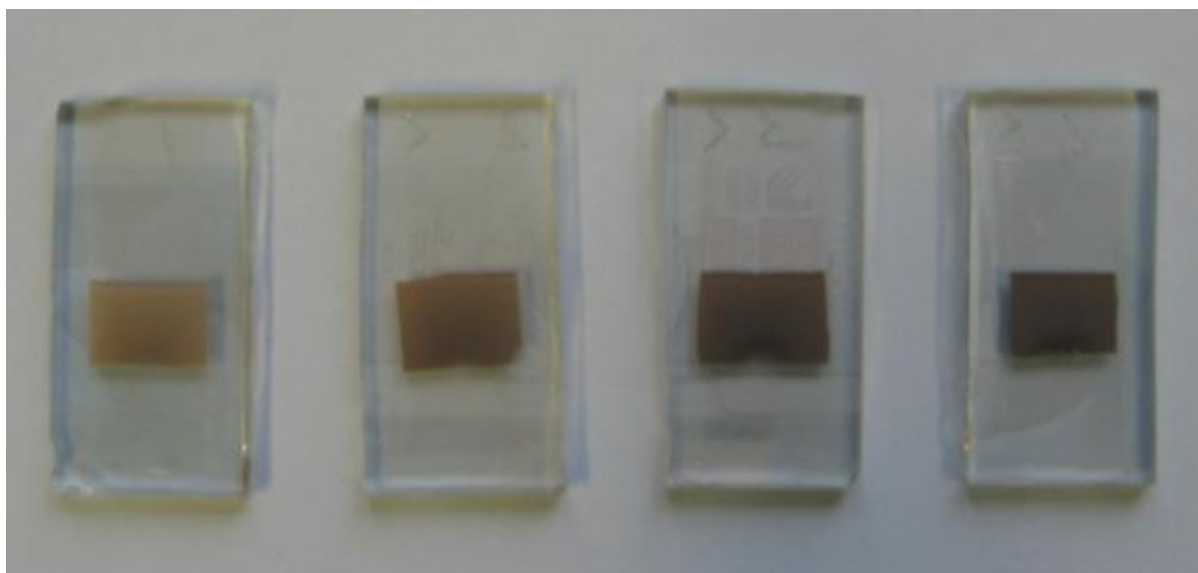


Figure 4.9. Photographic images of PbS-GSH QDs-sensitized macroporous TiO₂ electrodes with four different thicknesses. From the left to the right ($3.5\pm 0.5\ \mu\text{m}$), ($7.5\pm 0.5\ \mu\text{m}$), ($14\pm 1\ \mu\text{m}$) and ($19\pm 1\ \mu\text{m}$).

Sensitized macroporous TiO₂ electrodes with different thicknesses and covered with additional protecting ZnS layer were used as photoanodes for polysulfide electrolyte-based QDSCs (see Experimental Section). I-V characteristics of the cells measured under standard global AM 1.5 G irradiation (Figure 4.10) show that with increasing the thickness of the TiO₂ electrode the photocurrent also increases, reaching its maximum value at a thickness of about $14\pm 1\ \mu\text{m}$. A summary of the performance data for the cells is presented in Table 4.1. The increase of short circuit current with increase of the electrode thickness up to $14\pm 1\ \mu\text{m}$ is possibly originated due to enhanced light harvesting for thicker PbS QD-sensitized electrodes. However, further increase in electrode thickness ($19\pm 1\ \mu\text{m}$), thus, light harvesting is not followed by additional increase in short circuit current. This, possibly, originates from

increased recombination, thus, decreased charge collection for thicker electrodes.³⁷

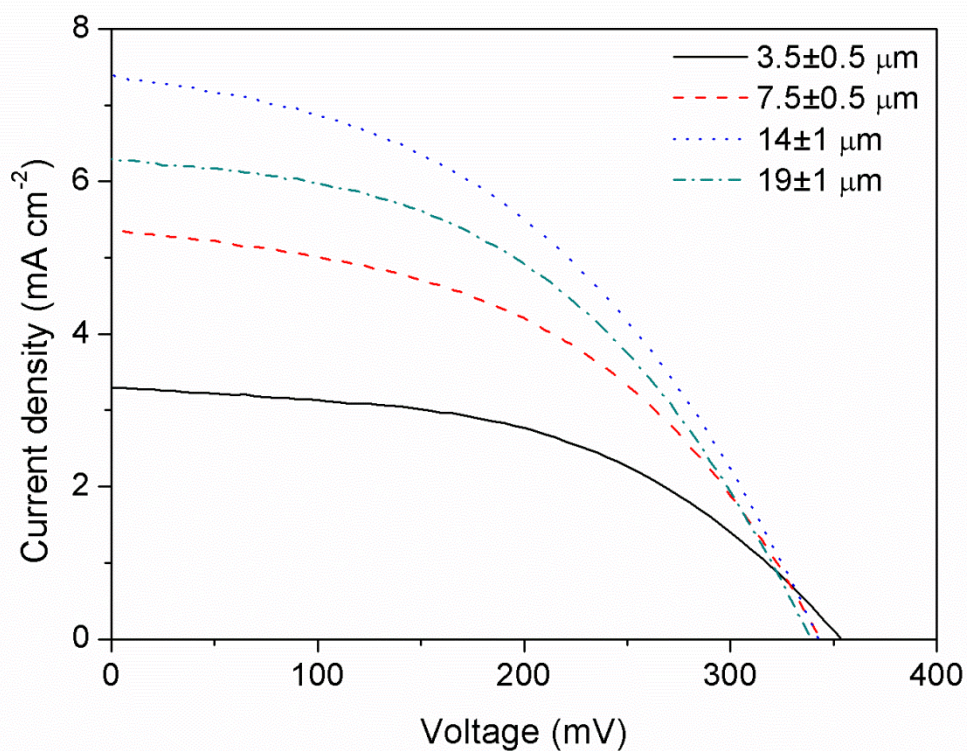


Figure 4.10. I-V characteristics of polysulfide electrolyte-based QDSCs with different thickness of macroporous TiO₂ electrodes tested under standard global AM 1.5 G irradiation.

Table 4.1. Solar cell parameters of QDSCs with different thickness of TiO₂ electrodes tested under standard global AM 1.5 G irradiation.

d_f (μm)	J_{SC} (mA cm^{-2})	V_{OC} (mV)	FF (%)	η (%)
3.5±0.5	3.3	354	49	0.58
7.5±0.5	5.4	343	47	0.86
14±1	7.4	343	44	1.11
19±1	6.3	339	47	1.00

The AM 1.5 G short circuit current (7.4 mA cm^{-2}) obtained for the device with $14 \pm 1 \text{ }\mu\text{m}$ thick macroporous TiO_2 electrode is one of the highest reported for polysulfide electrolyte-based QDSCs made using pre-synthesised PbS QDs with a first excitonic peak at 968 nm. Benekohal et al.¹⁸ reported a short circuit current of $7.3 \pm 0.7 \text{ mA cm}^{-2}$ for a similar system, using pre-synthesised PbS QDs with a first excitonic peak at 743 nm and a high surface area $15 \pm 1 \text{ }\mu\text{m}$ thick mesoporous TiO_2 electrode. In spite of the lower available internal surface area of the macroporous TiO_2 electrode and the larger PbS QD size, our cells were still able to produce similar currents densities. However, our cells showed rather low fill factors.

Solar cell parameters of the cell with $14 \pm 1 \text{ }\mu\text{m}$ electrode thickness were also measured at different AM 1.5 G illumination intensities using neutral density (ND) filters (Figure 4.11a). A plot of the short circuit current against illumination intensity shows a linear dependence, which suggests that there are no diffusion limitations within the illumination range used in our experiments (Figure 4.11b). The relationship between open circuit voltage and light intensity can be written as follows (4.1):³⁸

$$V_{OC} = \frac{mk_B T}{e} \ln(I_0), \quad (4.1)$$

where k_B is Boltzmann's constant, T is the temperature and e is the elementary charge, I_0 is light intensity and parameter m is an empirical non-ideality factor. The value for m obtained from Figure 4.11c yielded value of 1.56. This suggests that the device departs from ideal diode behaviour ($m = 1$). This could be due to some shunting in the cell. A summary of the performance data for the cell at different illumination intensities is presented in Table 4.2.

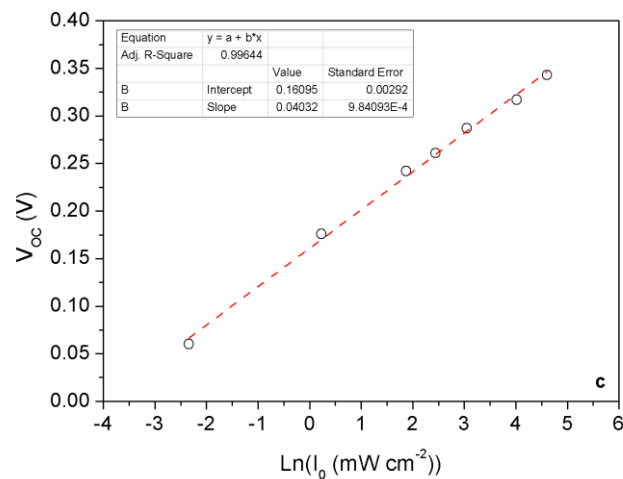
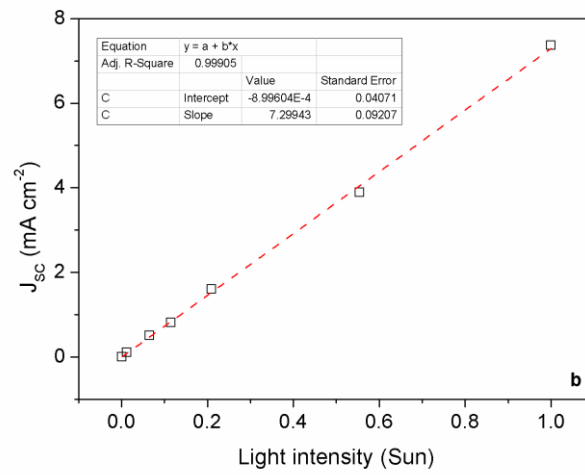
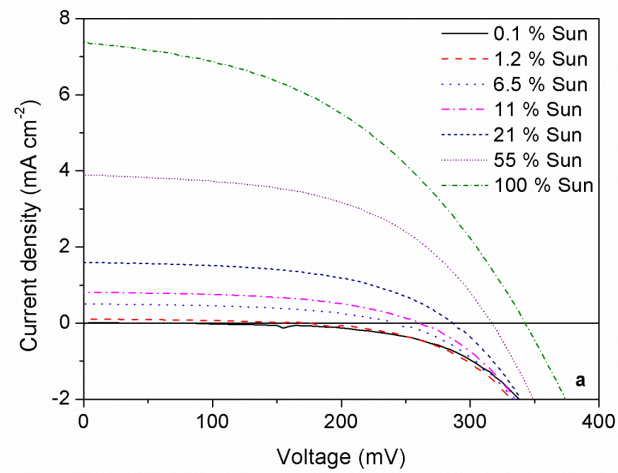


Figure 4.11. (a) I-V characteristics of QDSC with 14 ± 1 μm thick TiO_2 electrode tested under standard global AM 1.5 G irradiation measured with different ND filters, dependence of (b) short circuit current and (c) open circuit potential on illumination intensity. Red lines in (b) and (c) are linear fits to the J_{SC} vs. light intensity and V_{OC} vs. light intensity correspondingly.

Table 4.2. Solar cell parameters of QDSC with 14±1 μm thick TiO₂ electrode at different AM 1.5 G irradiation intensities.

<i>I</i> (% Sun)	<i>J</i> _{SC} (mA cm ⁻²)	<i>V</i> _{OC} (mV)	<i>FF</i> (%)	<i>η</i> (%)
0.1	0.002	60.2	--	--
1.2	0.11	176	36.8	0.55
6.5	0.51	242	49.3	0.92
11	0.81	261	50.7	0.94
21	1.6	287	52.1	1.13
54	3.9	317	52.4	1.17
100	7.4	343	44	1.11

QDSC with 14±1 μm thick electrode was further studied with EIS in order to characterise the physical parameters of the cell. For this, impedance spectra of the cell were recorded at different intensities of AM 1.5 G irradiation at open-circuit (Figures 4.12a – 4.12c). Different open-circuit voltages were obtained by changing the intensity of the AM 1.5 G irradiation using ND filters.

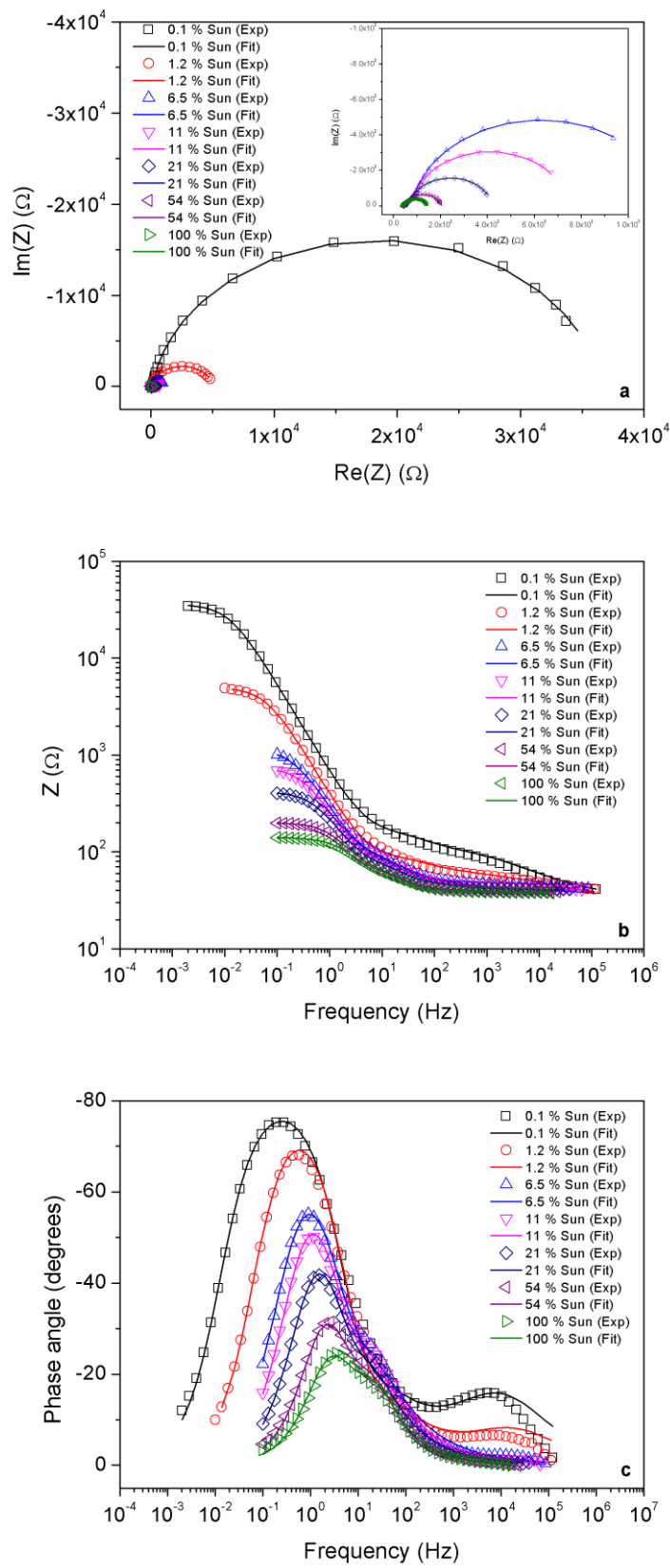


Figure 4.12. (a) Nyquist, (b) Bode and (c) phase angle plots of impedance spectra of the QDSC with 14 ± 1 μm thick TiO_2 electrode under different open circuit conditions.

The impedance data were analysed using ZView software with a model (Figure 4.13) proposed by Bisquert et al.^{39, 40} In the model, a transmission line (TL) represents the photoanode whereas $R_{cathode}$ and $CPE_{cathode}$ and R_s represent counter electrode and series resistance respectively. The parameters for each component of the model were obtained by fitting the experimental data and presented in Table A-3.2 in Appendix.

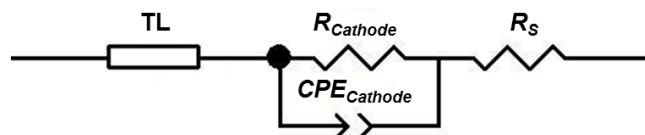


Figure 4.13. Equivalent circuit used to fit experimental impedance spectra.

The light intensity dependence of the values for recombination resistance, R_{ct} , transport resistance, R_{trans} , and chemical capacitance, C_{μ} , extracted from fitting the experimental data, are shown in Figures 4.14a and 4.14b. The values obtained for R_{ct} correspond well with findings of Benekohal et al.¹⁸ for similar system, however, our values for C_{μ} are slightly larger. Using these values, the electron lifetime, diffusion length and diffusion coefficient were calculated based on the model proposed by Bisquert et al.⁴⁰⁻⁴² The diffusion length, L_n , of electrons in TiO_2 was calculated from the values for R_{ct} and R_{trans} using the relationship $L_n = d_f \times (R_{ct} \times R_{trans}^{-1})^{1/2}$, where d_f is the thickness of the photoanode film.⁴² The electron lifetime, τ_n , was calculated from the relationship $\tau_n = R_{ct} \times C_{\mu}$, whereas the diffusion coefficient, D_n , was obtained from L_n and τ_n by using the expression $D_n = L_n^2 \times \tau_n^{-1}$.⁴⁰⁻⁴² The light intensity dependence of the calculated values of L_n , τ_n and D_n is presented in Figures 4.14c and 4.14d.

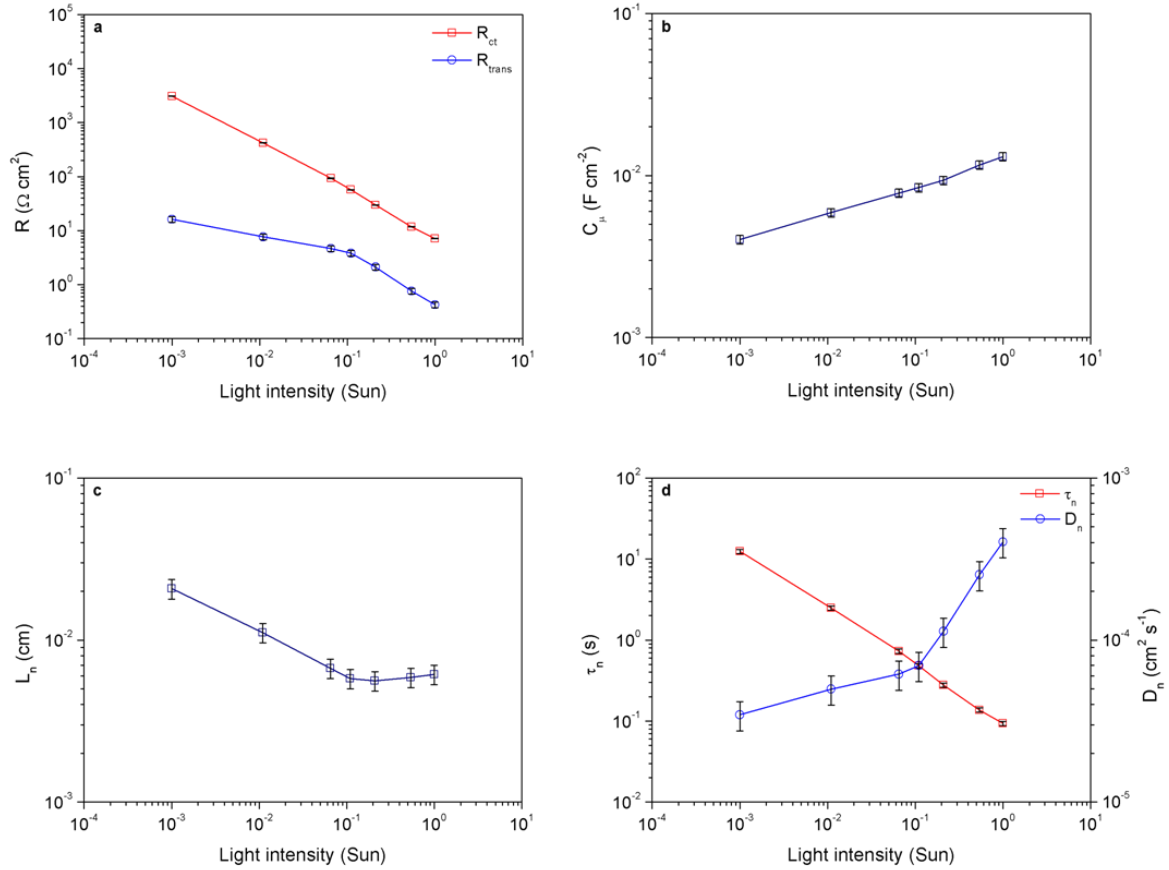


Figure 4.14. Results for impedance measurements. Dependence of (a) recombination resistance and transport resistance, (b) chemical capacitance, (c) electron diffusion length in TiO_2 and (d) electron lifetime and diffusion coefficient on applied light intensity.

The light intensity dependence shows that the electron diffusion length decreases slightly to $\sim 50 \mu\text{m}$ at 1 Sun from its initial value of $\sim 200 \mu\text{m}$ at low light intensities (Figure 4.14c). Nevertheless, the electron diffusion length is several times greater than the thickness of the TiO_2 electrode throughout the entire illumination range used in the experiments, which suggests that electron collection is efficient.³⁹ The values calculated for τ_n and D_n show that the electron lifetime decays with increasing light intensity, whereas the diffusion coefficient increases (Figure 4.14d). The obtained values for τ_n and D_n are in good agreement with findings of other groups for similar systems.^{18, 39, 43, 44} The values obtained for L_n , τ_n and D_n for our system were compared with the findings of Braga et al.⁴⁴ for a similar system in which

PbS QDs were deposited using the SILAR technique. From the comparison it is evident that the use of pre-synthesised PbS QDs with well protected surfaces substantially increases the electron diffusion length. This increase is due to an increase in the electron lifetime by almost two orders of magnitude, while the electron diffusion coefficient remains the same.⁴⁴ Fitting the experimental EIS data shows that R_S are rather insensitive to illumination intensities, whereas the faradaic resistance of the Cu_xS_y cathode becomes smaller as the illumination intensity increases (cf. Table A-3.2 in Appendix).

The loading of PbS-GSH QDs adsorbed onto the walls of the 14 ± 1 μm thick macroporous TiO_2 electrode was estimated by dissolving the QDs in acid and determining the lead concentration using inductively-coupled plasma atomic absorption spectroscopy (ICP/AAS) measurements. The ICP/AAS measurements gave the total mass of QDs adsorbed onto the walls of a 14 ± 1 μm thick macroporous TiO_2 electrode with 0.5 cm^2 effective area (cf. Table A-9.1 in Appendix).

The total mass was then used to calculate the optical path length of the PbS in the device. The absorbance of PbS-GSH QDs adsorbed onto the walls of a 14 ± 1 μm thick macroporous TiO_2 electrode was then calculated using the Lambert-Beer law and values for the absorption coefficient, $\alpha(\lambda)$, (see above). The total masses of PbS QDs for all three substrates examined were similar and therefore the reconstruction resulted in more or less the same absorbance curves for all three electrodes (Figure 4.15).

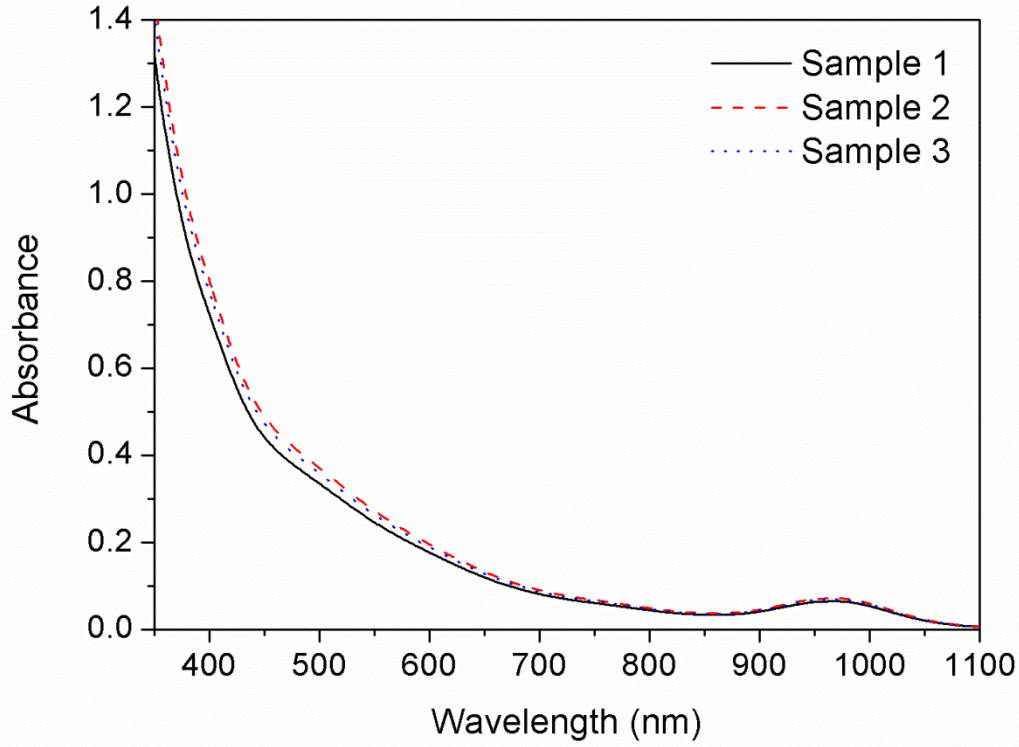


Figure 4.15. Calculated absorbance of PbS-GSH QDs from the PbS loading of three different macroporous TiO₂ electrodes.

The absorbance spectrum of PbS-GSH QDs was used to calculate the theoretical short circuit current for the device using the relationship (4.2):²

$$J_{SC} = \int e \cdot F(\lambda) \cdot \eta_{LHE} \cdot \eta_{inj} \cdot \eta_c d\lambda, \quad (4.2)$$

where e is the electron charge, $F(\lambda)$ is incident photon flux density,⁴⁵ η_{LHE} the light harvesting efficiency, η_{inj} is the electron injection efficiency and η_c is the electron collection efficiency. Integration was performed over the wavelength range from 350 up to 1100 nm. η_{LHE} is calculated using the following relationship (4.3):²

$$\eta_{LHE} = 1 - 10^{-A(\lambda)}, \quad (4.3)$$

where $A(\lambda)$ is the absorbance of PbS-GSH QDs. The theoretical short circuit current calculated from equation (4.2) assuming that η_{inj} and η_c are unity, yielded a value of 11.5 mA cm⁻². Since the experimental short circuit current is 7.4 mA cm⁻² and the EIS measurements showed that η_c is close to unity, we conclude that the injection efficiency $\eta_{inj} = 0.64$. Possible reasons for non-unity injection efficiency could be agglomeration of PbS QDs and also slow transfer of holes into the electrolyte.⁴⁶ Nevertheless, the relatively high injection efficiency suggests that highly efficient QD solar cell devices could be fabricated using our approach if a replacement can be found for the polysulfide electrolyte, which is responsible for the low open circuit voltage and the poor fill factor.

4.3 Conclusions

QDSCs cells have been fabricated successfully using water-soluble pre-synthesized PbS QDs. Water-solubilisation of OA-capped PbS QDs was achieved by using the GSH ligand. Successful sensitization of TiO₂ P25 NPs and porous TiO₂ electrodes with PbS QDs was achieved by exploiting the additional electrostatic attraction that was created by carefully adjusting the pH of the QD solution in order to induce opposing surface charging of the TiO₂ (positively charged) and PbS-SGH QDs (negatively charged). The ability of the GSH capping molecule to bind to TiO₂ and transfer charge carriers (electrons) into the conduction band of TiO₂ upon formation of excitons in PbS QDs was demonstrated by PL quenching experiments. Macroporous TiO₂ electrodes sensitized with GSH-protected PbS QDs were used in the fabrication of QDSCs with a polysulfide electrolyte and Cu_xS_y cathode. AM 1.5 G solar cell performances of 1.1% conversion efficiency and short circuit current up to 7.4 mA cm⁻² were obtained for the cell with a 14±1 μm thick photoanode. Impedance measurements of the cell were performed and physical parameters of the cell such as electron

diffusion length, electron lifetimes and diffusion coefficients were extracted from modelling and further analysis. The electron collection and injection efficiencies were found to be ~1 and 0.64, respectively.

4.4 Experimental Section

4.4.1 Materials

Oleic acid (Sigma-Aldrich), lead(II) oxide (Sigma-Aldrich), hexamethyldisilathiane (Sigma-Aldrich), 1-octadecene (Sigma-Aldrich), chloroform (Merck), toluene (Sigma-Aldrich), ethanol (Sigma-Aldrich), L-glutathione (Sigma-Aldrich), sodium hydroxide (Sigma-Aldrich), titanium(IV) ethoxide (Alfa Aesar), titanium(IV) chloride (Sigma-Aldrich), hydrochloric acid 37% (Sigma-Aldrich), nitric acid (Sigma-Aldrich), ~100 nm PMMA spheres (home-made), sulfur (Sigma-aldrich), sodium sulfide hydrate (Fluka), zinc acetate dihydrate (Alfa Aesa), P25 TiO₂ NPs (Degussa).

4.4.2 Preparation of Water-Soluble PbS QDs

PbS QDs capped with OA were synthesised as described by Tang et al.¹³(cf. subsection A-5 in Appendix). The water solubilisation of PbS-OA QDs was achieved by the ligand exchange procedure as described by Deng et al.³⁰(cf. subsection A-6 in Appendix).

4.4.3 Zeta Potential Measurements

For the determination of the zeta potential curve of P25 TiO₂ NPs, two drops of a dispersion of P25 TiO₂ NPs in Milli-Q water (50 mg mL⁻¹) were mixed with 1 mL commercial Hydrion buffer solution of the appropriate pH prior to measurement. The zeta potential of P25 TiO₂ NPs was determined for pH values of the buffer solution in the range of pH 2 to pH 9 (see Characterization Methods).

4.4.4 Photoluminescence Experiments

PL spectra of PbS-OA QDs in chloroform and PbS-GSH QDs in water solutions of the same concentrations (0.11 mM) were recorded in the range of 600 to 1600 nm. The excitation wavelength for the PL experiments was 400 nm (see Characterization Methods). For PL quenching experiments, the spectra of 0.11 mM PbS-GSH-water solution with pH = 5 was measured before and after adding 0.3 mL of aqueous TiO₂ P25 nanoparticle solution. The aqueous TiO₂ P25 nanoparticle solution was prepared by mixing 10 mg of TiO₂ P25 nanoparticle powder with 10 mL of water.

4.4.5 TiO₂ Photoanode Preparation

Macroporous TiO₂ electrodes were prepared on FTO (Pilkington, TEC15) glass substrates (1.5×3 cm²) according to the method described by Mandlmeier et al.³⁶ PMMA spheres sized 100 nm were used as templating agent, and the thickness of the electrodes was varied from 3.5±0.5 μm up to 19±1 μm. The sol-gel solution was prepared by mixing 0.62 g Titanium(IV) ethoxide (TEOT) and hydrochloric acid (HCl) mixture with a solution of 300 mg of PMMA

spheres redispersed in 3 mL ethanol. The TEO/HCl mixture was prepared by mixing 0.5 mL TEOT with 0.4 mL HCl (37%). Macroporous TiO₂ electrodes were prepared by spin-coating the sol-gel solution onto FTO substrates precoated with a dense ~60 nm TiO₂ layer (cf. subsection A-4 in Appendix).^{47, 48} In order to achieve thicker films additional layers of the sol-gel solution were spin-coated with intermediate calcination of the substrates at 100 °C for 30 min in air after each layer deposition. Finally, the substrates were calcined at 450 °C for 30 min in air to remove the templating PMMA spheres and obtain crystalline macroporous TiO₂ electrodes. The electrodes were also subjected to an additional 20 mM TiCl₄ treatment at 70 °C for 30 min with subsequent calcination at 500 °C for 30 min in air.

4.4.6 Fabrication of Solar Cells

The porous TiO₂ electrodes (0.5×0.5 cm²) were immersed at room temperature in the dark for 18 h in 10 mL of an aqueous 3 mM PbS-GSH QD solution (pH 5) (closed vial). The electrodes were then removed from the QD solution and immersed into 10 mL pure Milli-Q water for 10 min to wash away unattached PbS-GSH QDs. Thicker electrodes were employed to achieve improved light harvesting of TiO₂/PbS composite films. The QD-sensitized electrodes were coated with a ZnS protecting layer by the SILAR method by alternatively immersing the electrodes into 0.1 M Zn(CH₃OOH)₂ and 0.1 M Na₂S water solution for 1 min each at room temperature and subsequently washing with pure water.^{18, 49} Nine complete SILAR cycles were performed in order to grow a ZnS protective layer onto TiO₂/PbS QD walls.⁵⁰ This number of cycles was chosen to give the best performance (cf. Figure A-10.1 in Appendix). The cells were characterized in two-electrode mode in which the ZnS-coated QD-sensitized TiO₂ electrode and a counter electrode were immersed into an optical glass cuvette

filled with aqueous polysulfide electrolyte. The distance between the electrodes was about 0.5 cm.

A Cu_xS_y electrode prepared as described by Benekohal et al.¹⁸ was used as counter electrode. For that purpose a $2.5 \times 1.5 \text{ cm}^2$ brass plate was immersed into concentrated HCl solution at 70°C for 5 min and then rinsed with water. After drying the brass plate with stream of nitrogen it was immersed into polysulfide electrolyte solution. The polysulfide electrolyte (also used as hole mediator) consisted of an aqueous solution of 1 M sulfur, 1 M sodium sulfide and 0.1 M sodium hydroxide.³⁹ The plate turned black within a few seconds forming a Cu_xS_y electrode.

4.4.7 Determination of the Amount of Adsorbed PbS QDs

Three macroporous TiO_2 electrodes deposited onto FTO substrate with $14 \pm 1 \mu\text{m}$ thickness and 0.5 cm^2 active areas were immersed into an aqueous 3 mM PbS-GSH QD solution at pH 5 overnight (18 h), at room temperature in the dark. The next day, the brown-coloured electrodes were removed from the QD solution, immersed into pure Milli-Q water for 10 min to wash away unattached PbS-GSH QDs and then dried with a stream of air. The dried electrodes were immersed into 2.5 mL concentrated nitric acid (2 M) in clean vials to dissolve the PbS-GSH QDs. The clean white-coloured TiO_2 electrodes were removed from the solution vials, and the solutions were analysed with ICP/AAS to determine the amount of Pb present.

4.4.8 Characterization Methods

The structure and phase of the macroporous TiO_2 films were characterized by wide-angle

XRD using a Bruker D8 Discover diffractometer with Cu-K α radiation ($\lambda = 1.5418 \text{ \AA}$) and equipped with a LynxEye position sensitive detector. Average film thickness values were measured with a profilometer (Dektak150). Nitrogen sorption measurements on powder samples prepared by scratching off the templated TiO $_2$ films were done using a NOVA 4000e surface area and pore size analyser (Quantachrome). NovaWin software (version 10, Quantachrome) was used to evaluate the data. The morphology of the samples was examined using a JEOL-JSM-6500F SEM equipped with a 4 kV field emission gun. Zeta potential measurements of P25 TiO $_2$ water dispersion were performed using a Malvern Zetasizer-Nano instrument equipped with a 4 mW He-Ne laser (633 nm) and an avalanche photodiode.

Absorbance spectra of the PbS QDs were recorded using an UV-Vis-NIR spectrophotometer (model: Lambda 1050, PerkinElmer). The structure of the PbS QDs was characterized by wide-angle XRD using a Bruker D8 Discover diffractometer. HRTEM imaging of the PbS-GSH QDs were performed using a FEI TITAN 80-300 TEM equipped with a field emission gun operating at 300 kV. PL measurements were performed using a Fluorolog 3 (Horiba Jobin Yvon) spectrometer equipped with double monochromator and water-cooled photomultiplier for the visible range (300-1000 nm) and iHR320 turret monochromator for the NIR range (up to 1600 nm) with thermo-electrically cooled detector (H10330-75, Hamamatsu). High-sensitivity measurements were achieved by monitoring fluctuations in the lamp intensity with a reference photodiode. All measurements were corrected for the quantum efficiency of the detectors.

The I-V characteristics of the QDSCs were measured under simulated solar light using a 300 W xenon lamp and a filter calibrated to approximate AM 1.5 G irradiation at 100 mW cm $^{-2}$ (model: XPS 400, Solar Light Company Inc.). I-V curves were recorded in the two electrode mode with illumination from the TiO $_2$ side with 0.085 cm 2 active area of the cells. Calibration was performed using a silicon diode (model: S1337-BR66, Hamamatsu). The I-V

characteristics were recorded with a potentiostat (Zahner Elektrik XPot) and LabVIEW software. The EIS data were obtained using a potentiostat equipped with a frequency response analyser (model: FRA2 μ AUTOLAB III, Metrohm). The EIS measurements were carried out under AM 1.5 G irradiation at open-circuit conditions over the frequency range from 1 MHz up to 2 mHz with an AC voltage amplitude of 10 mV.

References

1. P. V. Kamat, *The Journal of Physical Chemistry C*, 2008, **112**, 18737-18753.
2. Z. Yang, C.-Y. Chen, P. Roy and H.-T. Chang, *Chemical Communications*, 2011, **47**, 9561-9571.
3. M. A. Hines and G. D. Scholes, *Advanced Materials*, 2003, **15**, 1844-1849.
4. R. Vogel, P. Hoyer and H. Weller, *The Journal of Physical Chemistry*, 1994, **98**, 3183-3188.
5. B.-R. Hyun, Y.-W. Zhong, A. C. Bartnik, L. Sun, H. D. Abruña, F. W. Wise, J. D. Goodreau, J. R. Matthews, T. M. Leslie and N. F. Borrelli, *ACS Nano*, 2008, **2**, 2206-2212.
6. I. Moreels, K. Lambert, D. Smeets, D. De Muynck, T. Nollet, J. C. Martins, F. Vanhaecke, A. Vantomme, C. Delerue, G. Allan and Z. Hens, *ACS Nano*, 2009, **3**, 3023-3030.
7. R. J. Ellingson, M. C. Beard, J. C. Johnson, P. Yu, O. I. Micic, A. J. Nozik, A. Shabaev and A. L. Efros, *Nano Letters*, 2005, **5**, 865-871.

8. Y. Yang, W. Rodríguez-Córdoba and T. Lian, *Nano Letters*, 2012, **12**, 4235-4241.
9. H. Rahnamai, H. J. Gray and J. N. Zemel, *Thin Solid Films*, 1980, **69**, 347-350.
10. A. Zaban, O. I. Mičić, B. A. Gregg and A. J. Nozik, *Langmuir*, 1998, **14**, 3153-3156.
11. I. Robel, V. Subramanian, M. Kuno and P. V. Kamat, *Journal of the American Chemical Society*, 2006, **128**, 2385-2393.
12. D. F. Watson, *The Journal of Physical Chemistry Letters*, 2010, **1**, 2299-2309.
13. J. Tang, K. W. Kemp, S. Hoogland, K. S. Jeong, H. Liu, L. Levina, M. Furukawa, X. Wang, R. Debnath, D. Cha, K. W. Chou, A. Fischer, A. Amassian, J. B. Asbury and E. H. Sargent, *Nature Materials*, 2011, **10**, 765-771.
14. P. Yu, K. Zhu, A. G. Norman, S. Ferrere, A. J. Frank and A. J. Nozik, *The Journal of Physical Chemistry B*, 2006, **110**, 25451-25454.
15. S. Giménez, I. Mora-Seró, L. Macor, N. Guijarro, T. Lana-Villarreal, R. Gómez, L. J. Diguna, Q. Shen, T. Toyoda and J. Bisquert, *Nanotechnology*, 2009, **20**, 295204.
16. N. J. Smith, K. J. Emmett and S. J. Rosenthal, *Applied Physics Letters*, 2008, **93**, 043504-043503.
17. A. Salant, M. Shalom, I. Hod, A. Faust, A. Zaban and U. Banin, *ACS Nano*, 2010, **4**, 5962-5968.
18. N. Parsi Benekohal, V. González-Pedro, P. P. Boix, S. Chavhan, R. Tena-Zaera, G. P. Demopoulos and I. Mora-Seró, *The Journal of Physical Chemistry C*, 2012, **116**, 16391-16397.

19. L. M. Peter, D. J. Riley, E. J. Tull and K. G. U. Wijayantha, *Chemical Communications*, 2002, 1030-1031.
20. C. Ratanatawanate, C. Xiong and K. J. Balkus, *ACS Nano*, 2008, **2**, 1682-1688.
21. K. S. Leschkies, R. Divakar, J. Basu, E. Enache-Pommer, J. E. Boercker, C. B. Carter, U. R. Kortshagen, D. J. Norris and E. S. Aydil, *Nano Letters*, 2007, **7**, 1793-1798.
22. J. B. Sambur, T. Novet and B. A. Parkinson, *Science*, 2010, **330**, 63-66.
23. P. V. Kamat, *Accounts of Chemical Research*, 2012, **45**, 1906-1915.
24. J. Tang, L. Brzozowski, D. A. R. Barkhouse, X. Wang, R. Debnath, R. Wolowiec, E. Palmiano, L. Levina, A. G. Pattantyus-Abraham, D. Jamakosmanovic and E. H. Sargent, *ACS Nano*, 2010, **4**, 869-878.
25. P. T. Erslev, H.-Y. Chen, J. Gao, M. C. Beard, A. J. Frank, J. van de Lagemaat, J. C. Johnson and J. M. Luther, *Physical Review B*, 2012, **86**, 155313.
26. A. H. Ip, S. M. Thon, S. Hoogland, O. Voznyy, D. Zhitomirsky, R. Debnath, L. Levina, L. R. Rollny, G. H. Carey, A. Fischer, K. W. Kemp, I. J. Kramer, Z. Ning, A. J. Labelle, K. W. Chou, A. Amassian and E. H. Sargent, *Nature Nanotechnol.*, 2012, **7**, 577-582.
27. C. B. Murray, D. J. Norris and M. G. Bawendi, *Journal of the American Chemical Society*, 1993, **115**, 8706-8715.
28. U. Holzwarth and N. Gibson, *Nature Nanotechnol.*, 2011, **6**, 534-534.
29. L. Brus, *The Journal of Physical Chemistry*, 1986, **90**, 2555-2560.

30. D. Deng, J. Xia, J. Cao, L. Qu, J. Tian, Z. Qian, Y. Gu and Z. Gu, *Journal of Colloid and Interface Science*, 2012, **367**, 234-240.
31. L. M. Peter, *The Journal of Physical Chemistry Letters*, 2011, **2**, 1861-1867.
32. B. Xue, J. Cao, D. Deng, J. Xia, J. Jin, Z. Qian and Y. Gu, *Journal of Materials Science: Materials in Medicine*, 2012, **23**, 723-732.
33. M. Kosmulski, *Advances in Colloid and Interface Science*, 2002, **99**, 255-264.
34. D. L. Rabenstein, *Journal of the American Chemical Society*, 1973, **95**, 2797-2803.
35. N. Sakai and T. Tatsuma, *Advanced Materials*, 2010, **22**, 3185-3188.
36. B. Mandlmeier, J. M. Szeifert, D. Fattakhova-Rohlfing, H. Amenitsch and T. Bein, *Journal of the American Chemical Society*, 2011, **133**, 17274-17282.
37. J. Tian, R. Gao, Q. Zhang, S. Zhang, Y. Li, J. Lan, X. Qu and G. Cao, *The Journal of Physical Chemistry C*, 2012, **116**, 18655-18662.
38. A. B. Walker, L. M. Peter, K. Lobato and P. J. Cameron, *The Journal of Physical Chemistry B*, 2006, **110**, 25504-25507.
39. V. González-Pedro, X. Xu, I. Mora-Seró and J. Bisquert, *ACS Nano*, 2010, **4**, 5783-5790.
40. F. Fabregat-Santiago, G. Garcia-Belmonte, I. Mora-Seró and J. Bisquert, *Physical Chemistry Chemical Physics*, 2011, **13**, 9083-9118.
41. J. Bisquert, F. Fabregat-Santiago, I. Mora-Seró, G. Garcia-Belmonte and S. Giménez, *The Journal of Physical Chemistry C*, 2009, **113**, 17278-17290.

42. F. Fabregat-Santiago, J. Bisquert, L. Cevey, P. Chen, M. Wang, S. M. Zakeeruddin and M. Grätzel, *Journal of the American Chemical Society*, 2009, **131**, 558-562.
43. I. Mora-Seró, S. Giménez, F. Fabregat-Santiago, R. Gómez, Q. Shen, T. Toyoda and J. Bisquert, *Accounts of Chemical Research*, 2009, **42**, 1848-1857.
44. A. Braga, S. Giménez, I. Concina, A. Vomiero and I. Mora-Seró, *The Journal of Physical Chemistry Letters*, 2011, **2**, 454-460.
45. Reference Solar Spectral Irradiance: ASTM G-173, <http://rredc.nrel.gov/solar/spectra/am1.5/ASTMG173/ASTMG173.html>, 2013.
46. P. V. Kamat, *The Journal of Physical Chemistry Letters*, 2013, **4**, 908-918.
47. L. Kavan and M. Grätzel, *Electrochimica Acta*, 1995, **40**, 643-652.
48. P. J. Cameron and L. M. Peter, *The Journal of Physical Chemistry B*, 2003, **107**, 14394-14400.
49. Q. Shen, J. Kobayashi, L. J. Diguna and T. Toyoda, *Journal of Applied Physics*, 2008, **103**, 084304-084305.
50. S. Hachiya, Q. Shen and T. Toyoda, *Journal of Applied Physics*, 2012, **111**, 104315-104314.

5 Hybrid Solid-State PbS Quantum-Dot-Sensitized Solar Cells with SnO₂ Electrodes

The results described in this chapter were partially obtained with the help of the research trainee (Forschungspraktikant) BSc. Daniel Böhm.

Abstract

Mesoporous SnO₂ electrodes were employed to create solid-state quantum-dot-sensitized solar cells using pre-synthesized PbS quantum dots (QDs) capped with L-glutathione (GSH) ligands and spiro-OMeTAD as solid-state hole transport mediator. The effect of surface passivation of SnO₂ electrodes with MgO and TiO₂ was investigated. Improvements in the open circuit voltage and conversion efficiency by a factor of more than two were obtained after passivation of the SnO₂ electrodes with TiO₂ alone or with TiO₂ and MgO in combination. The electron lifetime and electron transport time of the devices were examined using intensity-modulated photovoltage and photocurrent spectroscopy (IMVS/IMPS) techniques.

5.1 Introduction

After seminal work done by O'Regan and Grätzel¹ with mesoporous TiO₂ as an electrode material, a variety of semiconducting porous metal oxides (MO) such as TiO₂, ZnO and SnO₂

with high internal surface area have been utilized as scaffolding host anode material in dye-sensitized solar cells (DSCs) as well as in quantum-dot-sensitized solar cells (QDSCs).¹⁻⁵ There are several requirements that MO semiconductors need to fulfil in order to use them for DSC and QDSC applications.⁶ First of all, the MO should have a wide band gap that has minimal overlap of light absorbance with the sensitizer. Secondly, the conduction band energy of the MO should be lower than the lowest unoccupied molecular orbital (LUMO) of the sensitizer to allow successful electron transfer from the sensitizer to the MO. Finally, the charge carrier mobility of the MO should be high enough and undesired recombination processes slow enough to allow for the efficient diffusion of injected electrons to the external circuit.

Porous TiO₂ became one of the most commonly used MOs explored in both DSCs and QDSCs. However, the use of SnO₂ as a semiconducting MO scaffold for the working electrode of QDSCs in conjunction with PbS quantum dots (QDs) has several potential advantages over TiO₂. First, the electron mobility in SnO₂ is 100 times higher than in TiO₂, which should have a positive impact on the diffusion of photoinjected electrons in the electrode.^{7, 8} Second, the conduction band edge of SnO₂ is 0.2 – 0.3 eV lower in energy compared to TiO₂.^{7, 8} This should facilitate the injection of excited electrons from relatively narrow band gap PbS QDs into the conduction band of SnO₂ and therefore increase the photocurrent.⁸ However, we note that a decrease of photovoltage might also be expected due to the lowered conduction band edge of SnO₂ compared to TiO₂.^{2, 7}

In recent years, a number of studies have demonstrated the successful application of porous SnO₂ as a scaffolding electrode for DSCs and QDSCs. For instance, Onwona-Agyeman et al.⁹ reported solid-state DSCs with 2.8% conversion efficiency using indoline dyes and CuI hole transporting material (HTM). Later, Snaith et al.^{10, 11} reported fabrication of solid-state DSCs and QDSCs with 2.8% and 0.56% efficiencies, respectively, with Spiro-OMeTAD HTM

using mesoporous SnO₂ electrodes passivated with thin TiO₂ and MgO layers. In these studies, the authors showed that passivation of SnO₂ electrodes with TiO₂ and MgO enhances the effective electron lifetime, diffusion coefficient and electron diffusion length and, thus, higher efficiency cells can be obtained.^{10, 11} Similar results have also been reported by Huang et al.¹² for the case of liquid electrolyte based QDSCs. The common feature in these studies is the passivation of the SnO₂ electrode surface with another MO or a combination of MOs. These treatments of the electrode material were employed to increase the open circuit voltage and photocurrent by reducing charge recombination via the MO/QD, MO/dye and/or the MO/redox couple interfaces.¹⁰⁻¹³ Therefore, the SnO₂/PbS-QD can be a suitable model system to study charge injection and separation as well as the impact of acceptor/donor interface design on recombination processes.¹²

Here we report on the use of porous nanocrystalline SnO₂ thin films for applications in solid-state PbS QDSCs with spiro-OMeTAD organic HTM.¹¹ The SnO₂/PbS-QDs/HTM system is of interest because so far only few studies have examined the mechanisms of charge injection, regeneration and recombination at the PbS QD, MO and HTM interfaces.^{11, 12} Additionally the surface treatment of SnO₂ electrodes with thin layers of MgO and TiO₂ was investigated to examine the effect of surface passivation on solar cell performance.¹⁰ The solar cell parameters of the devices were characterized with current-voltage (I-V) measurements, whereas the electron lifetime and electron transport time of the cells were obtained using intensity-modulated photovoltage and photocurrent spectroscopy (IMVS/IMPS) techniques. We demonstrate that passivation of the porous SnO₂ electrode surface with TiO₂ improves the open circuit voltage as well as the electron lifetime and electron transport time, thus, resulting in higher conversion efficiencies.

5.2 Results and Discussion

Mesoporous SnO₂ electrodes with three different thicknesses (1.8±0.1 μm, 3.2±0.1 μm and 4.8±0.1 μm) were prepared on fluorine-doped tin oxide substrates (FTO, Pilkington, TEC7). The FTO substrates were pre-coated with a ~30 nm dense SnO₂ blocking layer (BL) via the method of spray pyrolysis deposition.¹⁰ Mesoporous SnO₂ electrodes were obtained by depositing SnO₂-paste onto FTO substrates with BL and silicon wafer via spin-coating and subsequently annealing in air at 500 °C for 30 min. Wide angle X-ray diffraction (XRD) measurements on a silicon wafer show that the cassiterite phase of SnO₂ films was formed under these conditions (cf. Figure A-1.3 in Appendix). Nitrogen sorption measurements yielded 35.3 m² g⁻¹ for the Brunauer-Emmett-Teller (BET) surface area and ~30 nm average pore size for the powder of mesoporous SnO₂ prepared by scratching off the mesoporous SnO₂ films deposited onto glass microscope slides (cf. Figure A-2.3 in Appendix).

Mesoporous SnO₂ electrodes with different thicknesses were sensitized with pre-synthesized, water-soluble PbS QDs capped with L-glutathione (GSH) ligands (PbS-GSH QDs). PbS QDs were synthesised via a ‘hot injection’ method using oleic acid (OA) as a capping agent and subsequently water solubilized via a ligand exchange procedure in which GSH ligands were used to replace the OA. The resulting PbS-GSH QDs have an average size of 3.1 nm obtained from a calculation based on the first excitonic peak of the wavelength-dependent absorption coefficient spectrum (cf. Figure A-7.1 in Appendix). Ultraviolet-visible-near infrared (UV-Vis-NIR) absorbance spectra of PbS-GSH QDs attached to the surface of the SnO₂ electrodes are presented in Figure 5.1a. The first excitonic peak of QDs attached to the SnO₂ electrodes appears at 954 nm which corresponds to a size of 3.1 nm for the PbS-GSH QDs.¹⁴ The absorbance of the QDs increases with the increase of the thickness of the mesoporous SnO₂ electrode, which indicates a higher total loading of QDs. This can also be seen from the

photographic image of the corresponding PbS-GSH QD-sensitized SnO₂ electrodes with different thicknesses (Figure 5.1b).

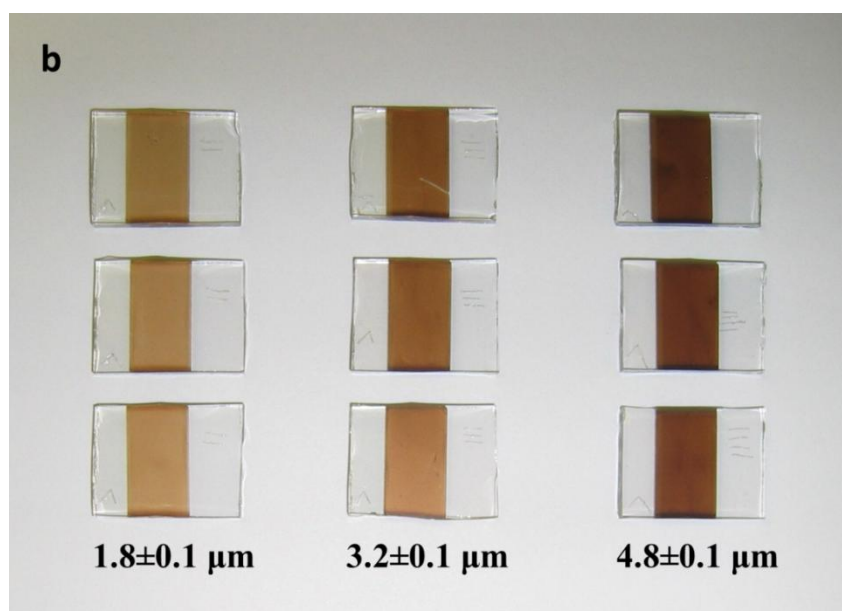
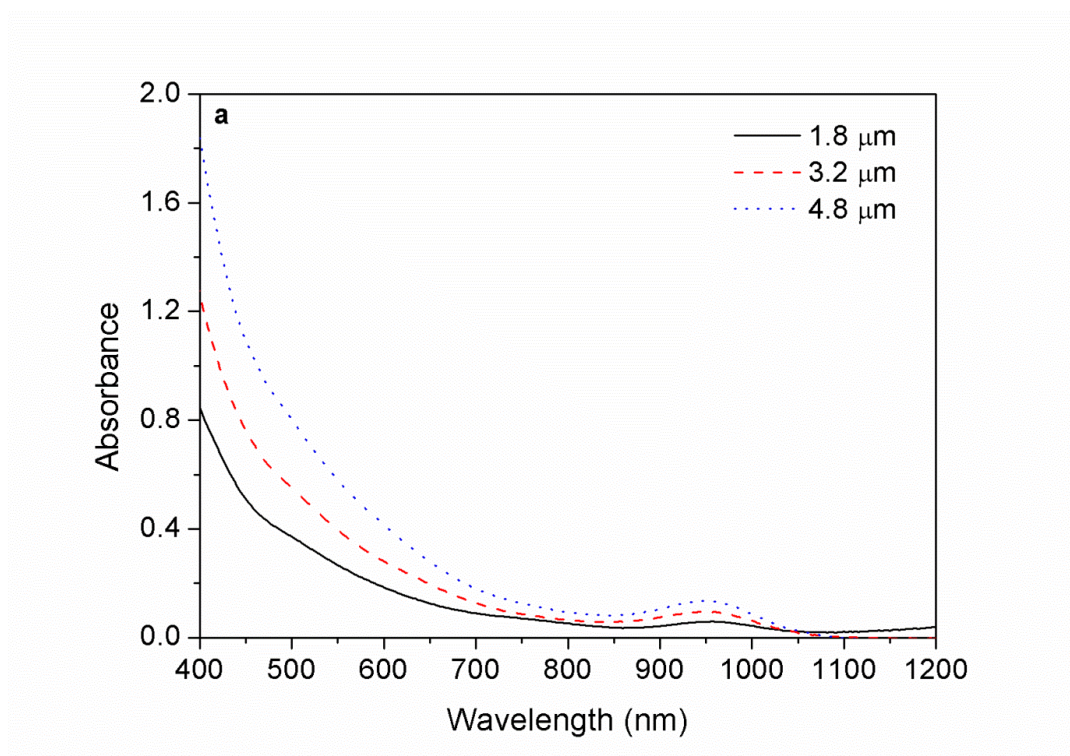


Figure 5.1. (a) UV-Vis-NIR spectra of ~3 nm sized PbS-GSH QDs adsorbed onto the surface of mesoporous SnO₂ electrodes with three different thicknesses; (b) Photographic images of PbS-GSH QD-sensitized SnO₂ electrodes with three different thicknesses.

The PbS-GSH QD-sensitized SnO₂ electrodes were assembled into solid-state QDSCs using spiro-OMeTAD as HTM. The cells had a sandwich structure incorporating a 2 mm glass substrate, 200 nm FTO, ~30 nm of dense blocking layer of SnO₂, with three different thicknesses (1.8, 3.2 and 4.8 μm) of active layer (mesoporous SnO₂/PbS QDs/HTM), around 1 μm of a spiro-OMeTAD HTM capping layer (deposited via spin-coating) and 500 nm thick sputtered silver contacts (Figure 5.2).

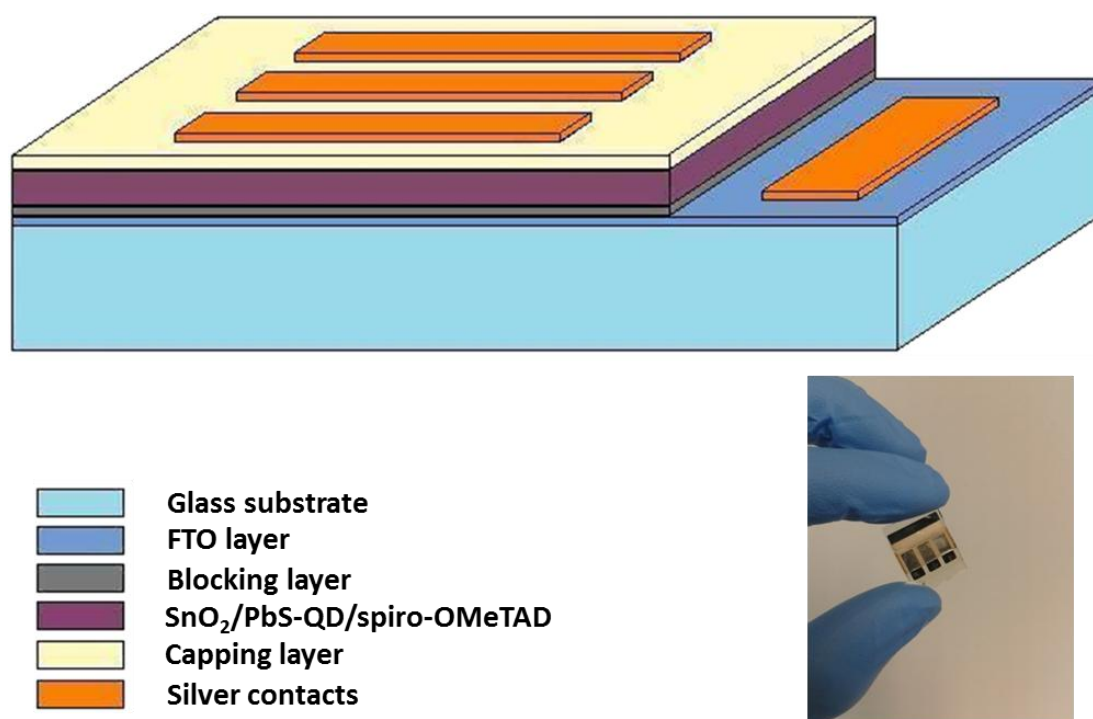


Figure 5.2. Sketch of solid-state QDSC with a mesoporous SnO₂ electrode, and photographic image (inset) of a solid-state QDSC with 1.8±0.1 μm mesoporous SnO₂.

The performance of the cells was tested with I-V measurements under AM 1.5 G at 100 mW cm⁻² irradiation, and the resulting solar cell performance parameters are given in Table 5.1. The highest performance observed was for cells with 1.8±0.1 μm thick SnO₂ electrodes that showed a short circuit current exceeding 1.2 mA cm⁻² and an open circuit voltage around 110 mV, which resulted in around 0.04% conversion efficiency. This low value for the conversion efficiency is partly due to the low open circuit voltages for SnO₂

electrodes. The performance of the cells decreased further as the thickness of the SnO₂ layer was increased (cf. Table 5.1). One of the reasons for this could be an increased roughness of the SnO₂ films with higher thickness that results in a poor quality of the HTM capping layer. This increases shunting and even short-circuiting via pinholes formed in the HTM capping layer. Moreover, electrodes with thickness above 2 μm are known to result in poor HTM infiltration, which significantly affects the performance of the cells.¹⁵

Table 5.1. AM 1.5 G solar cell performances of solid-state PbS QDSCs with different thickness of mesoporous SnO₂ electrodes.

d_f (μm)	J_{SC} (mA cm ⁻²)	V_{OC} (mV)	FF (%)	η (%)
1.8±0.1	1.21	109	28	0.037
3.2±0.1	0.23	27.3	25	0.001
4.8±0.1	0.09	5.3	28	-

Due to the poor performance of cells with thicker layers, only mesoporous SnO₂ electrodes with a thickness of 1.8±0.1 μm were used in further experiments. In order to increase the open circuit voltage of solid-state DSCs, Snaith et al.¹⁰ used Mg(OAc)₂ or TiCl₄ alone and a combination of both in order to passivate the SnO₂ electrode surface. The authors showed that these treatments result in the formation of MgO and TiO₂ coatings on the SnO₂ electrode surface and thus cause enhanced open circuit voltages as well as short circuit currents due to reduced charge recombination.¹⁰ For the aforementioned reason, 1.8±0.1 μm thick mesoporous SnO₂ electrodes were passivated in the course of the experiment with MgO or TiO₂ alone and in combination. This was done in a similar way as described by Snaith et al.¹⁰ to enhance the performance of the cells (see Experimental Section).

In order to compare the surface passivation effect of these different MO (MgO and TiO₂) coatings, the electrodes with bare SnO₂, SnO₂ treated with Mg(OAc)₂ (SnO₂/MgO), SnO₂ treated with TiCl₄ (SnO₂/TiO₂) and SnO₂ treated with a combination of TiCl₄ and Mg(OAc)₂ (SnO₂/TiO₂/MgO) were prepared. Then, SnO₂ electrodes with and without surface passivation were sensitized with PbS-GSH QDs and assembled into solid-state QDSCs using spiro-OMeTAD as HTM. A cross-section scanning electron microscopy (SEM) image of one of the cells is presented in Figure 5.3.

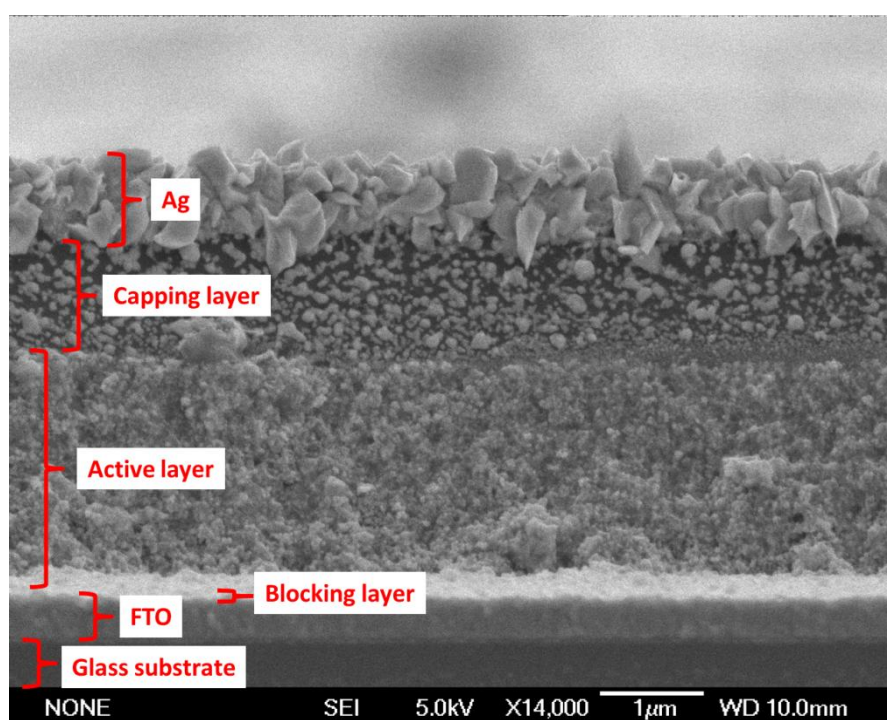


Figure 5.3. Cross-section SEM micrograph of a solid-state QDSC with $1.8\pm 0.1 \mu\text{m}$ mesoporous SnO₂ electrode. Visible from bottom to top: glass substrate, 600 nm FTO, ~30 nm BL, $1.8\pm 0.1 \mu\text{m}$ mesoporous SnO₂, around 1 μm thick HTM capping layer and about 500 nm silver top electrode.

Furthermore, the solar cell performance parameters of the cells were obtained from I-V measurements under AM 1.5 G at 100 mW cm^{-2} irradiation. The I-V curves of the best performing cells for each type of surface passivation are presented in Figure 5.4 and the solar cell performance values are compared in Table 5.2.

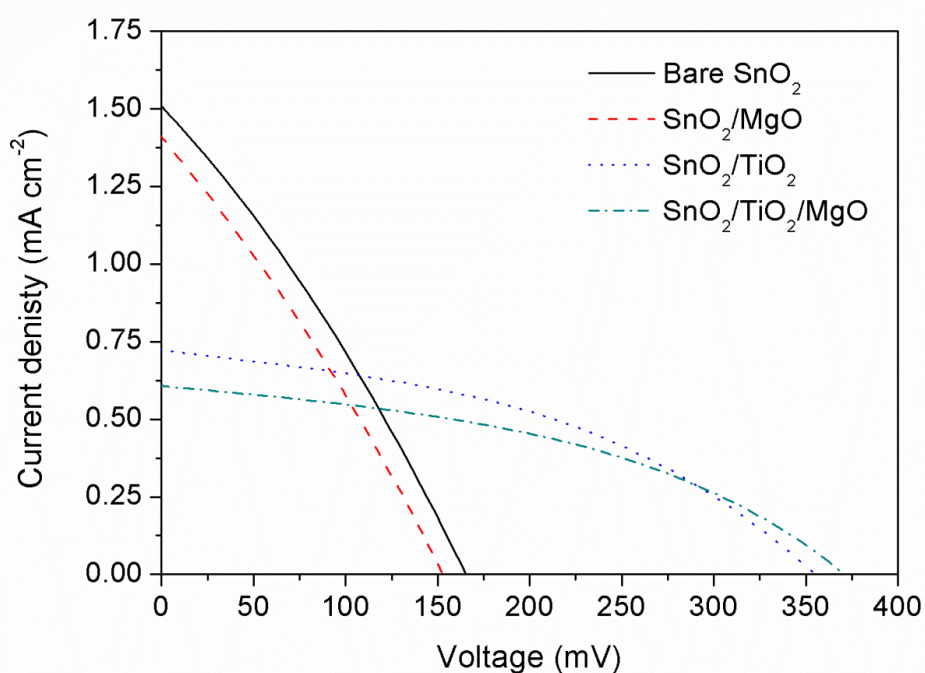


Figure 5.4. I-V curves of best performing solid-state PbS QDSCs with 1.8 ± 0.1 μm thick mesoporous SnO₂ electrodes and different surface passivation.

Table 5.2. AM 1.5 G solar cell performance of solid-state PbS QDSCs with 1.8 ± 0.1 μm thick mesoporous SnO₂ electrodes and different surface passivation.

Passivation	J_{SC} (mA cm ⁻²)	V_{OC} (mV)	FF (%)	η (%)
Bare SnO ₂	1.38	151	27.1	0.057
SnO ₂ /MgO	1.09	144	29.1	0.046
SnO ₂ /TiO ₂	1.14	326	36.0	0.134
SnO ₂ /TiO ₂ /MgO	0.8	352	41.5	0.117

The comparison of solar cell performance parameters of the cells revealed that the passivation of the SnO₂ electrode surface has a generally positive impact except for the MgO coating alone. A comparison of the performance of the cells with SnO₂/MgO electrode with the reference cell (bare SnO₂ electrode) shows that the cell parameters are slightly lowered after Mg(OAc)₂ treatment of SnO₂, which results in a 20% reduction in conversion efficiency. However, the treatment with TiCl₄ significantly improved cell performance (two-fold vs. reference), attributed to an improved open circuit voltage (326 mV) and fill factor (36%). Nevertheless, it should be noted that the short circuit current drops by about 20% after passivation with TiO₂ compared to the reference cell. This can be explained by a reduction in electron injection from PbS QDs into the SnO₂/TiO₂ electrode due to a smaller offset between the conduction band edges of TiO₂ and PbS QDs compared to SnO₂ and PbS QDs (Figure 1.6). This, reduces the driving force for the excited electrons in PbS QDs to inject into the SnO₂/TiO₂ electrode and therefore hinders the exciton separation process.

Double coating of the SnO₂ surface with TiO₂ and MgO further decreased the short circuit current but had a positive effect on the open circuit voltage and fill factor. Overall, the cells with SnO₂/TiO₂/MgO electrodes show an inferior performance compared to the ones with SnO₂/TiO₂ electrodes. This is again attributed to significantly decreased electron injection from PbS QDs into the n-type MO scaffold since the thin MgO layer acts as an energetic barrier. Comparison of these results with the work of Snaith et al.¹⁰ shows partial agreement, however, unlike in Snaith's findings no increase in the short circuit current was observed upon passivation of the SnO₂ electrode. In fact, short circuit current values in all of the cells with passivation were lowered compared to the reference cells with unpassivated SnO₂ electrodes. These differences between the findings of Snaith et al.¹⁰ and our results could be due to some differences in preparation conditions and thickness of the passivation layers.

In order to gain further understanding of the surface passivation effect, cells with bare SnO₂ and SnO₂/TiO₂ electrodes were studied with IMVS and IMPS techniques providing an estimation of the electron lifetime, τ_n , and the electron transport time, τ_{trans} , respectively. The IMVS and IMPS spectra of the cells were recorded under different illumination intensities at both open circuit and short circuit conditions (Figures 5.5a and 5.5b).

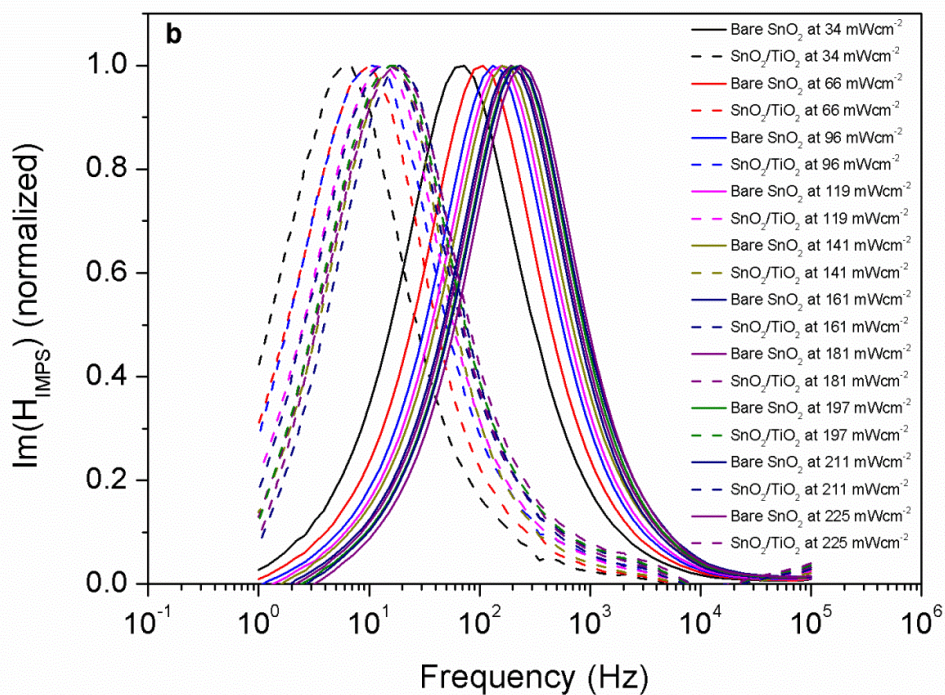
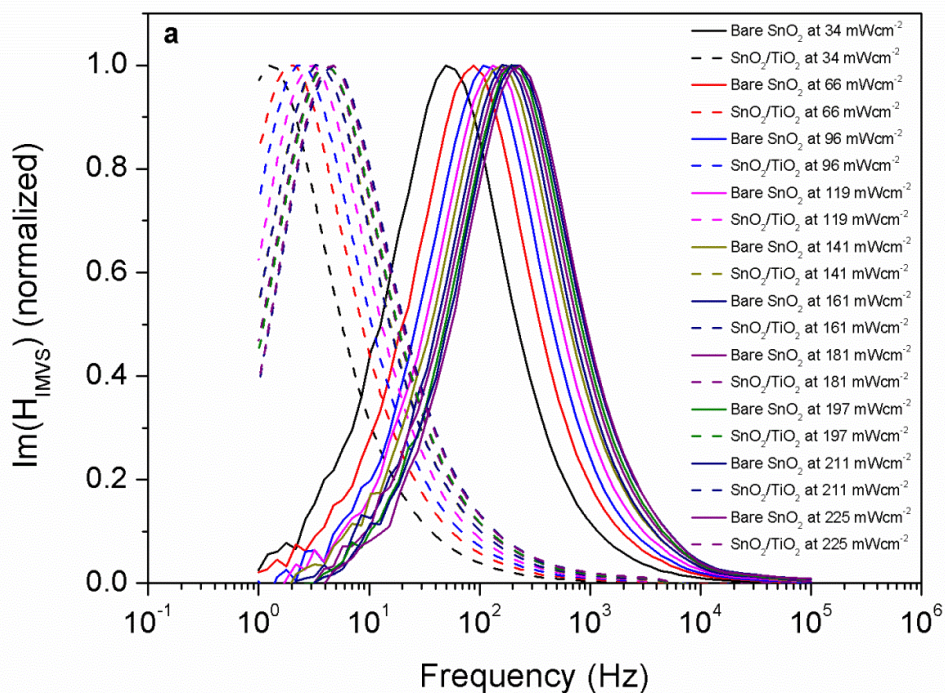


Figure 5.5. (a) Frequency dependence of the normalized imaginary part of (a) IMVS and (b) IMPS spectra at different illumination intensities for solid-state QDSCs with bare and TiO₂-coated mesoporous SnO₂ electrodes.

IMVS and IMPS spectra were used to calculate the electron lifetime, τ_n , and electron transport time, τ_{trans} , according to the following relationships (5.1) and (5.2):

$$\tau_n = \frac{1}{2\pi \cdot f_{max}^{IMVS}}, \quad (5.1)$$

$$\tau_{trans} = \frac{1}{2\pi \cdot f_{max}^{IMPS}}, \quad (5.2)$$

where f_{max}^{IMVS} and f_{max}^{IMPS} are frequency values at the imaginary part maxima of the IMVS and IMPS spectra, respectively. The obtained values of τ_n and τ_{trans} for cells with bare SnO₂ and SnO₂/TiO₂ electrodes are presented in Figures 5.6a and 5.6b.

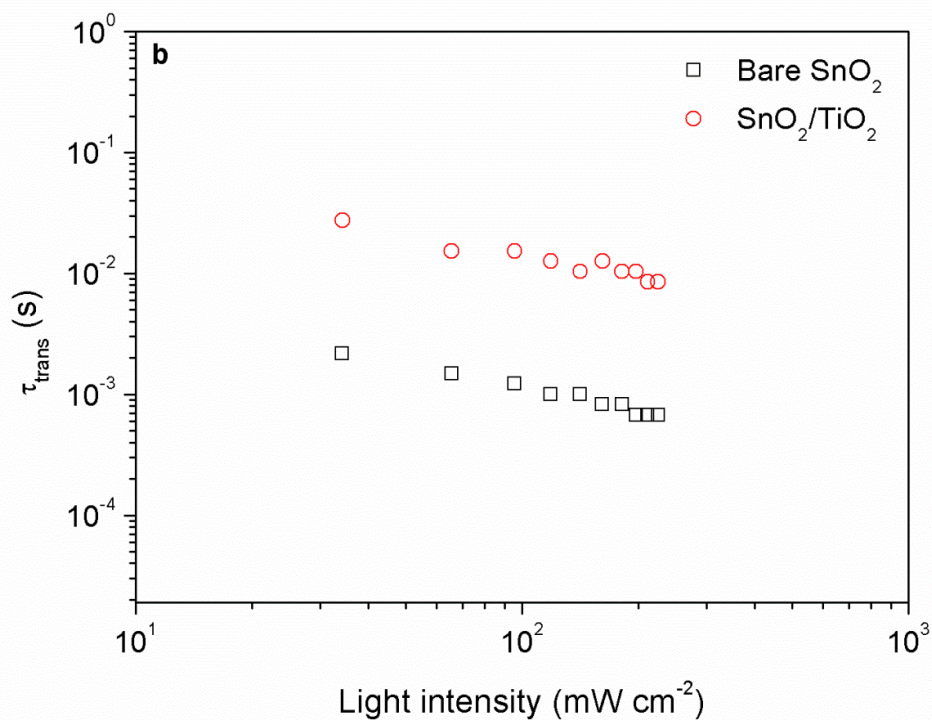
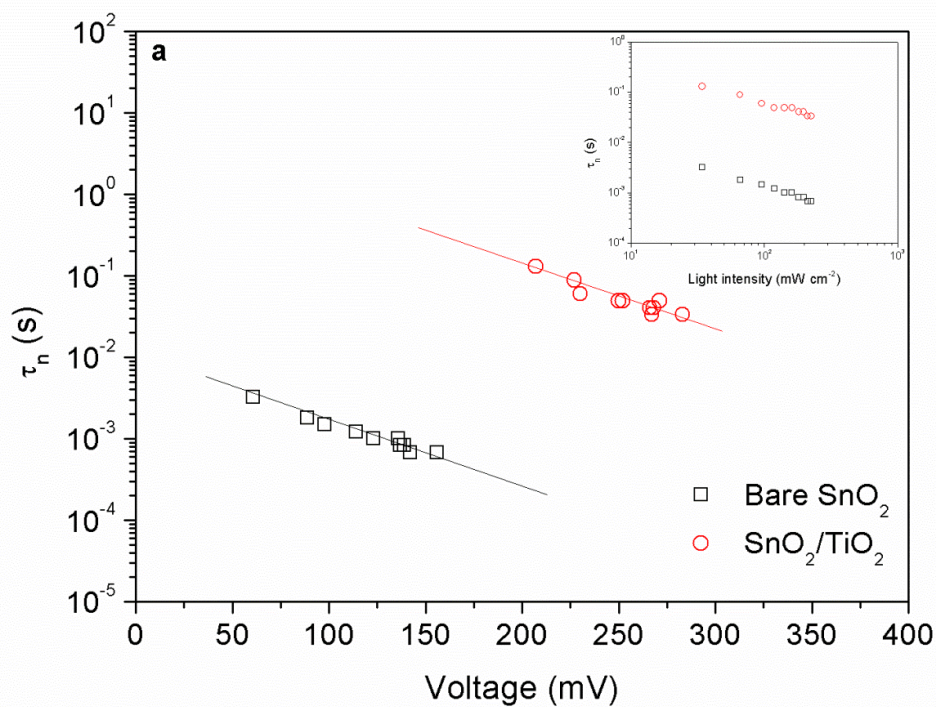


Figure 5.6. (a) Voltage and light intensity (inset) dependence of electron lifetimes for cells with bare SnO₂ and SnO₂/TiO₂ electrodes (solid lines are plotted as a guidance for the eye); (b) Light intensity dependence of electron transport times for cells with bare SnO₂ and SnO₂/TiO₂ electrodes.

A comparison of the passivated cell with the reference cell shows that there is a significant difference in the values of the electron lifetimes, τ_n , between the two devices. The electron lifetime in the passivated cell is two orders of magnitude greater than in the reference cell. Snaith et al.¹⁰ and Huang et al.¹² have also shown increased electron lifetimes for TiO₂-passivated solid-state DSCs and liquid electrolyte based QDSCs compared to reference, unpassivated cells. It should be noted that unlike the illumination intensity plot of τ_n (inset of Figure 5.6a) the voltage dependence plot results in a shift of values for the reference and passivated cells along the abscissa axis. This is due to the different displacement of the quasi Fermi levels of SnO₂ and SnO₂/TiO₂ from the redox level of the HTM or, in other words, different open circuit voltages in the reference and passivated cells for the same illumination intensities. A comparison of the electron transport times, τ_{trans} , between the TiO₂ passivated and the reference cells shows that for the former cell τ_{trans} is an order of magnitude higher than the reference throughout all illumination intensities. The electron transport time is inversely proportional to the diffusion coefficient ($\tau_{trans} \sim D_n^{-1}$), which means that the devices with passivated electrodes have a lower diffusion coefficient compared to the reference electrode device. Similar results were obtained by Snaith et al.¹⁰ for SnO₂ electrodes coated with TiO₂ and by Docampo et al.¹³ for MgO coated SnO₂. The longer values of transport time in case of the passivated cells can be explained by the relatively lower Fermi level (less injection) compared to the bare cell. The ‘driving force’ for the transport of electrons in the electrode is the gradient of free energy or gradient of the Fermi energy, $\partial E_F / \partial x$.¹⁶ Nevertheless, overall TiO₂-passivated cells result in a better performance compared to the reference, unpassivated cells.

5.3 Conclusion

In summary, mesoporous SnO₂ films on FTO substrates were examined as an n-type scaffold electrode in solid-state QDSCs. Water-soluble pre-synthesized PbS QDs capped with GSH ligands were used as sensitizer, whereas spiro-OMeTAD was employed as HTM. The I-V measurements showed that SnO₂ electrodes with a thickness of ~2 μm are the best choice for the fabrication of solid-state QDSCs. It was demonstrated that bare SnO₂ electrodes used to fabricate solid-state QDSCs are more suitable for efficient electron injection from PbS QDs compared to ones with passivating overlayer(s), but the devices suffered from low open circuit voltages. Passivation of the surface of SnO₂ electrodes with TiO₂ and MgO in combination or with TiO₂ only significantly increased the open circuit voltage. Passivation of SnO₂ electrodes resulted in lower short circuit currents compared to the devices with unpassivated electrodes. This effect was attributed to the decrease of electron injection since the passivating TiO₂ and MgO shells act as energetic barrier between SnO₂ and PbS QDs due to their elevated conduction bands. IMVS studies on cells with bare SnO₂ and with TiO₂-coated electrodes showed that the devices with TiO₂-passivation have significantly higher electron lifetimes, which indicates a reduction of the charge carrier recombination upon passivation. IMPS studies on the devices showed that the diffusion coefficient for cells with TiO₂-passivation is decreased compared to the reference cells due to a lower quasi-Fermi level in the TiO₂-coated electrodes. The results of the IMVS and IMPS studies are consistent with finding of other groups.^{10, 12}

5.4 Experimental Section

5.4.1 Materials

Oleic acid (Sigma-Aldrich), lead(II) oxide (Sigma-Aldrich), hexamethyldisilathiane (Sigma-Aldrich), 1-octadecene (Sigma-Aldrich), chloroform (Merck), toluene (Sigma-Aldrich), sodium hydroxide (Sigma-Aldrich), titanium(IV) chloride (Sigma-Aldrich), magnesium acetate tetrahydrate (Sigma-Aldrich), butyltin trichloride (Sigma-Aldrich), tin(IV) oxide nanoparticles (Sigma-Aldrich), ethyl cellulose (Fluka), terpineol (Fluka), ethanol (Sigma-Aldrich), L-glutathione (Sigma-Aldrich), spiro-OMeTAD (Merck), 4-*tert*-butylpyridine (Sigma-Aldrich), bis(trifluoromethane)sulfonimide lithium salt (Sigma-Aldrich), chlorobenzene (Sigma-Aldrich), acetonitrile (Sigma-Aldrich).

5.4.2 Preparation of Colloidal QDs

PbS QDs capped with oleic acid were synthesised as described by Tang et al.¹⁷ (cf. subsection A-5 in Appendix), and water-solubilized PbS QDs capped with GSH were obtained by a ligand exchange procedure as described by Deng et al.¹⁸ (cf. subsection A-6 in Appendix).

5.4.3 Preparation of SnO₂ Electrodes

SnO₂ nanoparticles with <100 nm size (Sigma-Aldrich, CAS Number: 18282-10-5) were used to prepare the SnO₂-paste as described by Ito et al.^{19, 20} (cf. subsection A-14 in Appendix). The resulting paste was deposited by spin-coating onto FTO substrates (1.5×2 cm²) pre-coated with a compact ~30 nm SnO₂ blocking layer (cf. subsection A-4 in Appendix).¹⁰ The

films were then annealed in air at 500 °C for 30 min to obtain mesoporous SnO₂ electrodes. Two and three layers of SnO₂ paste were deposited with intermediate drying at 70 °C for 30 min in order to increase the thickness of the electrodes. Finally, the electrodes were subjected to a 20 mM aqueous TiCl₄ solution treatment (10 mL per substrate) at 70 °C for 1 h in 20 mL volume glass vials and annealing at 500 °C for 45 min in air to passivate the surface of SnO₂ electrodes with TiO₂. For MgO passivation, the SnO₂ electrodes were treated with a 120 mM aqueous solution of Mg(OAc)₂ (10 mL per substrate) for 1 min at room temperature in 20 mL volume glass vials and rinsed with ethanol and annealed at 500 °C for 45 min in air.

5.4.4 Fabrication of Solar Cells

For the sensitization with PbS-GSH QDs, bare and passivated mesoporous SnO₂ electrodes (1.5×1 cm²) were immersed for 3 days in 20 mL of a 3 mM aqueous solution (pH 5) of PbS-GSH QD to achieve saturated loading of the QDs onto the internal walls of porous electrodes. Then the sensitized electrodes were rinsed with deionized water (usually 10 mL) to remove unattached QDs and excess GSH ligands. 210 mM spiro-OMeTAD in chloroform with 15 mM bis(trifluoromethane)sulfonimide lithium salt and 15 mM 4-*tert*-butylpyridine additives were spin-coated onto sensitized electrodes at 1200 rpm for 30 sec.^{15, 21-23} 500 nm silver contacts were then deposited via evaporation onto the substrates through a mask using a Univex 350 sputter system (Oerlikon Leybold).

5.4.5 Characterisation Methods

The structure and phase of the porous SnO₂ films were characterized by wide angle XRD using a Bruker D8 Discover diffractometer with Cu-K_α radiation ($\lambda = 1.5418 \text{ \AA}$) and equipped with a LynxEye position-sensitive detector. Average film thickness values were measured with a Dektak 150 profilometer. Absorbance spectra of the PbS QD-sensitized SnO₂ electrodes were recorded using a UV-Vis-NIR spectrophotometer (model: Lambda 1050, PerkinElmer). The absorbance spectra of the sensitized electrodes were measured with a 0.16 cm² mask and were corrected for the absorbance of the SnO₂ electrodes. The cross-section image of the solar cell was observed with a 4 keV electron beam using a JEOL-JSM-6500F SEM equipped with a field emission gun. The I-V characteristics of the solid-state QDSCs were measured under simulated solar light at an irradiance of 100 mW cm⁻² using a 300 W xenon lamp equipped with an AM 1.5 G filter (XPS 400, Solar Light Company Inc.). The I-V characteristics were recorded using a Keithley 2400 source meter, with cells having 0.11 cm² active area. IMVS and IMPS data were obtained using a potentiostat equipped with a frequency response analyser (model: PGSTAT302N, Autolab, Metrohm) and LED driver. IMVS and IMPS measurements were carried out with green LED (model: LDC530, Metrohm) irradiation at open-circuit and short circuit conditions, respectively, over the frequency range from 100 kHz to 1 Hz. The amplitude of the AC modulation current was 10% of the DC current applied to the LED.

References

1. B. O'Regan and M. Gratzel, *Nature*, 1991, **353**, 737-740.
2. P. Tiwana, P. Docampo, M. B. Johnston, H. J. Snaith and L. M. Herz, *ACS Nano*, 2011, **5**, 5158-5166.
3. R. Vogel, P. Hoyer and H. Weller, *The Journal of Physical Chemistry*, 1994, **98**, 3183-3188.
4. S. Hotchandani and P. V. Kamat, *The Journal of Physical Chemistry*, 1992, **96**, 6834-6839.
5. C. Nasr, P. V. Kamat and S. Hotchandani, *Journal of Electroanalytical Chemistry*, 1997, **420**, 201-207.
6. H. J. Snaith and L. Schmidt-Mende, *Advanced Materials*, 2007, **19**, 3187-3200.
7. A. N. M. Green, E. Palomares, S. A. Haque, J. M. Kroon and J. R. Durrant, *The Journal of Physical Chemistry B*, 2005, **109**, 12525-12533.
8. H. C. Leventis, F. O'Mahony, J. Akhtar, M. Afzaal, P. O'Brien and S. A. Haque, *Journal of the American Chemical Society*, 2010, **132**, 2743-2750.
9. O.-A. Boateng, K. Shoji, K. Asoka, O. Masayuki, M. Kenji, K. Akinori and T. Kirthi, *Japanese Journal of Applied Physics*, 2005, **44**, L731.
10. H. J. Snaith and C. Ducati, *Nano Letters*, 2010, **10**, 1259-1265.
11. H. J. Snaith, A. Stavrinadis, P. Docampo and A. A. R. Watt, *Solar Energy*, 2011, **85**, 1283-1290.

12. Q. Huang, F. Li, Y. Gong, J. Luo, S. Yang, Y. Luo, D. Li, X. Bai and Q. Meng, *The Journal of Physical Chemistry C*, 2013, **117**, 10965-10973.
13. P. Docampo, P. Tiwana, N. Sakai, H. Miura, L. Herz, T. Murakami and H. J. Snaith, *The Journal of Physical Chemistry C*, 2012, **116**, 22840-22846.
14. I. Moreels, K. Lambert, D. Smeets, D. De Muynck, T. Nollet, J. C. Martins, F. Vanhaecke, A. Vantomme, C. Delerue, G. Allan and Z. Hens, *ACS Nano*, 2009, **3**, 3023-3030.
15. I. K. Ding, N. Tétreault, J. Brillet, B. E. Hardin, E. H. Smith, S. J. Rosenthal, F. Sauvage, M. Grätzel and M. D. McGehee, *Advanced Functional Materials*, 2009, **19**, 2431-2436.
16. K. Kalyanasundaram, *Dye-Sensitized Solar Cells*, CRC Press, Boca Raton, 2010.
17. J. Tang, K. W. Kemp, S. Hoogland, K. S. Jeong, H. Liu, L. Levina, M. Furukawa, X. Wang, R. Debnath, D. Cha, K. W. Chou, A. Fischer, A. Amassian, J. B. Asbury and E. H. Sargent, *Nature Materials*, 2011, **10**, 765-771.
18. D. Deng, J. Xia, J. Cao, L. Qu, J. Tian, Z. Qian, Y. Gu and Z. Gu, *Journal of Colloid and Interface Science*, 2012, **367**, 234-240.
19. S. Ito, P. Chen, P. Comte, M. K. Nazeeruddin, P. Liska, P. Péchy and M. Grätzel, *Progress in Photovoltaics: Research and Applications*, 2007, **15**, 603-612.
20. S. Ito, T. N. Murakami, P. Comte, P. Liska, C. Grätzel, M. K. Nazeeruddin and M. Grätzel, *Thin Solid Films*, 2008, **516**, 4613-4619.

21. P. Docampo, S. Guldin, M. Stefik, P. Tiwana, M. C. Orilall, S. Hüttner, H. Sai, U. Wiesner, U. Steiner and H. J. Snaith, *Advanced Functional Materials*, 2010, **20**, 1787-1796.
22. A. Abate, T. Leijtens, S. Pathak, J. Teuscher, R. Avolio, M. E. Errico, J. Kirkpatrick, J. M. Ball, P. Docampo, I. McPherson and H. J. Snaith, *Physical Chemistry Chemical Physics*, 2013, **15**, 2572-2579.
23. P. Docampo and H. J. Snaith, *Nanotechnology*, 2011, **22**, 225403.

6 Comparison of Solid-State Quantum-Dot-Sensitized Solar Cells with *Ex Situ* and *In Situ* Grown PbS Quantum Dots

The chapter is based on the following publication:

Askhat N. Jumabekov, Timothy D. Siegler, Niklas Cordes, Dana D. Medina, Daniel Böhm, Pelle Garbus, Simone Meroni, Laurence M. Peter and Thomas Bein, *The Journal of Physical Chemistry C*, 2014, DOI: 10.1021/jp5051904.

Abstract

Differences in the solar cell performance of solid-state PbS quantum-dot-sensitized solar cells (QDSCs) fabricated with *ex situ* and *in situ* grown PbS quantum dots (QDs) were investigated. The PbS QDs were either anchored on mesoporous TiO₂ via L-glutathione (GSH) linker or prepared *in situ* by the successive ionic layer adsorption/reaction (SILAR) method to sensitize mesoporous TiO₂ electrodes and to create solid-state QDSCs. Spiro-OMeTAD was used as the organic p-type hole transporting material (HTM). The solar cell performance of the cells were evaluated with current-voltage, incident-photon-to-collected-electron efficiency and electrochemical impedance spectroscopy (EIS) measurements, and electron lifetimes were measured with open circuit voltage decay (OCVD), intensity-modulated photovoltage spectroscopy (IMVS) techniques as well as with EIS measurements. Analysis of the experimental data indicates that the SILAR route provides more intimate contacts at both TiO₂/PbS and PbS/HTM interfaces, which results in more efficient charge injection and separation, and thus higher photocurrents. However, the results of the OCVD,

IMVS and EIS measurements demonstrate that the cells sensitized with PbS quantum dots prepared *ex situ* have longer electron lifetimes, indicating that back transfer of electrons to the HTM is slower, probably as a consequence of passivation of surface states by the GSH ligands.

6.1 Introduction

Much effort has been dedicated in recent years to investigate hybrid solid-state quantum-dot-sensitized solar cells (QDSCs) with different types of quantum dots (QDs) and hole transporting materials (HTMs).¹⁻⁹ Efficiencies as high as 3.3% in the case of PbS QDs with P3HT HTM and about 6.2% in case of Sb₂S₃ QDs with a PCPDTBT HTM have been reported.^{9, 10} Nearly all studies of QDSCs have utilized either *in situ* (chemical bath deposition (CBD),¹¹ successive ionic layer adsorption/reaction (SILAR)¹² and ion layer gas adsorption/reaction (ILGAR)¹³) or *ex situ* methods (physisorption,^{14, 15} chemisorption¹⁶⁻¹⁸ and electrophoretic deposition (EPD)^{19, 20}) for loading QDs. Surprisingly, there are very few studies on comparing the solar cell efficiency of these different loading techniques.^{21, 22} An example of such a study was reported by Yang et al.²¹ in which they found significant difference in solar cell performances and parameters for the cells made via *in situ* or *ex situ* loading methods. The study showed that the cells with *in situ* deposited QDs provide better interfacial contact between the electron acceptor TiO₂ and the electron donor CdTe QDs, thus delivering higher photocurrents and efficiencies in comparison with the cells with *ex situ* (via EPD) deposited QDs. In another recent study, Tao et al.²² reported similar results for a comparative study of solar cell efficiencies of liquid electrolyte based QDSCs with *ex situ* and *in situ* grown PbS QDs. The authors also found higher short circuit currents in cells with *in situ* compared to the *ex situ* grown QDs.²² However, these reports both deal with liquid

electrolyte-based QDSCs rather than, as here, solid-state QDSCs. Therefore, an investigation of the differences between cells made with *ex situ* and *in situ* grown inorganic absorber layers in solid-state cells is needed to provide a better understanding of the physical and chemical processes happening at the interface of different components of the solid-state QDSCs, aimed at improvements in cell performance.

Here we report on comparative study of hybrid solid-state QDSCs with *ex situ* and *in situ* grown PbS QDs employing spiro-OMeTAD as a HTM. The performance of the devices was characterized with current-voltage (I-V), incident-photon-to-collected-electron efficiency (IPCE) and electrochemical impedance spectroscopy (EIS) measurements. In addition, the electron lifetimes of the cells were measured over a range of intensities using intensity-modulated photovoltage spectroscopy (IMVS) and EIS techniques as well as with open circuit voltage decay (OCVD) measurements. We conclude that differences in interfacial contacts between the sensitizer (PbS QDs) and the n-type (TiO_2) and p-type (spiro-OMeTAD HTM) conductors significantly affect charge injection and separation.²¹ We demonstrate that passivation of QD surface states and formation of a barrier layer between n- and p-type conductors greatly increase electron lifetimes in the cells.^{21, 23, 24}

6.2 Results and Discussion

Freshly made mesoporous TiO_2 anatase electrodes on fluorine-doped tin oxide glass substrates (FTO, Pilkington, TEC7) were used as the n-type scaffolding anodes for solid-state QDSCs. The anatase phase of TiO_2 was confirmed by wide angle X-ray diffraction measurements (cf. Figure A-1.4 in Appendix). The estimation of the mean domain size of the TiO_2 NPs from the peak corresponding to the 101 plane using the Scherrer equation gave a

value of 30 nm. The Brunauer-Emmett-Teller (BET) surface area ($56.1 \text{ m}^2 \text{ g}^{-1}$) was determined from nitrogen sorption experiments (cf. Figure A-2.4 in Appendix). The roughness factor, A_R , of the mesoporous TiO_2 electrode estimated by the dye desorption method yielded a value of 362 ± 23 (see Experimental Section).²⁵ Further, the mesoporous TiO_2 electrodes sensitized with PbS QDs via two different approaches: (a) *in situ*, using SILAR method and (b) *ex situ* in which the mesoporous TiO_2 electrodes were soaked into a water solution of presynthesized colloidal PbS QDs capped with L-glutathione (GSH) ligands. Ultraviolet-visible-near infrared (UV-Vis-NIR) spectra of *ex situ* and *in situ* grown PbS QDs deposited onto the walls of mesoporous TiO_2 electrodes are presented in Figure 6.1.

The absorption spectrum for *ex situ* grown PbS QDs shows a characteristic first excitonic peak at 947 nm (inset in Figure 6.1). The calculation of the mean size of the PbS QDs from the first excitonic peak resulted in a size of about 3.1 nm.²⁶ The scanning electron microscope (SEM) and energy-dispersive X-ray (EDX) spectroscopy analysis of the cross-section of a mesoporous TiO_2 electrode sensitized with *ex situ* grown PbS QDs shows a homogeneous distribution of QDs throughout the mesoporous TiO_2 electrode (cf. Figure A-11.1 in Appendix). Sensitization of mesoporous TiO_2 with *ex situ* grown PbS QDs was also confirmed with transmission electron microscopy (TEM) analysis (cf. Figure A-11.2 in Appendix). Unlike the absorbance spectra for *ex situ* grown PbS QDs, the spectrum of *in situ* grown PbS QDs deposited onto the walls of mesoporous TiO_2 does not show any characteristic excitonic peaks. This was also observed by other groups for SILAR grown PbS QDs, and it indicates that deposited PbS QDs have a broad size distribution of up to a few nm.⁴ The TEM analysis of a mesoporous TiO_2 film sensitized with *in situ* grown PbS QDs shows the presence of QDs with a broad size distribution on the surface of TiO_2 . The scanning transmission electron microscopy (STEM) analysis of the specimen shows that the majority of the QDs has a size of less than 1 nm (cf. Figure A-11.3 in Appendix). The comparison of the

absorbance spectra of *ex situ* and *in situ* grown PbS QDs suggests that the SILAR grown PbS QD layers absorb better throughout the visible range; however the absorbance is weaker above 800 nm compared to the absorbance of *ex situ* grown PbS QDs.

We analysed the UV-Vis-NIR spectrum in order to estimate the coverage of the walls of the mesoporous TiO₂ by *ex situ* grown PbS-GSH QDs. For this purpose we fitted the absorbance spectrum, $A(\lambda)$, using the Beer–Lambert law (Figure 6.1):

$$A(\lambda) = \frac{\alpha(\lambda) \cdot d_s}{2.303}, \quad (6.1)$$

where $\alpha(\lambda)$ is the absorption coefficient for PbS-GSH QDs and d_s is the equivalent optical thickness of the PbS. The wavelength dependent absorption coefficient was obtained separately for 0.11 mM PbS-GSH QDs in water from UV-Vis-NIR spectra (cf. Figure A-7.1 in Appendix). The fitting of the absorbance of the *ex situ* grown PbS QDs resulted in the value of $d_s = 238$ nm, which corresponds to a number of 2.54×10^{14} of 3.1 nm sized QDs per 0.16 cm² effective illumination area. The corresponding surface coverage with the QDs calculated using a surface roughness factor of 362 ± 23 is therefore in the range 35-41%, depending on whether one assumes cubic or hexagonal close packing coverage by a single layer of QDs. Coverage calculations for *in situ* grown PbS QDs are complicated by the uncertainty of the size distribution of the PbS QDs deposited onto the walls of the mesoporous TiO₂ electrode.

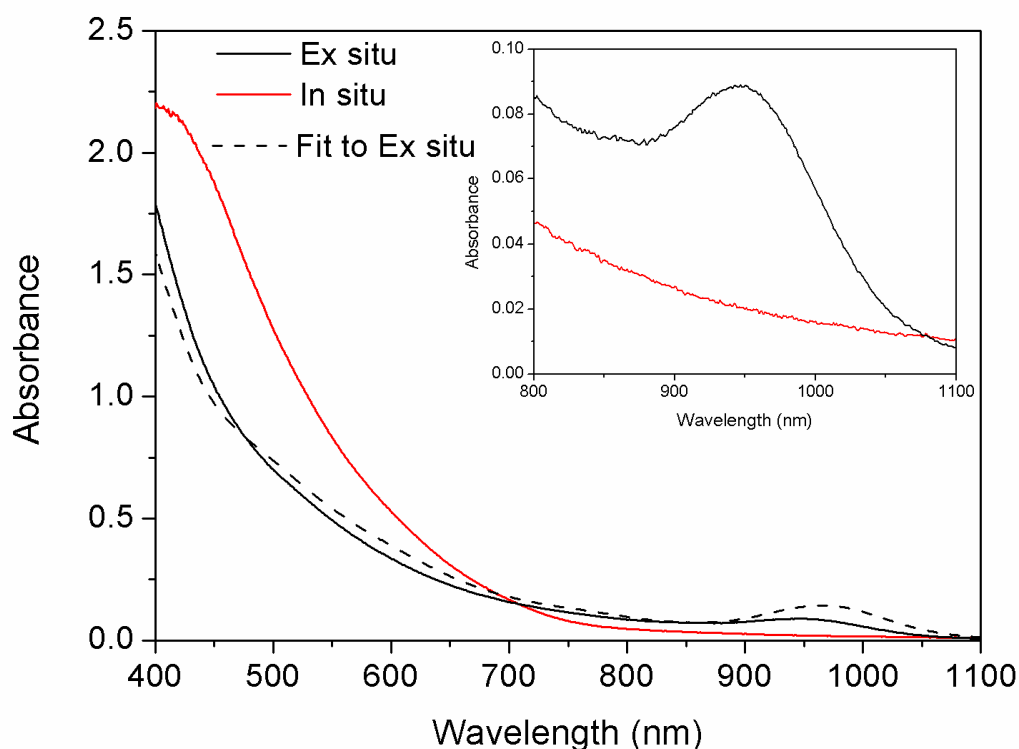


Figure 6.1. UV-Vis-NIR spectra of *ex situ* and *in situ* grown PbS QDs deposited onto the walls of $3\pm 0.1\ \mu\text{m}$ thick mesoporous TiO_2 . The dashed line shows a fit to the absorbance of *ex situ* PbS QDs. Inset is the magnification of the part of spectra from 800 to 1100 nm.

The PbS QD-sensitized mesoporous TiO_2 electrodes were used as photoanodes for solid-state QDSCs with spiro-OMeTAD HTM. For convenience, the cell with *ex situ* grown sensitizer is further referred to as C1, whereas the cell with *in situ* grown sensitizer is referred to as C2. The I-V characteristics are presented in Figure 6.2, and a summary of the performance of the C1 and C2 cells are given in Table 6.1. Comparison of I-V curves for AM 1.5 G at $100\ \text{mW cm}^{-2}$ irradiation shows that the short circuit current for device C2 is more than 4 times higher than for C1. However, the open circuit voltage and fill factor of C2 is slightly lower than for C1. Overall the performance of the cell C2 is about 3 times higher than that of C1.

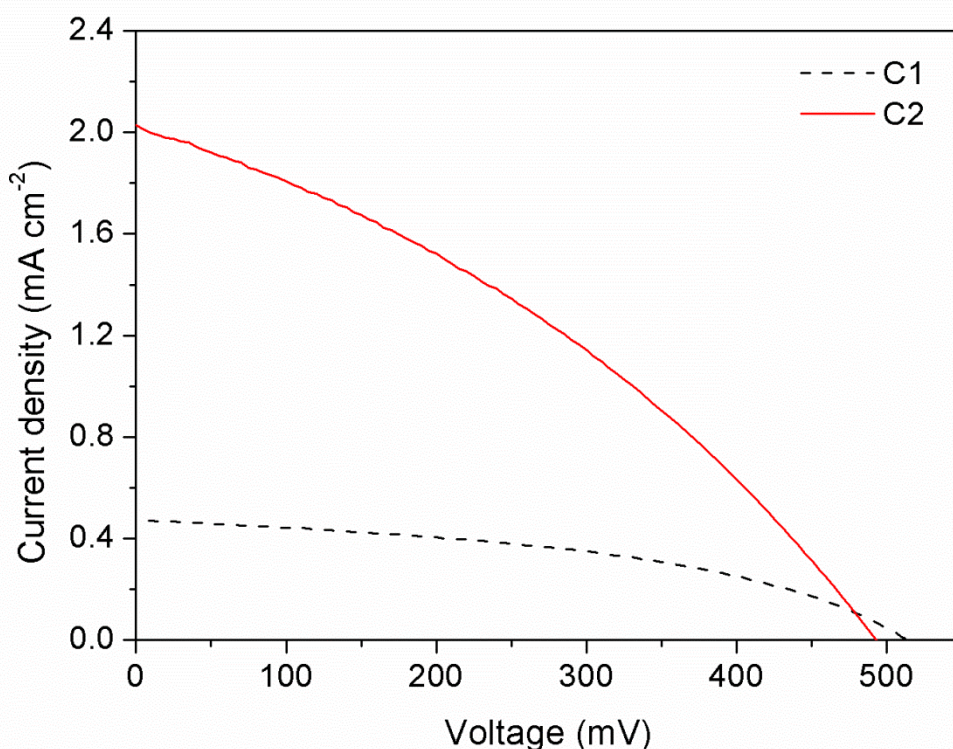


Figure 6.2. I-V characteristics of the C1 and C2 cells under AM 1.5 G at 100 mW cm⁻² irradiation.

Table 6.1. Summary of the performance of the cells under AM 1.5 G at 100 mW cm⁻² irradiation.

Cell	V_{OC} (mV)	J_{SC} (mA cm ⁻²)	FF (%)	η (%)
C1	512	0.46	43.4	0.10
C2	486	1.97	33.5	0.32

The IPCE of the cells were recorded in order to obtain spectral response of the cells (Figure 6.3). The IPCE of C2 is much higher than that of C1, and this is consistent with the I-V measurements. Calculation of the short circuit current densities for C1 and C2 from IPCE spectra results in values of 0.44 and 2.06 mA cm⁻², respectively, and these are in very good agreement with the values obtained from I-V measurements (Table 6.1).

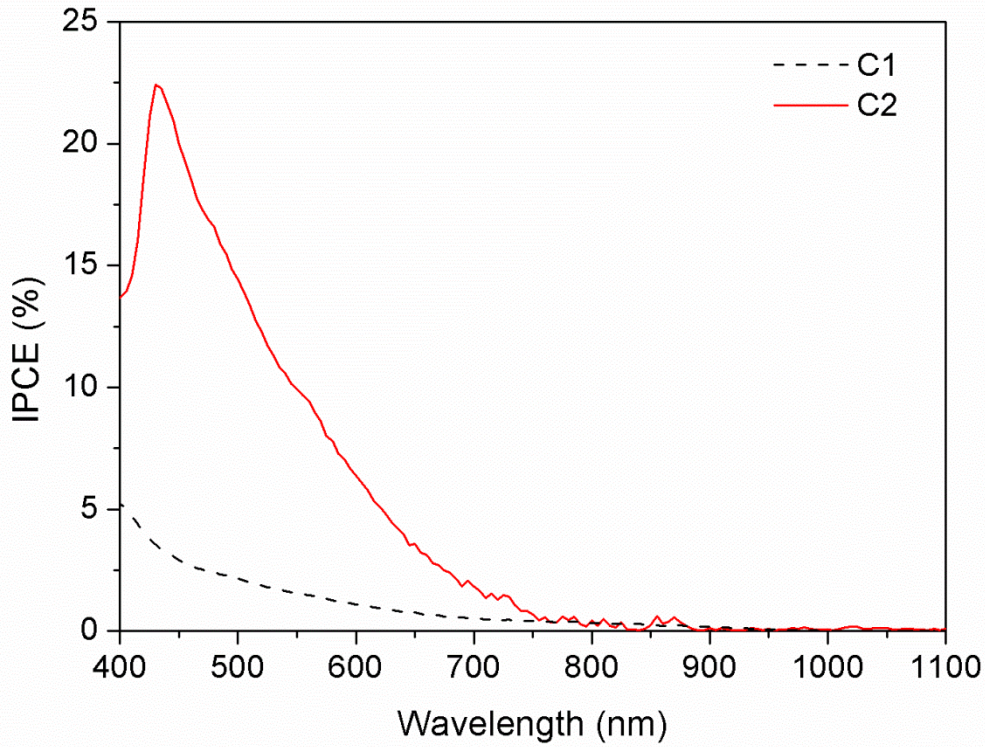


Figure 6.3. IPCE spectra of the C1 and C2 cells.

Theoretical short circuit currents can be obtained for the cells from the corresponding absorbance spectra (Figure 6.1) using the following relationship (6.2):²⁷

$$J_{SC} = \int e \cdot F(\lambda) \cdot \eta_{LHE} \cdot \eta_{inj} \cdot \eta_c d\lambda, \quad (6.2)$$

where e is the electron charge, $F(\lambda)$ is the incident photon flux density,²⁸ η_{LHE} the light harvesting efficiency, η_{inj} is the electron injection efficiency and η_c is the electron collection efficiency. Integration was performed over the wavelength range from 400 to 1100 nm. The light harvesting efficiency is calculated from absorbance using the following relationship (6.3):

$$\eta_{LHE} = 1 - 10^{-A(\lambda)} \quad (6.3)$$

Here, $A(\lambda)$ is absorbance of PbS QDs (Figure 6.1). The theoretical short circuit currents calculated from equation (6.2), assuming that η_{inj} and η_c are unity, yielded values of 15.7 and 16.4 mA cm⁻² for C1 and C2, respectively. Although the calculated theoretical short circuit currents are similar, the experimental values for both C1 and C2 are much lower, indicating either poor injection efficiency or poor collection efficiency. The difference between the experimental short circuit currents for C1 and C2 could have two explanations. First, in the C2 cell the sizes of PbS QDs are generally smaller. This, according to Marcus theory, guarantees better injection of electrons due to larger offset of the PbS QD conduction band relative to the conduction band of TiO₂ (Figures 6.4b and 6.4d).²⁹ Second, higher photocurrents for C2 could originate from more intimate contact between the TiO₂ and the PbS QDs, facilitating better charge injection compared to C1, where there is a spacer GSH ligand between the TiO₂/PbS and PbS/HTM interfaces (cf. Figures 6.4a and 6.4c). Similar findings were reported by Yang et al.²¹ for liquid electrolyte cells in which they showed that the cells with *in situ* grown CdTe QDs deliver higher photocurrents relative to the cells with *ex situ* grown QDs.

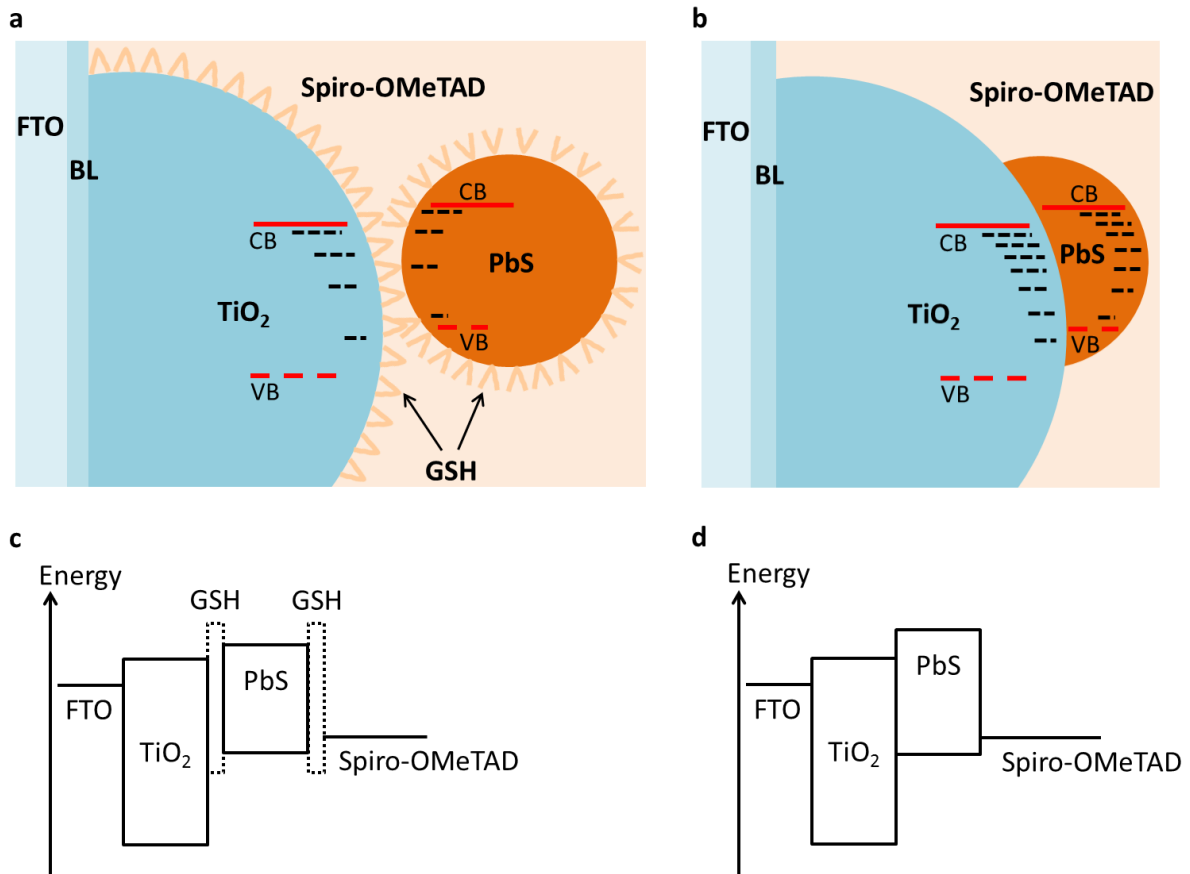


Figure 6.4. Sketch of solid-state QDSCs with (a) *ex situ* and (b) *in situ* grown PbS QDs, and respective energy diagrams (c) and (d).

The behavior of the C1 and C2 cells was studied further by analysis of the open circuit voltages obtained at different AM 1.5 G illumination intensities (Figure 6.5). The relationship between open circuit voltage and light intensity can be written as follows (6.4):³⁰

$$V_{OC} = \frac{m \cdot k_B \cdot T}{e} \ln(I_0), \quad (6.4)$$

where k_B is Boltzmann's constant, T is the temperature and e is the elementary charge, I_0 is light intensity and parameter m is an empirical non-ideality factor. The values of m for C1 and C2 obtained from a linear fit of plots of V_{OC} vs. $\ln(I_0)$ are 1.00 and 0.9 respectively. These values of m suggest that the cell C1 behaves as an ideal diode within the measurement range, whereas the cell C2 departs from ideal diode behavior. In conventional dye-sensitized solar

cells (DSCs), where $m \neq 1$, nonideal behaviour is often attributed to recombination via surface states.^{30, 31} If we assume that this also applies to QDSCs, then this could explain the difference in non-ideality factors between C1 and C2 as the former might be expected to have lower surface state densities on both the PbS QDs and the TiO₂ due to passivation by GSH ligands.^{23, 32} Passivation of surface states, and therefore, reduction of recombination at the TiO₂/PbS, PbS/HTM and TiO₂/HTM interfaces by GSH ligands is most likely responsible for the higher open circuit voltage and fill factor of the C1 compared to the C2 cell (Table 6.1).³³⁻

35

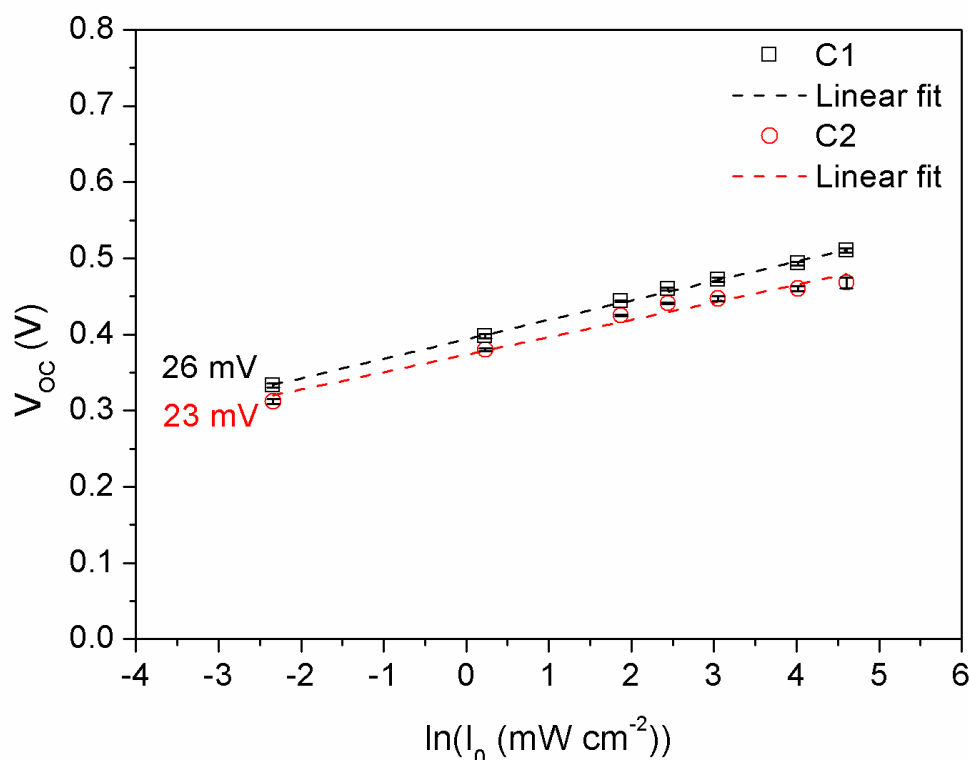


Figure 6.5. Semilogarithmic plots of open circuit voltage vs. light intensity for the C1 and C2 cells. Slopes are labelled in the graph.

In order to gain a better understanding of the charge transfer process in C1 and C2 cells, electron lifetime measurements with OCVD and IMVS techniques were performed.³⁶ The

comparison of OCVDs for C1 and C2 cells are presented in Figure 6.6a. The electron lifetimes, τ_n , were calculated for C1 and C2 from OCVD curves using the relationship (6.5):³⁷

$$\tau_n^{(OCVD)} = -\frac{k_B \cdot T}{e} \left(\frac{dV_{OC}}{dt} \right)^{-1} \quad (6.5)$$

Plots of electron lifetimes vs. V_{OC} calculated from OCVD measurements for C1 and C2 are presented in Figure 6.6b. The comparison of the lifetimes show that the τ_n vs. V_{OC} curves for both cells follow a similar trend; however, the lifetime values for C1 are about one order of magnitude higher than the values for C2, and this observation accentuates at lower voltages. A possible reason for this could be due to the role of GSH ligands acting as a spacer not only at the TiO₂/PbS interface but also at the TiO₂/HTM interface, due to co-adsorption of free GSH ligands in the QD solution onto the surface of TiO₂ via its –COO[–] carboxylic groups (Figure 6.4a).¹⁶ The inhibition of charge recombination might be due to a number of reasons. Firstly, the GSH molecular layer could create an energy barrier at the TiO₂/PbS and TiO₂/HTM interfaces, hindering the back-reaction of electrons in the conduction band of TiO₂ with holes in PbS QDs and HTM.^{24, 38} Secondly, bond formation between TiO₂ and GSH ligands may passivate the TiO₂ surface states, thus reducing recombination. This is consistent with findings of Yang and co-workers²¹ in which they also reported higher electron lifetimes for the cells with *ex situ* grown QDs compared to the ones with *in situ* grown QDs.

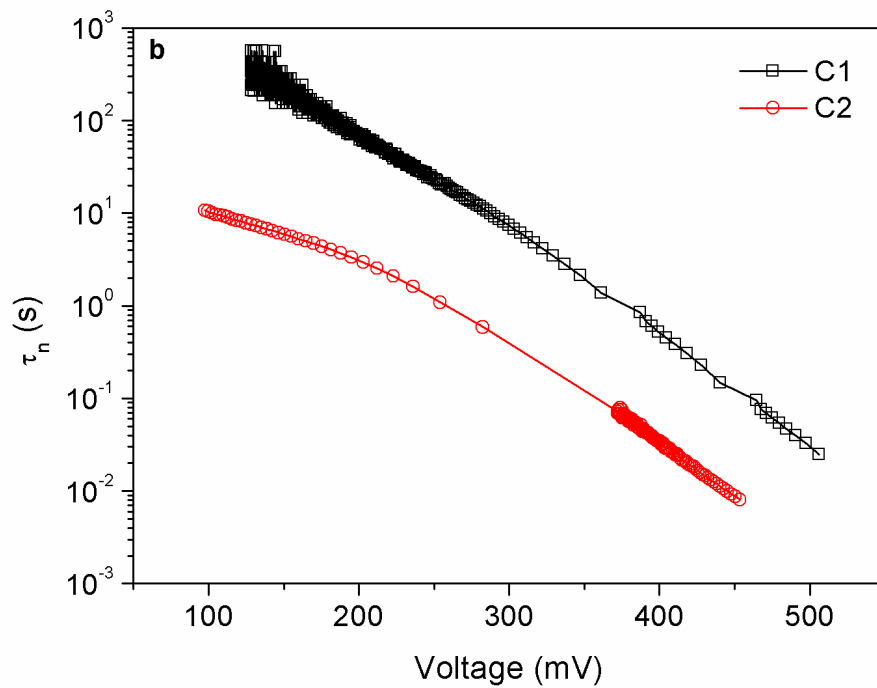
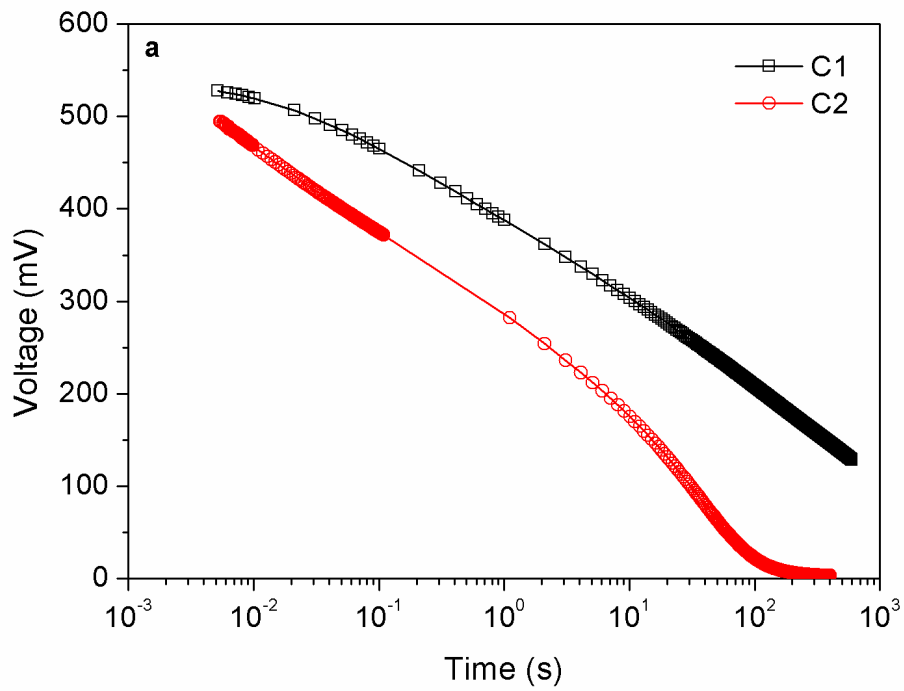


Figure 6.6. (a) OCVDs for the C1 and C2 cells; (b) Electron lifetimes for the C1 and C2 cells obtained from OCVD measurements.

It is noteworthy to mention that the open circuit voltage decay measurements were recorded in the dark. However, Shalom et al.³⁹ have suggested that the mechanisms of charge recombination can be different in QDSCs under illuminated and dark conditions. Therefore, we also studied the cells using IMVS, which allows measurement of electron lifetimes, τ_n , under illumination.^{31, 36} The frequency dependence of the normalized imaginary parts of the IMVS spectra of C1 and C2 cells obtained for open circuit conditions ranging from 100 to 500 mV are presented in Figures 6.7a and 6.7b. The values of the frequency at maxima, f_{max} , of the spectra were used to calculate the electron lifetimes using the relationship (6.6):³⁶

$$\tau_n^{(IMVS)} = \frac{1}{2\pi \cdot f_{max}} \quad (6.6)$$

The values of τ_n vs. V_{OC} for C1 and C2 obtained from IMVS measurements are also plotted in Figure 6.7c (solid lines with open symbols) superimposed with the electron lifetimes obtained from OCVD measurements (solid and dashed lines) for the sake of comparison. The comparison of $\tau_n^{(OCVD)}$ and $\tau_n^{(IMVS)}$ for C1 and C2 cells shows that there is a good agreement, particularly for C1, between these two techniques. However, below 250 mV for C2 electron lifetimes obtained from the OCVD measurements fall below those obtained by IMVS.

The higher values of electron lifetimes for C2 obtained by IMVS relative to OCVD below 250 mV could possibly originate from charging of the PbS QDs leading to an upward movement of the Fermi level of PbS QDs, under constant background illumination in the IMVS measurements.³⁹ This may reduce the loss of electrons in the conduction band of TiO₂ to the trap states of PbS QDs.³³⁻³⁵ The more or less pronounced deflection of $\tau_n^{(IMVS)}$ from $\tau_n^{(OCVD)}$ below 250 mV for C1 compared to C2 could be due to the layer of GSH ligands which acts as an energy barrier layer. Such a barrier layer would hinder the back-reaction of electrons in the conduction band of TiO₂ and FTO with holes in the PbS QDs and HTM via TiO₂ surface trap states and, most importantly, via the TiO₂ blocking layer.^{34, 40} The GSH ligands may also

reduce the density of TiO_2 surface states by forming covalent bonds between GSH ligands and TiO_2 , thus reducing the number of dangling bonds on the surface of TiO_2 NPs.

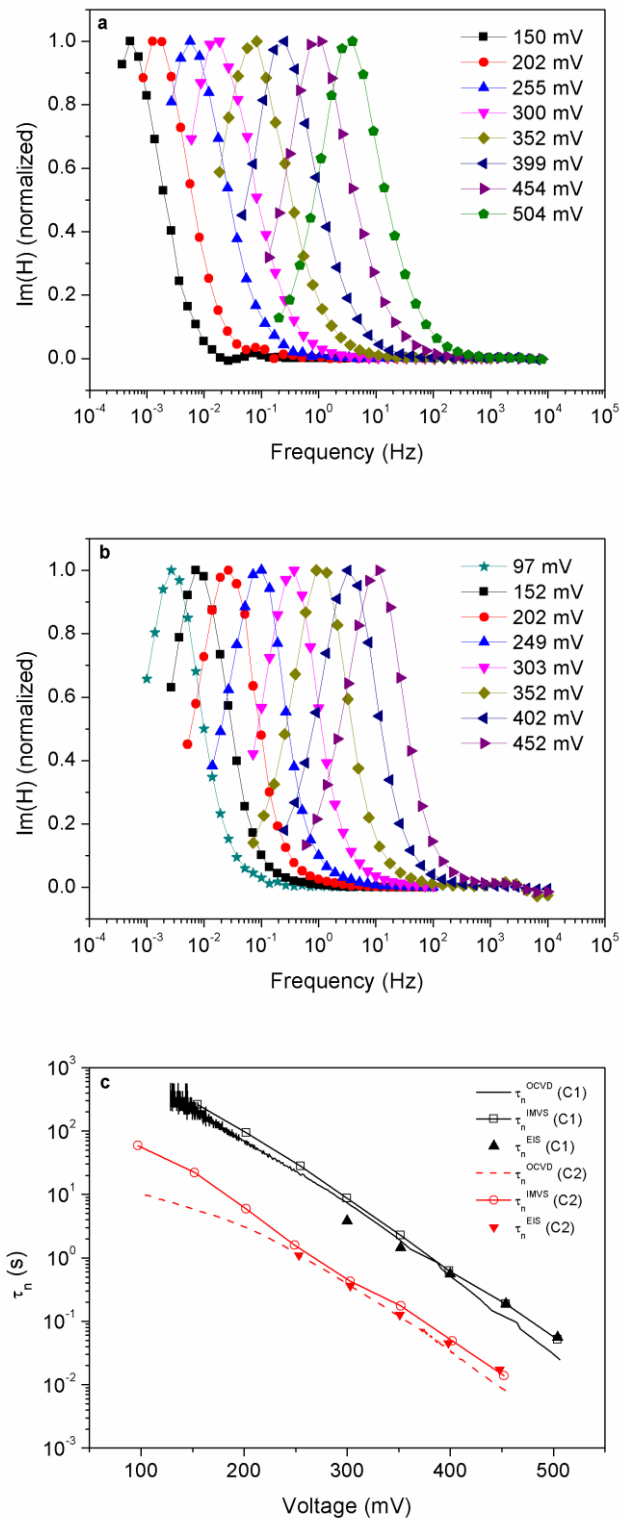


Figure 6.7. (a) and (b) are frequency dependence of normalized imaginary parts of the IMVS spectra for the C1 and C2 cells respectively; (c) Electron lifetimes for the C1 and C2 cells obtained from OCVD, IMVS and EIS measurements.

To study processes taking place in the cells, impedance spectroscopy measurements were performed on C1 and C2 cells as well as on additional blank cells (cells without the QD absorber layer) with (cell C3) and without (cell C4) a GSH layer between the TiO₂ electrode and the spiro-OMeTAD HTM. The impedance data were analysed using the ZView software with a model proposed by Dualeh et al.⁴¹ (Figure 6.8).

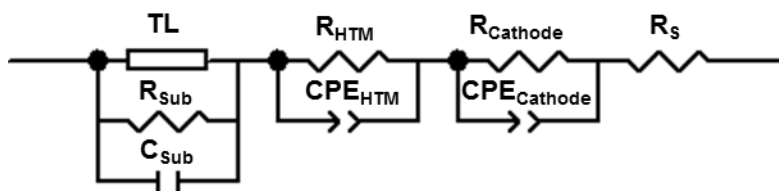


Figure 6.8. Equivalent circuit used to fit experimental impedance spectra of the cells.

In the model, a transmission line (TL) together with R_{sub} and C_{sub} represent the photoanode, R_{HTM} and CPE_{HTM} represent spiro-OMeTAD, and $R_{cathode}$, $CPE_{cathode}$ and R_s represent counter electrode and series resistance, respectively. The signature of the R_{sub} and C_{sub} circuit was not significant and therefore was omitted in the equivalent circuit which was used to fit the experimental impedance data. Impedance spectra of the cells C1 and C2 were recorded at different intensities of LED irradiation at open-circuit conditions, whereas for cells C3 and C4 impedance spectra were recorded in the dark at different applied DC potentials. Bode plots of impedance spectra of the cells are presented in Figures 6.9a – 6.9d. The parameters of the elements of the circuit obtained from fitting the experimental spectra for different voltages are presented in Table A-3.3 in Appendix.

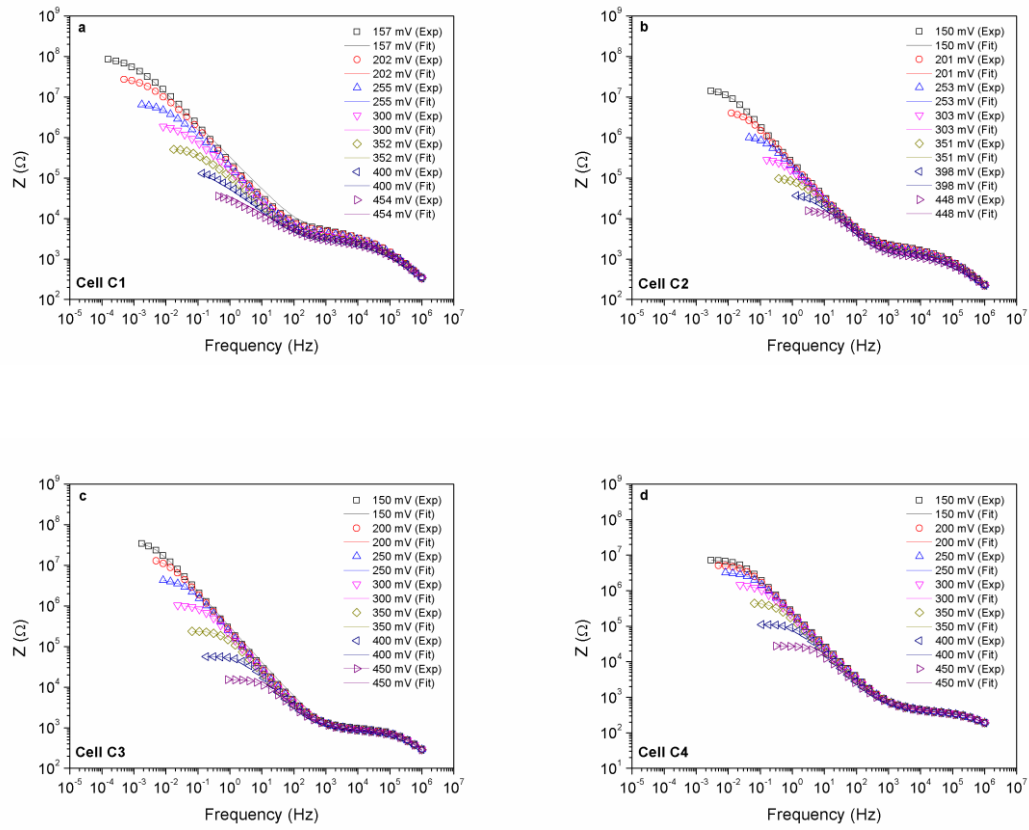


Figure 6.9. Bode plots of impedance spectra of (a) C1, (b) C2, (c) C3 and (d) C4 under different open circuit conditions.

The voltage dependence of the values of chemical capacitance, C_{μ} , and recombination resistance, R_{ct} , for C1-C4 cells extracted from fitting the experimental data is shown in Figures 6.10a and 6.10b.

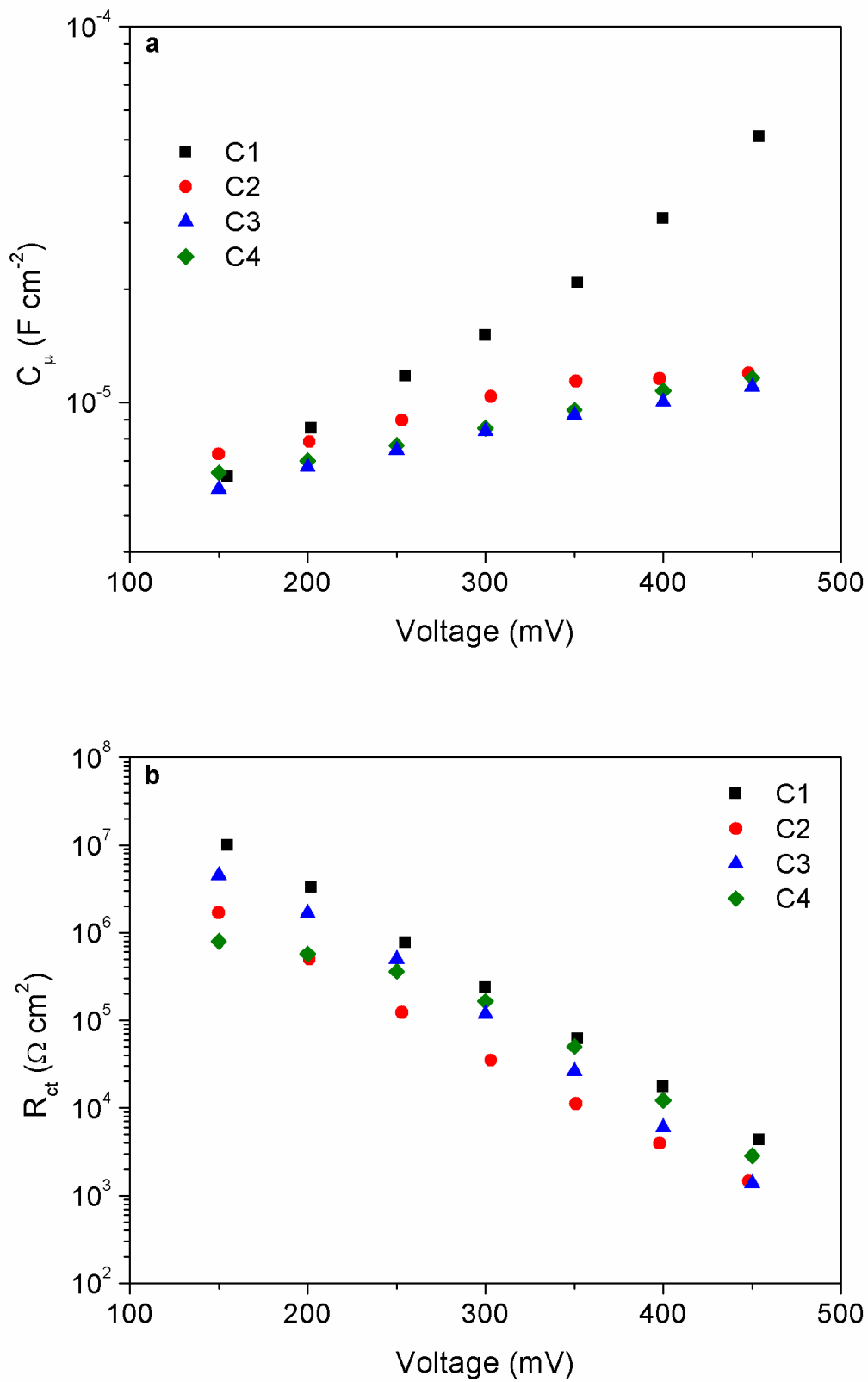


Figure 6.10. Results from impedance measurements. Voltage dependence of (a) chemical capacitance and (b) recombination resistance for C1-C4 cells.

The analysis of the impedance data shows that chemical capacitance, C_{μ} , of cells C2, C3 and C4 stay the same. This indicates that the functionalization of the TiO₂ surface with GSH ligands or sensitization with *in situ* grown PbS QDs have little influence on the conduction band tail of the TiO₂ electrode. Chemical capacitance of cell C1, on the other hand, becomes slightly larger at higher voltages compared to C2, C3 and C4. Since comparison of the chemical capacitances of C3 and C4 shows that GSH ligands have no effect on the conduction band tail change of TiO₂, it can be assumed that the relative large magnitude of C_{μ} for C1 is associated with the nature of *ex situ* grown QDs. As was mentioned above, the GSH ligand layer around *ex situ* grown QDs may act as energetic barrier between TiO₂ and PbS QDs, limiting charge injection from QDs into TiO₂. Therefore, the large magnitude of C_{μ} could be due to charge accumulation not only in TiO₂ but also due to additional charge accumulated in the QDs.³⁴

The recombination resistance plot shows that the magnitude of R_{ct} for C1 is significantly larger compared C2 throughout the entire measurement range. The observed increase in recombination resistance for C1 can be attributed to the hindrance of back-reaction of electrons in the conduction band of TiO₂ with holes in PbS QDs and HTM, due to the GSH barrier layer separating QDs and HTM from TiO₂. The GSH ligand layer around *ex situ* grown PbS QDs also passivates the surface trap states, suppressing electron back transfer at the PbS/HTM interface as well.^{34, 42} Comparison of R_{ct} for C3 and C4 shows that below 250 mV for the blank GSH-functionalized cell (C3) the resistance between TiO₂ and spiro-OMeTAD becomes significantly larger compared with the cell without GSH-functionalization (C4). This could be due to suppression of recombination path via the substrate and, possibly, via TiO₂ surface states.⁴⁰ Above 250 mV, the values for R_{ct} for C3 is slightly lower than for C4. This is possibly caused by slight differences in HTM infiltration due to changes in wettability of TiO₂ after GSH-functionalization. Overall, comparison of R_{ct} for the cells C1, C2, C3 and C4

suggests that the GSH ligand acts as a resistive barrier layer for electrons, and that this effect is more pronounced at lower voltages. Electron lifetimes, τ_n , for C1 and C2 around the maximum power points were also calculated (Figure 6.7c) from the results of impedance measurements based on the model proposed by Bisquert et al.,^{37, 43, 44} by using the relationship $\tau_n^{EIS} = R_{ct} \times C_{\mu}$.⁴⁴⁻⁴⁶ Comparison of electron lifetimes for C1 and C2 cells shows excellent agreement between values of τ_n obtained by the three different techniques.

6.3 Conclusions

In summary, solid-state QDSCs were sensitized with *ex situ* and *in situ* grown PbS QDs and assembled with a spiro-OMeTAD hole transporter. The performances of the devices were characterised with I-V and IPCE measurements, and the *in situ* method was shown to produce higher efficiency cells. A relatively high value of short circuit current for C2 is attributed to more intimate contact between TiO₂ and PbS QDs as well as PbS QDs and spiro-OMeTAD HTM. The comparison of theoretical short circuit currents with experimental ones showed that there is plenty of room for improvement in order to realize the full potential of the devices. Analysis of electron lifetimes with OCVD measurements shows that the cell C2 suffers from recombination losses. This is also supported by relatively low values of fill factor and open circuit voltage for the device compared to C1. Analysis of OCVD and IMVS measurements show that there is a significant difference in electron lifetimes for C2 at lower voltages when measured in the dark and under illumination. We attributed this difference to an upward movement of Fermi level of PbS QDs under illumination and, therefore, to a different scenario for conduction band electron relaxation.³⁹ All four types of solar cells (C1-C4) were studied with impedance spectroscopy measurements. Analysis of the impedance spectroscopy data shows that adsorbed GSH ligands form an energetic insulating barrier layer

at the interface of TiO₂/QDs, TiO₂/HTM and QD/HTM, thus reducing recombination losses via back-reaction of charge carriers. The relatively large value of chemical capacitance for C1 is attributed to additional charge accumulation in *ex situ* grown PbS QDs due to the insulating effect of GSH ligand around the QDs. Based on the significant improvement of electron lifetimes observed for the cells prepared by the *ex situ* method compared to their *in situ* counterparts, we conclude that GSH ligands play an important role in surface passivation of PbS QDs and possibly TiO₂ trap states, forming an energy barrier layer at the TiO₂/PbS, TiO₂/HTM and PbS/HTM interfaces.^{24, 38} However, this improvement in electron lifetimes for C1 comes at the expense of the short circuit current, as GSH ligands hinder the charge injection and separation in the photo-excited PbS QDs.²¹ If an energy barrier layer could be placed selectively at the interface of bare parts of TiO₂ and HTM, the fabrication of high performance cells with SILAR grown PbS QDs should be possible, provided that good protection of PbS QDs from oxidation is established.^{23, 24, 38, 47}

6.4 Experimental Section

6.4.1 Materials

Oleic acid (Sigma-Aldrich), lead(II) oxide (Sigma-Aldrich), hexamethyldisilathiane (Sigma-Aldrich), 1-octadecene (Sigma-Aldrich), chloroform (Merck), toluene (Sigma-Aldrich), sodium hydroxide (Sigma-Aldrich), titanium(IV) ethoxide (Alfa Aesar), titanium(IV) chloride (Sigma-Aldrich), hydrochloric acid 37% (Sigma-Aldrich), ammonia 28% (Sigma-Aldrich), hydrogen peroxide (Sigma-Aldrich), ethyl cellulose (Fluka), terpineol (Fluka), ethanol (Sigma-Aldrich), methanol (Sigma-Aldrich), L-glutathione (Sigma-Aldrich), lead(II) nitrate (Sigma-Aldrich), sodium sulfite (Alfa Aesar), spiro-OMeTAD (Merck), 4-*tert*-butylpyridine

(Sigma-Aldrich), bis(trifluoromethane)sulfonimide lithium salt (Sigma-Aldrich), chlorobenzene (Sigma-Aldrich), acetonitrile (Sigma-Aldrich).

6.4.2 Preparation of Colloidal QDs

PbS QDs capped with oleic acid were synthesized as described by Tang et al.⁴⁸ (cf. subsection A-5 in Appendix), and water-solubilized PbS QDs capped with GSH were obtained by a ligand exchange procedure as described by Deng et al.⁴⁹ (cf. subsection A-6 in Appendix).

6.4.3 Preparation of TiO₂ Electrodes

TiO₂ NPs sized ~30 nm were synthesized according to Baek et al.⁵⁰ (cf. subsection A-13 in Appendix) and were used to prepare the TiO₂ paste as described by Ito et al.^{51, 52} (cf. subsection A-14 in Appendix). The resulting paste was deposited by spin-coating onto FTO (Pilkington, TEC7) glass substrates (1.5×2 cm²) pre-coated with a compact TiO₂ blocking layer (cf. subsection A-4 in Appendix).^{53, 54} Two layers of TiO₂ paste were deposited with intermediate drying at 100 °C for 30 min in order to increase the thickness of the electrodes. The films were then calcined in air at 500 °C for 30 min to obtain mesoporous TiO₂ electrodes. Finally, the electrodes were subjected to a 40 mM aqueous TiCl₄ treatment at 70 °C for 30 min (10 mL per electrode) and annealing at 500 °C for 30 min in air.

6.4.4 Estimation of Roughness Factor

A mesoporous TiO₂ electrode with 3.0±0.1 μm thickness and effective (geometrical) area of 0.4 cm² was immersed overnight into 10 mL of a 0.5 mM N719 dye solution dissolved in (1:1) acetonitrile/*tert*-butanol. Then the electrode was removed from the dye solution and immersed into 10 mL of pure acetonitrile for 10 min to wash away unattached N719 dye molecules. The cleaned electrode was dried with a stream of nitrogen and immersed into 3 mL of a 0.1 M solution of KOH in (1:1) ethanol/water solution for 1-2 min. The clean mesoporous TiO₂ electrode was then removed from the solution vial and the UV-VIS spectrum of the solution was analysed in order to determine the total number of desorbed dye molecules (cf. Figure A-12.1 in Appendix). The roughness factor, A_R , was obtained as the ratio of total ‘footprint’ of the dye molecules to the effective area of the electrode (**):^{25, 55}

$$A_R = \frac{N_{dye} \times a_{dye}}{0.4}, \quad (**)$$

where, N_{dye} is the number of dye molecules and a_{dye} is the ‘footprint’ of a single dye molecule (1.36×10^{-14} cm²), assuming monolayer coverage.

6.4.5 Fabrication of Solar Cells

Mesoporous TiO₂ electrodes (1.5×1 cm²) were sensitized with *ex situ* and *in situ* grown PbS QDs. For sensitization with *ex situ* grown QDs, the mesoporous TiO₂ electrodes were immersed for ~18 h in 10 mL of a 3 mM aqueous solution of PbS-GSH QD. Then the sensitized electrodes were immersed in 10 mL of deionized water for 10 min to rinse away

unattached QDs and excess GSH ligands.⁵⁶ Sensitization with *in situ* grown QDs was carried out by the conventional SILAR process.⁶ Five and half cycles of SILAR were performed to sensitize the mesoporous TiO₂ electrodes using 0.02 M solutions of Pb(NO₃)₂ and Na₂S in methanol (usually 10 mL) as precursors. 40 μ L of 15 vol.% spiro-OMeTAD in chloroform with 10 mM bis(trifluoromethane)sulfonimide lithium salt and 5.5 mM 4-*tert*-butylpyridine additives were spin-coated onto the sensitized electrodes at 2000 rpm for 30 sec.^{8, 57-59} 100 nm silver contacts were then deposited via evaporation onto the substrates through a mask using a Univex 350 sputter system (Oerlikon Leybold). Blank cells with and without GSH layers were also prepared as described above by immersing the mesoporous electrodes in 0.15 M aqueous solution (usually 10 mL) of GSH in step one instead of 3 mM PbS-GSH quantum dots.

6.4.6 Characterization Methods

The structure and phase of the porous TiO₂ films were characterized by wide angle XRD using a Bruker D8 Discover diffractometer with Cu-K α radiation ($\lambda = 1.5418 \text{ \AA}$) and equipped with a LynxEye position sensitive detector. Average film thickness values were measured with a Dektak150 profilometer. Absorbance spectra of the N719 dye- and PbS QD-sensitized TiO₂ electrodes were recorded using a UV-Vis-NIR spectrophotometer (model: Lambda 1050, Perkin Elmer) and were corrected for the absorbance of the TiO₂ electrodes. The absorbance spectra of the QD-sensitized electrodes were measured with a 0.16 cm² mask. The cross-section SEM image and EDX chemical mapping of the solid-state QDSC was obtained using a JEOL-JSM-6500F SEM equipped with a 4 kV field emission gun. HRTEM and STEM analyses of the PbS QD-sensitized TiO₂ samples were performed using an FEI TITAN 80-300 TEM equipped with a field emission gun operating at 300 kV. The I-V characteristics

of the solid-state QDSCs were measured under simulated solar light using a 300 W xenon lamp equipped with an AM 1.5 G filter at an irradiance of 100 mW cm^{-2} (XPS 400, Solar Light Company Inc.). The I-V characteristics were recorded using a Keithley 2400 source meter with 0.11 cm^2 active cell area. The IPCE spectra of the cells were measured using chopped monochromatic light provided by a 150 W xenon lamp (Lot-Oriel) and monochromator (Micro HR) with order sorting filters (Thorlabs). Measurements were done with biased light intensity (11.5 mW cm^{-2}), and the signal was detected by a DSP lock-in amplifier (model: 7230, Signal Recovery). The IPCE data were recorded using the Keithley 2400 source meter. OCVD, IMVS and EIS data were obtained using a potentiostat equipped with a frequency response analyzer (model: PGSTAT302N, Autolab, Metrohm) and LED driver. IMVS measurements of C1 (cell with *ex situ* grown sensitizer) and C2 (cell with *in situ* grown sensitizer) were carried out under cool white LED (model: LDCCW, Metrohm) irradiation at open-circuit conditions over the frequency range from 10 kHz to 0.1 mHz. Different open-circuit voltages were obtained by changing the intensity of the LED irradiation using neutral density filters. The amplitude of the AC modulation current was 10% of the DC current applied to the LED. EIS measurements of C1 and C2 cells were carried out under cool white LED illumination at open-circuit conditions, whereas EIS of blank cells C3 (with GSH layer) and C4 (without GSH layer) were measured in the dark. The frequency range of AC modulation voltage was varied between 1 MHz and 0.1 mHz. The amplitude of AC modulation voltage was kept at 10% of the open-circuit voltage in case of C1 and C2 and at 10% of the DC voltage applied to the cells in case of C3 and C4.

References

1. H. Lee, M. Wang, P. Chen, D. R. Gamelin, S. M. Zakeeruddin, M. Grätzel and M. K. Nazeeruddin, *Nano Letters*, 2009, **9**, 4221-4227.
2. S.-J. Moon, Y. Itzhaik, J.-H. Yum, S. M. Zakeeruddin, G. Hodes and M. Grätzel, *The Journal of Physical Chemistry Letters*, 2010, **1**, 1524-1527.
3. J. A. Chang, J. H. Rhee, S. H. Im, Y. H. Lee, H.-j. Kim, S. I. Seok, M. K. Nazeeruddin and M. Gratzel, *Nano Letters*, 2010, **10**, 2609-2612.
4. R. Plass, S. Pelet, J. Krueger, M. Grätzel and U. Bach, *The Journal of Physical Chemistry B*, 2002, **106**, 7578-7580.
5. R. Bayón, R. Musembi, A. Belaidi, M. Bär, T. Guminskaya, C. H. Fischer, M. C. Lux-Steiner and T. Dittrich, *Comptes Rendus Chimie*, 2006, **9**, 730-734.
6. H. Lee, H. C. Leventis, S.-J. Moon, P. Chen, S. Ito, S. A. Haque, T. Torres, F. Nüesch, T. Geiger, S. M. Zakeeruddin, M. Grätzel and M. K. Nazeeruddin, *Advanced Functional Materials*, 2009, **19**, 2735-2742.
7. A. Guchhait, A. K. Rath and A. J. Pal, *Applied Physics Letters*, 2010, **96**, 073505-073503.
8. H. J. Snaith, A. Stavrinnadis, P. Docampo and A. A. R. Watt, *Solar Energy*, 2011, **85**, 1283-1290.
9. S. Kim, S. H. Im, M. Kang, J. H. Heo, S. I. Seok, S.-W. Kim, I. Mora-Seró and J. Bisquert, *Physical Chemistry Chemical Physics*, 2012, **14**, 14999-15002.
10. S. H. Im, C.-S. Lim, J. A. Chang, Y. H. Lee, N. Maiti, H.-J. Kim, M. K. Nazeeruddin, M. Grätzel and S. I. Seok, *Nano Letters*, 2011, **11**, 4789-4793.
11. H. Rahnamai, H. J. Gray and J. N. Zemel, *Thin Solid Films*, 1980, **69**, 347-350.
12. R. Vogel, P. Hoyer and H. Weller, *The Journal of Physical Chemistry*, 1994, **98**, 3183-3188.

13. I. Kaiser, K. Ernst, C. H. Fischer, R. Könenkamp, C. Rost, I. Sieber and M. C. Lux-Steiner, *Solar Energy Materials and Solar Cells*, 2001, **67**, 89-96.
14. A. Zaban, O. I. Mičić, B. A. Gregg and A. J. Nozik, *Langmuir*, 1998, **14**, 3153-3156.
15. P. Yu, K. Zhu, A. G. Norman, S. Ferrere, A. J. Frank and A. J. Nozik, *The Journal of Physical Chemistry B*, 2006, **110**, 25451-25454.
16. I. Robel, V. Subramanian, M. Kuno and P. V. Kamat, *Journal of the American Chemical Society*, 2006, **128**, 2385-2393.
17. B.-R. Hyun, Y.-W. Zhong, A. C. Bartnik, L. Sun, H. D. Abruña, F. W. Wise, J. D. Goodreau, J. R. Matthews, T. M. Leslie and N. F. Borrelli, *ACS Nano*, 2008, **2**, 2206-2212.
18. H. Zhang, K. Cheng, Y. M. Hou, Z. Fang, Z. X. Pan, W. J. Wu, J. L. Hua and X. H. Zhong, *Chemical Communications*, 2012, **48**, 11235-11237.
19. N. J. Smith, K. J. Emmett and S. J. Rosenthal, *Applied Physics Letters*, 2008, **93**, 043504-043503.
20. N. Parsi Benekohal, V. González-Pedro, P. P. Boix, S. Chavhan, R. Tena-Zaera, G. P. Demopoulos and I. Mora-Seró, *The Journal of Physical Chemistry C*, 2012, **116**, 16391-16397.
21. H. Yang, W. Fan, A. Vaneski, A. S. Susa, W. Y. Teoh and A. L. Rogach, *Advanced Functional Materials*, 2012, **22**, 2821-2829.
22. L. Tao, Y. Xiong, H. Liu and W. Shen, *Nanoscale*, 2014, **6**, 931-938.
23. A. H. Ip, S. M. Thon, S. Hoogland, O. Voznyy, D. Zhitomirsky, R. Debnath, L. Levina, L. R. Rollny, G. H. Carey, A. Fischer, K. W. Kemp, I. J. Kramer, Z. Ning, A. J. Labelle, K. W. Chou, A. Amassian and E. H. Sargent, *Nature Nanotechnol.*, 2012, **7**, 577-582.
24. Z. Tachan, I. Hod, M. Shalom, L. Grinis and A. Zaban, *Physical Chemistry Chemical Physics*, 2013, **15**, 3841-3845.

25. A. G. Agrios and A. Hagfeldt, *The Journal of Physical Chemistry C*, 2008, **112**, 10021-10026.
26. I. Moreels, K. Lambert, D. Smeets, D. De Muynck, T. Nollet, J. C. Martins, F. Vanhaecke, A. Vantomme, C. Delerue, G. Allan and Z. Hens, *ACS Nano*, 2009, **3**, 3023-3030.
27. Z. Yang, C.-Y. Chen, P. Roy and H.-T. Chang, *Chemical Communications*, 2011, **47**, 9561-9571.
28. Reference Solar Spectral Irradiance: ASTM G-173, <http://rredc.nrel.gov/solar/spectra/am1.5/ASTMG173/ASTMG173.html>, 2013.
29. R. A. Marcus, *The Journal of Chemical Physics*, 1965, **43**, 679-701.
30. A. B. Walker, L. M. Peter, K. Lobato and P. J. Cameron, *The Journal of Physical Chemistry B*, 2006, **110**, 25504-25507.
31. E. Guillén, L. M. Peter and J. A. Anta, *The Journal of Physical Chemistry C*, 2011, **115**, 22622-22632.
32. D. A. Hines and P. V. Kamat, *The Journal of Physical Chemistry C*, 2013, **117**, 14418-14426.
33. M. S. de la Fuente, R. S. Sánchez, V. González-Pedro, P. P. Boix, S. G. Mhaisalkar, M. E. Rincón, J. Bisquert and I. Mora-Seró, *The Journal of Physical Chemistry Letters*, 2013, **4**, 1519-1525.
34. I. Hod, V. González-Pedro, Z. Tachan, F. Fabregat-Santiago, I. Mora-Seró, J. Bisquert and A. Zaban, *The Journal of Physical Chemistry Letters*, 2011, **2**, 3032-3035.
35. B. Ehrler, K. P. Musselman, M. L. Böhm, F. S. F. Morgenstern, Y. Vaynzof, B. J. Walker, J. L. MacManus-Driscoll and N. C. Greenham, *ACS Nano*, 2013, **7**, 4210-4220.
36. P. J. Cameron and L. M. Peter, *The Journal of Physical Chemistry B*, 2005, **109**, 7392-7398.

37. J. Bisquert, F. Fabregat-Santiago, I. Mora-Seró, G. Garcia-Belmonte and S. Giménez, *The Journal of Physical Chemistry C*, 2009, **113**, 17278-17290.
38. T. P. Brennan, O. Trejo, K. E. Roelofs, J. Xu, F. B. Prinz and S. F. Bent, *Journal of Materials Chemistry A*, 2013, **1**, 7566-7571.
39. M. Shalom, Z. Tachan, Y. Bouhadana, H.-N. Barad and A. Zaban, *The Journal of Physical Chemistry Letters*, 2011, **2**, 1998-2003.
40. S. Rühle, S. Yahav, S. Greenwald and A. Zaban, *The Journal of Physical Chemistry C*, 2012, **116**, 17473-17478.
41. A. Dualeh, T. Moehl, M. K. Nazeeruddin and M. Grätzel, *ACS Nano*, 2013, **7**, 2292-2301.
42. Z. Pan, I. Mora-Seró, Q. Shen, H. Zhang, Y. Li, K. Zhao, J. Wang, X. Zhong and J. Bisquert, *Journal of the American Chemical Society*, 2014, **136**, 9203-9210.
43. F. Fabregat-Santiago, J. Bisquert, L. Cevey, P. Chen, M. Wang, S. M. Zakeeruddin and M. Grätzel, *Journal of the American Chemical Society*, 2009, **131**, 558-562.
44. F. Fabregat-Santiago, G. Garcia-Belmonte, I. Mora-Seró and J. Bisquert, *Physical Chemistry Chemical Physics*, 2011, **13**, 9083-9118.
45. I. Mora-Seró, S. Giménez, F. Fabregat-Santiago, R. Gómez, Q. Shen, T. Toyoda and J. Bisquert, *Accounts of Chemical Research*, 2009, **42**, 1848-1857.
46. V. González-Pedro, X. Xu, I. Mora-Seró and J. Bisquert, *ACS Nano*, 2010, **4**, 5783-5790.
47. J. Tang, L. Brzozowski, D. A. R. Barkhouse, X. Wang, R. Debnath, R. Wolowiec, E. Palmiano, L. Levina, A. G. Pattantyus-Abraham, D. Jamakosmanovic and E. H. Sargent, *ACS Nano*, 2010, **4**, 869-878.
48. J. Tang, K. W. Kemp, S. Hoogland, K. S. Jeong, H. Liu, L. Levina, M. Furukawa, X. Wang, R. Debnath, D. Cha, K. W. Chou, A. Fischer, A. Amassian, J. B. Asbury and E. H. Sargent, *Nature Materials*, 2011, **10**, 765-771.

49. D. Deng, J. Xia, J. Cao, L. Qu, J. Tian, Z. Qian, Y. Gu and Z. Gu, *Journal of Colloid and Interface Science*, 2012, **367**, 234-240.
50. I. C. Baek, M. Vithal, J. A. Chang, J.-H. Yum, M. K. Nazeeruddin, M. Grätzel, Y.-C. Chung and S. I. Seok, *Electrochemistry Communications*, 2009, **11**, 909-912.
51. S. Ito, P. Chen, P. Comte, M. K. Nazeeruddin, P. Liska, P. Péchy and M. Grätzel, *Progress in Photovoltaics: Research and Applications*, 2007, **15**, 603-612.
52. S. Ito, T. N. Murakami, P. Comte, P. Liska, C. Grätzel, M. K. Nazeeruddin and M. Grätzel, *Thin Solid Films*, 2008, **516**, 4613-4619.
53. L. Kavan and M. Grätzel, *Electrochimica Acta*, 1995, **40**, 643-652.
54. P. J. Cameron and L. M. Peter, *The Journal of Physical Chemistry B*, 2003, **107**, 14394-14400.
55. G. Boschloo and A. Hagfeldt, *The Journal of Physical Chemistry B*, 2005, **109**, 12093-12098.
56. A. N. Jumabekov, F. Deschler, D. Böhm, L. M. Peter, J. Feldmann and T. Bein, *The Journal of Physical Chemistry C*, 2014, **118**, 5142-5149.
57. P. Docampo, S. Guldin, M. Stefiik, P. Tiwana, M. C. Orilall, S. Hüttner, H. Sai, U. Wiesner, U. Steiner and H. J. Snaith, *Advanced Functional Materials*, 2010, **20**, 1787-1796.
58. A. Abate, T. Leijtens, S. Pathak, J. Teuscher, R. Avolio, M. E. Errico, J. Kirkpatrick, J. M. Ball, P. Docampo, I. McPherson and H. J. Snaith, *Physical Chemistry Chemical Physics*, 2013, **15**, 2572-2579.
59. P. Docampo and H. J. Snaith, *Nanotechnology*, 2011, **22**, 225403.

7 Effect of L-Glutathione and Iodide Passivation on the Performance of PbS Quantum-Dot-Sensitized Solar Cells

The results described in this chapter were partially obtained with the help of the research trainee (Forschungspraktikant) BSc. Niklas Cordes.

Abstract

The effect of surface passivation of PbS QDs with the tripeptide L-glutathione (GSH) and with iodide anion (I⁻) on the solar cell performance of solid-state PbS quantum-dot-sensitized solar cells with spiro-OMeTAD hole transporter was investigated. An enhancement in short circuit currents of the cells for both types of passivation was demonstrated, and it was attributed to improved charge injection from PbS QDs into the conduction band of TiO₂. Moreover, a significant improvement in the power conversion efficiency of the cells with GSH-passivation was attributed to a suppression of surface state-mediated charge recombination in PbS QDs. The cells were characterized by current-voltage and incident-photon-to-collected-electron efficiency measurements. The electron lifetimes were determined with intensity-modulated photovoltage spectroscopy and open circuit photovoltage decay. The electron lifetime measurements show that the reference and GSH-passivated cells have similar kinetics for the loss of electrons from the TiO₂ by transfer to the hole transport layer, whereas for iodide-passivated cells electron transfer is faster relative to the reference cell.

7.1 Introduction

Interest in quantum dot-sensitized solar cells (QDSCs) - particularly those sensitized with PbS quantum dots (QDs) and utilizing both liquid and solid hole mediators - has increased substantially over the past few years due to their size-dependent tunable bandgap, high absorption coefficient and the possibility to generate and split multiple excitons.¹⁻⁷ The efficiencies of PbS QDSCs have reached values as high as 5.7% and 3.3% for devices with liquid (polysulfide electrolyte) and solid (P3HT, poly-3-hexyl-thiophene) hole mediators, respectively.^{8, 9} However, these values are still smaller by at least a factor of two than the efficiencies of dye-sensitized solar cells (DSCs).^{10, 11} One of the major performance-limiting factors in QDSCs compared to DSCs is the presence of sub-bandgap states in QDs originating from defect sites and surface states formed by surface oxidation or corrosion.^{12, 13} These sub-band states may hinder charge injection and separation processes in QDSCs and also act as recombination centers, causing a significant deterioration of device performance.^{14, 15}

The surface treatment of QDs with different inorganic and organic agents has been shown to passivate the sub-bandgap states effectively.^{13, 16, 17} For instance, Tachan et al.¹⁷ recently showed that the deposition of a thin MgO layer onto QD-sensitized porous TiO₂ electrodes helps to increase the short circuit current and open circuit voltage. In their report, the authors stress the importance of tuning the interface between the QDs and the metal oxide (MO) in order to improve efficiencies.¹⁷ Another recent report by Brennan et al.¹⁸ describes the use of an ultrathin alumina barrier layer in a solid-state PbS quantum dot-sensitized solar cell, resulting in an enhanced efficiency of 0.57%. Related studies were also reported by de la Fuente et al.,¹⁹ who explored the effect of a range of surface-adsorbed species including dimethylamine, ethanedithiol, hexadecyl trimethylammonium chloride and

tetrabutylammonium iodide on the performance of QDSCs with polysulfide electrolyte. It is clear that a better understanding of the surface properties of QDs and of the interfaces between QDs, electron acceptor and electron donor materials is crucial for the fabrication of efficient QDSCs.

Here we report the use of L-glutathione (GSH) and iodide anions (I⁻) as passivation agents for PbS QD-sensitized mesoporous TiO₂ electrodes, aimed at understanding the impact of passivation on the performance of solid-state QDSCs with spiro-OMeTAD (2,2',7,7'-tetrakis(N,N-di-methoxy-phenylamine)-9,9'-spiro bifluorene) acting as hole transporter (Figures 7.1a and 7.5a). The GSH ligand is particularly interesting because it is able to coordinate both with the PbS QDs via the SH group and with the TiO₂ surface via the COOH group.^{20, 21} Passivation of the Pb²⁺ terminated PbS QDs with iodide anions, on the other hand, could be favorable for the protection against oxidation of the QDs in comparison with bulky organic or thick inorganic passivation layers.^{18, 22, 23} Iodide anions are expected to provide a very thin atomic layer coverage of PbS QDs, which could improve the escape of holes from the QD into redox electrolyte.^{19, 24}

We found that the passivation of PbS QD-sensitized mesoporous TiO₂ electrodes with GSH and iodide anions significantly improves the short circuit current compared to reference, unpassivated cells. However, we also noticed that passivation with iodide anions increases recombination of charge carriers, thus resulting in reduced open circuit voltages for iodide-treated cells. Intensity-modulated photovoltage spectroscopy (IMVS) measurements and open circuit photovoltage decay (OCVD) showed that the electron lifetimes for GSH-passivated and unpassivated cells are similar, whereas iodide-passivated cells have lower electron lifetimes than the reference unpassivated cells.

7.2 Results and Discussion

7.2.1 GSH-Passivation

Mesoporous TiO₂ anatase electrodes (cf. Figure A-1.4 in Appendix) with 3±0.1 μm thickness were deposited onto fluorine-doped tin oxide glass substrates (FTO, Pilkington, TEC7) pre-coated with a compact TiO₂ blocking layer (BL). The anatase electrodes were sensitized with PbS QDs grown by the successive ion layer adsorption/reaction (SILAR) method.⁴ 5.5 SILAR cycles were performed to sensitize the electrodes, resulting in PbS QDs with a Pb²⁺ terminated surface deposited onto walls of mesoporous TiO₂. One half of the sensitized mesoporous TiO₂/PbS electrodes were then passivated with GSH dissolved in ethanol. The GSH-passivation is expected to result in TiO₂/PbS electrodes covered with a monolayer of GSH molecules in which GSH molecules are attached to PbS QD sites via Pb-S bond formation between Pb²⁺ surface atoms of the QDs and the mercapto group of the GSH molecules. At the same time, bare TiO₂ sites of the TiO₂/PbS electrode are also expected to be covered with a monolayer of GSH, in which GSH molecules are attached to TiO₂ via –COO[–] groups as shown in Figure 7.1a. The ultraviolet-visible (UV-Vis) absorbance spectra of the mesoporous TiO₂/PbS electrodes are similar for unpassivated and GSH-passivated TiO₂/PbS electrodes (Figure 7.1b).

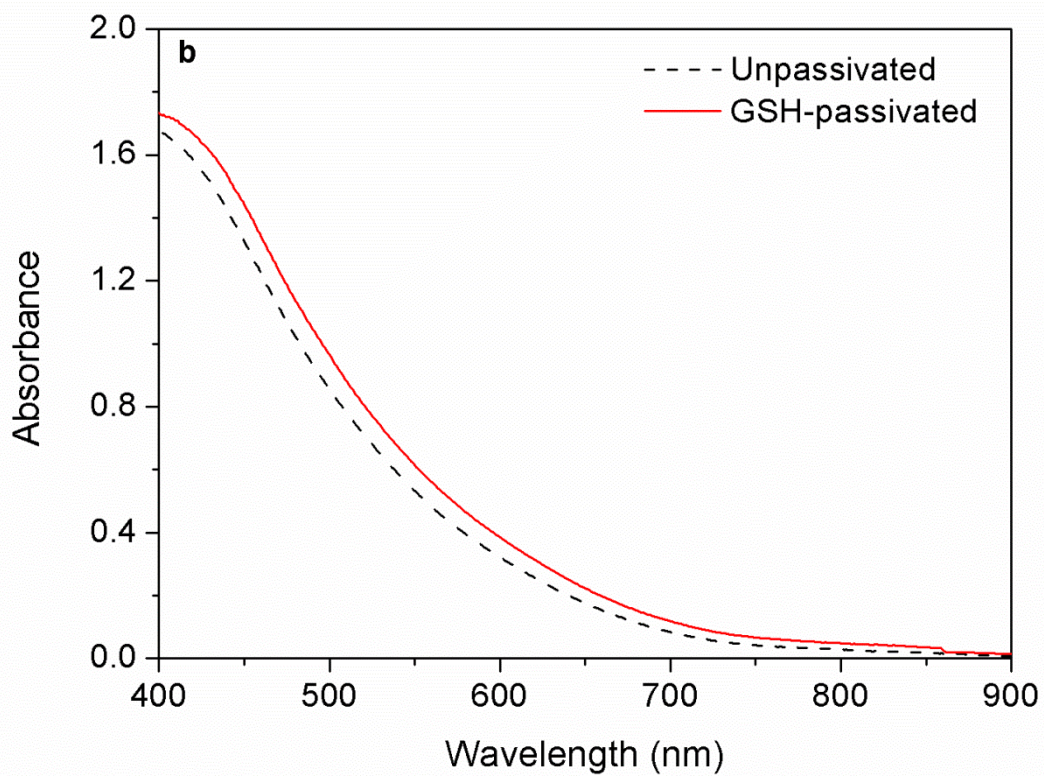
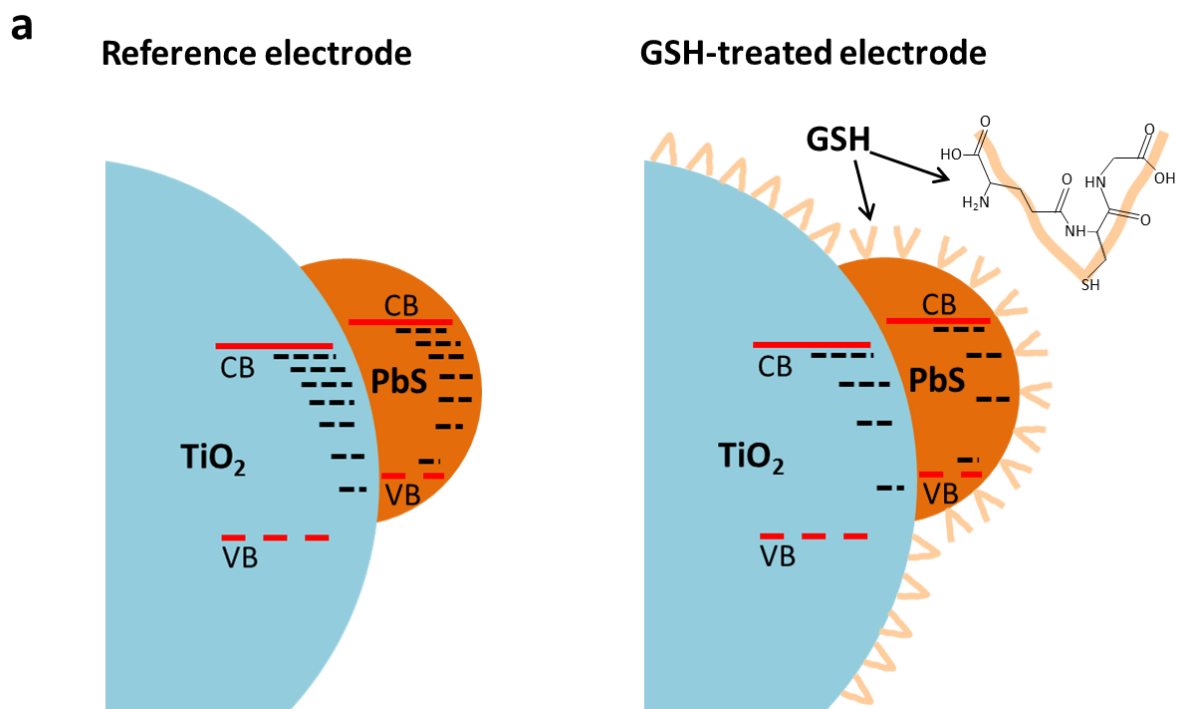


Figure 7.1. (a) Illustration of PbS QD-sensitized TiO₂ electrodes with and without GSH-passivation; (b) UV-Vis spectra of PbS QD-sensitized TiO₂ electrodes with and without GSH-passivation.

The PbS QD-sensitized TiO₂ electrodes without and with GSH-passivation were used to fabricate solid-state QDSCs with Spiro-OMeTAD hole transporting material (HTM). The current-voltage characteristics (I-V) of solid-state QDSCs were recorded under standard AM 1.5 G irradiance of 100 mW cm⁻², and the results are presented in Figure 7.2. The I-V measurements show that treatment of PbS QD-sensitized mesoporous TiO₂ electrodes with GSH significantly increases the short circuit current. The short circuit current of the GSH-passivated cells is more than a factor of two higher (3.84 mA cm⁻²) compared to the unpassivated cell (1.7 mA cm⁻²). The open circuit voltage of the GSH-passivated cell is slightly higher, but the fill factor is lower than for the reference, unpassivated cell. Overall, the performance of the GSH-passivated cell was superior to that of the reference cell, resulting in about 1% efficiency at 1 Sun AM 1.5 G. The solar cell parameters of the unpassivated and GSH-passivated cells are contrasted in Table 7.1.

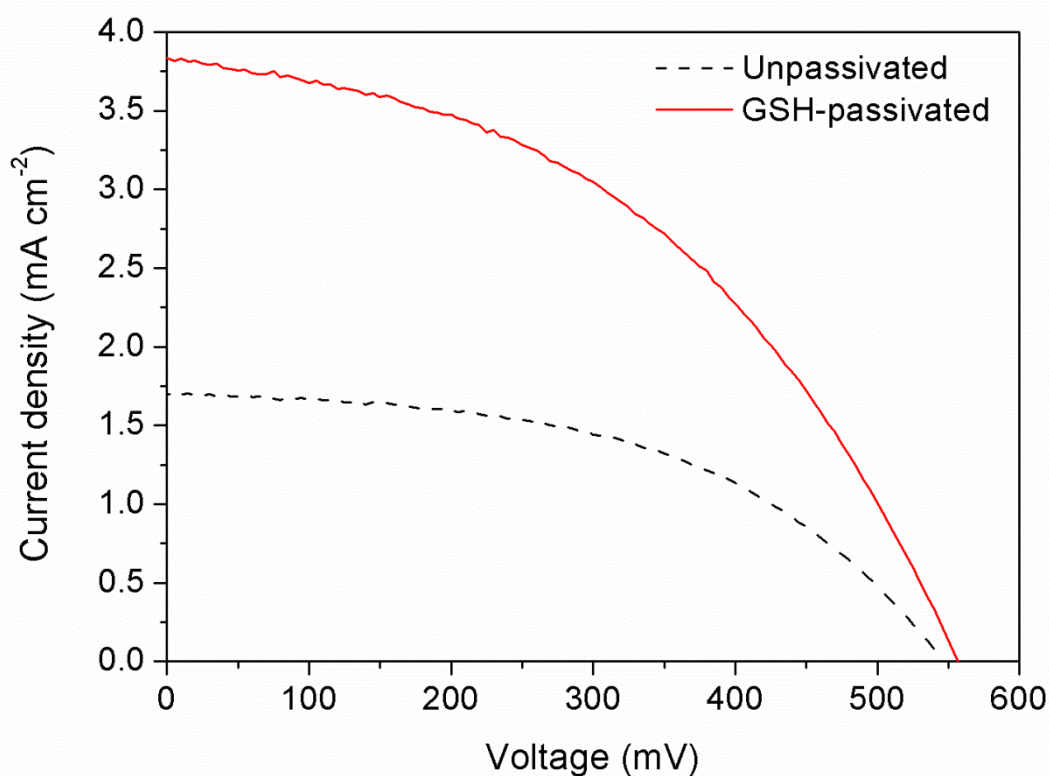


Figure 7.2. I-V characteristics of solid-state QDSCs with and without GSH-passivation.

Table 7.1. Summary of the solar cell performance of the reference and GSH-treated cells under AM 1.5 at 100 mW cm⁻² illumination.

Cell	V_{OC} (mV)	J_{SC} (mA cm ⁻²)	FF (%)	η (%)
Unpassivated	547	1.70	50	0.47
GSH-passivated	557	3.84	44.5	0.95

The incident-photon-to-collected-electron efficiency (IPCE) spectra of the cells were recorded in order to obtain the spectral response of the devices (Figure 7.3). The IPCE spectra of both cells follow the same trend as the UV-Vis absorbance spectra, and the GSH-passivated cell

has a factor of two higher IPCE throughout the entire visible range relative to the unpassivated cell. This indicates either improved injection or collection efficiency of charge carriers in the GSH-passivated device since the absorbance spectra of both electrodes are almost the same. The GSH-passivated cell gives a maximum IPCE of 35% at 435 nm, whereas the reference, unpassivated cell shows only 18% at the same wavelength. The onset of the IPCE spectrum of the GSH-passivated cell is slightly red-shifted compared to the spectrum of the unpassivated cell. This may indicate that the reference cell has slightly smaller sized PbS QDs, possibly as a result of shrinkage due to partial oxidation creating shells of PbSO_3 and/or PbSO_4 around the PbS QDs.^{15, 25} The calculation of the AM 1.5 G short circuit current densities from the IPCE spectra resulted in values of 1.62 and 3.72 mA cm^{-2} for the unpassivated and GSH-passivated cells, respectively. These values are in excellent agreement with the data in Table 7.1.

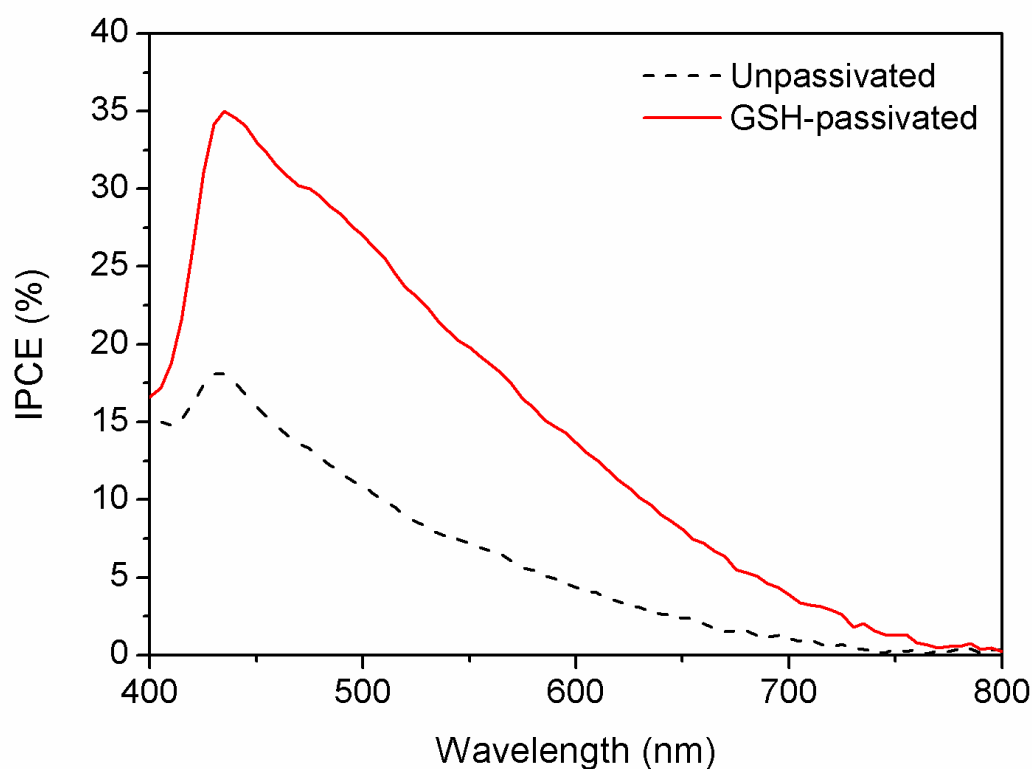


Figure 7.3. IPCE spectra of solid-state QDSCs with and without GSH-passivation.

Electron lifetime measurements were performed on the cells using two methods; intensity-modulated photovoltage spectroscopy (IMVS) and open circuit photovoltage decay (OCVD) (Figures 7.4a-7.4c).²⁶ The electron lifetimes for the reference cell obtained by the OCVD and IMVS measurements show a reasonably good agreement, with slight deviation of τ^{OCVD} from τ^{IMVS} at lower voltages (below 200 mV; Figure 7.4d). The electron lifetimes for the GSH-treated cell, on the other hand, show excellent agreement between τ^{OCVD} and τ^{IMVS} throughout the entire measurement range. However, the comparison of electron lifetimes of the reference and GSH-treated cells does not show much difference, which indicates that the kinetics of the loss of electrons from the TiO₂ by transfer to the hole transport layer is similar for both devices. It should be noted that the IMVS and OCVD techniques detect the back reaction of electrons in the TiO₂ with holes in HTM, but not the recombination of electrons and holes in the PbS QDs via surface states. The latter process happens at much faster time scales and does not affect the relaxation of electrons in the TiO₂.^{27, 28} Instead, recombination of electron-hole pairs in the PbS QDs via surface states will be apparent as a reduction of the injection efficiency in the device. This is consistent with the results of the IPCE measurements, which show a lower IPCE for the reference cell compared to the GSH-treated one.

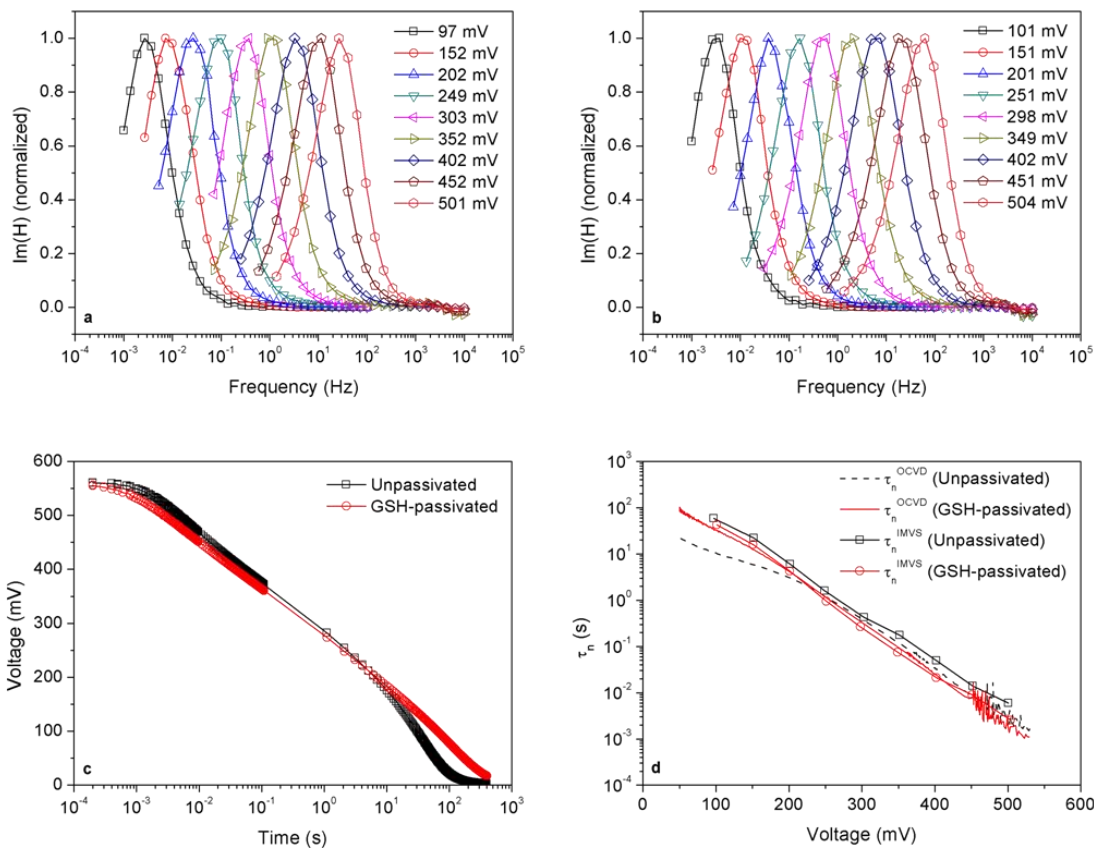


Figure 7.4. Frequency dependence of normalized imaginary parts of the IMVS spectra for the cells (a) without and (b) with GSH-passivation for different photovoltages obtained by varying the light intensity; (c) OCVDs of solid-state QDSCs with and without GSH-passivation; (d) voltage dependence of the electron lifetimes of solid-state QDSCs with and without GSH-treatment.

7.2.2 Iodide-Passivation

The effect of atomic ligand passivation with iodide anions was examined in the same way as described above for the GSH-passivation experiments. Half of the $3 \pm 0.1 \mu\text{m}$ thick mesoporous TiO_2 electrodes sensitized with SILAR-grown (5.5 cycles) PbS QDs with Pb^{2+} terminated surface were immersed into 0.15 M methylammonium iodide ($\text{CH}_3\text{NH}_3\text{I}$) in methanol solution (pH 6.7) to passivate the surface of TiO_2/PbS electrodes with iodide anions.

Upon immersion of the TiO₂/PbS electrode into methylammonium iodide solution, negatively charged iodide ions are expected to form ionic bonds with surface Pb²⁺ atoms of PbS QDs, possibly resulting in a PbI₂ monolayer around the PbS QDs. It should be noted that at pH 6.7 the surface of TiO₂ can still be positively charged since the isoelectric point of TiO₂ (anatase) is 6.9 and, therefore, attachment of iodide ions onto the surface of TiO₂ is also expected (Figure 7.5a).^{29, 30} UV-Vis absorbance spectra of unpassivated and iodide-passivated electrodes did not show much difference (Figure 7.5b).

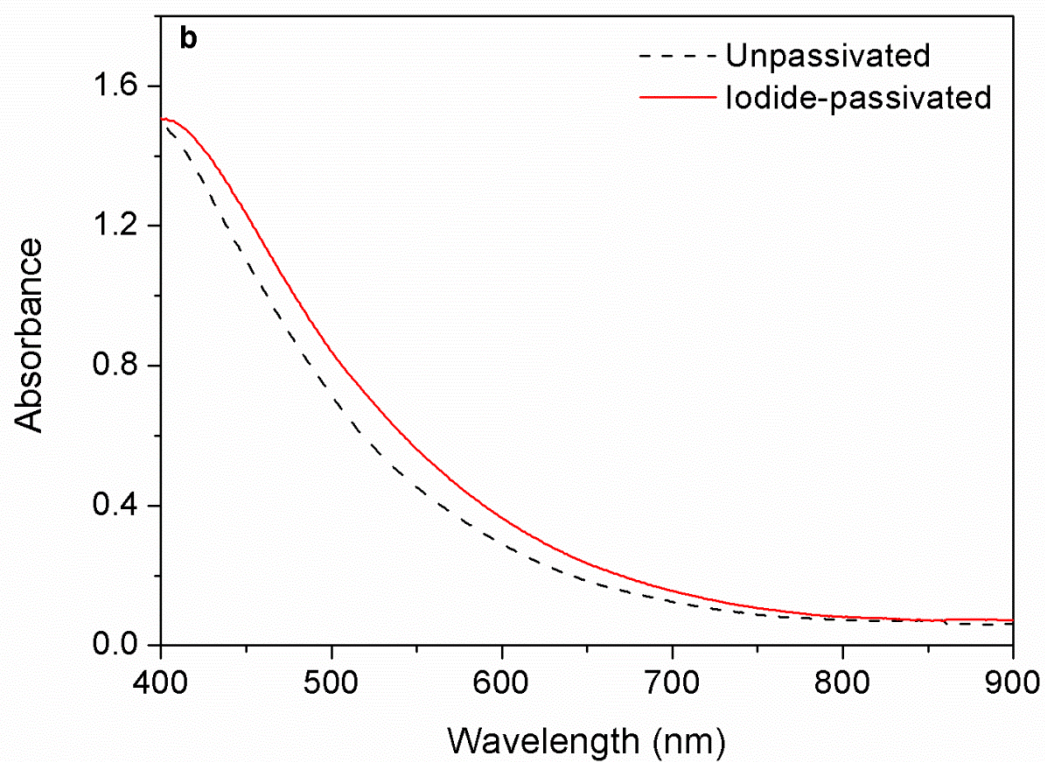
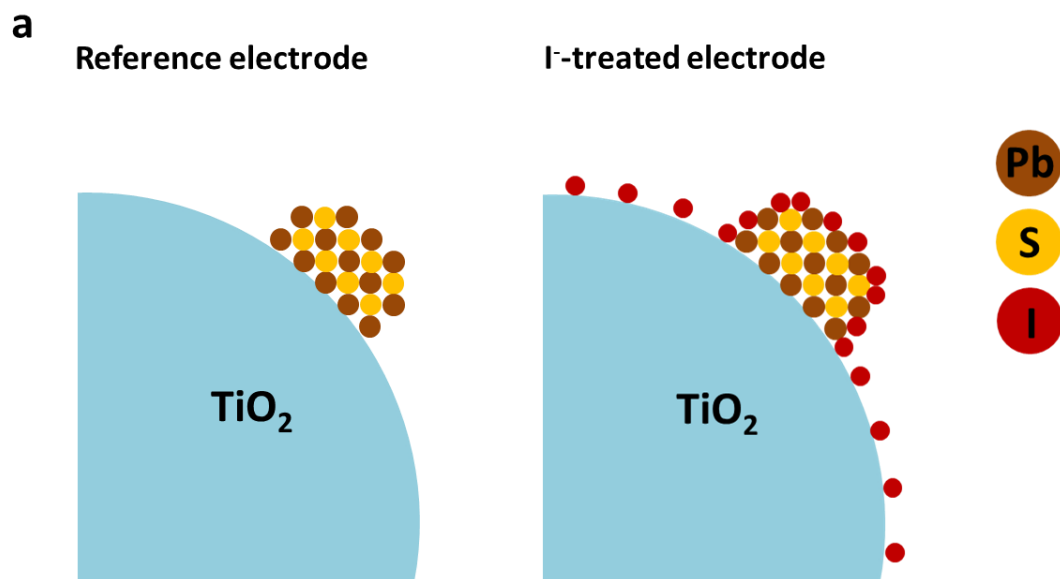


Figure 7.5. (a) Illustration of iodide-passivation of a PbS QD-sensitized TiO₂ electrode and (b) UV-Vis spectra of PbS QD-sensitized TiO₂ electrodes with and without iodide passivation.

The sensitized TiO₂/PbS electrodes with and without passivation were assembled into solid-state QDSCs as described in the experimental section. The I-V characteristics of the cells were recorded under AM 1.5 G irradiation, and the resulting I-V curves are presented in Figure 7.6. The results of I-V measurements show that iodide-passivation of TiO₂/PbS electrodes significantly improves the short circuit current (2.2 mA cm⁻²) resulting in an 57% increase compared to the unpassivated cell. However, the open circuit voltage and fill factor of the iodide-passivated cell decreased compared to the reference, unpassivated cell. The open circuit voltage of the iodide-passivated cell was only 430 mV, which is 100 mV less than for the unpassivated cell. These findings are consistent with findings of de la Fuente et al.,¹⁹ who also observed a decrease of open circuit voltage in liquid electrolyte QDSCs when a similar passivating agent, tetrabutylammonium iodide (N(C₄H₉)₄I), was used to passivate TiO₂/CdS electrodes. Overall, the significant increase in short circuit current is offset by the decrease of open circuit voltage and fill factor such that the performance of the iodide-passivated cell was similar to that of the reference. The solar cell parameters of the unpassivated and iodide-passivated cells are contrasted in Table 7.2.

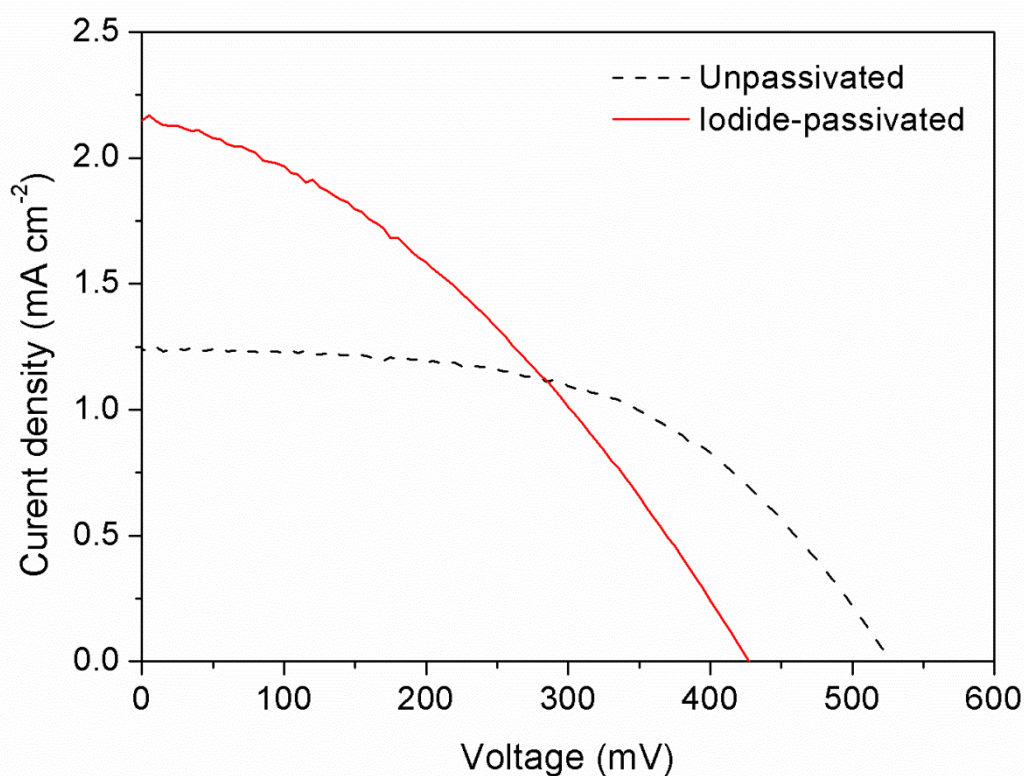


Figure 7.6. I-V characteristics of solid-state QDSCs with and without iodide passivation.

Table 7.2. Summary of the solar cell performance of the reference and iodide-passivated cells under AM 1.5 at 100 mW cm⁻² illumination.

Cell	V_{OC} (mV)	J_{SC} (mA cm ⁻²)	FF (%)	η (%)
Unpassivated	530	1.25	53	0.34
Iodide-passivated	430	2.2	36	0.33

The IPCE measurements of both unpassivated and iodide-passivated cells also indicate the improvement of the short circuit current for the latter as the IPCE spectrum of the iodide-passivated cells is enhanced compared to the unpassivated cell (Figure 7.7). The calculation of

the AM 1.5 G short circuit currents from the IPCE spectra resulted in values of 1.3 and 2.02 mA cm⁻² for the unpassivated and iodide-passivated cells, respectively. These values are in good agreement with the data in Table 7.2.

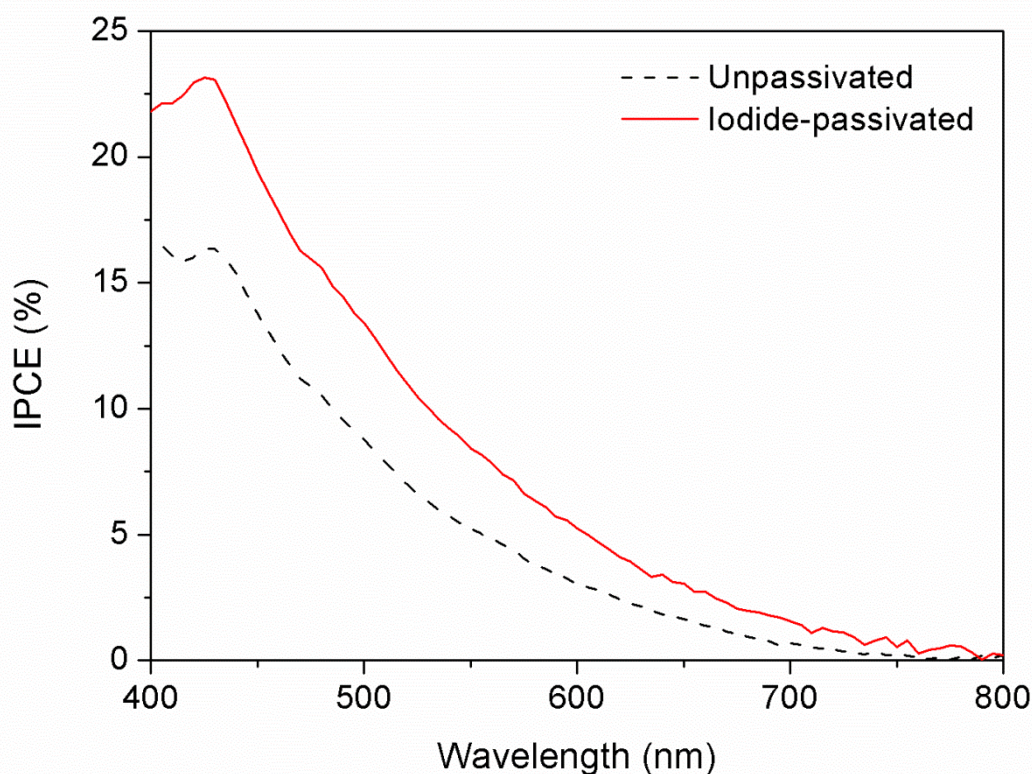


Figure 7.7. IPCE spectra of solid-state QDSCs with and without iodide passivation.

The OCVD measurements of the cells show rather fast conduction band electron relaxation for the iodide-passivated cell compared to the unpassivated cell (Figure 7.8a). The calculations of the electron lifetime as a function of photovoltage based on OCVDs measurements show that iodide-passivated cells have around one order of magnitude lower values compared to unpassivated cells between a photovoltage of 100 and 450 mV (Figure 7.8b). These findings indicate that the iodide-passivated cell suffers from enhanced charge carrier recombination after passivation with iodide anions. This is also well correlated with the I-V measurements showing that the iodide-passivated cells result in lower open circuit

potential and fill factor compared to the reference unpassivated cell. The origin of this effect is not fully understood. However, a possible reason could be a downward shift of the TiO₂ conduction band, which would explain the increased short circuit current for the passivated cell since lowering the conduction band of TiO₂ would mean that (i) the driving force for injection is increased, and (ii) that even larger QDs would be able to inject electrons into the TiO₂. Downward displacement of the TiO₂ conduction could also explain the low open circuit voltage of the passivated cell as well as the difference in electron lifetimes between reference and passivated cells.

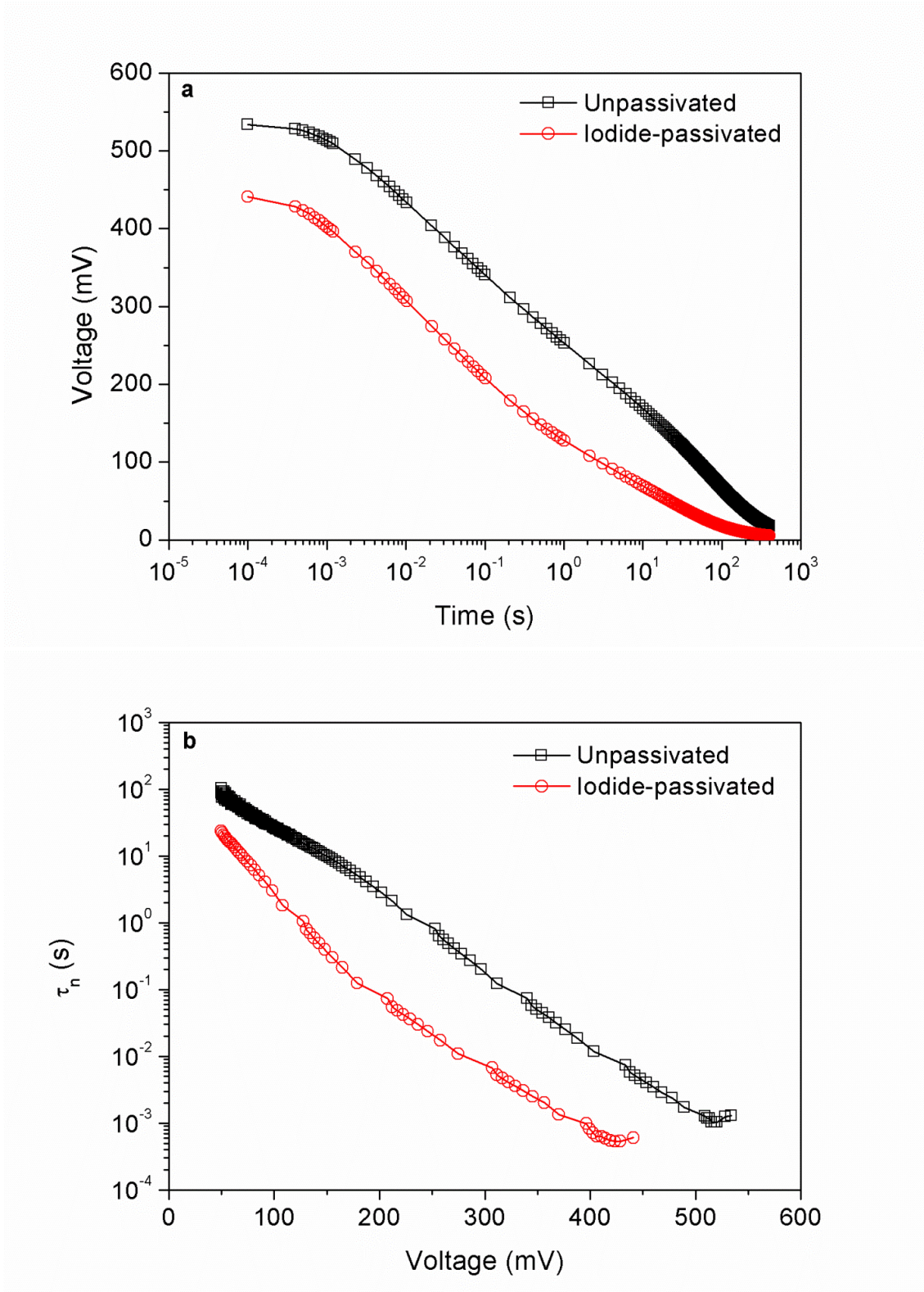


Figure 7.8. (a) OCVDs of solid-state QDSCs with and without iodide passivation and (b) voltage dependence of the electron lifetime of solid-state QDSCs with and without iodide-treatment, respectively.

7.3 Conclusions

In summary, solid-state QDSCs with SILAR-grown PbS QDs and spiro-OMeTAD HTM were fabricated. The effect of GSH- and iodide-treatments for surface passivation has been examined. The comparison of solar cell performance of the GSH-passivated electrodes with the reference electrodes without any surface passivation showed superior performance of the GSH-treated cells. GSH-treatment of the QD-sensitized electrodes results in improvements in the short circuit current and conversion efficiency by more than a factor of two. A maximum IPCE value of 35% at 435 nm was recorded for the GSH-treated cell compared to only 18% for the reference cell. Both OCVD and IMVS techniques showed that there is not much difference in the electron lifetimes of the GSH-treated and reference cells, except for a slight deviation of OCVD results from IMVS data at lower voltages (below 200 mV) for the reference cell. Overall, combining the findings of the I-V, IPCE and electron lifetime measurements, we conclude that the enhanced cell performance of the GSH-treated cells originates from the suppression of surface state-mediated electron-hole recombination in the PbS QDs, leading to improved charge injection efficiency.

In contrast, iodide-passivation enhanced the short circuit current but lowered the open circuit potential and fill factor compared to the reference, unpassivated cell. Due to the trade-off between the short circuit current and open circuit voltage, the efficiency of the iodide-passivated cell did not result in a higher conversion efficiency, which remained the same as for the reference cell. The electron lifetime measurements obtained by OCVD showed that the iodide-passivated cell has one order of magnitude lower values compared to the reference cell in the measurement range from 100 to 450 mV. Overall, combining the results of I-V, IPCE and OCVD electron lifetime measurements we conclude that iodide passivation increases charge injection and separation, but the same time increases charge transfer from the TiO₂ to

the HTM, which negatively affects the charge collection. Our study shows that both molecular and ionic passivation agents can have a profound impact on the performance of QD-sensitized solar cells.

7.4 Experimental Section

7.4.1 Materials

Titanium(IV) ethoxide (Alfa Aesar), titanium(IV) chloride (Sigma-Aldrich), hydrochloric acid 37% (Sigma-Aldrich), ammonia 28% (Sigma-Aldrich), hydrogen peroxide (Sigma-Aldrich), ethyl cellulose (Fluka), terpineol (Fluka), ethanol (Sigma-Aldrich), methanol (Sigma-Aldrich), L-glutathione (Sigma-Aldrich), methylamine 33% (Sigma-Aldrich), hydroiodic acid 57% (Sigma-Aldrich), lead(II) nitrate (Sigma-Aldrich), sodium sulfide (Alfa Aesar), spiro-OMeTAD (Merck), 4-*tert*-butylpyridine (Sigma-Aldrich), bis(trifluoromethane)sulfonimide lithium salt (Sigma-Aldrich), chlorobenzene (Sigma-Aldrich), acetonitrile (Sigma-Aldrich).

7.4.2 TiO₂ Photoanode Preparation

The FTO substrates cut to 1.5×2 cm² were patterned by selectively etching the FTO layer and were coated with a compact TiO₂ blocking layer (cf. subsection A-4 in Appendix).^{31, 32} For the preparation of mesoporous TiO₂ electrodes, 100 μL of TiO₂-paste with around 30 nm sized TiO₂ nanocrystallites was spin-coated onto FTO substrates with a freshly made blocking layer. The TiO₂ nanoparticles (NPs) were prepared according to Baek et al.,³³ (cf. subsection A-13 in Appendix) and the TiO₂ paste was prepared as described by Ito et al.^{34, 35} (cf.

subsection A-14 in Appendix). The coated substrates were calcined in air at 500 °C for 30 min to obtain mesoporous TiO₂ electrodes. The electrodes were then subjected to an additional treatment in aqueous 40 mM TiCl₄ (10 mL per electrode) at 70 °C for 30 min, and were subsequently calcined again in air at 500 °C for 30 min.⁴

7.4.3 Synthesis of Methylammonium Iodide

The synthesis of methylammonium iodide (CH₃NH₃I) was performed as described by Lee et al.³⁶ 24 mL of 33 wt% methylamine (CH₃NH₂) in absolute ethanol was mixed with 10 mL of 57 wt% hydroiodic acid (HI) in water and 100 mL absolute ethanol under nitrogen atmosphere at room temperature. The resulting methylammonium iodide (CH₃NH₃I) product (white powder) was separated via crystallization with a rotary evaporator.³⁶

7.4.4 Fabrication of Solar Cells

Sensitization of mesoporous TiO₂ electrodes (1.5×1 cm²) with PbS QDs was carried out by the SILAR process. 0.02 M solutions of Pb(NO₃)₂ and Na₂S each in methanol were used as precursors for PbS QD deposition.⁴ The electrodes were dipped in each solution (usually 10 mL) for 1 min at room temperature followed by rinsing with pure methanol and drying with a nitrogen stream to complete one SILAR cycle. In total, 5.5 SILAR cycles were performed to sensitize mesoporous TiO₂ electrodes with PbS QDs.⁴ For surface passivation with GSH, 0.2 g of GSH was mixed with 20 mL of ethanol at room temperature to obtain a saturated solution. Then the solution was filtered with a 0.22 μm pore size filter to remove the excess solid GSH. The freshly QD-sensitized TiO₂ electrodes were immersed into the GSH-solution

(usually 10 mL) for 30 min in order to passivate the surface of TiO₂/PbS electrodes. Afterwards, the electrodes were rinsed with pure ethanol (usually 10 mL) for 10 min to wash away unattached GSH ligands and dried with a stream of nitrogen. For surface passivation with iodide anions the freshly-made QD-sensitized TiO₂ electrodes were immersed into a 0.15 M solution of methylammonium iodide (CH₃NH₃I) in methanol (usually 10 mL) for 30 min. Afterwards, the electrodes were rinsed with pure methanol (usually 10 mL) for 10 min to wash away residual CH₃NH₃⁺ cations and unattached iodide anions and dried with a stream of nitrogen.

Subsequently, 40 μL of the spiro-OMeTAD solution (see below) was dropped onto the sensitized mesoporous TiO₂ electrodes with and without surface-passivation and left for 20 s to infiltrate, and then spin-coated at 1500 rpm for 40 sec. The spiro-OMeTAD solution contained 37.5 mg Spiro-OMeTAD dissolved in 250 μL chlorobenzene. 2 μL 4-*tert*-butylpyridine, and 4.2 μL of bis(trifluoromethane)sulfonimide lithium salt pre-dissolved in acetonitrile (170 mg/mL) were added to the spiro-OMeTAD solution as dopant additives.³⁷ Finally, 150 nm thick silver contacts were deposited on the electrodes via vacuum evaporation through a mask to complete the solar cells.

7.4.5 Characterization Methods

The absorbance spectra of the PbS QD-sensitized TiO₂ electrodes were measured with a UV-Vis-NIR spectrophotometer (model: Lambda 1050, PerkinElmer) and were corrected for the absorbance of the TiO₂ electrodes. The absorbance spectra of the QD-sensitized electrodes were measured with a 0.16 cm² mask. The thickness of the mesoporous TiO₂ films was measured with a Dektak 150 profilometer. The I-V characteristics of the solid-state QDSCs

were measured under simulated solar light using a 300 W xenon lamp with an AM 1.5 G irradiance of 100 mWcm^{-2} (model: XPS 400, Solar Light Company Inc.). The I-V characteristics were recorded using a Keithley 2400 source meter with 0.11 cm^2 active cell area. The IPCE spectra of the cells were measured using chopped monochromatic light provided by a 150 W xenon lamp (Lot-Oriel) and monochromator (Micro HR) with order sorting filters (Thorlabs). Measurements were made using bias light with AM 1.5 G irradiance of 11.5 mW cm^{-2} , and the signal was detected by a DSP lock-in amplifier (model: 7230, Signal Recovery). The IPCE data were recorded using the Keithley 2400 source meter. The OCVD and IMVS measurements were carried out using a potentiostat equipped with a frequency response analyzer (model: PGSTAT302N, Autolab, Metrohm) and LED driver. IMVS measurements were carried out under cool white LED (model: LDCCW, Metrohm) irradiation at open-circuit conditions over the frequency range from 10 kHz to 1 mHz. The amplitude of the AC modulation current was 10% of the DC current applied to the LED.

References

1. J. H. Rhee, C.-C. Chung and E. W.-G. Diau, *NPG Asia Mater*, 2013, **5**, e68.
2. J. B. Sambur, T. Novet and B. A. Parkinson, *Science*, 2010, **330**, 63-66.
3. J.-W. Lee, D.-Y. Son, T. K. Ahn, H.-W. Shin, I. Y. Kim, S.-J. Hwang, M. J. Ko, S. Sul, H. Han and N.-G. Park, *Scientific Reports*, 2013, **3**, 1-8.
4. H. Lee, H. C. Leventis, S.-J. Moon, P. Chen, S. Ito, S. A. Haque, T. Torres, F. Nüesch, T. Geiger, S. M. Zakeeruddin, M. Grätzel and M. K. Nazeeruddin, *Advanced Functional Materials*, 2009, **19**, 2735-2742.

5. S. H. Im, H.-j. Kim, S. W. Kim, S.-W. Kim and S. I. Seok, *Energy & Environmental Science*, 2011, **4**, 4181-4186.
6. I. Moreels, K. Lambert, D. Smeets, D. De Muynck, T. Nollet, J. C. Martins, F. Vanhaecke, A. Vantomme, C. Delerue, G. Allan and Z. Hens, *ACS Nano*, 2009, **3**, 3023-3030.
7. Z. Hens and I. Moreels, *Journal of Materials Chemistry*, 2012, **22**, 10406-10415.
8. S. D. Sung, I. Lim, P. Kang, C. Lee and W. I. Lee, *Chemical Communications*, 2013, **49**, 6054-6056.
9. S. Kim, S. H. Im, M. Kang, J. H. Heo, S. I. Seok, S.-W. Kim, I. Mora-Seró and J. Bisquert, *Physical Chemistry Chemical Physics*, 2012, **14**, 14999-15002.
10. A. Yella, H.-W. Lee, H. N. Tsao, C. Yi, A. K. Chandiran, M. K. Nazeeruddin, E. W.-G. Diao, C.-Y. Yeh, S. M. Zakeeruddin and M. Grätzel, *Science*, 2011, **334**, 629-634.
11. J. Burschka, A. Dualeh, F. Kessler, E. Baranoff, N.-L. Cevey-Ha, C. Yi, M. K. Nazeeruddin and M. Grätzel, *Journal of the American Chemical Society*, 2011, **133**, 18042-18045.
12. G. Hodes, *The Journal of Physical Chemistry C*, 2008, **112**, 17778-17787.
13. A. H. Ip, S. M. Thon, S. Hoogland, O. Voznyy, D. Zhitomirsky, R. Debnath, L. Levina, L. R. Rollny, G. H. Carey, A. Fischer, K. W. Kemp, I. J. Kramer, Z. Ning, A. J. Labelle, K. W. Chou, A. Amassian and E. H. Sargent, *Nature Nanotechnol.*, 2012, **7**, 577-582.

14. I. Hod, V. González-Pedro, Z. Tachan, F. Fabregat-Santiago, I. Mora-Seró, J. Bisquert and A. Zaban, *The Journal of Physical Chemistry Letters*, 2011, **2**, 3032-3035.
15. J. Tang, L. Brzozowski, D. A. R. Barkhouse, X. Wang, R. Debnath, R. Wolowiec, E. Palmiano, L. Levina, A. G. Pattantyus-Abraham, D. Jamakosmanovic and E. H. Sargent, *ACS Nano*, 2010, **4**, 869-878.
16. Q. Shen, J. Kobayashi, L. J. Diguna and T. Toyoda, *Journal of Applied Physics*, 2008, **103**, 084304-084305.
17. Z. Tachan, I. Hod, M. Shalom, L. Grinis and A. Zaban, *Physical Chemistry Chemical Physics*, 2013, **15**, 3841-3845.
18. T. P. Brennan, O. Trejo, K. E. Roelofs, J. Xu, F. B. Prinz and S. F. Bent, *Journal of Materials Chemistry A*, 2013, **1**, 7566-7571.
19. M. S. de la Fuente, R. S. Sánchez, V. González-Pedro, P. P. Boix, S. G. Mhaisalkar, M. E. Rincón, J. Bisquert and I. Mora-Seró, *The Journal of Physical Chemistry Letters*, 2013, **4**, 1519-1525.
20. D. Deng, J. Xia, J. Cao, L. Qu, J. Tian, Z. Qian, Y. Gu and Z. Gu, *Journal of Colloid and Interface Science*, 2012, **367**, 234-240.
21. A. N. Jumabekov, F. Deschler, D. Böhm, L. M. Peter, J. Feldmann and T. Bein, *The Journal of Physical Chemistry C*, 2014, **118**, 5142-5149.
22. V. Chakrapani, D. Baker and P. V. Kamat, *Journal of the American Chemical Society*, 2011, **133**, 9607-9615.
23. P. V. Kamat, *The Journal of Physical Chemistry Letters*, 2013, **4**, 908-918.

24. J. Tang, K. W. Kemp, S. Hoogland, K. S. Jeong, H. Liu, L. Levina, M. Furukawa, X. Wang, R. Debnath, D. Cha, K. W. Chou, A. Fischer, A. Amassian, J. B. Asbury and E. H. Sargent, *Nature Materials*, 2011, **10**, 765-771.
25. J. P. Clifford, G. Konstantatos, K. W. Johnston, S. Hoogland, L. Levina and E. H. Sargent, *Nature Nanotechnol.*, 2009, **4**, 40-44.
26. P. J. Cameron and L. M. Peter, *The Journal of Physical Chemistry B*, 2005, **109**, 7392-7398.
27. B. Ehrler, K. P. Musselman, M. L. Böhm, F. S. F. Morgenstern, Y. Vaynzof, B. J. Walker, J. L. MacManus-Driscoll and N. C. Greenham, *ACS Nano*, 2013, **7**, 4210-4220.
28. I. Robel, V. Subramanian, M. Kuno and P. V. Kamat, *Journal of the American Chemical Society*, 2006, **128**, 2385-2393.
29. N. Sakai and T. Tatsuma, *Advanced Materials*, 2010, **22**, 3185-3188.
30. B. Ohtani, Y. Okugawa, S. Nishimoto and T. Kagiya, *The Journal of Physical Chemistry*, 1987, **91**, 3550-3555.
31. P. J. Cameron and L. M. Peter, *The Journal of Physical Chemistry B*, 2003, **107**, 14394-14400.
32. L. Kavan and M. Grätzel, *Electrochimica Acta*, 1995, **40**, 643-652.
33. I. C. Baek, M. Vithal, J. A. Chang, J.-H. Yum, M. K. Nazeeruddin, M. Grätzel, Y.-C. Chung and S. I. Seok, *Electrochemistry Communications*, 2009, **11**, 909-912.

34. S. Ito, P. Chen, P. Comte, M. K. Nazeeruddin, P. Liska, P. Péchy and M. Grätzel, *Progress in Photovoltaics: Research and Applications*, 2007, **15**, 603-612.
35. S. Ito, T. N. Murakami, P. Comte, P. Liska, C. Grätzel, M. K. Nazeeruddin and M. Grätzel, *Thin Solid Films*, 2008, **516**, 4613-4619.
36. M. M. Lee, J. Teuscher, T. Miyasaka, T. N. Murakami and H. J. Snaith, *Science*, 2012, **338**, 643-647.
37. P. Docampo, S. Guldin, M. Stefiik, P. Tiwana, M. C. Orilall, S. Hüttner, H. Sai, U. Wiesner, U. Steiner and H. J. Snaith, *Advanced Functional Materials*, 2010, **20**, 1787-1796.

8 Conclusions and Outlook

This thesis describes investigations of the application of PbS quantum dots (QDs) in solar energy conversion. PbS QDs grown either by *in situ* or *ex situ* methods were used as light-harvesting and exciton-generating agents (sensitizer) for nanostructured solar cells with n-type porous TiO₂ and SnO₂ scaffolding electrodes and with liquid redox electrolytes or solid hole conductors. Diverse synthetic methods were employed to influence and improve the performance of the resulting devices, and the underlying physical properties and processes were studied with a variety of experimental techniques.

The choice of PbS QDs as sensitizer was motivated by their high absorption coefficient, size-dependent bandgap tunability as well as the potential to generate and split multiple excitons, which makes them highly attractive for applications in energy conversion technologies such as solar cells. Chapter 3 discusses the use of PbS QDs in fully inorganic extremely thin absorber (ETA) solar cells in which an *in situ* grown absorber PbS QD layer was deposited on the walls of a sol-gel derived mesoporous TiO₂ scaffolding electrode, and CuSCN was used as solid hole conductor. The preparation of thin, highly crystalline mesoporous TiO₂ films with high internal surface area and porosity was demonstrated using an amphiphilic polystyrene-block-poly(ethylene oxide) (PS-*b*-PEO) block copolymer (collaboration with Dr. Mihaela Nedelcu and the group of Prof. Ulrich Wiesner, Cornell University, USA). The experimental studies showed that the ETA solar cells have a small electron diffusion coefficient and short electron lifetimes leading to poor collection efficiencies. The origin of this issue was attributed to low surface coverage of TiO₂ with QDs, leaving a large fraction of bare TiO₂ surface to interact with CuSCN and increase charge recombination. Also, surface oxidation of PbS QDs and poor CuSCN infiltration are believed to be additional factors that affect the successful charge generation and splitting processes.

In an attempt to resolve these issues, pre-synthesized colloidal PbS QDs were employed in further studies. Pre-synthesized colloidal PbS QDs are usually covered with long alkyl chain organic ligands such as oleic acid (OA), which can make them difficult to use for sensitization of n-type metal oxides (MOs) such as meso- or macroporous TiO₂. To address this point, QDs were subjected to a ligand exchange procedure in which L-glutathione (GSH) was used to replace the OA ligands. Highly stable colloidal aqueous solutions of PbS QDs protected with GSH ligands were obtained after the ligand exchange. Efficient PL quenching was observed when QDs were brought in contact with colloidal TiO₂ NPs (collaboration with Prof. Jochen Feldmann and Dr. Felix Deschler from the LMU physics department). Successful sensitization of TiO₂ P25 NPs and porous TiO₂ electrodes with PbS QDs was achieved by exploiting the additional electrostatic attraction that was created by carefully adjusting the pH of the QD solution in order to induce opposite surface charging of the metal oxide and the PbS-SGH QDs. The corresponding PbS quantum-dot-sensitized solar cells (QDSCs) with polysulfide based liquid electrolyte gave high short circuit currents and over 1% conversion efficiency. Electrochemical impedance spectroscopy (EIS) studies revealed an electron collection efficiency close to unity as well as a high electron injection efficiency from PbS QDs into TiO₂.

To extend our understanding of charge injection and separation processes, we changed the metal oxide used as n-type semiconductor electrode to mesoporous SnO₂ (with help from the research trainee '*Forschungspraktikant*' BSc. Daniel Böhm). More effective charge injection from PbS-GSH QDs into SnO₂ electrodes compared to TiO₂ was demonstrated in solid-state QDSCs with spiro-OMeTAD serving as organic hole transporter. Due to a shift in band position, a decrease in open circuit voltage was observed with the SnO₂ electrodes, and passivation of the surface of the electrodes with MgO and TiO₂ was investigated in order to increase the open circuit voltage. The highest performance of the cells was obtained with

TiO₂-passivated SnO₂ electrodes, although the combination of TiO₂- and MgO-passivation resulted in the highest open circuit voltage. Investigation of the physical properties of the solar cells revealed that the devices with TiO₂-passivated SnO₂ electrodes have remarkably high electron lifetimes compared to the unpassivated ones, which was a direct indication of slower charge recombination and therefore improved device performance.

To shed light on the role of the interface between PbS QDs and the acceptor metal oxide (MO), the difference in performance of solid-state QDSCs with *ex situ* and *in situ* grown PbS QDs was investigated (with help from the research trainee ‘*Forschungspraktikant*’ BSc. Timothy Siegler). It was demonstrated that an intimate contact between the PbS QD sensitizer and the MO acceptor is required for efficient charge injection and separation. This result was obtained by comparing the AM 1.5 G solar cell characteristics of cells with *in situ*, successive ionic layer adsorption/reaction (SILAR) grown PbS QDs and *ex situ*, pre-synthesized PbS QDs anchored on mesoporous TiO₂ via GSH linkers. The low values for the short circuit current of cells with *ex situ* grown PbS QDs were attributed to the effect of the GSH ligands connecting TiO₂ and PbS QD acting as an energetic barrier, hindering the electron injection process. Further, it was shown that despite high charge carrier injection rates the cells with *in situ* grown PbS QDs exhibit a deviation from ideal diode behavior, thus, sub-linear recombination (recombination of electrons with holes governed not only via direct relaxation of conduction band electrons into the hole transporter, but recombination of electrons with holes via TiO₂ and QD surface states), as well as low electron lifetimes compared to the cells with *ex situ* grown PbS QDs, which we suggest leaves room for possible further tuning the interface between *in situ* grown PbS QDs and TiO₂.

Finally, to tackle the issue of PbS QD surface oxidation, passivation of QD-sensitized TiO₂ electrodes was investigated and the effect of passivation on the performance of solid-state QDSCs with *in situ*, SILAR grown PbS QDs and spiro-OMeTAD hole transporter was

examined (with help from the research trainee '*Forschungspraktikant*' BSc. Niklas Cordes). In the course of these studies, passivation of the TiO₂/PbS QD surface with organic GSH ligands and iodide anions (I⁻) was explored. It was found that the passivation of the surface of PbS QDs greatly improves charge injection and separation and results in a factor of two or higher improvement in short circuit currents. An increase in conversion efficiency by a factor of two was observed in the case of GSH-passivation. This effect is attributed to a reduction of the number of surface states of PbS QDs upon passivation.

To summarize, the use of different strategies for the deposition of PbS QDs on the walls of porous TiO₂ or SnO₂ metal oxide electrodes and surface engineering and tuning of the materials at the metal oxide/quantum dot, metal oxide/hole mediator and quantum dot/hole mediator interfaces has led to an extended understanding of charge injection and separation processes as well as the importance of surface and interfacial effects for the successful application of these materials in photovoltaic cells. The outcome of the research work presented in this thesis could be interesting for further development of improved solar cells with PbS or many other QDs of interest in order to achieve efficient devices that are inexpensive, moisture and air stable. Some of the findings of this research may also be interesting for understanding hybrid perovskite-based solar cells that appear to be very promising in terms of power conversion efficiencies.

9 Appendices

Appendix A: Supplementary Information

A-1 Analysis of Porous TiO_2 Electrodes with Wide Angle X-ray Diffraction (XRD)

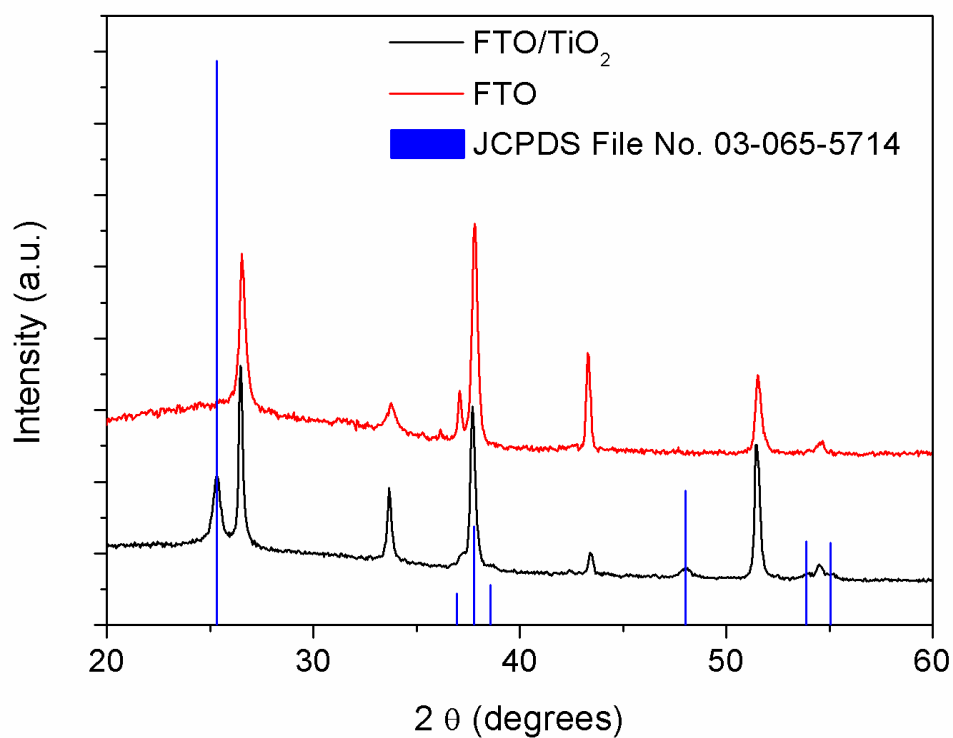


Figure A-1.1. Wide-angle XRD patterns of FTO substrate and a BCP-templated mesoporous TiO_2 film on FTO.

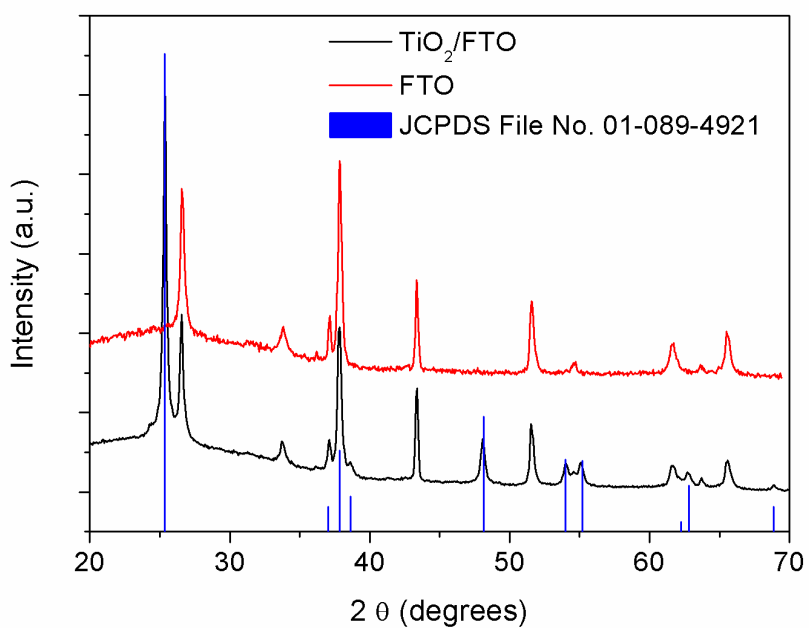


Figure A-1.2. Wide-angle XRD patterns of FTO and poly(methyl methacrylate) (PMMA) templated macroporous TiO₂ film on FTO.

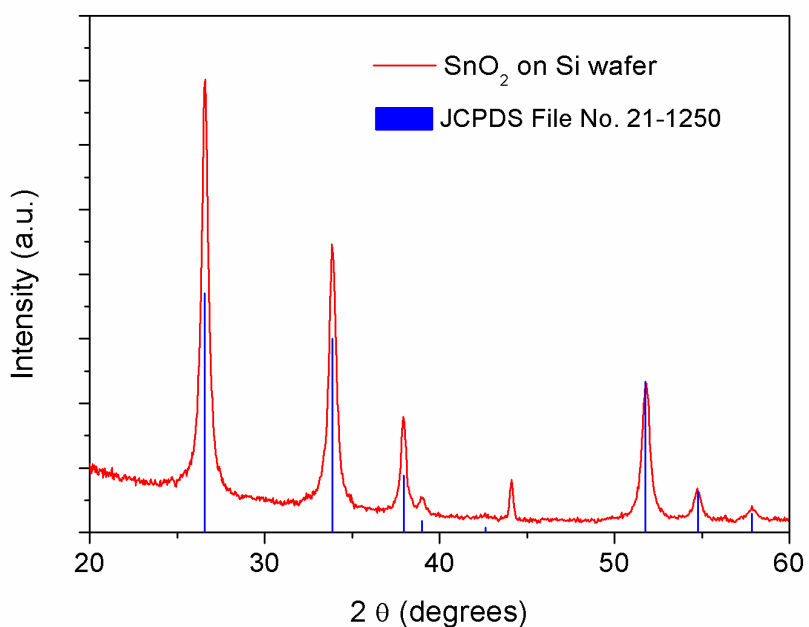


Figure A-1.3. Wide-angle XRD pattern of mesoporous SnO₂ film (made of sintering SnO₂ nanoparticles) on a silicon wafer.

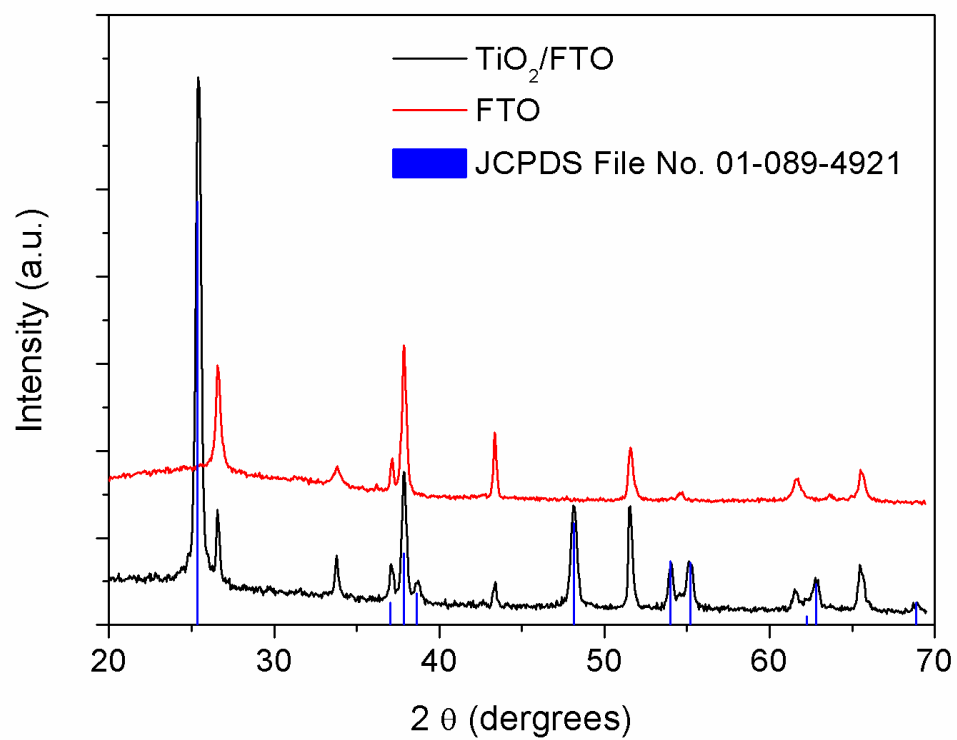


Figure A-1.4. Wide-angle XRD patterns of FTO and mesoporous TiO₂ film (made of sintering TiO₂ nanoparticles) on FTO.

A-2 Nitrogen Sorption Studies on Porous TiO₂ Electrodes

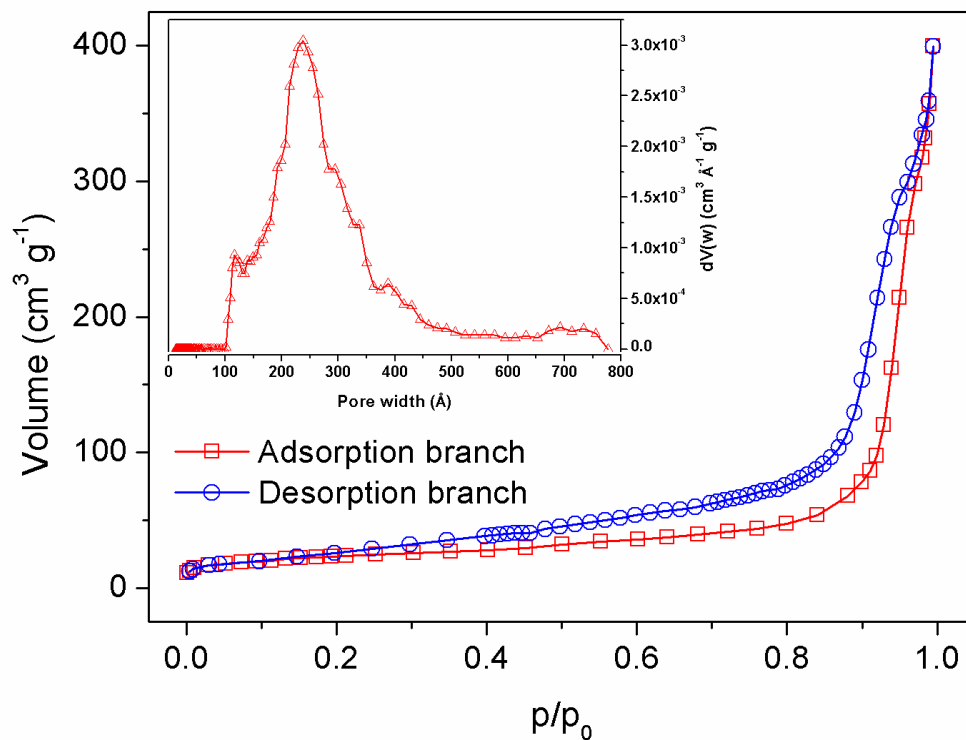


Figure A-2.1. Nitrogen sorption isotherm and pore size distribution (inset) of powder prepared from BCP-templated TiO₂ films. The BET surface area of the mesoporous TiO₂ was calculated using experimental points from the linear part of the adsorption branch. The total pore volume was calculated by the amount of N₂ adsorbed at the highest relative pressure $p/p_0 = 0.995$. The DFT pore size distribution (inset) was calculated from the adsorption branch using an SiO₂ kernel and assuming cylindrical pore geometry for the films.

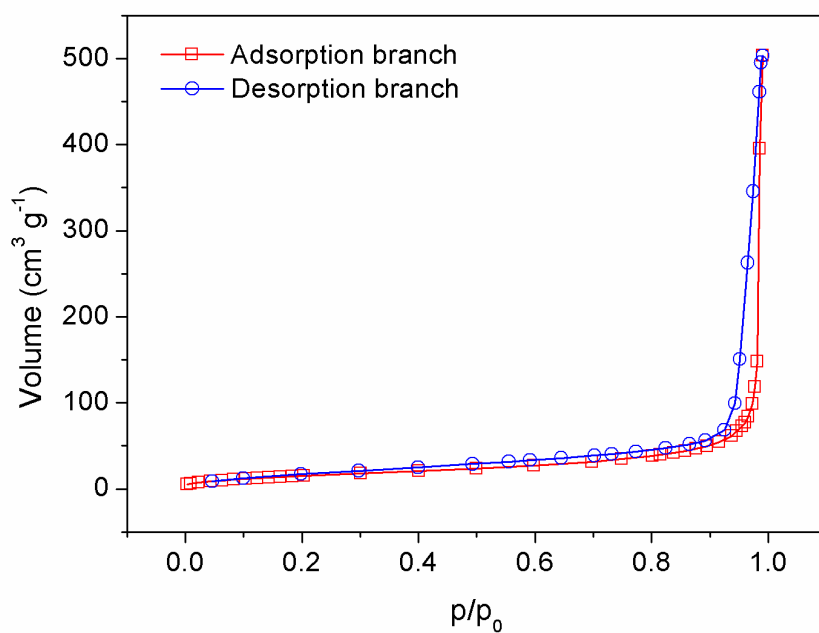


Figure A-2.2. Nitrogen sorption isotherm of powder obtained from PMMA-templated macroporous TiO₂ films.

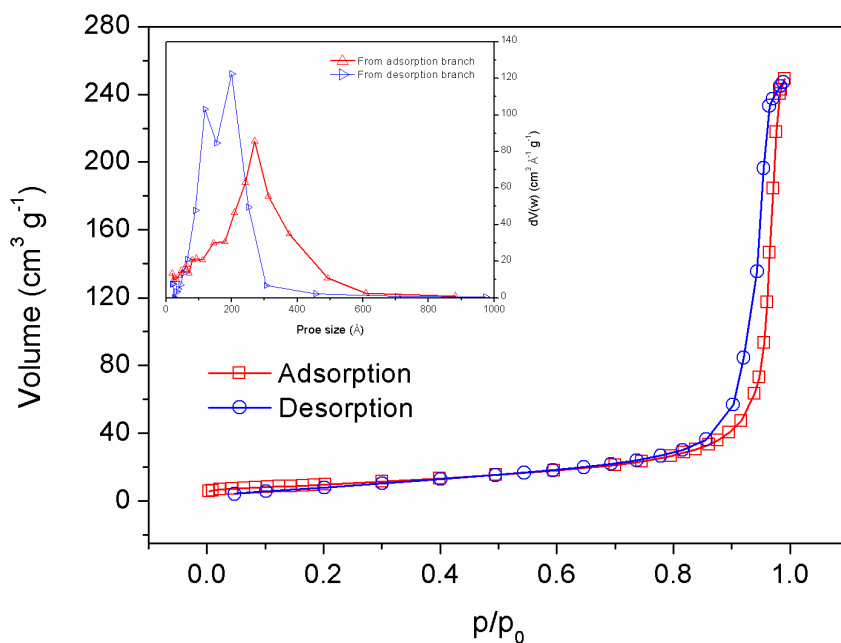


Figure A-2.3. Nitrogen sorption isotherm and pore size distribution (inset) of powder obtained from mesoporous SnO₂ films.

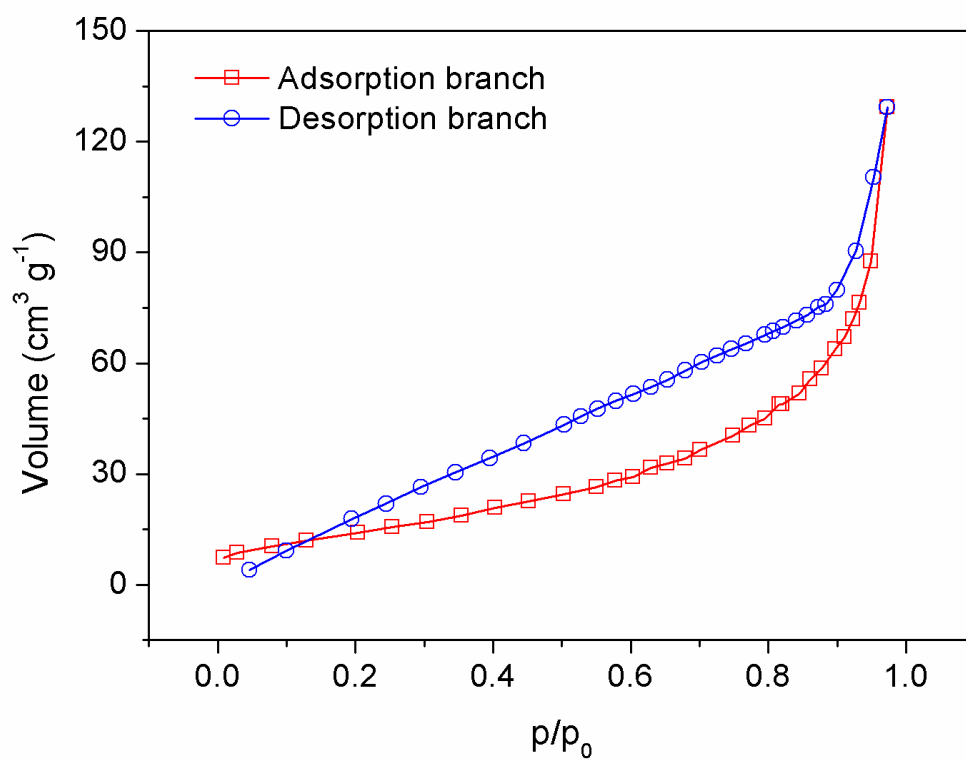


Figure A-2.4. Nitrogen sorption isotherm of powder obtained from mesoporous TiO_2 films (made of sintering TiO_2 nanoparticles). For unknown reasons, the shape of the desorption branch is unusual for this sample.

A-3 Analysis of Solar Cells with Electrochemical Impedance Spectroscopy

(EIS)

Table A-3.1. Parameters for the equivalent circuit obtained by fitting the experimental impedance spectra of the complete extremely thin absorber (ETA) solar cell.

Light intensity (mWcm ⁻²)	R_{ct} (Ω cm ²)	R_{trans} (Ω cm ²)	C_{μ} (F cm ⁻²)	R_{Sub} (Ω)	C_{Sub} (F)	R_{CuSCN} (Ω)	CPE_{CuSCN}	n_{CPE}	R_S (Ω)
1.26	3410.2	560	1.43×10^{-5}	1×10^6	1×10^{-7}	2146	1×10^{-7}	0.79	17
6.51	984.9	380	2.51×10^{-5}	1×10^6	1×10^{-7}	1956	1.2×10^{-7}	0.78	17
11.5	539.7	230	3.8×10^{-5}	1×10^6	8×10^{-8}	1893	1.3×10^{-7}	0.77	17
21.1	295	150	4.3×10^{-5}	1×10^6	2×10^{-8}	1480	1.4×10^{-7}	0.77	17
55.5	113.2	50	4.3×10^{-5}	1×10^6	1.8×10^{-8}	724	1.1×10^{-7}	0.8	17
100	76.65	42	4.4×10^{-5}	1×10^6	6×10^{-9}	327	7.8×10^{-8}	0.85	17

Table A-3.2. Parameters for the equivalent circuit obtained by fitting the experimental impedance spectra of polysulfide electrolyte based quantum-dot-sensitized solar cell (QDSCs) with 14 ± 1 μ m thick TiO₂ electrode.

Light intensity (% Sun)	R_{ct} (Ω cm ²)	R_{trans} (Ω cm ²)	C_{μ} (F cm ⁻²)	$R_{Cathode}$ (Ω)	$CPE_{Cathode}$	n_{CPE}	R_S (Ω)
0.1	3092.045	16.15	0.00403	55	4×10^{-5}	0.6	35
1.2	421.175	7.65	0.0059	20	4.5×10^{-5}	0.62	39
6.5	93.5	4.675	0.00781	20	4.7×10^{-4}	1	40
11	57.12	3.825	0.00843	20	4.7×10^{-4}	1	40
21	29.75	2.125	0.00934	20	4.1×10^{-4}	1	40
55	11.815	0.765	0.01162	19	4.3×10^{-4}	1	38.5
100	7.14	0.425	0.0131	18	4.1×10^{-4}	1	37.8

Table A-3.3. Parameters for the equivalent circuit obtained from fitting the experimental impedance spectra of complete (C1 and C2) and blank (C3 and C4) solid-state QDSCs.

Voltage (mV)	Cells	R_{ct} ($\Omega \text{ cm}^2$)	C_{μ} (F cm^{-2})	R_{HTM} (Ω)	CPE_{HTM}	n_{CPE}	$R_{Cathode}$ (Ω)	$CPE_{Cathode}$	n_{CPE}	R_S (Ω)
157	C1	9.93×10^6	6.33×10^{-6}	1500	5.78×10^{-4}	0.5	3200	4.93×10^{-8}	0.72	25
150	C2	1.68×10^6	7.29×10^{-6}	2500	3.82×10^{-6}	0.89	1400	4.33×10^{-8}	0.76	55
150	C3	4.47×10^6	5.89×10^{-6}	2000	2×10^{-5}	0.69	760	9.73×10^{-9}	0.82	45
150	C4	794772	6.50×10^{-6}	1500	4.22×10^{-5}	0.5	270	3.61×10^{-8}	0.77	66
202	C1	3.29×10^6	8.52×10^{-6}	1500	2.33×10^{-4}	0.5	3100	3.62×10^{-8}	0.74	25
201	C2	494879	7.86×10^{-6}	2500	2.32×10^{-6}	0.87	1300	4.21×10^{-8}	0.76	55
200	C3	1.67×10^6	6.72×10^{-6}	1700	5.47×10^{-6}	0.69	740	1.47×10^{-8}	0.79	45
200	C4	571461	6.98×10^{-6}	1500	2.73×10^{-5}	0.6	270	3.52×10^{-8}	0.77	66
255	C1	763884	1.18×10^{-5}	1500	7.77×10^{-5}	0.55	3050	5.6×10^{-8}	0.71	25
253	C2	122738	8.96×10^{-6}	2500	2.45×10^{-6}	0.87	1150	2.91×10^{-8}	0.79	55
250	C3	493779	7.46×10^{-6}	1700	9.44×10^{-6}	0.69	740	1.33×10^{-8}	0.8	45
250	C4	361702	7.69×10^{-6}	1500	3.92×10^{-5}	0.55	270	3.67×10^{-8}	0.77	66
300	C1	236929	1.51×10^{-5}	1500	5.53×10^{-5}	0.65	2650	6.73×10^{-8}	0.7	25
303	C2	35097.7	1.04×10^{-5}	2500	3.51×10^{-6}	0.87	1050	3.45×10^{-8}	0.78	55
300	C3	117282	8.39×10^{-6}	1700	5.72×10^{-6}	0.76	730	1.17×10^{-8}	0.81	45
300	C4	164692	8.54×10^{-6}	1500	1.87×10^{-5}	0.65	270	3.53×10^{-8}	0.77	66
352	C1	61571.4	2.08×10^{-5}	1500	1.18×10^{-5}	0.9	2550	7.29×10^{-8}	0.69	25
351	C2	11138.6	1.14×10^{-5}	2500	3.38×10^{-6}	0.87	1100	3.92×10^{-8}	0.77	55
350	C3	26251.5	9.23×10^{-6}	1700	2.96×10^{-6}	0.86	720	1.17×10^{-8}	0.81	45
350	C4	50206.2	9.54×10^{-6}	1500	1.04×10^{-5}	0.71	270	3.56×10^{-8}	0.77	66
400	C1	17288.7	3.09×10^{-5}	1500	4.07×10^{-6}	0.9	2400	8.22×10^{-8}	0.68	25
398	C2	3921.5	1.16×10^{-5}	2500	2.62×10^{-6}	0.87	1000	3.85×10^{-8}	0.77	55
400	C3	5975.86	1.00×10^{-5}	1700	3.08×10^{-6}	0.85	720	1.35×10^{-8}	0.8	45
400	C4	12189.1	1.07×10^{-5}	1500	8.64×10^{-6}	0.75	265	3.07×10^{-8}	0.78	66
454	C1	4305.18	5.09×10^{-5}	1500	1.68×10^{-6}	0.93	2300	7.87×10^{-8}	0.68	25
448	C2	1456.51	1.19×10^{-5}	2000	2.09×10^{-6}	0.87	900	3.5×10^{-8}	0.79	55
450	C3	1365.98	1.10×10^{-5}	1800	2.38×10^{-6}	0.87	720	1.34×10^{-8}	0.8	45
450	C4	2846.91	1.16×10^{-5}	1500	5.83×10^{-6}	0.78	280	3.24×10^{-8}	0.77	55

A-4 TiO₂ and SnO₂ Blocking Layer (BL) Preparation

The TiO₂ BL was deposited via spray pyrolysis. Briefly, the substrates were placed on a hot plate and partially covered with microscope glass slides to ensure the selective application of the TiO₂ BL. The hot plate was heated to 450 °C for 30 min and then precursor solution (see below) was applied using an airbrush set with compressor to deposit the TiO₂ BL. The BL deposition was done manually by spraying the precursor solution for 2 sec at approximately 15 cm distance above the substrates. This procedure was repeated 12 times with 10 sec interval to achieve ~60 nm thick TiO₂ BL on the substrates. After spraying, the hot plate was kept for 5 min at 450 °C and then cooled down to room temperature. A 0.2 M solution of titanium(IV)bis(acetylacetonate)-diisopropylate in isopropanol was used as precursor for the TiO₂ BL. For deposition of the SnO₂ BL the above-described procedure was repeated using a 1:10 volume mix of butyltintrichloride in absolute ethanol as precursor solution.

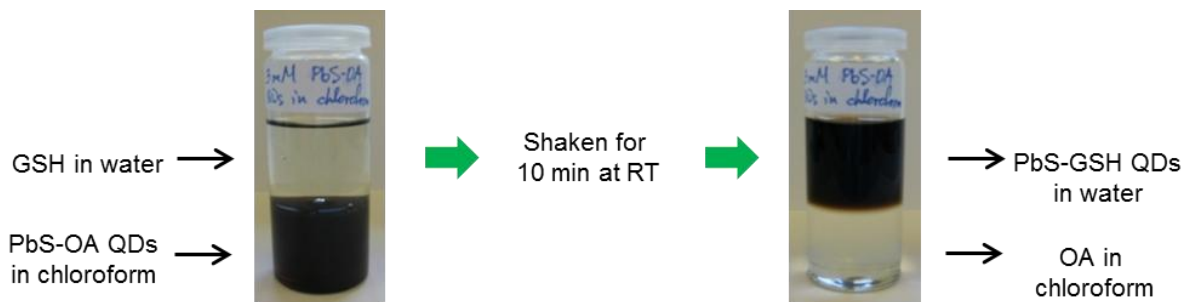
A-5 Synthesis of Oleic Acid Capped PbS Quantum Dots (PbS-OA QDs)

A stock solution of lead oleate was obtained by mixing 0.45 g of PbO, 1.5 mL of OA and 3 mL of 1-octadecene (ODE, degassed at 80 °C prior to use) and pumping under vacuum in a two-necked flask at 95 °C for 5 h while stirring. Then, 15 mL of ODE was added to the mixture and the mixture was heated to 125 °C under argon atmosphere. A mixture of 180 µL hexamethyldisilathiane ((TMS)₂S) with 10 mL of ODE was rapidly injected into the stock solution under vigorous stirring. The colour of the solution turned brown immediately. The heating oil bath was removed immediately and argon flow was reduced to a minimum. The mixture was allowed to cool down naturally over 40 min while stirring. Then the mixture was briefly pumped off to remove accumulated and possibly toxic gases, after which the mixture

was quenched with 55 mL of anhydrous acetone and stirred for 2 min. The resulting oleic acid capped PbS quantum dots (PbS-OA QDs) were collected by precipitation via centrifugation at 4000 rpm for 6 min. The PbS-OA QDs were redispersed in 6 mL of toluene and precipitated by adding 24 mL of anhydrous acetone and centrifuging at 12000 rpm for 5 min. The last step was repeated two more times to remove unreacted starting materials. Around 300 mg of PbS-OA QDs were collected after drying the precipitate under nitrogen. Finally, dry QDs were redispersed in toluene to produce 50 mg mL⁻¹ QD solution and stored in a refrigerator at -25 °C until performing the next step.

A-6 Water Solubilisation of PbS Quantum Dots Capped with Oleic Acid

The amount of 7.2 mg PbS-OA QD in 10 mL chloroform (3 mM solution) and 0.46 g GSH in 10 mL water (0.15 M solution) were mixed in a 40 mL glass vial by shaking at room temperature for 10 min. Prior to mixing, the pH of the GSH-water solution was adjusted to 5.0 by adding NaOH. Upon shaking, the GSH replaces OA and transfers the QDs into the aqueous phase. The two-phase water/chloroform system was then allowed to rest to separate the PbS QDs into the water and OA into the chloroform (Scheme A-6.). The water-soluble and GSH-capped PbS QDs (PbS-GSH QDs) were then collected and filtered with a 0.22 µm pore size filter and left in the dark in ambient atmosphere at room temperature until the next step. The pH of the PbS-GSH QDs in water remained at close to the initial pH value of the GSH-water solution. A typical aqueous QD solution contained 3 mM GSH-capped PbS QDs (PbS-GSH QDs) together with some additional free GSH ligands. A ratio of the number of PbS-GSH QDs to the number of free GSH ligands of approximately 1:1000 was utilized in order to optimize the stability and photoluminescence of the water-solubilized QDs.



Scheme A-6.1. Ligand exchange procedure.

A-7 Absorption Coefficient $\alpha(\lambda)$ of PbS-GSH Quantum Dots

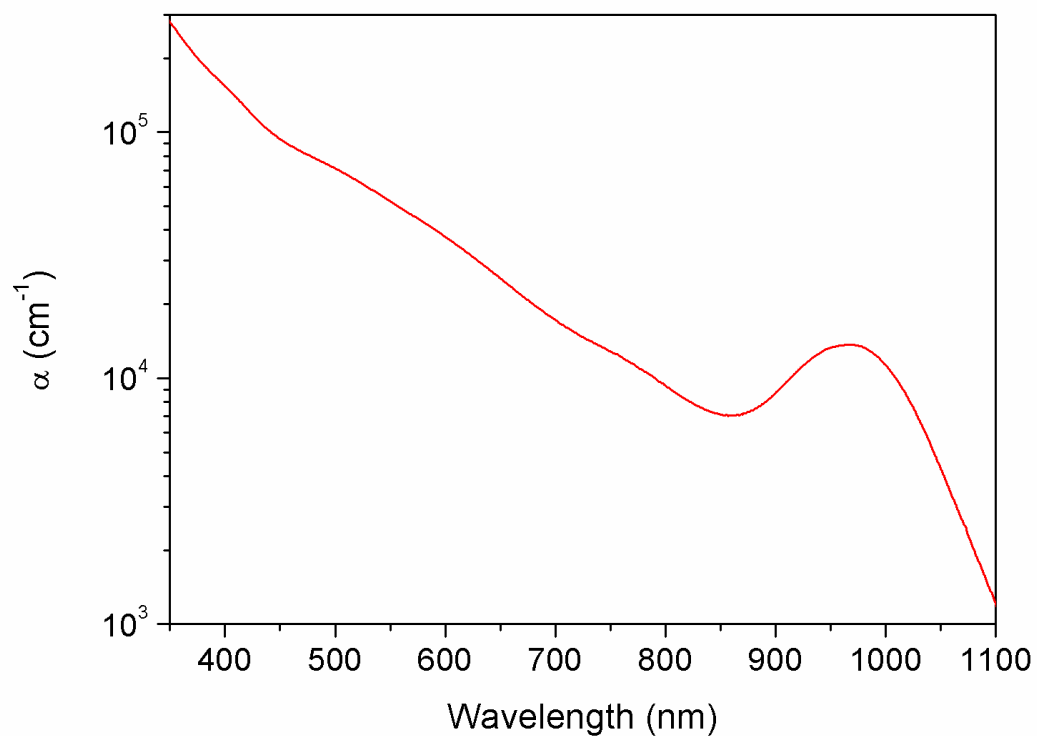


Figure A-7.1. Absorption coefficient of 3.1 nm sized PbS-GSH QDs as a function of wavelength.

A-8 Zeta Potential Measurements on P25 TiO₂ Nanoparticles

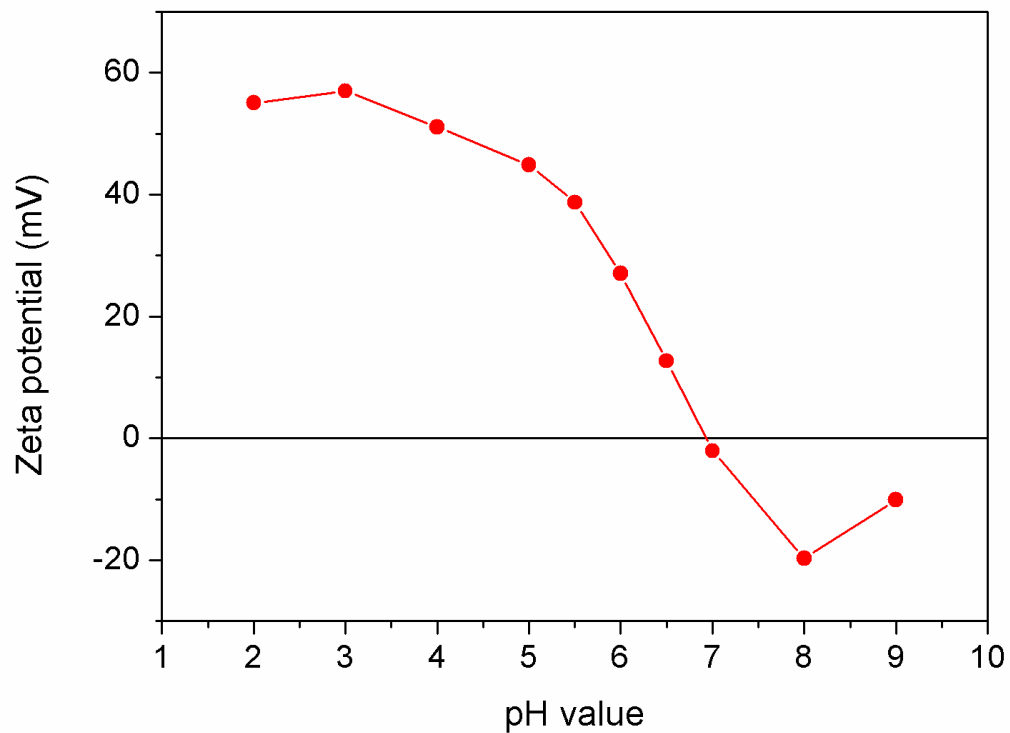


Figure A-8.1. pH dependence of zeta potential of TiO₂ P25 NPs.

A-9 Analysis of PbS-GSH Loading of the Macroporous TiO₂ Electrodes with Inductively-Coupled Plasma Atomic Absorption Spectroscopy (ICP/AAS) Measurements

Table A-9.1. ICP/AAS data for PbS mass and calculations for the optical thickness of the PbS.

Sample	Mass of PbS from ICP/AAS (g mL ⁻¹)	Total solution amount (mL)	Total mass of PbS (g)	Density of PbS (g cm ⁻³)	Volume of PbS (cm ³)	Geometric area of cell (cm ²)	Optical thickness of PbS (cm)
1	1.65×10 ⁻⁵	2.5	4.12×10 ⁻⁵	7.6	5.42×10 ⁻⁶	0.5	1.08×10 ⁻⁵
2	1.82×10 ⁻⁵	2.5	4.56×10 ⁻⁵	7.6	6×10 ⁻⁶	0.5	1.2×10 ⁻⁵
3	1.76×10 ⁻⁵	2.5	4.4×10 ⁻⁵	7.6	5.79×10 ⁻⁶	0.5	1.16×10 ⁻⁵

A-10 Analysis of the Effect of ZnS Protective Layer on the Performance of the Polysulfide Electrolyte Based QDSCs

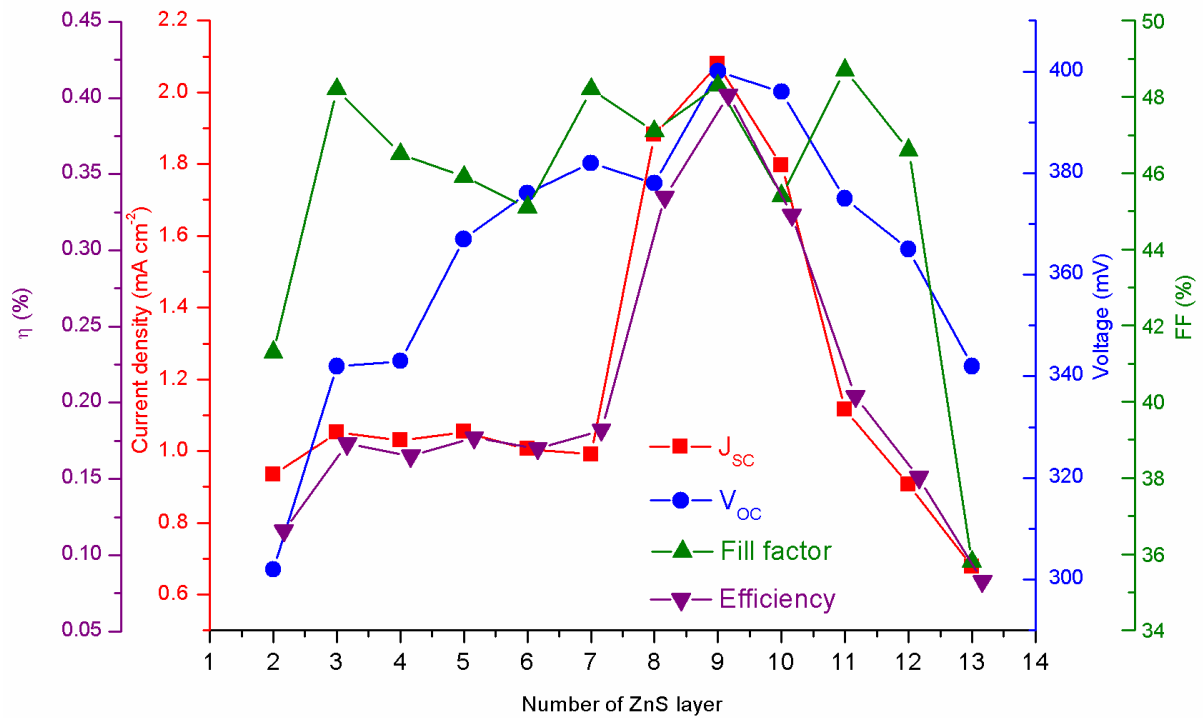


Figure A-10.1. Dependence of short circuit current density, J_{sc} , open circuit voltage, V_{oc} , fill factor, FF , and conversion efficiency, η , on the number of ZnS protective layers.

A-11 Analysis of the PbS QD-Sensitized TiO₂ Electrodes with Electron Microscopy

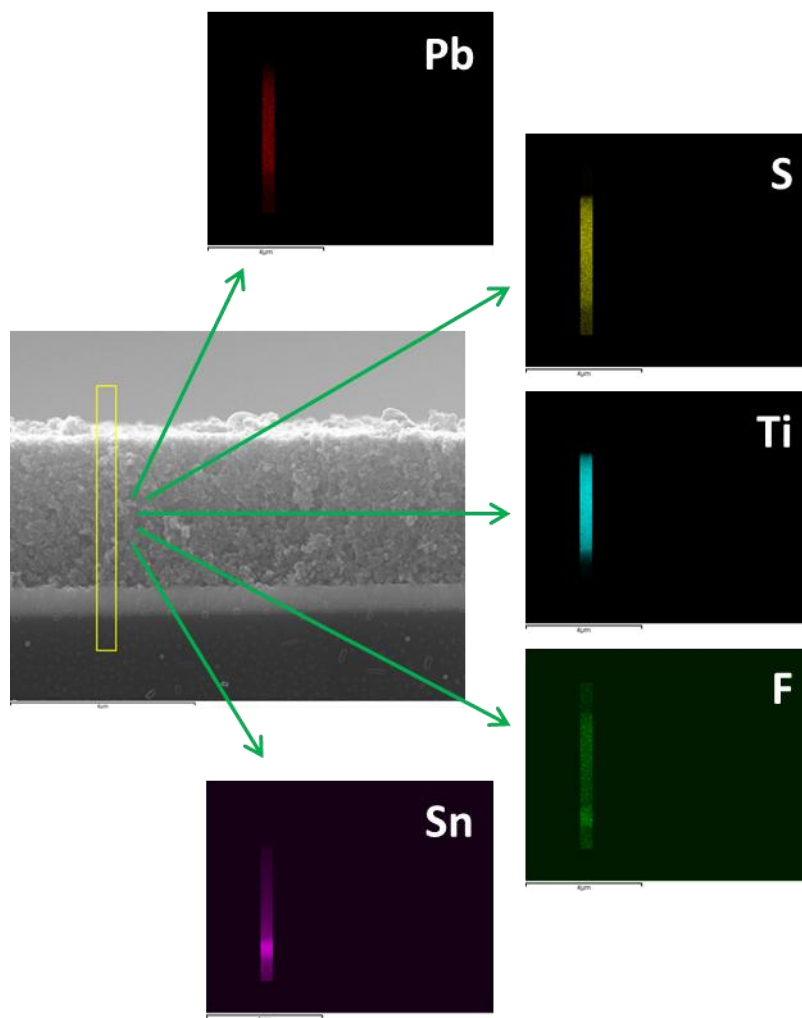
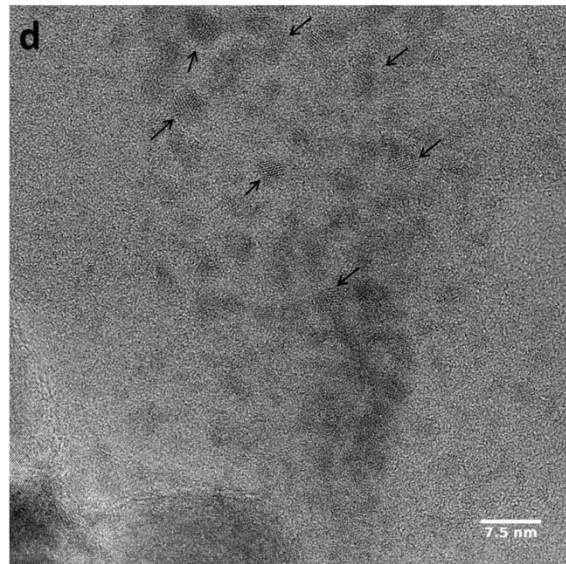
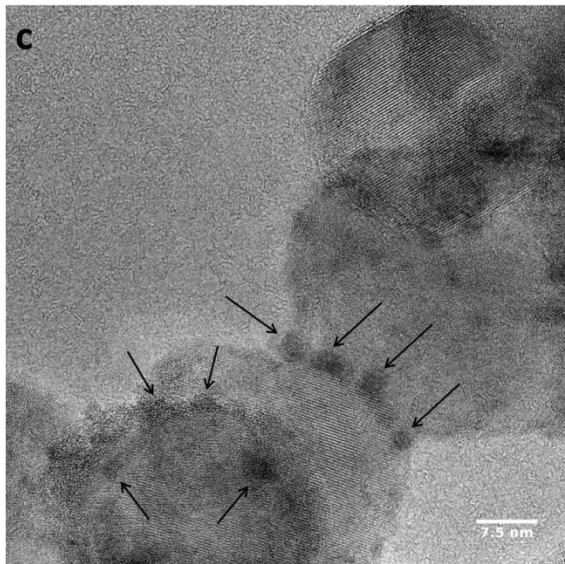
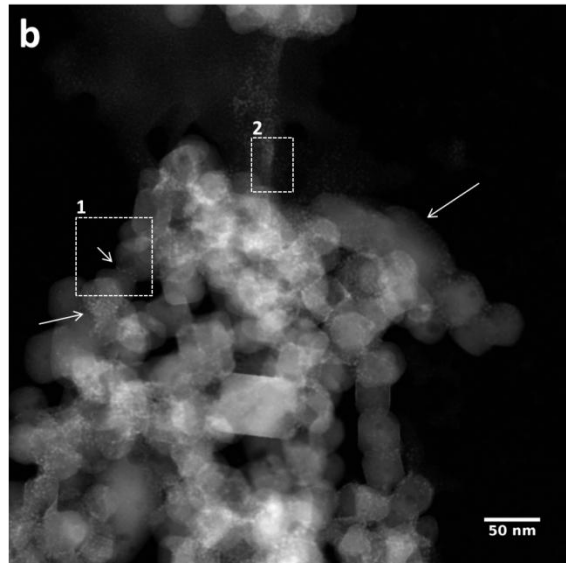
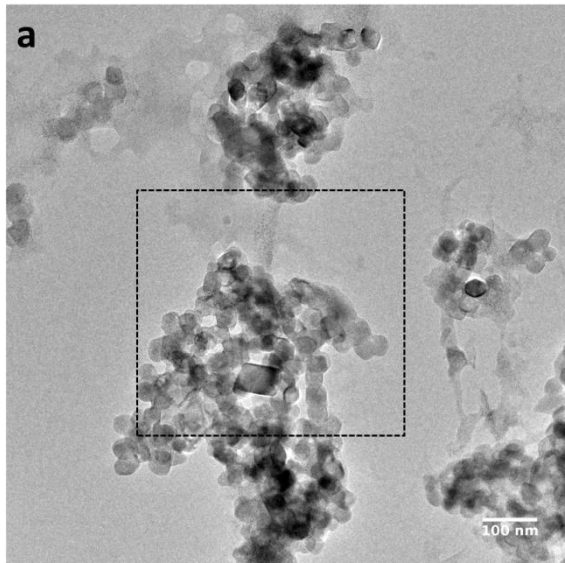


Figure A-11.1. Chemical mapping of a cross-section of a PbS-GSH QD-sensitized 3 ± 0.1 μm mesoporous TiO₂ electrode. Scale bars on the images are 4 μm.



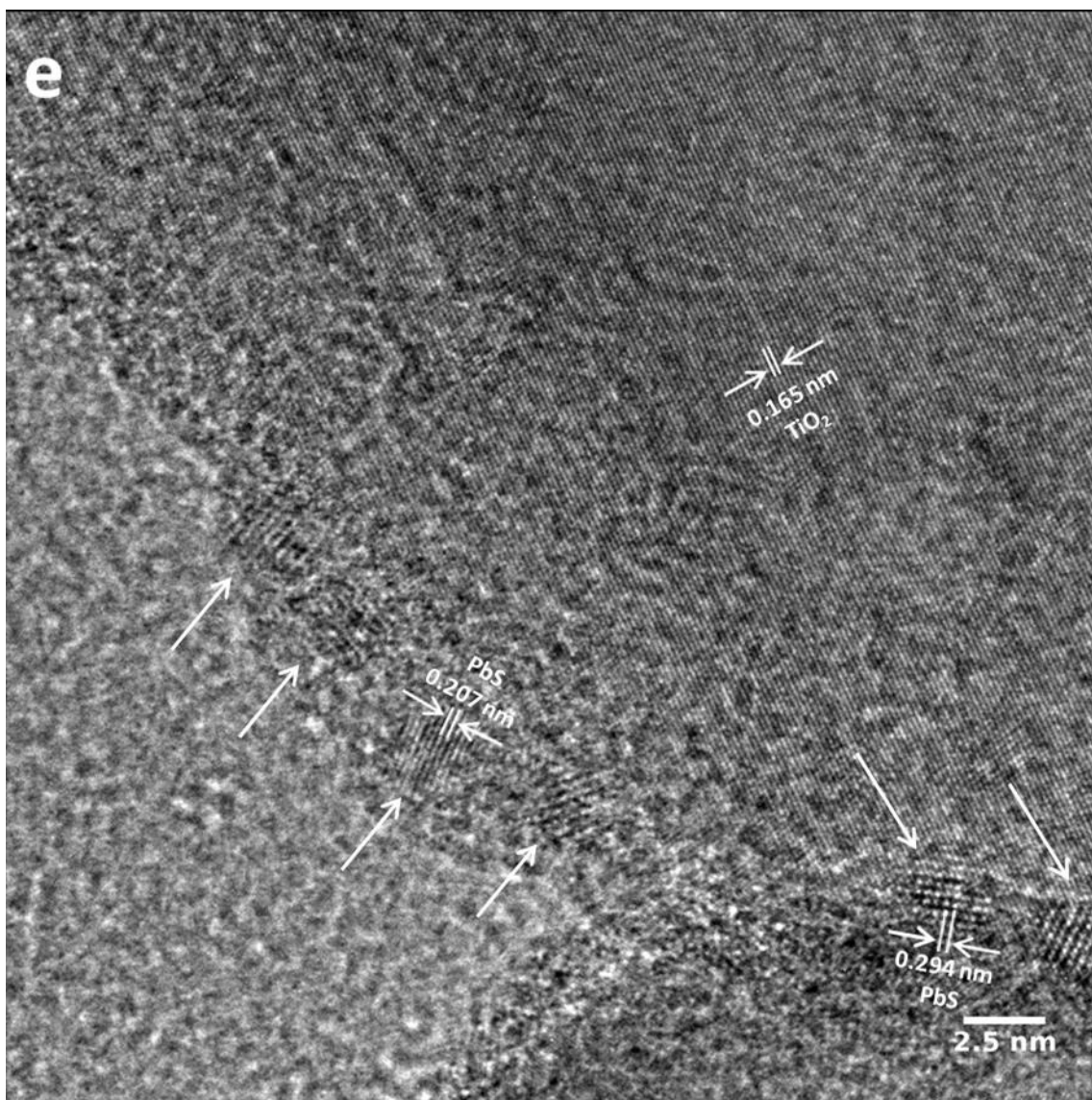


Figure A-11.2. TEM analysis of mesoporous TiO_2 sensitized with *ex situ* grown PbS QDs. (a) Bright field TEM image of TiO_2/PbS sample. (b) STEM image of an area (indicated as a dashed rectangle in the picture (a)) of the TiO_2/PbS sample. PbS QDs are visualised as bright spots on TiO_2 NPs (grey crystallites). High-resolution TEM (HRTEM) images of area 1 and area 2 (indicated as a dashed rectangles in the picture (b)) are shown in (c) and (d) correspondingly. Some of the PbS QDs (a few of them showing distinct crystalline fringes) are indicated with arrows in the pictures (c) and (d). Picture (d) shows that some of the PbS QDs have moved onto the carbon grid. This could be because a slightly more basic (pH \sim 7) aqueous solution was used to prepare a suspension from the TiO_2/PbS sample (the as-prepared aqueous solution of PbS QDs has pH of 5 (see experimental section in the main text)). Also the mild sonication of the sample may have resulted in the detachment of a few PbS-GSH QDs from TiO_2 and migration onto the carbon grid upon drying. Picture (e) depicts an HRTEM image of a TiO_2/PbS sample

in which edges of TiO_2 NPs decorated with PbS-GSH QDs can be seen. The estimated values of the d-spacing of PbS QDs (0.207 and 0.294 nm) as indicated in picture (e) are in excellent agreement with the literature values of 0.209 and 0.296 nm corresponding to the (220) and (200) lattice planes of PbS.² Estimation of the d-spacing of TiO_2 resulted in a value of 0.165 nm, which is in excellent agreement with the value of 0.166 nm corresponding to the (211) lattice plane of the standard (JCPDS File No. 01-089-4921). It should be noted that estimation of PbS QD coverage of the walls of TiO_2 from TEM analysis alone is complicated due to possible alterations occurring during the sample preparation process as mentioned above. Nevertheless, based on, for example, the STEM image (b), it is evident that surface coverage of TiO_2 with PbS-GSH QDs is quite high.

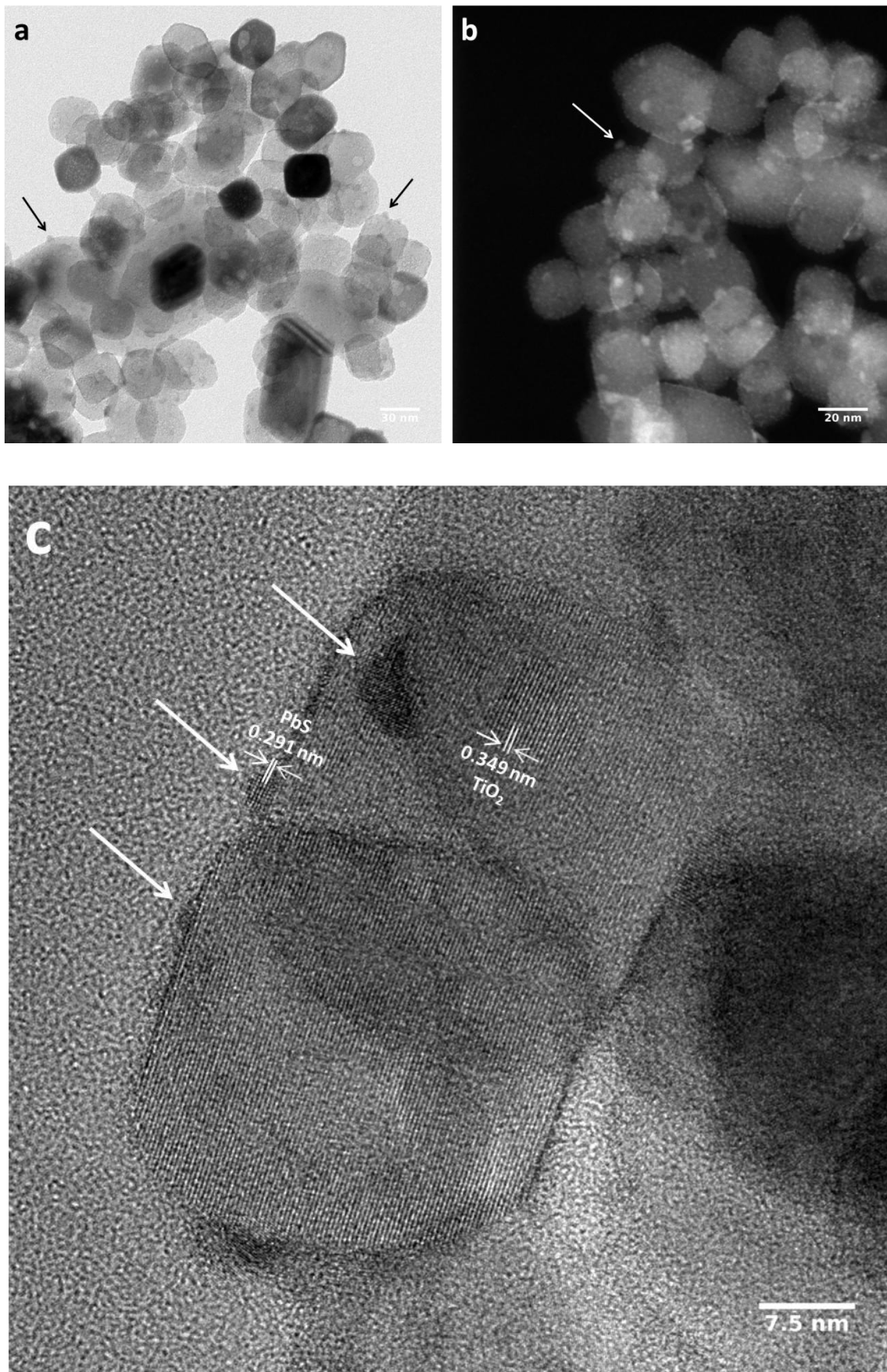


Figure A-11.3. TEM analysis of mesoporous TiO₂ sensitized with *in situ* grown PbS QDs. (a) Bright field TEM image of the TiO₂/PbS sample. (b) STEM image of the TiO₂/PbS sample in which PbS QDs are

visible as bright spots (with inhomogeneous size distribution) on TiO₂ NPs (grey crystallites). Picture (c) is the HRTEM image of the TiO₂/PbS sample in which the edges of TiO₂ NPs decorated with irregular-sized SILAR grown PbS QDs can be seen. The estimated d-spacing of PbS QD (0.291 nm) as indicated in picture (c) is in good agreement with the literature value of 0.296 nm, which corresponds to the (200) lattice plane of PbS.² Estimation of the d-spacing of TiO₂ resulted in 0.349 nm, which again is in excellent agreement with the value of 0.350 nm corresponding to the (101) lattice plane of the standard (JCPDS File No. 01-089-4921).

A-12 Dye desorption experiment

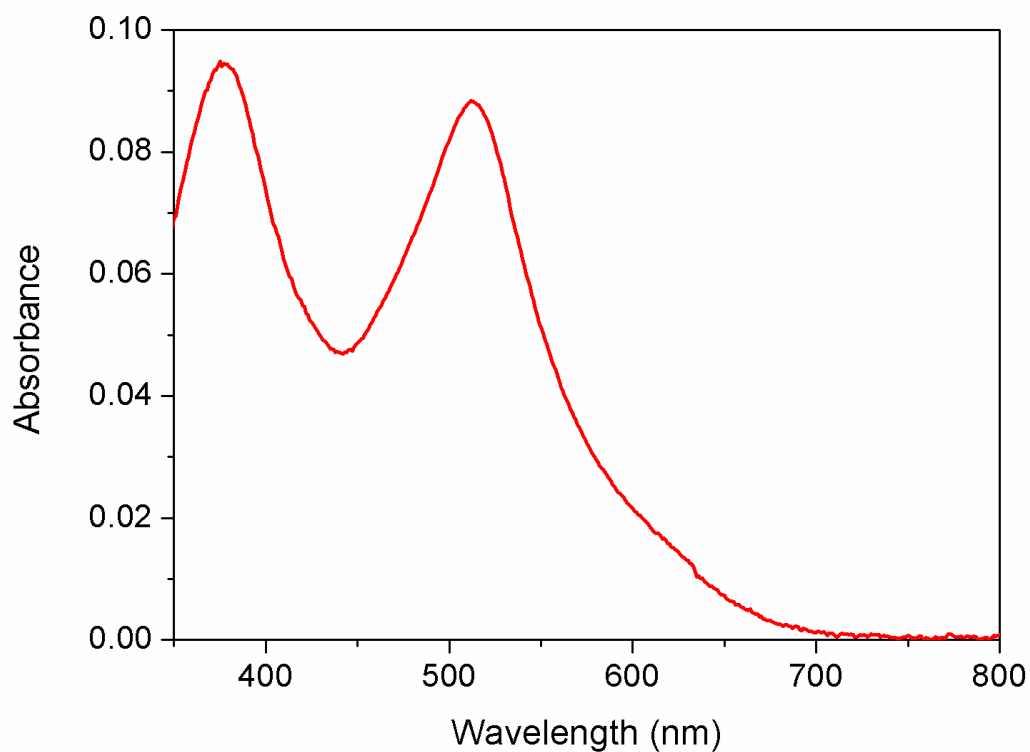


Figure A-12.1. UV-Vis spectrum of N719 dye desorbed from a mesoporous TiO₂ electrode with $3.0 \pm 0.1 \mu\text{m}$ thickness and 0.4 cm^2 effective area.

A-13 Synthesis of TiO₂ Nanoparticles

For the preparation of TiO₂ NPs, 2.2 mL of TiCl₄ was added to 60 mL of distilled water while stirring and the pH of the solution was adjusted to 7.0 by adding dropwise 28% ammonia solution (NH₄OH). The mixture was then heated at 90 °C for 1 h after which the white precipitate was filtered and washed with distilled water. Then, 100 mL of hydrogen peroxide (H₂O₂) was added to the precipitate and the suspension was stirred for 9 h at 100 °C. Afterwards, the mixture was transferred into a Teflon autoclave and heated for 24 h at 230 °C. The resulting TiO₂ NPs (~30 nm) were filtered and redispersed and washed with 10 mL of ethanol/water (1:1) and isolated via centrifugation at 1000 rpm.

A-14 Preparation of TiO₂ and SnO₂ Paste

For the preparation of the TiO₂ paste, 0.69 g of TiO₂ NPs was mixed with two types of ethyl cellulose (EC) (3.05 g of EC46070 (10 wt.% in ethanol) and 2.06 g of EC46080 (10 wt.% in ethanol) and 6 g of terpineol. The mixture was sonicated and stirred for 30 min with an ultrasonic horn and a hand-held mixer (Turrax), respectively. This last step was repeated three times to obtain a white viscous TiO₂ paste. For the preparation of the SnO₂ paste, the above procedure was repeated using SnO₂ NPs instead of TiO₂.

Appendix B: Glossary of Symbols

Symbol	Quantity	Unit
E^*	Energy of first excited electronic state (lowest eigenvalue)	eV
E_g	Bulk bandgap	eV
\hbar	Reduced Planck constant	eV s
m_e	Mass of electron	kg
m_h	Mass of hole	kg
R_p	Radius of particle	nm
ϵ	Dielectric constant	
a_B	Bohr exciton radius	nm
a_0^H	Bohr radius of hydrogen	nm
d_{QD}	Diameter of particle	nm
J_{SC}	Short circuit current	mA cm ⁻²
V_{OC}	Open circuit voltage	V
FF	Fill factor	%
η	Power conversion efficiency	%
P_{in}	Power of incident light	mW cm ⁻²
λ	Wavelength	nm
d	Spacing between atomic planes	Å
θ	Brag angle	degrees
p	Pressure	N m ⁻²
p_0	Saturation pressure	N m ⁻²
n^a	Amount of adsorptive	
n_m^a	Monolayer capacity	
C	BET constant	
L	Avogadro constant	mol ⁻¹
a_m	Footprint of adsorptive	Å ²
r	Principal radius of curvature	nm

R	Universal gas constant	$\text{J K}^{-1} \text{mol}^{-1}$
T	Absolute temperature	K
σ^{1g}	Surface tension	N m^{-1}
v_1	Molar volume	$\text{m}^3 \text{mol}^{-1}$
h	Planck constant	eV s
m_0	Electron rest mass	kg
e	Electron charge	C
c	Speed of light	m s^{-1}
V	Voltage	V
A	Absorbance	
I	Intensity of transmitted light	$\text{cm}^{-2} \text{s}^{-1}$
I_0	Intensity of incident light	$\text{cm}^{-2} \text{s}^{-1}$
ε	Molar absorptivity	$\text{cm}^2 \text{mol}^{-1}$
c_s	Concentration of absorbing species	mol cm^{-3}
d_s	Path length of sample	cm
P_{mpp}	Maximum power point	mW cm^{-2}
J_{mp}	Current density at maximum power point	mA cm^{-2}
V_{mp}	Voltage at maximum power point	V
η_{LHE}	Light harvesting efficiency	
η_{inj}	Injection efficiency	
η_c	Collection efficiency	
P_{in}	Power of incident light	mW cm^{-2}
τ_n	Electron lifetime	s
k_B	Boltzmann constant	J K^{-1}
t	Time	s
i	Current	A
Φ	Photon flux	$\text{photons m}^{-2} \text{sec}^{-1}$
ω	Angular frequency	rad s^{-1}
τ_{trans}	Electron transport time	s
d_f	Thickness of the active layer film	cm
γ	IMPS factor	
D_n	Diffusion coefficient	$\text{cm}^2 \text{s}^{-1}$
α	Absorption coefficient	cm^{-1}

Z	Impedance	ohm
R_{Sub}	Substrate resistance	ohm
C_{Sub}	Substrate capacitance	F
R_{CuSCN}	Resistance of CuSCN hole transporter	ohm
C_{CuSCN}	Capacitance of CuSCN hole transporter	F
R_S	Series resistance	ohm
R_{ct}	Electron recombination resistance	ohm cm ²
R_{trans}	Electron transport resistance	ohm cm ²
C_μ	Chemical capacitance	F cm ⁻²
L_n	Effective electron diffusion length	cm
m	Non-ideality factor	
$R_{cathode}$	Faradaic resistance of cathode	ohm
A_R	Roughness factor	cm ² cm ⁻²
f	Frequency	Hz
R_{HTM}	Resistance of hole transporter	ohm
N_{dye}	Number of dye molecules	
a_{dye}	Footprint of a single dye molecule	Å ²

10 Curriculum Vitae

Personal Information

Name: Askhat N. Jumabekov
Gender: Male
Date of Birth: 25.03.1986
Place of Birth: Almaty, Kazakhstan
Nationality: Kazakhstan

Education

2010-present Ludwig-Maximilians-Universität München (LMU), Germany
PhD candidate in Physical Chemistry
2009-2010 Imperial College London, London, United Kingdom
Master of Research, Chemistry (Nanomaterials)
2009-2009 University College London, London, United Kingdom
Pre-sessional Courses (Premaster)
2003-2008 Al Farabi Kazakh National University, Almaty, Kazakhstan
Engineer-Physicist (BSc), Physics (Radiophysics and Electronics)
1991-2003 School №19, Golovatsky Town, Kazakhstan

Awards and Scholarship

2010-2013 DAAD scholarship for postgraduate studies
2009-2010 International Educational Award of Kazakhstan
2003-2008 Educational Grant of Ministry of Education of Kazakhstan

Languages

Kazakh Mother Tongue
Russian Fluent
English Fluent
German Beginner level (A2)

11 Publications and Presentations

11.1 Publications

1. A. N. Jumabekov, T. D. Siegler, N. Cordes, D. D. Medina, D. Böhm, P. Garbus, S. Meroni, L. M. Peter, T. Bein, *J. Phys. Chem. C*, 2014, **DOI**: 10.1021/jp5051904.
2. A. N. Jumabekov, F. Deschler, D. Böhm, L. M. Peter, J. Feldmann, T. Bein, *J. Phys. Chem. C*, 2014, **118**, 5142.
3. T. S. Ramazanov, A. N. Jumabekov, S. A. Orazbayev, M. K. Dosbolayev, M. N. Jumagulov, *Phys. Plasmas*, 2012, **19**, 023706.
4. T. S. Ramazanov, S. K. Kodanova, O. F. Petrov, S. N. Antipov, K. N. Dzhumagulova, M. K. Dosbolayev, A. N. Jumabekov, *J. Phys. A: Math. Theor.*, 2009, **42**, 214026.
5. G. I. Sukhinin, A. V. Fedoseev, T. S. Ramazanov, R. Zh. Amangaliyeva, M. K. Dosbolayev, A. N. Jumabekov, *J. Phys. D: Appl. Phys.*, 2008, **41**, 245207.
6. S. A. Moiorov, T. S. Ramazanov, K. N. Dzhumagulova, M. K. Dosbolayev, A. N. Jumabekov, *Phys. Plasmas*, 2008, **15**, 093701.
7. T. S. Ramazanov, K. N. Dzhumagulova, A. N. Jumabekov, and M. K. Dosbolayev, *Phys. Plasmas*, 2008, **15**, 053704.

11.2 Poster Presentations

1. Hybrid Solid-State PbS Quantum-Dot-Sensitized Solar Cells with SnO₂ Electrodes.
A. N. Jumabekov, D. Böhm, L. M. Peter and T. Bein, 6th Hybrid Organic Photovoltaic Conference - Lausanne 2014 (HOPV14), **2014**, Lausanne, Switzerland.
2. Extremely Thin Absorber Solar Cells with *In Situ* Grown Lead Sulfide Quantum Dots.
A. N. Jumabekov, M. Nedelcu, H. Sai, U. Wiesner, L. M. Peter and T. Bein, CeNS Workshop 2013, **2013**, Venice, Italy.
3. Impedance Spectroscopy Studies on Extremely Thin Absorber Solar Cells.
A. Jumabekov, L. M. Peter and T. Bein, NIM Winter School 2013, **2013**, Kirchberg, Tyrol, Austria.
4. Block Copolymer Templated TiO₂ Films in Extremely Thin Absorber Solar Cells.

- A. N. Jumabekov, M. Nedelcua, L. M. Peter, H. Sai, U. Wiesner, and T. Bein, 4th Hybrid and Organic Photovoltaic Conference - Uppsala 2012 (HOPV12), **2012**, Uppsala, Sweden.
5. Optical Investigation of Dusty Particles Distribution in RF and DC Discharges.
T. S. Ramazanov, M. K. Dosbolayev, A. N. Jumabekov, R. Zh. Amangaliyeva, I. I. Filatova and V. V. Azharonok, Multifacets of Dusty Plasmas : Fifth International Conference on the Physics of Dusty Plasmas (ICPDP5), **2008**, Ponta Delgada, Azores, Portugal.
 6. Dependence of Dusty Particle's Charge on its Displacement in a Stratum of DC Discharge.
T. S. Ramazanov, G. I. Sukhinin, A. V. Fedoseev, R. Zh. Amangaliyeva, A. N. Jumabekov, M. K. Dosbolayev, A. A. Kambarov, 2nd International Conference on the Physics of Dusty and Burning Plasmas, **2007**, Odessa, Ukraine.

11.3 Oral Presentations

1. The Potential of Silicon-Based Ligands in Metal-Organic Frameworks.
R. P. Davies, A. N. Jumabekov, R. J. Less, P. D. Lickiss, K. Robertson, K. G. Sandeman, A. J. P. White, TechConnect World 2010: Nanotech, Clean Technology, Microtech, Bio Nanotech, **2010**, Anaheim, California, USA
2. Characteristics of Buffer Low Temperature Gas-Discharge Plasma in Plasma-Dust Experiments. Data of Probe Diagnostics.
T. S. Ramazanov, A. N. Jumabekov, M. K. Dosbolayev, 5th International Conference on Plasma Physics and Plasma Technology, **2006**, Minsk, Belarus